Macrocyclic Oligothiophene Bridged Perylene Bisimide Donor−Acceptor Dyads

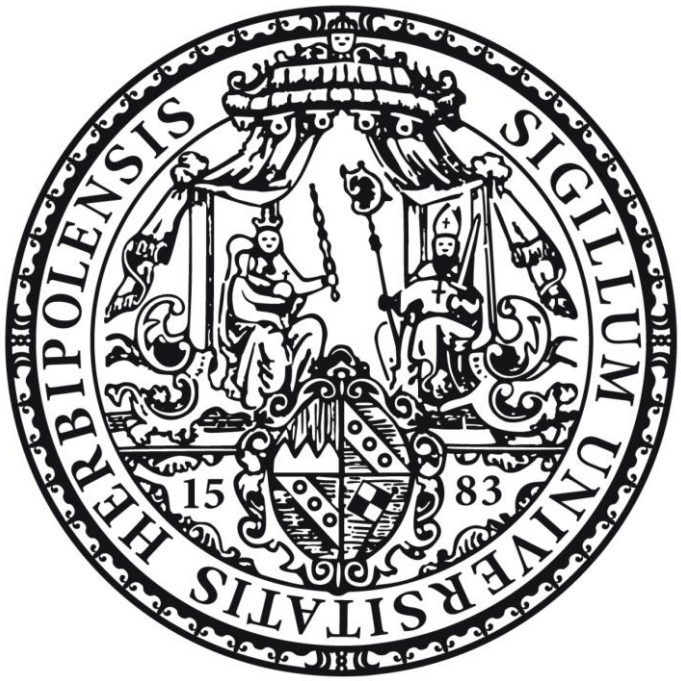

Dissertation zur Erlangung des

naturwissenschaftlichen Doktorgrades

der Julius-Maximilians-Universität Würzburg

vorgelegt von

Kevin Bold

aus Hannover

Würzburg 2022

Eingereicht bei der Fakultät für Chemie und Pharmazie am

03.02.2022

Gutachter der schriftlichen Arbeit:

1. Gutachter: Prof. Dr. Frank Würthner

2. Gutachter: Prof. Dr. Holger Helten

Prüfer des öffentlichen Promotionskolloquiums:

1. Prüfer: Prof. Dr. Frank Würthner

2. Prüfer: Prof. Dr. Holger Helten

3. Prüfer: Jun.-Prof. Dr. Ann-Christin Pöppler

Datum des öffentlichen Promotionskolloquiums:

04.05.2022

Doktorurkunde ausgehändigt am:

_____

List of Abbreviations:

A	acceptor
Ac	acetyl
ADP	adenosine diphosphate
Ar	aryl
ATP	adenosine triphosphate
Bu	butyl
BuLi	butyllithium
C[*n*]T	cyclo[*n*]thiophene
COD	1,5-cyclooctadiene
CPP	cycloparaphenylene
CSS	charge separated state
CT	charge transfer
CV	cyclic voltammetry
D	donor
dba	dibenzylideneacetone
DCTB	*trans*-2-[3-(4-*tert*-butylphenyl)-2-methyl-2-propenylidene]malononitrile
DDQ	2,3-dichloro-5,6-dicyano-*p*-benzochinone
DFT	density functional theory
dppe	1,2-bis(diphenylphosphino)ethane
dppf	1,1′-ferrocenediyl-bis(diphenylphosphine)
dppp	1,3-bis(diphenylphosphino)propane
DPV	differential pulse voltammetry
EA	excited state absorption
EADS	evolution-associated difference spectra
ESI	electronspray ionization
ESR	electron spin resonance
ET	electron transfer
Et	ethyl

Fc^+/Fc	ferrocenium/ferrocene redox couple
FRET	Förster resonance energy transfer
GPC	gel permeation chromatography
GSB	ground state bleach
HOMO	highest occupied molecular orbital
HOPG	highly ordered pyrolytic graphite
HRMS	high-resolution mass spectrometry
IRF	instrument response function
LDA	lithium diisopropylamide
LUMO	lowest unoccupied molecular orbital
m	meta
m.p.	melting point
MALDI	matrix-assisted laser desorption ionization
MO	molecular orbital
NBI	naphthalene bis(dicarboximide)
NBS	*N*-bromosuccinimide
NICS	nucleus-independent chemical shift
NIR	near-infrared
NMR	nuclear magnetic resonance
o	ortho
OLED	organic light emitting diode
OSC	organic solar cell
OFET	organic field-effect transistor
p	para
PBI	perylene bis(dicarboximide)
PEDOT	poly(3,4-ethylenedioxythiophene)
PET	photoinduced electron transfer
PLQY	photoluminescence quantum yield
ROESY	rotating frame nuclear overhauser effect spectroscopy
SE	stimulated emission

SEC	spectroelectrochemistry
SOMO	singly occupied molecular orbital
STM	scanning tunneling microscopy
SWCNT	single-walled carbon nanotube
TA	transient absorption
TS	transition state
TBAF	tetrabutylammoniumfluoride
TCSPC	time-correlated single-photon counting
TD	time-dependent
TEXDMS	(2,3-dimethylbutan-2-yl)dimethylsilyl
THF	tetrahydrofurane
Thi	thianthrenium
TMEDA	tetramethylethylenediamine
TMS	trimethylsilyl
TOF	time of flight
UV	ultraviolet
Vis	visible

Physical Constants, Variables and Units

$\Delta G^{\ddagger}$	Gibbs free energy of activation
ΔG^{*}	energy barrier
ΔG^{00}	driving force
a.u.	arbitrary unit
c_0	concentration
cal	calorie(s)
$E_{ox,1}$	first oxidation potential
$E_{ox,2}$	second oxidation potential
$E_{ox,2} - E_{ox,1}$	difference between first and second oxidation potential
$E_{ox,3}$	third oxidation potential
$E_{ox,4}$	fourth oxidation potential

$E_{red,1}$	first reduction potential
$E_{red,1}$	second reduction potential
F	Faraday constant
h	hour(s)
h	Planck constant
$J(\lambda)$	overlap of normalized donor emission spectrum with absorption spectrum
k	kilo
k	rate constant
K	Kelvin
K	comproportionation constant
k_B	Boltzmann constant
min	minute(s)
n_{ref}	refractive index
r	center-to-center distance
R	universal gas constant
R_0	Förster distance
s	seconds
T	temperature
$t_{1/2}$	half-life time
V	electronic coupling between two redox centers
ε	molar extinction coefficient
κ	transition dipole orientation
λ	wavelength
λ_E	reorganization energy
λ_o	solvent reorganization energy
λ_v	inner reorganization energy
$\tilde{\nu}_{Stokes}$	Stokes shift
τ	lifetime
Φ	quantum yield

Table of Contents

Chapter 1
Introduction and Aim of the Thesis

The molecular mimicry of highly efficient natural photosynthesis with readily available laboratory systems displays the holy grail of research fields dedicated to renewable energies.[1-3] The conversion of solar energy into chemical potential was perfected by nature over billions of years and can be explained in the following simplified way.[4] Sunlight is absorbed by antenna pigments and the resulting excitation energy is transferred to a reaction center in order to launch a series of electron transfer (ET) processes, which results in a long-lived charge separation across the photosynthetic membrane. Subsequently, this energy potential creates an osmotic gradient by pumping protons through the membrane. The resulting charge disequilibrium enables the enzymatic conversion of adenosine diphosphate (ADP) to adenosine triphosphate (ATP), a highly efficient fuel for the final carbon fixation cycle.

The breakdown of this orchestrated interplay into individual photophysical and chemical processes is the method of choice when striving towards molecular systems that are capable of mimicking at least certain aspects of natural photosynthesis. A substance class, which can undergo such energy- as well as electron transfer upon photoexcitation are molecular dyads.[5] Here, a donating electron-rich (D) molecule is covalently linked to an accepting electron-deficient (A) system. Photoinduced electron transfer (PET) from the donor to the acceptor then creates a charge separated state (CSS), which subsequently recombines to the ground state. The prerequisites for an efficient artificial photosynthetic apparatus in form of a molecular dyad are effective panchromic light absorption, very fast CSS formation and a long lifetime thereof.[6-10] In this way *e.g.* in a bulk-heterojunction organic solar cell the deciding two-component active layer creates sufficient amounts of charges capable of producing electric current.[11-13] For this purpose, countless dyads with various donor-acceptor (D-A) combinations are described in literature.[14-21]

In natural photosynthesis, D-A architectures involved in the final charge separation step are constraint by a protein matrix.[22] This conformational captivation ensures constantly high ET

rates. On the other hand, flexible systems would lead to imperfect conformations potentially unable to deliver sufficient charge separation yields from the absorbed photons. Additionally, this restriction of D-A distance and orientation also dramatically facilitates the investigations thereof.[23-24] One possibility for a chemist to create rigid supramolecular structures is the synthesis of macrocycles.[25] In order to ascertain high extinction coefficients in the UV/Vis spectral region these cyclic arrangements must comprise conjugated π-systems.

The research field of functional and shape persistent π-conjugated macrocycles evolved tremendously in the last two decades.[26-27] These nanohoops not only display aesthetically appealing targets but also offer the possibility to widen the synthetic toolbox for novel application possibilities. While the synthesis of such structures remains challenging[28-33], the final products reveal highly interesting photophysical properties, especially in comparison to their respective non-cyclic counterparts.[34-35] In this regard, with their linear analogues representing a frequently utilized substance class *e.g.* in organic light emitting diodes (OLEDs)[36] as emitting layers, organic solar cells (OSCs)[37] or as transporting polymers in organic field-effect transisters (OFETs)[38-39], cyclic[*n*]oligothiophenes (C[*n*]T, (*n* = amount of thiophene subunits) display a classic example in the cosmos of π-conjugated nanorings.[40] Both research fields are discussed in more detail in *Chapter 2*.

The rigid embedment of a suitable acceptor in such a C[*n*]T ring architecture will complete the molecular design of the intended macrocyclic D-A dyad. Besides a wide variety of successfully implemented electron-poor compounds in D-A macrocycles[41-44] such as anthraquinones[45], pyridinium units[46], diketopyrrolopyrrols[47] or benzothiadiazole[48], perylene bis(dicarboximides) (PBIs)[49] appear as one of the most promising canditates for this purpose, as they exhibit exquisite optical properties such as quantum yields close to unity, are photochemically stable and can be readily substituted in various ways.[50-51] The unique combination of oligothiophenes with PBIs is reported several times in literature, mostly in form of flexibly linked dyads (Chart 1). [52-59] This kind of D-A combination is particularly useful in terms of panchromic light absorption[60] as the more or less (chain size-dependent) high energy oligothiophene absorption is extended far into the visible range by the PBI acceptor unit. Intriguingly, also macrocyclic bithiophene bay-bridged PBIs were synthesized more recently (Chart 1).[61-64] However, the large dimension between the imide units of a single PBI chromophore has never been covalently tethered. In this regard, the aim of the present thesis

is to combine a PBI as acceptor with oligothiophenes as donors in a macrocyclic architecture to construct highly rigid molecular dyads with extremely small D-A distances (Chart 1). This research combines interesting aspects of functional π-conjugated macrocycles with D-A dyads and thereby bridges the gap between the currently most advanced synthetic functional molecules and artificial photosynthetic scaffolds. The macrocyclic related property changes in comparison to the linear oligothiophene analogues is also highlighted within this thesis.

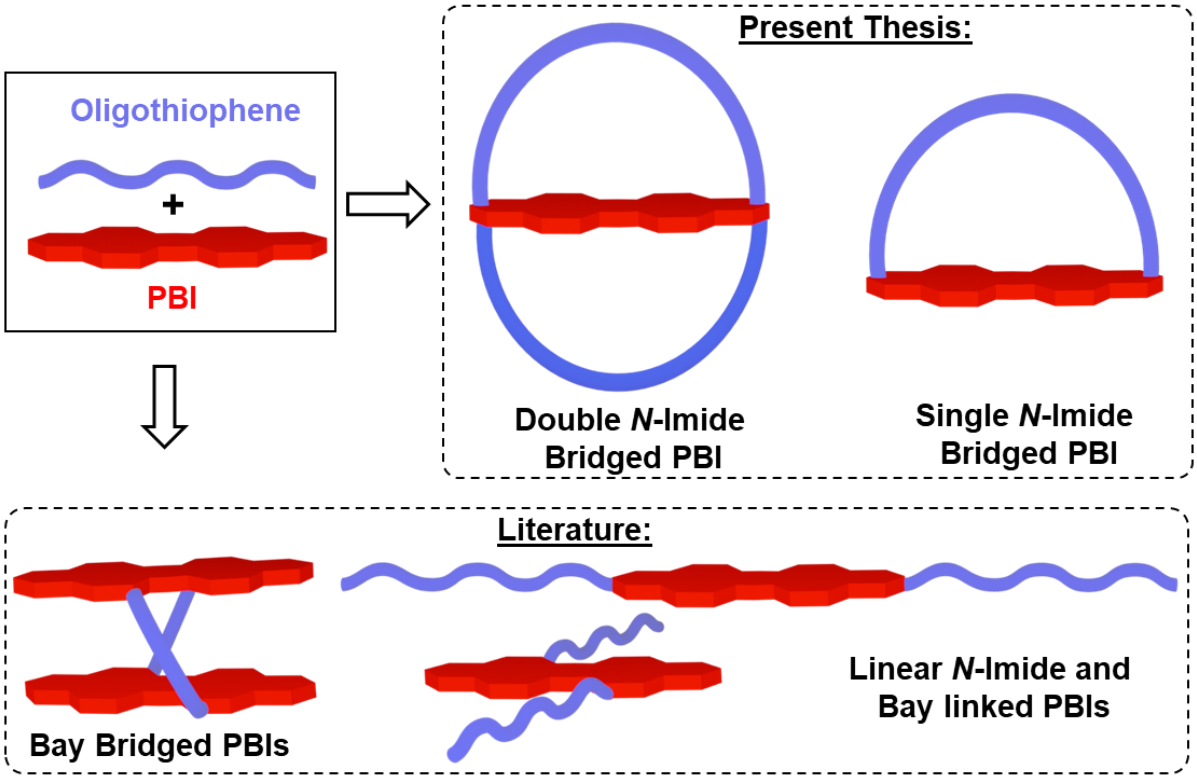

Chart 1. Simplified representation of the target structures presented in this thesis (above) in comparison to a selection of related literature known examples (below). All other structural elements next to the donating oligothiophene (blue) and accepting PBI (red) units in the dyads were omitted for clarity.

First, *Chapter 2* describes the synthesis and key features of linear α-oligothiophenes and especially highlights the charged state properties in solution. Subsequently synthetic approaches towards C[*n*]Ts as well as [*n*]cycloparaphenylenes ([*n*]CPPs, *n* = amount of phenyl subunits) are explained in detail and the optoelectronic properties of these bent π-conjugated systems are described. Lastly, the photoinitiated energy- and ET processes of PBI-oligothiophene D-A dyads as well as transient absorption (TA) spectra as the main monitoring tool thereof are elucidated.

In *Chapter 3* phenyl end-capped α-oligothiophenes are investigated regarding their length dependent photophysical behavior and especially their electronic properties, which are strongly influenced by the aliphatic decoration pattern of the chains (Chart 2).

Then, *Chapter 4* deals with the synthesis of the above discussed PBI dye, where the imide phenyl units are tethered by one and two quinquethiophene strands (Chart 2). This entirely novel cyclic oligothiophene enclosure of a PBI chromophore was also examined by single crystal structure analysis. Absorption, emission and redox properties as well as excited state dynamics revealed highly interesting insights into macrocycle specific features of these D-A dyads. All photophysical results were corroborated by DFT and TDDFT calculations.

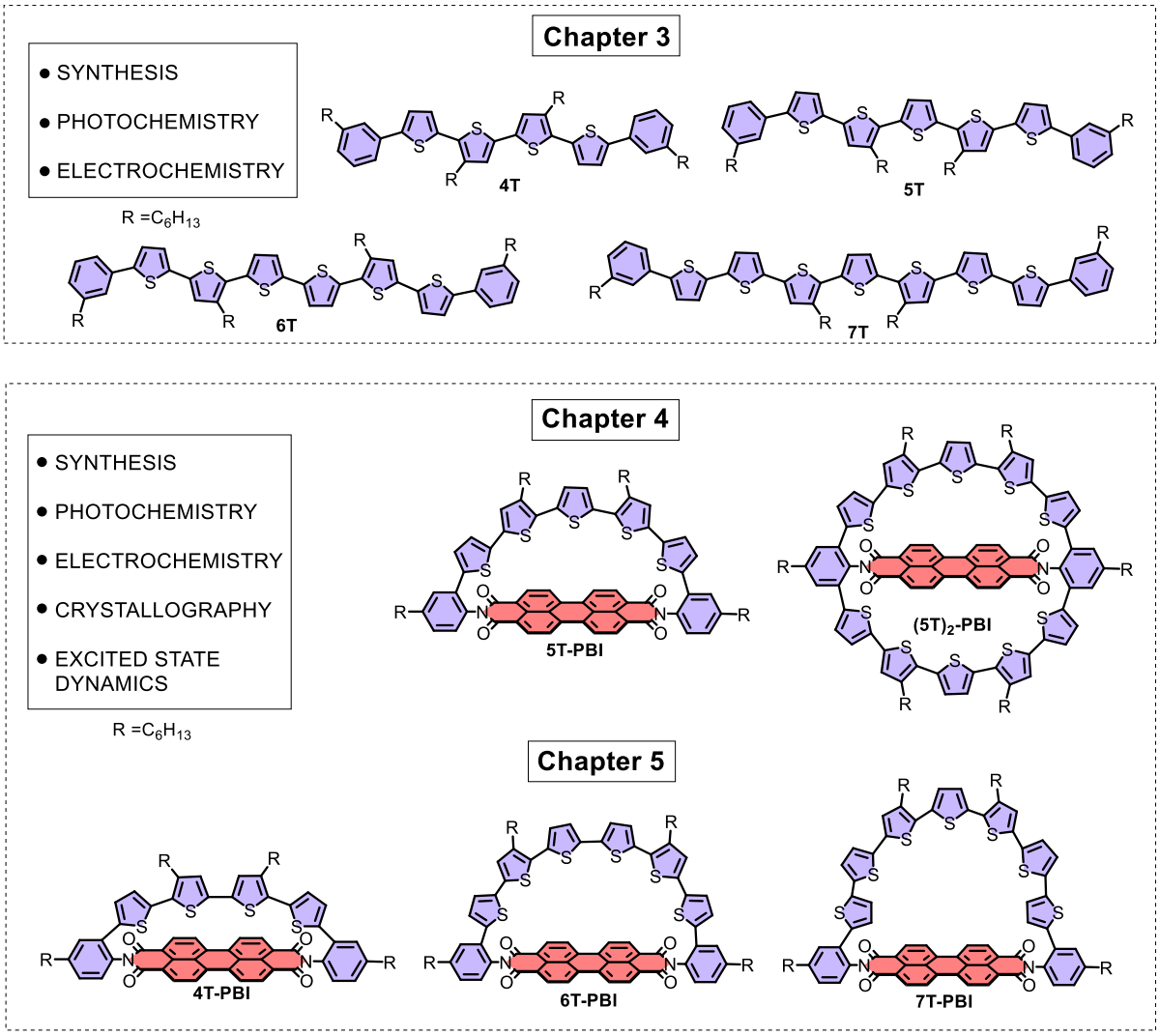

Chart 2. Chemical structures of the compounds described in this thesis.

In the following *Chapter 5*, the synthetic protocol of *Chapter 4* was exploited to bridge the dimension between the imide units of the PBI with oligothiophene chains of three different lengths (Chart 2). The resulting bridge geometry changes together with their influence on the macrocyclic photo- and electrochemical properties. TA spectroscopy in combination with spectroelectrochemistry (SEC) allowed for a comprehensive inference about the fast processes upon photoexcitation and a clear trend within the series could be derived.

Chapter 6 and *7* summarize and conclude the herein described work in English and German.

Chapter 2

State of Knowledge

2.1 Linear α-Oligothiophenes

2.1.1 General Aspects

Besides other prototypical conjugated oligomers (Figure 1a), in the last decades linear α-oligothiophenes advanced to one of the most frequently used π-conjugated materials in chemical research.[65-67] Key features such as the possibility for simple structural variation, electronic tunability of the molecular backbone and not least the high stability also in oxidized states attracted many chemists to this research field.[65] Due to a fast development of highly effective transition metal-catalyzed cross-coupling methods (*Chapter 2.1.2*) even the synthesis of extraordinarily long conjugated oligothiophenes[68] comprising up to 96 thiophene rings became reality.[69] In comparison to heteroatom free conjugated materials such as polyene or poly-paraphenylene the high polarizability of the sulfur atom additionally stabilizes the polymeric or oligomeric chain.[65]

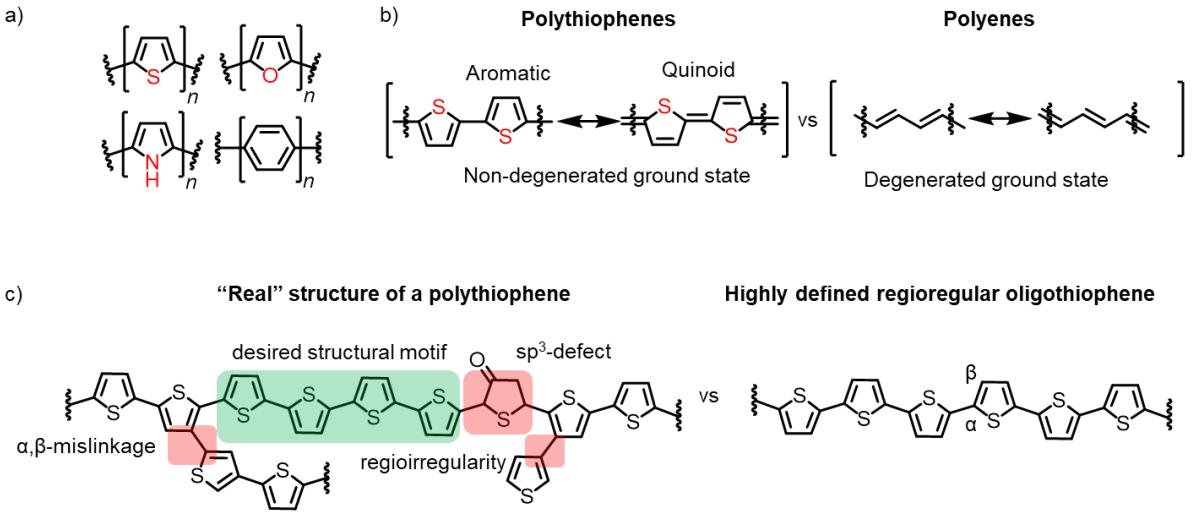

Figure 1. a) Prototypical oligomer structures. b) Comparison of oligothiophene and polyene resonance structures. c) Illustration of a more realistic polymer structure with possible defects versus a structurally defined oligomer.

To adequately describe the binding situation in the oligothiophene chain an aromatic and a quinoidal resonance structure can be drawn (Figure 1b).[70]

In reality, the latter plays only a minor role in the description of oligomeric thiophenes in the singlet ground state due to the fact that a reduced aromaticity in this regard equals destabilization of the π-system. Such systems, where one resonance form is favored over the other, have a non-degenerated ground state. This is in contrast to related substance classes, *e.g.*, polyenes with two isoenergetic limiting mesomeric forms (Figure 1b). The aromatic binding situation in the ground state drastically changes in the charged state for oligothiophenes which will be discussed in *Chapter 2.1.3*.

One of the major problems in thiophene based polymer research is the lack of structural homogeneity in the final structures. Although the choice of corresponding monomers as starting materials allows for a certain structural control of the reaction products, the polymerization process causes mislinkages, unwanted cross-couplings and other kind of defects in the final polythiophenes (Figure 1c). Therefore, precise predictions about the respective polymeric optoelectronic properties or the investigation of structure-property relationships is not unconditionally possible. This conflict of on the one hand simple and low-cost productions but on the other hand mostly undefined polymeric structures led to the idea of synthesizing well-defined oligothiophenes, which serve as "model" structures for the related conjugated polymers in the so called "oligomer approach".[70-71]

The disadvantage of the comparably synthetically more demanding oligothiophenes (*Chapter 2.1.2*) can be compensated by the resulting structurally defined target molecules, which allow for precise structure-property relationship investigations. In order to serve as model compounds for polymeric analogues sufficient solubility in commonly used organic solvents has to be guaranteed. Therefore, different aliphatic decoration patterns are introduced into the oligothiophene chain. Depending on the position of the solubilizing chains, structural and electronic changes are introduced into the scaffold which lead to modified electronic and spectral properties. For example, the introduction of alkyl chains in β-position results in a thiophene-thiophene torsion angle alternation because of proton repulsion and the concomitant donating effect also alters the electronic constitution of the molecule.[72] Another commonly used approach to solubilize longer oligothiophene chains is "end-capping" or, more precisely, the installation of substituents in the terminal positions of oligothiophenes, which is especially

advantageous for electrochemical investigations (*Chapter 2.1.3*) due to the suppression of oxidative coupling reactions.[73]

Within the scope of this work the term "oligomer" is defined as a conjugated molecule, which has a distinct chemical structure and consists of more than one covalently linked subunit (*e.g.* thiophene or benzene). In contrast, a "polymer" describes a molecule with an ambiguous chain length, lacking precise information about the number of subunits and exact chemical constitution. Exclusively linear, regioregular all-α-oligothiophenes will be discussed, whereas differently linked analogues (*e.g.* β-β linkages) or other substitution patterns (*e.g.* installation of donor/acceptor moieties or fusion etc.), which drastically change the oligomer properties, will be neglected.

Not only do oligothiophenes offer the possibility to approximate corresponding polymer characteristics, but sometimes their physical properties can even compete with those of the polymeric counterparts or do even surpass them. Back in 1989 a rather short α-sexithiophene was used as a semiconducting material with very high charge carrier mobilities in an OFET for the first time by Garnier and Fichou[74], which was followed by the first "all-organic" device in 1990.[75] After this breakthrough, several applications of functional oligothiophene materials in OLEDs[76] or OSCs[77] could be demonstrated. These findings paved the way for an oligothiophene research that not only approximates analogous polymer properties but is also capable of producing compounds for advanced molecular electronic devices.[68, 78]

2.1.2 Synthetic Methods

The first report of α-oligothiophenes goes back to the 1930s (during these times the substance class was called "polythienyls") where Steinkopf and co-workers almost accidently synthesized multiple brominated quarterthiophenes.[79] Later in 1941 the group also mastered the synthesis of a small unsubstituted oligothiophene series up to the α-septithiophene *via* Ullman coupling of 2-iodothiophene using Cu bronze (Figure 2).[80] After these tremendous achievements, in 1960, Gronowitz paved the way for a second era in oligothiophene synthesis using a slightly more sophisticated way.[81] Halogen-metal interconversion of bromothiophenes with *n*-butyllithium (*n*-BuLi) lead to the corresponding lithiated species, which could be readily coupled with cupric chloride and thus symmetric 2,2'/3,3'-bithiophenes

were obtained (Figure 2). The synthesis of the first thiophene polymer *via* electro-oxidation of a thiophene monomer on a metal surface in 1982 describes the start of the third deciding stage of oligo- and polythiophene synthesis.[82] Nowadays, transition metal catalyzed cross coupling reactions are one of the most frequently used methods for the preparation of oligothiophenes. Therefore, this chapter will focus on this approach as it often allows for a lot more structural control and variety of the final product in comparison to *e.g.* (electro-) oxidative coupling methods for thiophene polymers.[83]

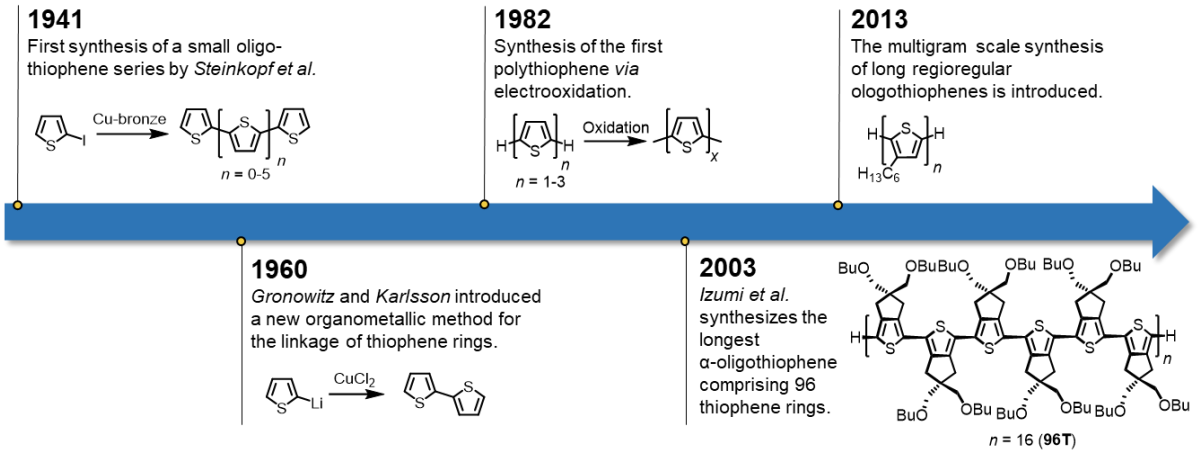

Figure 2. Historic development of oligothiophene synthesis.

Generally, aryl-aryl cross coupling reactions[84] for C-C bond formations most commonly require halide/Grignard and organometallic species. For example, the classical Ullmann reaction uses mostly electron-deficient arenes.[85] Here, an organocopper thiophene is reacted with the respective halide. While this procedure is more or less only of historic value for oligothiophene synthesis most of todays' synthetic protocols utilize nickel or palladium catalysts for thiophene-thiophene couplings. A very extensive report about the Ni-catalyzed coupling of Grignard and halide heterocycles (mostly thiophenes and pyridines) from Kumada *et al.*[86] in the 1980s inspired a lot of research groups to follow this approach for oligothiophene synthesis.[87-89] In this usually very selective and high-yielding Kumada-reaction most of the times active Ni-catalysts with phosphine ligands such as 1,2-bis(diphenylphosphino)ethane (dppe), 1,3-bis(diphenylphosphino)propane (dppp) or 1,1′-ferrocenediyl-bis(diphenylphosphine) (dppf) are used. The reactivity of the halide heterocycles increases from fluoro- to iodo-arenes due to the increased rate for the oxidative addition to the Ni-complex. Limitations of the cross couplings do only occur when the

Grignard reagents can not be formed in the first place, and *e.g.*, carbonyl functions lead to side products when reacted with Li- or Mg-agents. Another classic in cross-coupling procedures is the Suzuki reaction[90] which uses an organo halide and a boron compound. This can also be applied for the synthesis of oligothiophenes but is rather scarcely used in modern α-oligothiophene synthetic approaches. One example is presented by Guillerez and co-workers[91] for the selective synthesis of a small series of regioregular 3-octylthiophenes from monomer up to hexamer.

Combining the tolerance of many functional groups, a great regioselectivity and the possible usage of a large variety of electrophiles, the "Stille coupling" is one of the most versatile cross coupling reactions in oligothiophene synthesis. The methodology itself has been extensively reviewed[92-93] and is largely applied in the preparation of extended oligothiophenes.[94-96] Therefore, only selected features and interesting aspects of the coupling method are briefly discussed below.

For the reaction, mostly trialkyltin organyls (the most prominent examples are trimethyl- or tributyltin) are utilized. Due to the low polarity of the C-Sn bond the compounds are mostly air and moisture stable. This low polarity is in strong contrast to other already described cross couplings such as the Kumada reaction where highly polar Grignard reagents are used but is rather more similar to the B-C bond polarity in Suzuki coupling reagents. Another advantage of the organometallic tin compound in the Stille reaction can be found in the alkyl residues, which are typically not transferred and do thus not compete with the intended thiophene-thiophene coupling. The reaction partner of the tin compound is either a halide or triflate. The reaction mechanism[97] is very similar to the Kumada reaction.

Due to the fact that uncountable methods are existing for the modification of the thiophene core[98-99] the task of halide and trialkyltin attachment is easily achieved for this class of substances, especially in the electron-rich thiophene α-position. For the catalytic cycle Pd(0) catalysts are mandatory. Often very stable catalysts such as $Pd_2(dba)_3$, $Pd(PPh_3)Cl_2$ or $Pd(dppf)Cl_2$ with Pd(II) are utilized and the corresponding Pd(0) species is formed *in situ* by ligand exchange prior to the actual coupling event.[100] A very useful and prominent catalyst/ligand system is for example $Pd_2(dba)_3$/P(*o*-tolyl)$_3$[101], where a successful Pd(0) formation can be monitored visually. While $Pd_2(dba)_3$ has a violet colour the corresponding active catalyst system is more or less colourless.

The approach towards longer oligothiophene chains *via* Stille coupling procedures are usually conducted in a more or less iterative synthesis, where the oligothiophene is elongated by one or two monomers, which is then followed by the functionalization of the newly formed chain at the terminal α-positions and so on. This functionalization becomes more and more difficult as the number of thiophene units ascends due the increased possibility for reactions at the β-positions.[102] This can lead to miscouplings and inseperable reactions mixtures of α-and β-linked products. In this regard, the complete β-position blocking to avoid those side reactions was the key idea in the synthesis of the already mentioned 96mer (**96T**, Figure 2) by the group of Otsubo.[69]

A very impressive example of utilizing Stille coupling reactions for an extremely high structural control of the target compounds is shown by Koch *et al.*[103] Here, regioregular oligo-3-hexylthiophenes comprising up to 21 units could be synthesized in gram scales following "Fibonacci's route" (Scheme 1a).

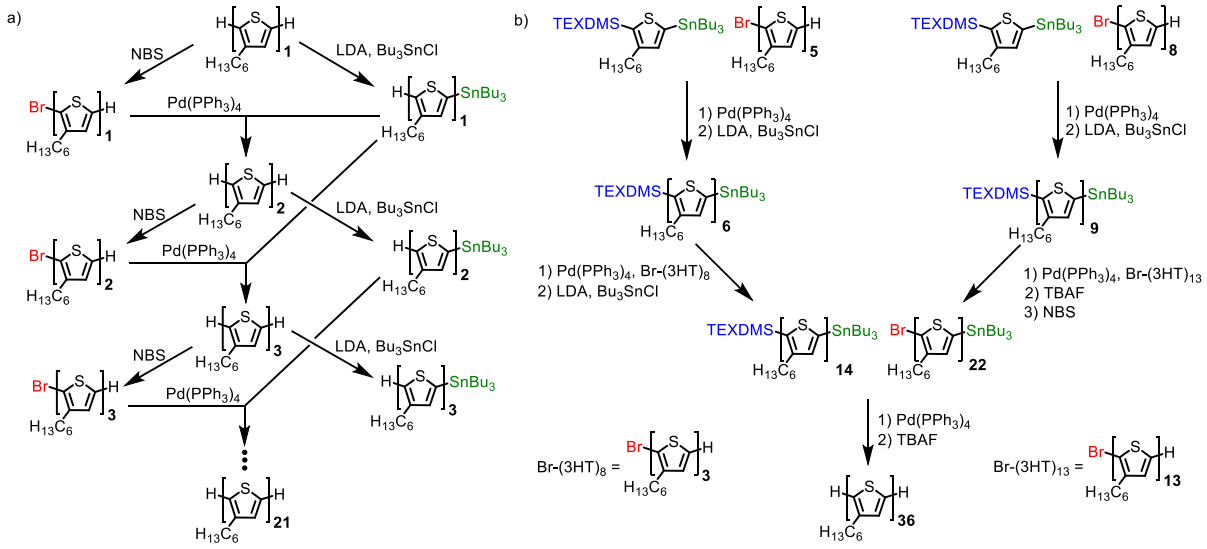

Scheme 1. Iterative Stille coupling procedures utilized for oligothiophene synthesis reported by Koch *et al.*[103] NBS = *N*-Bromosuccinimide. LDA = Lithium diisopropylamide. TEXDMS = (2,3-dimethylbutan-2-yl)dimethylsilyl.

The synthetic scheme started with 3-hexylthiophene and by repeating of thiophene bromination, stannylation and subsequent Stille coupling procedures the oligothiophene chain was built up. The introduction of silyl protecting groups in later stages even delivered regioregular chains with up to 36 thiophene subunits (Scheme 1b).

2.1.3 Electrochemical and Photophysical Properties

Electronic Properties

Unsubstituted α-oligothiophenes up to a certain size undergo electro-oxidation induced reactions at the free α-end positions of the chain, which lead to (unwanted) side products during the electrochemical investigation thereof.[72, 104] In these cases all oxidation events measured by cyclic voltammetry (CV) are not reversible and the half wave potentials cannot be determined. Especially for smaller oligothiophenes, end-capping of those terminal free α-positions to prevent radical induced α,α'- coupling side reactions is inevitable. The propensity for those undesired couplings decreases with increasing chain length due to enhanced stabilization of the charge through the entire chain.[105]

In 1992 the group of Bäuerle[106] synthesized cyclohexyl end-capped α-oligothiophenes **1**-**6**, which allowed for a very precise electrochemical investigation also of short chains comprising only three to six thiophene rings (chains with one or two subunits underwent follow-up reactions, *e.g.* deprotonation, Figure 3a). Besides the prevention of these side reaction, the cyclohexyl substitution in the terminal positions also dramatically enhanced the solubility of the oligomer in comparison to the unsubstituted α-oligothiophene chains.

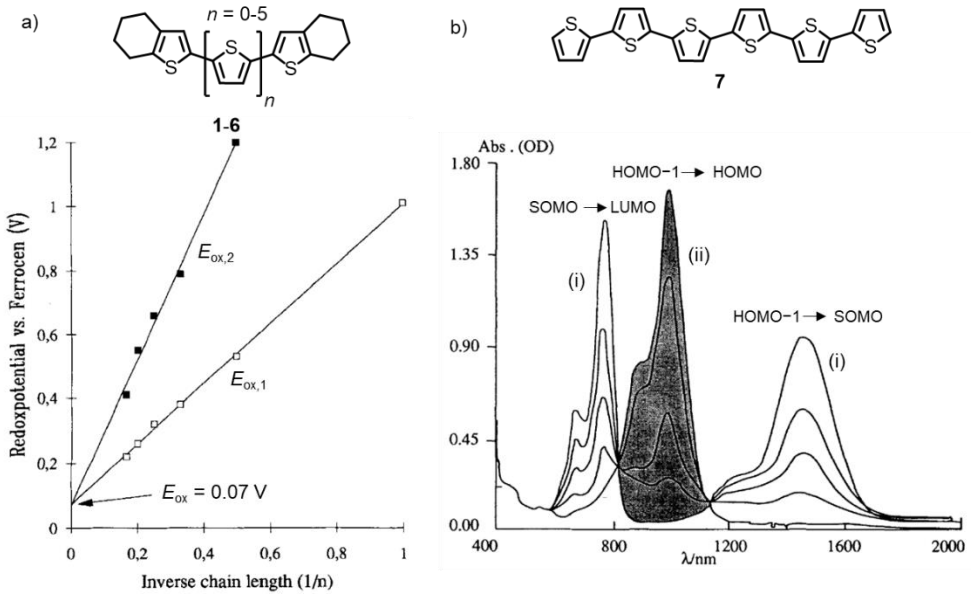

Figure 3. a) First ($E_{ox,1}$, open symbols) and second ($E_{ox,2}$, filled symbols) oxidation potentials of cyclohexane end-capped oligothiophenes **1**-**6** versus the reciprocal number of thiophene subunits n. Adapted with permission from ref. [106]. Copyright 1992 Wiley Verlag GmbH & Co. KGaA, Weinheim. b) Radical cation (i) and dication (ii) spectra of sexithiophene **7** in CH_2Cl_2 upon oxidation with $FeCl_3$. Adapted with permission from ref. [105]. Copyright 1990 Elsevier.

By plotting the first electron oxidation potential ($E_{ox,1}$) against the inverse number of thiophene units n (Figure 3a) a clear linear trend is observed. With an increasing number of thiophene rings, $E_{ox,1}$ is gradually lowered due to enhanced stabilization of the respective radical cation. Additionally, dication formation ($E_{ox,2}$) could be observed for all investigated chains, which overall follows a steeper linear trend. Due to the enlarged stabilization of charges, the number of possible redox states increases with chain elongation.[107] For example, in a different study, for a bithiophene only monocationic species are observed, whereas for longer oligothiophene chains bearing 18 subunits four reversible redox events were found.[69] Interestingly, the energy difference between $E_{ox,1}$ and $E_{ox,2}$ is also decreased for higher analogues due to the reduced coulomb repulsion of the charges (Figure 3a). The extrapolation of both linear curves to the intercept (1/n = 0) delivers valuable information about a theoretical infinite oligomer with no structural defects. The potential difference for cation and dication formation vanishes at this point (E_{ox} = 0.07 V). This would enable the removal of a certain number of electrons at the same oxidation potential as long as the charges can reside spatially separated within the conjugated chain.

This study is one of many examples for α-oligothiophenes serving as model compounds to adequately approximate inaccessible polymer properties in solution (*Chapter 2.1.1*). Confirming these results, several comparative investigations of α-oligothiophenes of various sizes bearing different end-caps were reported afterwards in the literature.[107-110]

The electronic structure of oxidized states in oligothiophenes was also intensively investigated and described in detail.[110-116] Upon application of positive voltage or simple addition of chemical oxidants such as $FeCl_3$ to an oligothiophene solution, drastic spectral changes in the UV/Vis and NIR (near-infrared) region can be monitored. Figure 3b shows the cation (i) and dication (ii) spectra of sexithiophene **7**. The occurrence of these pronounced absorption bands will be theoretically explained in more detail below.

Generally speaking, introduction of excess charges into an initially neutral oligothiophene chain leads to massive geometry changes in form of aromatic and quinoidal regions, which in most cases stretch over a finite area of the molecule (Figure 4). Depending on these structurally different segments the chain orbital energies are directly influenced. Unlike polymers where a valence and conduction band model would be suitable[117], α-oligomers can be treated as

discrete molecules and therefore the electronic description using molecular orbital (MO) theory appears most appropriate.[112] The description of electronic transitions in the cationic state of π-conjugated oligothiophenes is comparably well-known: Removal of one electron from the highest occupied molecular orbital (HOMO) of a neutral oligothiophene results in an open-shell configuration and two dipole-allowed subgap transitions are possible (Figure 5). The transition of one electron from the singly occupied molecular orbital (SOMO) to the lowest unoccupied molecular orbital (LUMO) can be spectrally observed in the visible region of the absorption spectrum, whereas the HOMO−1-SOMO transition results in a NIR absorption band (Figure 3b). Most of the times, the high-energy transition band is accompanied by a clear vibronic shoulder at higher energies. Upon oligothiophene chain elongation the above described orbital gaps become smaller and the absorption bands shift to lower energies.[118]

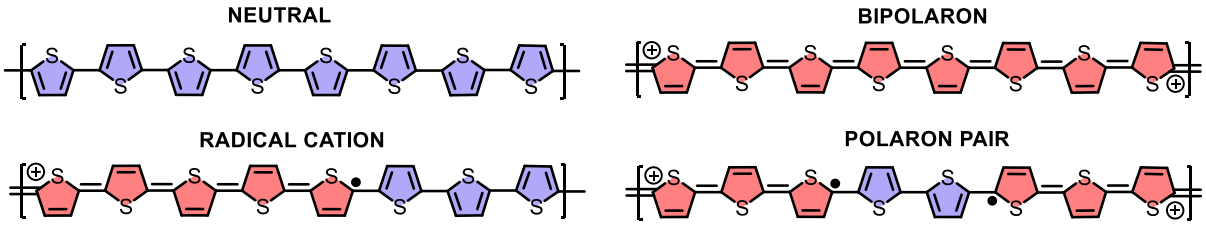

Figure 4. Structural representation of neutral, radical cation, bipolaron and polaron pair structures in oligothiophenes. Aromatic rings are marked in blue and quinoidal parts in red, respectively.

Upon further oxidation to the dicationic state another electron is removed from the former SOMO orbital (Figure 5). Depending on the oligothiophene nature two different theoretical electronic configurations can be formulated (Figure 4). Firstly, a bipolaron structure corresponds to a spinless dication where the two positive charges more or less remain together and are stabilized by a very strong geometry deformation in the molecule. Here, the transition from the HOMO to the lowest lying unoccupied bipolaron orbital is dipole allowed and is most of the times energetically situated in between both radical transitions. This transition is comparable to the NIR band of the radical cation but due to larger geometrical distortions it is shifted to lower wavelengths (Figure 3b).

Secondly, the polaron pair (two polarons) structure is characterized by two locally separated radical cations causing a minimum of structural distortion in the chain (Figure 4). Mostly larger oligothiophenes possess this kind of electronic structure due to the increasing chance of sufficiently spatially separating the two radical cations from each other.[119-120] Fully separated

charges lead to two sharp absorptions, whereas a certain degree of interaction between both radical cations leads to a broadening of the respective bands.[121] From the orbital point of view two radical cations are located in two different MOs in a either singlet or triplet configuration. This opens up the possibility for two transitions resulting in two bands in the absorption spectrum (Figure 5).

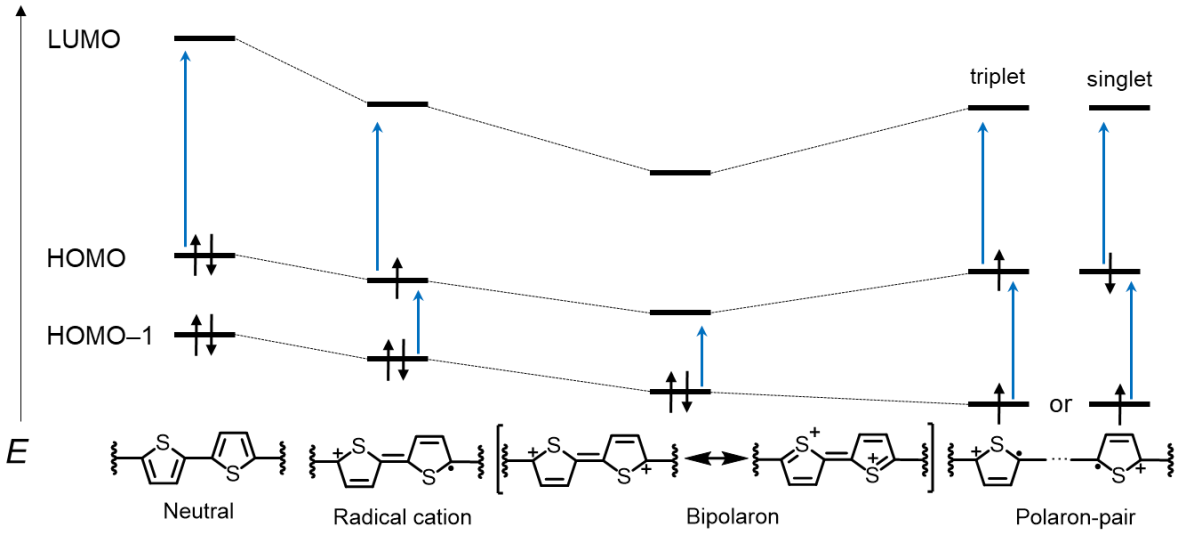

Figure 5. Qualitative energy diagram of the HOMO−1, HOMO and LUMO levels for neutral and charged oligothiophenes. The blue arrows indicate the respective transitions associated with the UV/Vis/NIR spectra in solution and the dotted lines serve as guide to the eye.

Bipolaron and polaron-pair configurations together are also observed. According to the calculations of Gao *et al.*[119], the transition between both electronic configurations can be found in oligothiophenes consisting of six to eight units due to a steady stabilization of the open-shell ground state (two polarons) in these chains.

Upon oxidation, with increasing chain length, also the formation of charged oligothiophene dimers, especially at low temperatures, is favored. This phenomenon was described first by Penneau and co-workers in 1992[122] for a diamagnetic terthiophene dimer and was further investigated by the group of Bäuerle[111] one year later for a small series of ter-up to quinquethiophene structures.[123] In order to generally prove the magnetic nature of oxidized states electron spin resonance (ESR) spectroscopy is utilized. In this way *e.g.* ESR-active paramagnetic radical cations can be differentiated from the ESR-silent diamagnetic bipolarons. Thus, upon cooling of radical cationic oligothiophene solutions both groups observed an enormous decrease of the ESR signal due to the formation of diamagnetic dimers. This aggregation behaviour is also associated with stark spectral changes, which are not further

discussed in this context.

Photophysical Properties

The UV/Vis spectra of α-oligothiophenes are broad and devoid of vibronic fine structure as the molecules prevail in a rotameric mixture in solution (Figure 6a), which in turn is owned to the low inversion barrier.[124] The major part of the longest wavelength absorption band can be assigned to the HOMO-LUMO (π-π*) transition, which is polarized along the oligothiophene chain. This main and most intense absorption band is followed by weaker, high energy, partly dipole forbidden transitions, which are polarized perpendicular to the molecular axis.[125] As the extent of the π-system increases, the absorption shifts to lower energies and a linear correlation between the absorption maxima and 1/n is found.[106] For example, whilst the absorption maximum of an end-capped thiophene molecule is located at 237 nm in dichloromethane (CH_2Cl_2) the hexamer exhibits absorption at 449 nm.[106] The red shift in comparison to the foregoing next smaller analogue decreases with increasing chain length.

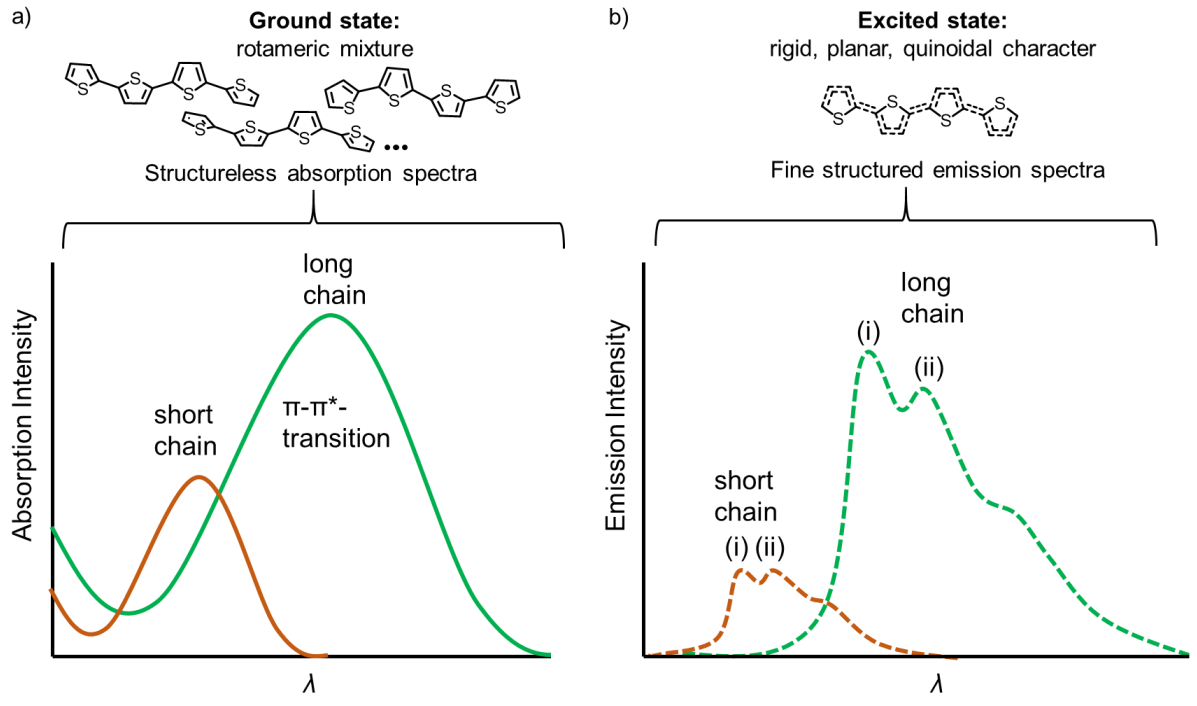

Figure 6. Schematic representation of a) absorption (solid lines) and b) emission spectra (dashed lines) of short (brown) and long (green) oligothiophenes. The chemical structures exemplarily illustrate in a simplified way the prevailing geometries in the respective states.

Oligothiophenes also show distinct solvatochromism[126-127]. In particular, a bathochromic shift of the absorption maximum upon changing the solvent from a less polar (*e.g. n*-hexane) to a more polar solvent (*e.g.* CH_2Cl_2) can be observed, which is clearly caused by the increased geometry difference between ground and exited state. This effect becomes even more apparent as the chain length increases.

While the absorption of α-oligothiophenes remains more or less structureless this class of molecules shows distinct vibrational structure in their emission spectra.[128] Also here a linear correlation between emission maximum and inverse number of thiophene rings (1/n) is observed.[106] Upon photoexcitation a more quinoidal structure is adopted, which leads to a rigid and planar structure of the molecules in the S_1 state (Figure 6b). This causes vibronic fine structure in the fluorescence spectra, characterized by two main bands which alter depending on the oligothiophene chain length in regard to their relative intensity. While for smaller oligothiophenes the low energy band is most prominent, a higher energy band emerges and becomes more intense for larger analogues. Also, the emission spectra are red-shifted upon chain elongation. Interestingly, the quantum yield increases with chain extension and becomes more or less constant in the region of 5-7 subunits.[129-130] This is mainly dictated by the non-radiative rate constant which behaves similarly to the quantum yield. All discussed spectral features are schematically summarized in Figure 6.

2.2 Cycloparaphenylene and Oligothiophene Nanohoops

2.2.1 Characteristics of π-Expanded Macrocycles

The molecular class of [*n*]CPPs (Figure 7a) displays the simplest structural unit of a single-walled carbon nanotube (SWCNT, Figure 7b) or a constituent of a fullerene (Figure 7c).[131] On the other hand, unlike [*n*]CPPs, C[*n*]Ts cannot be regarded as a part of a larger and more complex 3D structure. However, both, thiophene and phenylene based nanohoops can act as role models for infinite π-systems.

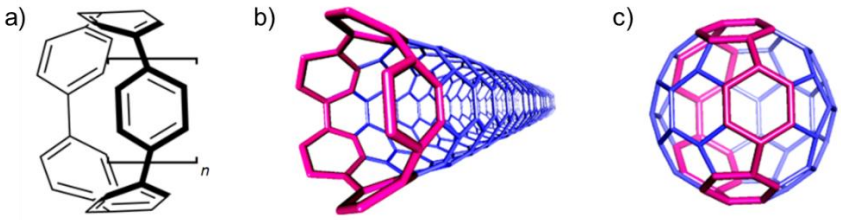

Figure 7. a) Molecular structure of [*n*]CPPs as well as **[5]CPP** highlighted in magenta as part of a b) SWCNT and c) fullerene. Reprinted with permission from ref. [131]. Copyright 2014 American Chemical Society.

Therefore, the electronic properties *e.g.* of long and idealized polymeric analogues can be simulated.[132] Besides this function of a role model compound, the bending of initially planar aromatic scaffolds into macrocyclic hoop shapes can significantly alter a huge variety of fundamental properties. In the case of linear π-conjugated compounds the p-orbitals are aligned perpendicularly to the aromatic backbone chain (Figure 8a).

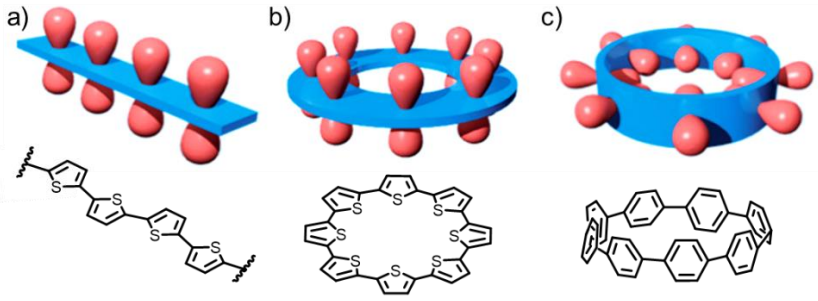

Figure 8. Sketched orientation of p-orbitals in a linear oligothiophene (a), cyclic oligothiophene (b) and cyclic oligophenylene (c). Adapted with permission from ref. [133]. Copyright 2015 Wiley-VCH Verlag GmbH & Co. KGaA.

While this pattern does not change for C[*n*]Ts (Figure 8b), [*n*]CPPs comprise the rather more uncommonly radially oriented p-orbitals (Figure 8c). The combination of benzene and thiophene in a nanohoop also leads to radial π-conjugation.[133]

[*n*]CPPs and C[*n*]Ts are antiaromatic structures in the neutral state due to their $4n$ π-

electrons.[134] Taking **[9]CPP**[135] as an example, double bonds are formed between the phenylene rings resulting in nine π-orbitals with four electrons which clearly shows the 4*n* (*n* = 9) antiaromaticity. However, the respective divalent cations ([*n*]CPP^{2+}/C[*n*]T^{2+}) and anions ([*n*]CPP^{2-}/C[*n*]T^{2-}) have an aromatic structure with 4*n*+2 π electrons. A comparison of both charged species reveals a larger aromaticity for the dianions according to nucleus-independent chemical shift (NICS) calculations due to the enlarged number of electrons in the π-orbitals. Additionally, the aromatic character decreases with increasing number of macrocyclic subunits.[134]

Another specifically macrocycle related issue to discuss is the strain, which influences a variety of factors such as reactivity, solubility and not least simply the difficulty of the synthetic preparation. The last-named aspect will be further discussed in *Chapter 2.2.2*. Within the field of C[*n*]Ts and [*n*]CPPs one comes across strain energy values ranging from extremely high to almost negligible. In this regard, C[*n*]Ts most of the times show much smaller strain energies than their benzenoid analogues. This already becomes apparent in the first respective publication of both structural families in 2000[136] and 2008[137], respectively. While Bäuerle's first C[*n*]Ts (here *n* = 12, 16 and 18) show strain energies from 0.0 kJ mol^{-1} to 7.5 kJ mol^{-1}, for Jasti and Bertozzi's [*n*]CPPs (here *n* = 9, 12 and 18) values of 21 kJ mol^{-1} to 197 kJ mol^{-1} are calculated. The strain energy for the smallest ever synthesized [*n*]CPP with *n* = 5[131] was computed as high as 491 kJ mol^{-1}[138] underlining an almost exponential increase in strain upon diminishment of the ring size.

One of the most commonly used workflow to calculate the macrocyclic ring strain is the homodesmic reaction method (Figure 9a).[139] The lowest energy conformation of the macrocycle ($E_{\text{macrocycle}}$) is determined by a geometry optimization at a suitable computational level. Subsequently one bond is virtually removed and the obtained radicals are capped by so-called "capping molecules", which closely resemble the former neighbouring group. This linear structure as well as the capping molecule is geometry optimized and the total energy (E_{linear} and E_{cap}) is calculated. The strain energy (E_{strain}) can then be determined according to:

$$E_{\text{strain}} = (E_{\text{macrocycle}} + E_{\text{cap}}) - E_{\text{linear}}. \quad (1)$$

Recently, another useful computational method for strain visualization was described.[140] With the help of this methodology the "weakest" fragments in the macrocycle can be localized which

potentially facilitates macrocycle design and more accurate stability predictions (Figure 9b). Also preferential reaction sites within the macrocylic architecture can be circumscribed and explained.

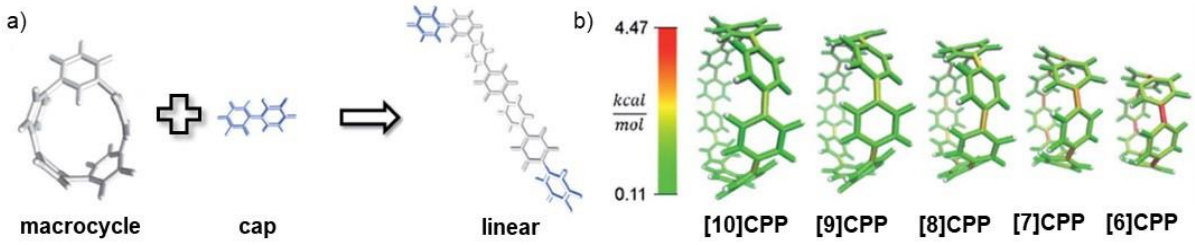

Figure 9. a) Schematic representation of the homodesmic reaction method for a macrocycle strain calculation. b) Results obtained for the distribution of strain for the individual parts of the nanohoops **[10]CPP**-**[6]CPP** (from left to right) using the strain visualization software StrainViz. Adapted with permission from ref. [140]. Copyright 2020 Royal Society of Chemistry.

By incorporating other structural elements such as D-A moieties into the cyclic π-systems the optoelectronic properties can be fine-tuned. The installation of electron-rich and electron-poor units within a covalently linked scaffold generally leads to a lowering of the optical band gap and a spatial separation of the HOMO and LUMO.[26] Consequently, these structures are also prone to charge separation upon photoexcitation. Depending on the solvent polarity the excited state of the respective D-A structure is stabilized to a different degree, which leads to a solvent-dependent emission wavelength.[141] This effect of solvatofluorochromism is further elucidated below.

Within the frame of nanohoop research, countless structural motifs for a D-A incorporation exist to date.[42] As already mentioned in *Chapter 1*, typical motifs for an accepting subunit are antraquinone, or pyridinium, whereas thiophene represents the classic donor moiety. Depending on the counterpart in the nanohoop, also the [*n*]CPP chain itself can act as a donor.[142] Two of the most intriguing D-A nanohoop examples were reported in 2015 and shall be highlighted here. Itami and co-workers[45] introduced an accepting antraquinone moiety into a donating **[10]CPP** resulting in structure **8** (Figure 10a). The accepting character of the antraquinone segment could even be enhanced by conversion to tetracyano-anthraquinodimethane in molecule **9**. While the absorption properties of both nanohoops **8** and **9** did not change to a great extend compared to parent **[12]CPP** (λ_{max} = 338 nm), the emission spectra of the compounds are strongly dependent on the solvent. Structure **8** shows green fluorescence in low polar CCl_4, while an increase of solvent polarity causes a bathochromic

shift and orange fluorescence can be observed for the compound in chlorobenzene. With increasing accepting character in nanohoop **9** the emission spectra undergo an even further red shift also in very nonpolar solvents and are non-emissive in polar solvents.

In the same year another example of a D-A nanohoop was reported by Jasti and co-workers[46]. Here, *N*-containing heterocycles as acceptor units were incorporated in a **[7]CPP** (Figure 10b) yielding **10** and **11**. While pyridine itself does not significantly alter the optical band gap and redox properties of **10** in comparison to all carbon **[8]CPP**, the alkylation of the nitrogen atoms leads to a stronger accepting character with almost entirely quenched emission and a reduced optical band gap for structure **11**.

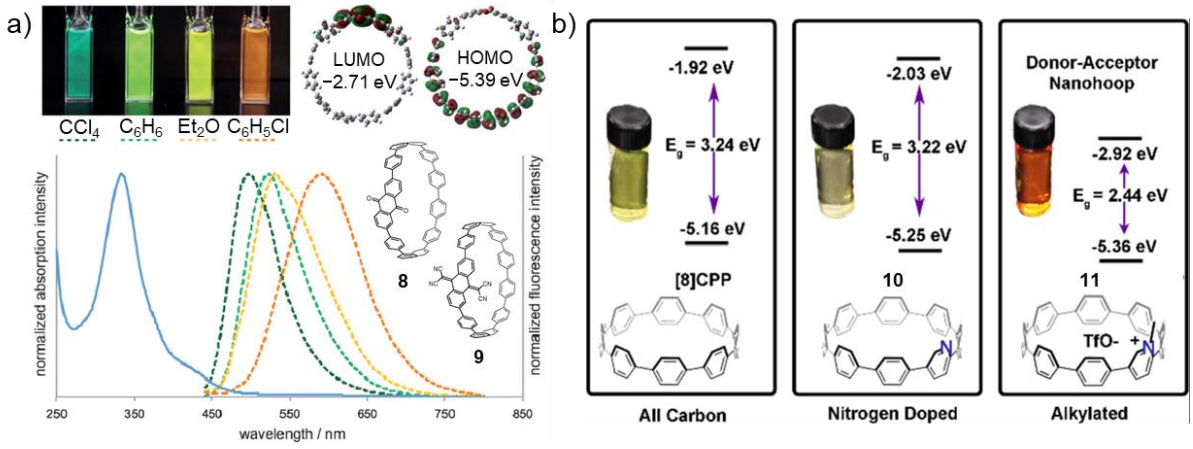

Figure 10. a) Normalized UV/Vis absorption spectrum (solid line) in $CHCl_3$ and emission spectra (dashed lines) in various solvents as well as a photograph of the respective solutions along with the HOMO/LUMO shape of compound **8**. Adapted with permission from ref. [45]. Copyright 2015 Wiley-VCH Verlag GmbH & Co. KGaA. b) Chemical structures, optical band gaps and photographs of CH_2Cl_2 solutions of the structures **10**-**11**. Adapted with permission from ref. [46], https://pubs.acs.org/doi/abs/10.1021/acscentsci.5b00269. Copyright 2015 American Chemical Society.

Several more examples of D-A nanohoops, which are nicely reviewed by Esser and co-workers[26], can be found in literature.

Overall it becomes clear, that C[*n*]Ts and [*n*]CPPs almost represent an entirely novel class of organic materials in comparison to their linear analogues. Additionally, shape persistent C[*n*]Ts and [*n*]CPPs show fascinating optical (*Chapter 2.2.3*), as well as self-assembly[136, 143-144] properties and are also capable of templating *e.g.* fullerene by concave-convex and/or D-A interactions[145-147].

While C[*n*]Ts can often nicely be visualized by scanning tunnelling microscopy (STM) techniques[148-149], crystallization appears to be a more difficult challenge. It took until 2011 to report the first crystal structure of a C[*n*]T, namely **C[10]T** (Figure 11a, b)[113], which also

remained to be the only fully resolved cyclic α-oligothiophene structure without any other extrinsic rings[133], connecting units (such as ethylenes[150-151] or acetylenes[152-154]) or β, β'-linkages[155] until today. One reason for that might be the utilization of solubilizing aliphatic chains within the synthesis of C[*n*]Ts (*Chapter 2.2.2*), which notoriously increases the entropic costs of crystal formation.

C[10]T partly exhibits a herringbone type of stacking, where neighbouring thiophene hoops partially overlap in a typical π-π distance of 3.4 Å, whereas rings of the same column exhibit a rather large distance of about 7 Å (Figure 11b). The thiophene rings all adopt an *s-cis* conformation in the macrocycle. Thereby, the induced strain is compensated with torsional angles between the thiophenes higher than the values observed for linear, less strained analogues.[156] Additionally, very short interatomic sulfur distances way below their sum of the van-der-Waals radii (3.70 Å) were found.

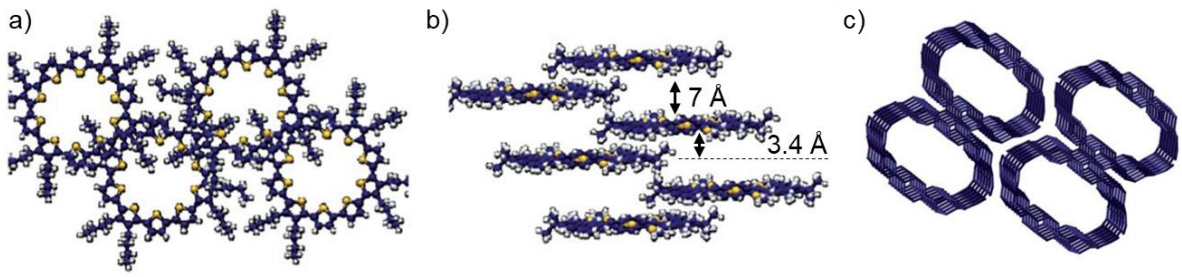

Figure 11. a) Top and b) side view of the **C[10]T** packing in the crystalline solid state with omitted solvent molecules. Adapted with permission from ref. [113]. Copyright 2011 Royal Society of Chemistry. c) Tube-like crystal packing of **[10]CPP**. Reprinted with permission from ref. [146]. Copyright 2012 Royal Society of Chemistry.

On the other hand [*n*]CPP rings of various sizes tend to crystallize with more ease as the crystal structures of **[5]-[12]CPP** are all published.[34, 146, 157-161] Remarkably, due to the way [*n*]CPPs are synthesized (*Chapter 2.2.2*) all [*n*]CPP crystal structures are free of aliphatic chains.

A tube-like arrangement can for example be observed in the crystal structure of **[6]CPP** and also partially for **[10]CPP** (Figure 11c) while all other [*n*]CPPs exhibit a herringbone stacking. Interestingly, within the macrocyclic [*n*]CPP rings, substantially bent and non-planar benzene rings can be observed especially for the highly strained small cycles with five or six phenyl units.[157-158] However, the benzenoid character of the rings could be confirmed even in the smallest nanohoop **[5]CPP**: The phenyl-phenyl interring bonds (A-A) are elongated and the intraring phenyl bonds (B-B) are of almost equal length (Figure 12).

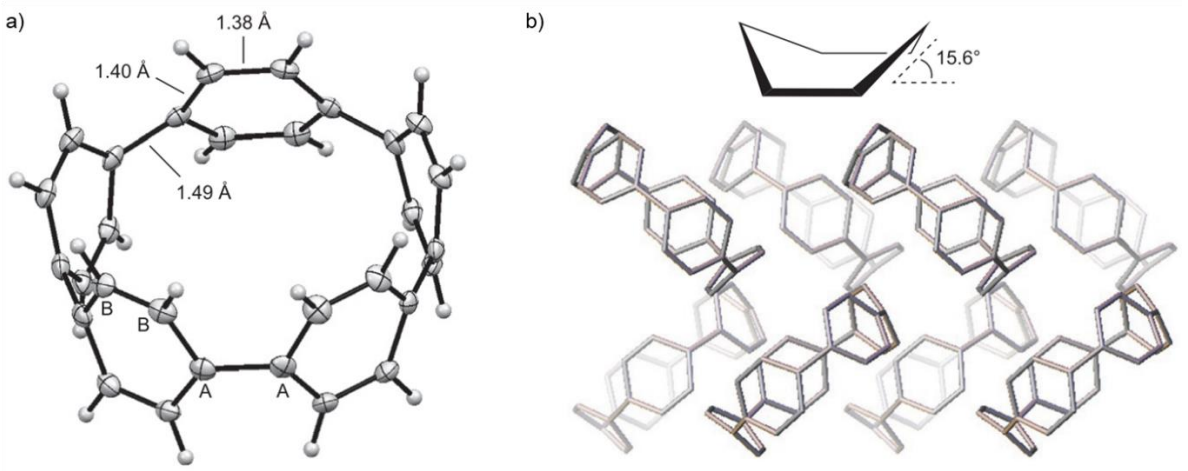

Figure 12. a) ORTEP representation of the **[5]CPP** crystal structure with ellipsoids set to 50% probability. b) Out-of-plane bending of the phenyl rings within the nanohoop and herringbone-type packing in the solid state (from top to bottom). Adapted from ref. [157]. Copyright 2014 Nature Publishing Group.

All mentioned π-conjugated macrocycle related features lead to severe electronic consequences which are further elucidated in *Chapter 2.2.3*. Among the described ring systems countless other functionalized π-expanded and shape persistent cycles exist.[26] However, within the scope of this thesis the following discussion will be focussing on purely phenylene or thiophene based macrocycles.

2.2.2 Synthesis of Bent π-Scaffolds

The preparation of macrocyclic π-scaffolds in form of [*n*]CPPs remained an unsolved synthetic challenge for almost 80 years after the first literature known attempts.[162-164] In the 1930's first efforts to accomplish the synthesis by a copper-mediated desulfurization of thiaparacyclophanes were reported.[165] It was Vögtle who pursued on this exact path more than 50 years later in 1984 by preparing phenylene and biphenylene sulfides initially without the ambition to synthesize an all conjugated carbon analogue.[166] However, in 1993 his research group suggested three possible synthetic routes towards the highly desired [*n*]CPPs.[167] Although all attempts turned out to be unsuccessful the synthetic ideas behind these approaches were invaluable for the upcoming research in this field and undoubtably contributed to the synthetic success fifteen years later (*vide infra*).

A very useful strategy to synthesize a less strained precursor macrocycle prior to the actual [*n*]CPP formation was already realized during these days. In total four synthetic approaches

were described in the publication of Vögtle and co-workers.[167] The main problem behind most of these strategies was not even the macrocycle formation itself but rather the aromatization reaction towards the [*n*]CPPs, which introduces the major part of the strain. One very remarkable attempt, almost resembling successful modern protocols shall be highlighted in this regard (Scheme 2). The combination of phenylenes (grey) and cyclohexanes (green) within a macrocycle would serve as a less strained precursor for the final [*n*]CPP formation. In this strategy, the drastic increase of strain energy in the last reaction step would be compensated by the energetic gain in aromatizing the cyclohexyl subunits. Unfortunately, the precursors **12** and **13** for this macrocycle formation turned out to be too conformationally flexible in solution and preorganization was not as high as expected. All attempts of structural rigidification failed during that time and oligomers **14-16** instead of the desired [*n*]CPPs were received. In the final remarks of this report "well preorganized molecules composed of 1,4-linked carbocyclic six-membered rings" were declared in wise foresight as the most promising candidates for a successful [*n*]CPP synthesis.

Based on this, the first successful synthesis of a [*n*]CCP was finally realized by the groups of Jasti and Bertozzi in 2008.[137] Here, the reduction of masked macrocyclic aromatic systems **19-21** with lithium naphthalenide was used as the last major strain introducing key step leading to **[9]CPP**, **[12]CPP** and **[18]CPP** (Scheme 2). A few month later, Itami and co-workers presented the selective synthesis of **[12]CCP** by an acid supported oxidative aromatization of macrocycle **24** comprising four cyclohexyl units.[168] Both approaches have unquestionably high conceptual similarity with the aforementioned ideas of Vögtle. Lastly, in 2010 Yamago made use of a reductive elimination of a tetranuclear platinum complex **27** to form a **[8]CCP**.[169] These three last-named protocols display the methodical cornerstones of [*n*]CCP synthesis and are widely utilized in this research field. To sequentially build up strain at the latest possible stage in the synthetic route represents the great similarity of all three mentioned methods. By using this fundamental idea, the synthetic tools for bending initially planar π-conjugated compounds into a macrocyclic shape was even further extended by three other groups. Although in these protocols the targeted nanohoop structure was not exclusively composed of phenyl rings, for completeness, the following reports shall not remain unmentioned.

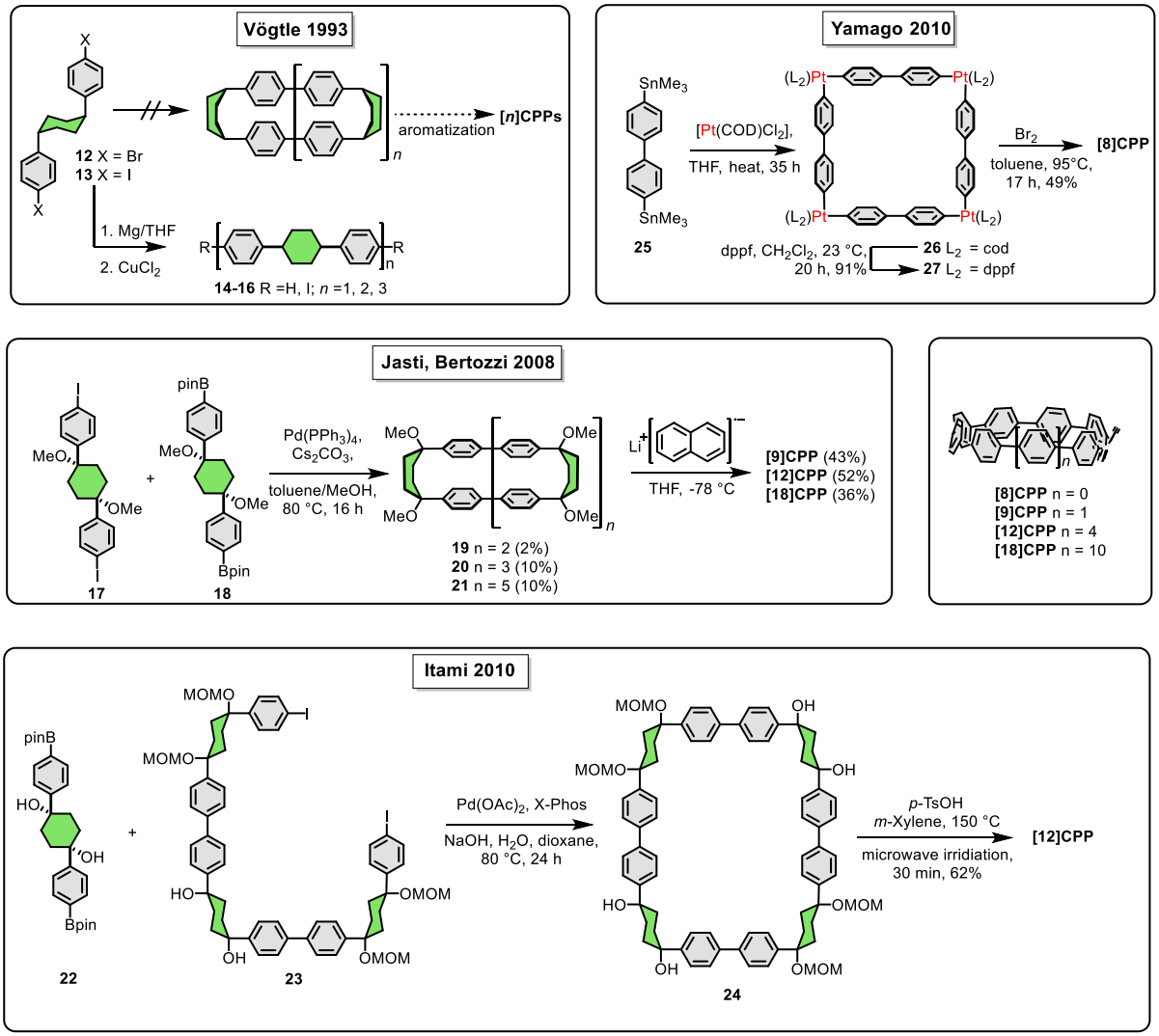

Scheme 2. Different synthetic approaches towards [*n*]CPPs from the groups of Vögtle[167], Jasti & Bertozzi[137], Yamago[169] and Itami[168].

Wang and co-workers introduced a cyclohexadiene based unit, which was oxidatively aromatized.[170] The utilization of an oxanorbornadiene derivative as corner unit allowed the installation of an anthracene moiety by the group of Isobe.[171] Lastly and very recently, a completely different approach was developed by Esser and co-workers.[172] Here, a chiral diketone precursor was aromatized to a pentalene *via* Grignard addition and water elimination.

The first macrocycles comprising exclusively thiophene rings were synthesized by the Bäuerle group already back in 2000, much earlier than the [*n*]CCPs (Scheme 3).[136] Eglington-Glaser coupling was the key step in preparing macrocycles **31**-**33** where the neighbouring triple bonds

(orange) underwent a very elegant thiophene ring (blue) formation upon treatment with the sulphur nucleophile Na_2S to give **C[12]T-C[18]T** with *n* = 12, 16 and 18 in the final step.[173]

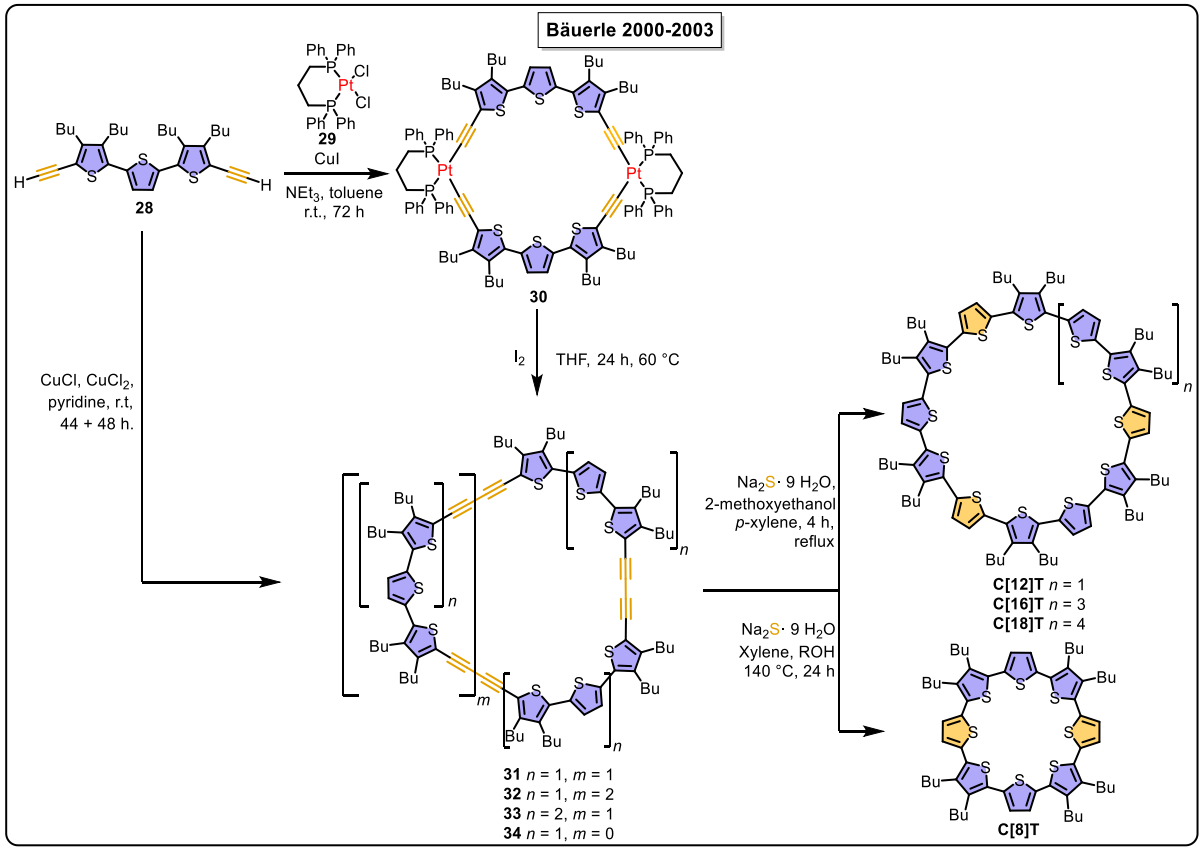

Scheme 3. Progress in the field of macrocyclic oligothiophene C[*n*]T synthesis by the Bäuerle group from 2000-2003.[136, 174]

Three years later, a smaller ring **C[8]T** was synthesized starting from similar precursor **28** but instead of a modified Glaser coupling procedure the macrocycle formation step involved Pt-complex **30** for the first time (*vide infra*).[174] Upon oxidation induced reductive elimination with iodine, disodium sulfide was utilized again to convert the triple bonds of **34** to thiophene rings yielding product **C[8]T** (Scheme 3).

After the development of a very elegant coupling method for linear oligothiophenes also by Bäuerle and co-workers[175], it was the same group who achieved the synthesis of giant C[*n*]Ts **C[10]T-C[35]T** with up to 35 thiophene rings utilizing a very similar method.[40] Here, yields over 80% could be achieved, which indicates that macrocyclization was even favored over polymerization processes in this reaction protocol. This successful "one pot" macrocyclization reaction reported in 2009 (Scheme 4) was the basis for the synthesis of the target molecules reported in *Chapter 4* and *Chapter 5*. Therefore, by describing the decisive findings in related

platinum-aryl complex chemistry for non-cyclic structures, this three-step cross coupling cascade towards large macrocycles is explained in more detail below.

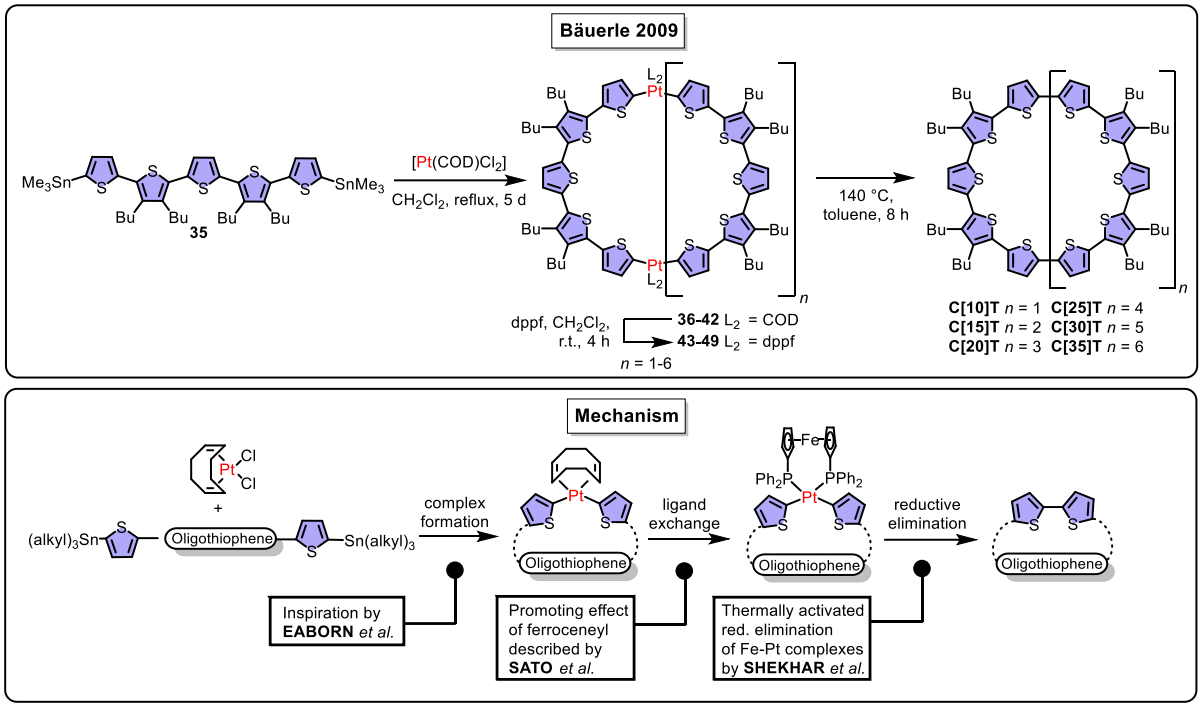

Scheme 4. Synthesis of giant oligothiophenes by the Bäuerle group in 2009[40] and the general mechanism for the C[*n*]T formation *via* the platinum-mediated cross coupling cascade as well as decisive findings of Eaborn[176], Sato[177] and Shekhar *et al.*[178] in the field of Pt-aryl complex chemistry.

The general idea to form macrocyclic Pt(COD) oligothienyl complexes in the first place was inspired by the early report of Eaborn *et al.*,[176] who describes a very strong interaction of $Pt(COD)Cl_2$ with 2-thienyl trimethylstannanes (complex formation, Scheme 4). An *in situ* COD-dppf ligand exchange in order to facilitate the subsequent reductive elimination is followed (ligand exchange, Scheme 4). Regarding this step, Sato *et al.*[177] describe an unprecedented promoting effect of a ferrocenyl group for the oxidatively induced reductive elimination of *cis*-ferrocenyl platinum (II) complexes. Here the ferrocene part gets oxidized by agents such as 2,3-dichloro-5,6-dicyano-*p*-benzochinone (DDQ) or $AgBF_4$ and a subsequent ET from the Pt(II) part to the ferrocene decreases the electron density on the Platinum center which in turn accelerates reductive elimination. Furthermore, in 2004, Shekhar *et al.*[178] demonstrated a smooth purely thermally activated reductive elimination of *cis*-Pt-(ArAr') complexes using dppf as ancillary ligand (reductive elimination, Scheme 4). It has to be noted at this point that in the same study COD complexes needed elevated temperatures of 150 °C

and more to undergo reductive elimination at acceptable reaction rates. This finding underlines the importance of the COD-dppf ligand exchange as a preparative step for a smooth reductive elimination - especially when applied to comparably fragile macrocyclic scaffolds. Additionally, the strength of platinum-aryl bonds in complexes with electron-withdrawing groups are greater due to an increased ionic character.[179] This means that a faster reductive elimination from complexes with more electron donating ligands, such as thiophenes, can be achieved.

Already back in 2007[175] linear oligothiophenes were synthesized similarly to the above described scheme by the Bäuerle group. Here, reductive elimination with silver triflate as a one electron oxidant had to be utilized, whereas only heating with no oxidation agent exclusively yielded polymeric products. On the other hand, as already mentioned, in the case of thiophene macrocycles **C[10]T-C[35]T** simple heating of the Pt(dppf) complexes **43-49** in a pressure vial ensured very smooth C-C bond formation *via* purely thermally activated reductive elimination (Scheme 4). Unfortunately, regarding the reductive elimination protocol, no comparative study towards an oligothiophene macrocyclization reaction with and without the utilization of an oxidative agent in the last step is present in literature. Nevertheless, the general reaction cascade described in Scheme 4 is widely used in the field in order to synthesize various types of bent π-scaffolds.

2.2.3 Size-Dependent Optical and Redox Properties

[n]Cycloparaphenylenes

While for linear paraphenylenes the main absorption band is strongly red-shifted upon chain elongation[180] for [*n*]CPPs such a size dependency is not observed. All [*n*]CPPs synthesized to date possess an absorption maximum of $\lambda_{max} \approx 340$ nm in chlorinated solvents (Table 1).[34] In order to explain this phenomenon the nature of the involved transitions have to be elaborated first. HOMO-LUMO transitions in this class of centrosymmetric molecules are Laporte forbidden due to the conservation of D_{6d} symmetry.[181] Therefore, these transitions can be assigned to the small and broad lower energy shoulder of the more intense absorption band in the spectra (Figure 13a). In contrast, the degenerated HOMO–1/HOMO–2 and

LUMO+1/LUMO+2, respectively, delocalize on the two opposite sites of the molecules (in order to simplify the following discussion instead of HOMO–1/HOMO–2 and LUMO+1/LUMO+2 only HOMO–1 and LUMO+1 are mentioned). Thus, the transitions HOMO–1-LUMO and HOMO-LUMO+1 cause a symmetry change and are accordingly strongly dipole allowed. Both transitions contribute to the main intense absorption band. Interestingly, the respective HOMO–1/LUMO and HOMO/LUMO+1 pairs show a very similar [*n*]CPP size-dependent energy curve (Figure 13b). For example, upon increasing *n* in [*n*]CPP the energy of HOMO–1 and LUMO almost simultaneously increases. Therefore, the energy gap between HOMO–1/LUMO and HOMO/LUMO+1 (~3.8 eV) remains rather constant throughout the series and thus almost no shift in the main absorption band can be observed. The extinction coefficient gradually increases with ring size due to the increased magnitude of the transition dipole moment. In contrast, the reverse energy trend of HOMO/LUMO and the concomitant shrink of the energy gap leads to a slight blue shift of the lower energy absorption band with increasing ring size.

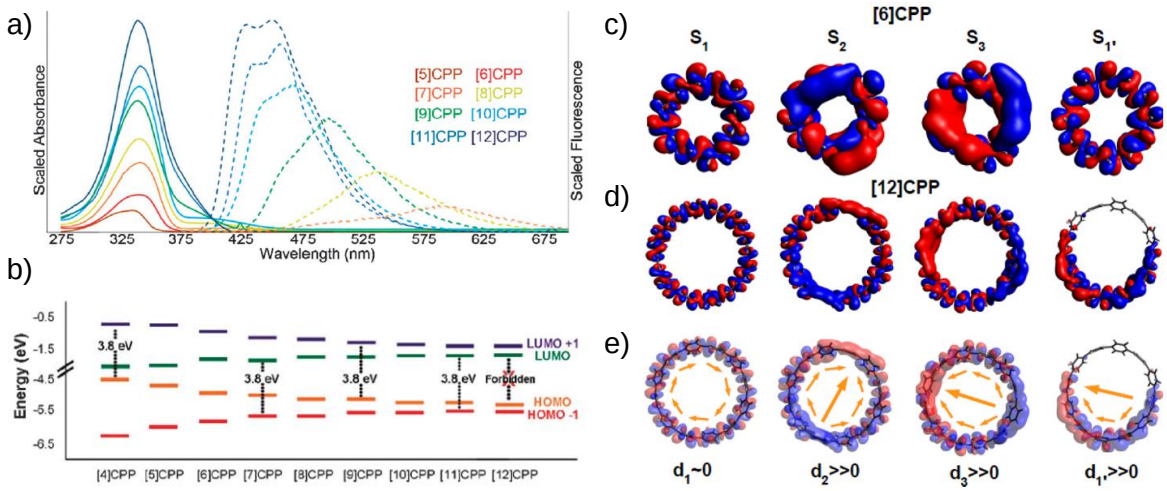

Figure 13. a) UV/Vis (solid lines) and fluorescence spectra (dashed lines) of **[5]-[12]CPP**. Reprinted with permission of ref. [34] Copyright 2015 Royal Society of Chemistry. b) Calculated energy levels of HOMO, HOMO–1, LUMO and LUMO+1 of differently sized [*n*]CPPs. Reprinted with permission from ref. [138]. Copyright 2011 American Chemical Society. Transition densities of the S_1, S_2, S_3 and $S_{1'}$ states for c) **[6]CPP** and d) **[12]CPP** as well as the e) transition dipole moments sketched for **[12]CPP**. Adapted with permission from ref. [182]. Copyright 2014 American Chemical Society.

In comparison to this invariance of the [*n*]CPP's main absorption band the emission properties show a great ring size dependency (Figure 13a). A decrease in size leads to a very strong red shift of the fluorescence and a lowered quantum yield. In this regard, referring to Kasha's rule[183], emission typically occurs from the lowest excited energy state S_1 to the ground state

S_0. However, nearly all allowed transitions (HOMO-LUMO+1 or HOMO–1-LUMO) populate the [*n*]CPP's S_2 and S_3 states. Tretiak and co-workers[182] found out that these states are able to internally convert to spatially localized excited $S_{1'}$ states within the femtosecond time regime, which is a lot faster than the measured excited state lifetimes (nanoseconds). Thus, the $S_{1'}$ - S_0 transition is the predominating process responsible for the emission spectra.

The geometries of the small [*n*]CPPs with $n < 8$ are completely planarized (decrease of dihedral angles between adjacent phenyls) in the excited state. This causes a complete transition density delocalization (Figure 13c) and the $S_{1'} – S_0$ transition get increasingly Laporte forbidden as ring size descends due to symmetry conservation (similarity to the ground state) leading to smaller quantum yields.[34] However, the small geometry difference to the ground state (completely planarized system in the excited state *vs*. marginally contorted in the ground state) also causes a very high vibrational coupling, a lowered $S_{1'} – S_0$ energy gap and therefore a gradual bathochromic shift of the emission maxima with decreasing ring size (Figure 13a).

On the other hand, larger [*n*]CPPs with $n > 8$ only develop a local planarization of about five phenyl rings in the excited $S_{1'}$ state with the rest mostly preserving ground state geometry. This creates a large transition dipole moment and highly fluorescent dyes (Figure 13d, e) with large quantum yields. On the other hand, the smaller fluorescence red shift can be explained by the decrease of π-conjugation and the concomitant lowering of vibrational coupling and an elevated $S_{1'} – S_0$ energy.

The described effects regarding different red shifts can also be summarized in very simple words: Whereas small rings are contorted to a very high degree and the potential for structural relaxation in the excited state is much higher, in larger circles such geometric changes compared to the ground state configuration are rather small which leads to a decreased Stokes shift.

Cyclo[n]thiophenes

Owing to an aliphatic decoration pattern, in the case of C[*n*]Ts generally two types of structures have to be differentiated into series 1 and 2 (Figure 14a, b), which incorporate different repeating units n. Independent of the aliphatic substitution, the optical properties of C[*n*]Ts are quite different from the afore discussed [*n*]CPPs. As elucidated in *Chapter 2.1.3* for linear oligothiophenes, also the longest wavelength absorption maxima (λ_{max}) of C[*n*]Ts undergo a

progressive red shift and intensity increase upon increasing of the cycle size. While the main absorption band of **C[10]T** is located at 417 nm in CH_2Cl_2, a bathochromic shift of almost 30 nm to 445 nm for **C[35]T** can be observed (Table 1). However, in comparison to their linear counterparts with about the same amount of repeating thiophene units the spectra of C[*n*]Ts are strongly shifted to higher energies.[121] For example, the value of λ_{max} found for **C[18]T** (418 nm) in comparison to linear **19T** (430 nm) is significantly different and rather corresponds to the absorption maximum found for linear **9T** (418 nm). [184] However, **C[18]T** exhibits approximately double of the absorption strength (ε_{max} = 123900 M^{-1} cm^{-1}) compared to linear **9T** (ε_{max} = 55700 M^{-1} cm^{-1}).

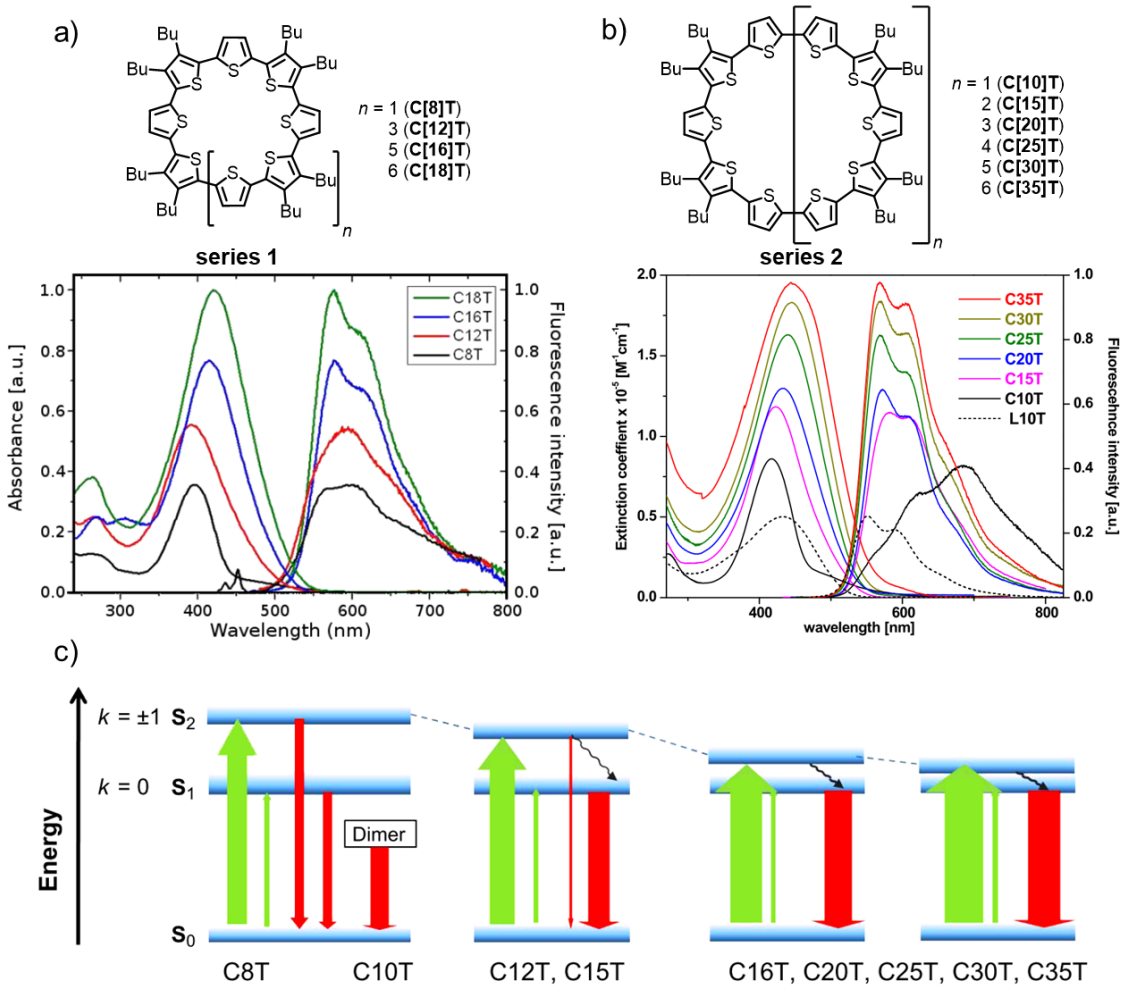

Figure 14. UV/Vis and emission spectra of cyclic oligothiophenes comprising different aliphatic decoration patterns summarized in a) series 1 and b) series 2. Adapted with permission from ref. [185] and ref. [40]. Copyright 2011 Beilstein-Institut and 2009 Wiley-VCH Verlag GmbH & Co. KGaA. c) Qualitative energy landscape including the S_0, S_1 and S_2 states of C[*n*]Ts with *n* = 8-35 thiophene rings as well as sketched absorption (green arrows) and emission (red arrows) processes. The arrows are weighted by the intensity of the respective transition. Reprinted with permission of ref. [185]. Copyright 2011 Beilstein-Institut.

From these observations a general trend that λ_{max} of the macrocyclic C[*n*]Ts are located at energies where linear compounds [*n*]Ts with approximately half the number of repeating units absorb can be derived.[121]

The absorption maxima of C[*n*]Ts can be assigned to the S_0-S_2 electronic transition (Figure 14c, green arrows), whereas the transition to the lowest excited state (S_1) is symmetry forbidden due to the centrosymmetric nature of the compounds. Different from [*n*]CPPs the energy of the S_1 states of C[*n*]Ts remain rather constant throughout the series, whereas the S_2 energy is lowered with ascending ring size (Figure 14c). This also explains the observed bathochromic shift of the absorption maximum for large macrocyclic oligothiophenes.

Table 1. Photophysical key figures for **[*n*]CPP**s and **C[*n*]T**s in chlorinated solvents at room temperature. The values in parenthesis are assigned to C[*n*]T series 1, whereas all other numbers in the column represent series 2.

	[*n*]CPP			**C[*n*]T**		
n	**λ_{max} / nm**	**ε / 10^4 M cm^{-1}**	**$\lambda_{em,max}$ / nm**	**λ_{max} / nm**	**ε / 10^4 M cm^{-1}**	**$\lambda_{em,max}$ / nm**
5	335[a,b]	5.7[a,b]	no fl.	–	–	–
6	340[c]	-	no fl.	–	–	–
7	340[d]	6.9[d]	587[d]	–	–	–
8	340[e]	10[e]	533[e]	(396)[j]	(5.1)[j]	(602)[j]
9	340[f]	12[f]	494[f]	–	–	–
10	341[g]	13[g]	466[g]	417[k]	8.6[k]	685[k]
11	340[h]	13[h]	458[h]	–	–	–
12	339[i]	14[i]	450[i]	(392)	(5.5)	(593)
15	–	–	–	423	12	582
16	–	–	–	(414)	(9.7)	(577)
18	–	–	–	(418)	(12)	(575)
20	–	–	–	434	13	572
25	–	–	–	440	16	570
30	–	–	–	444	18	568
35	–	–	–	445	20	567

[a]Ref [186]. [b]Ref[131]. [c]Ref [187]. [d] Ref [188]. [e] Ref [169]. [f] Ref [189]. [g] Ref [190]. [h] Ref[34]. [i] Ref [137]. [j] Ref [185] for series 1. [k]Ref [40] for series 2.

Upon optical excitation fast relaxation from the S_2 to the S_1 is observed and subsequently C[*n*]Ts with *n* = 12-35 emit from energetically almost equal S_1 states to the ground state S_0. This leads to very similar $\lambda_{em,max}$ values within the respective series 1 (~577 nm) and 2 (~570 nm). As ring size ascends, the transition probability (Figure 14c, red arrows) increases and higher ε_{max} values are observed (Table 1). Interestingly, for **C[10]T** a strongly red shifted emission in comparison to all other macrocycles within the series can be observed

(Figure 14b). This can be explained by the tendency of **C[10]T** to form dimers in the excited state (excimers) which then emit at higher wavelengths compared to a monomer emission.[121]

The **C[10]T** macrocycle was also the focus of very interesting optical studies in the oxidized state.[113] In *Chapter 2.1.3* the spectral signatures of various charged linear oligothiophenes and the basic theoretical considerations were already discussed in detail. Therefore, the following paragraph shall shortly and exemplarily highlight the findings for a cyclic analogue **C[10]T**. These are also of great importance for the understanding of spectral changes for the oligothiophene semicircle oxidation described in *Chapter 4* and *Chapter 5*.

C[10]T possesses very unusual optoelectronic properties in the oxidized state owned to its cyclic nature. Figure 15a shows the absorption spectra of the onefold (red line) and twofold (blue line) oxidized species.

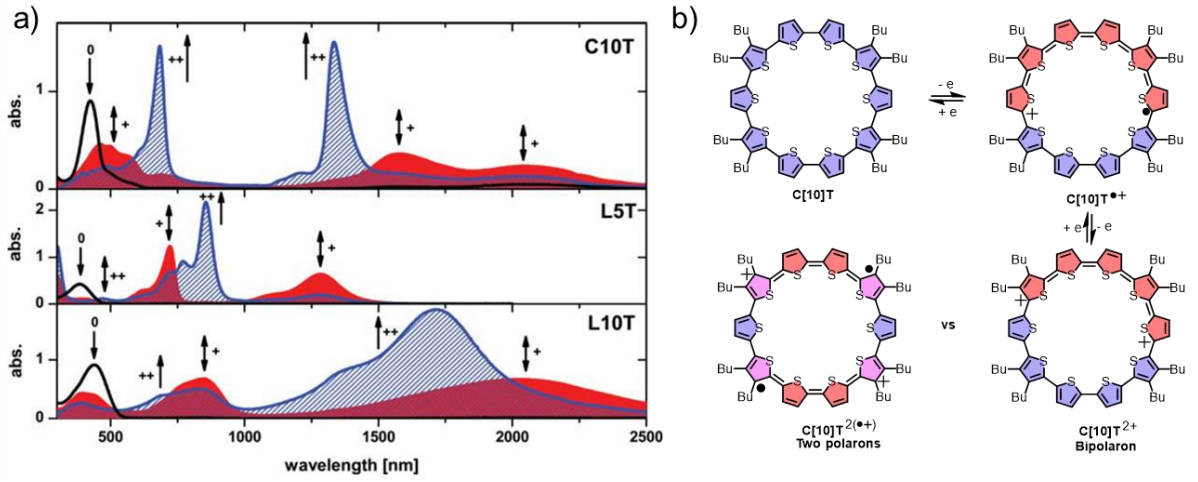

Figure 15. a) UV/Vis/NIR absorption spectra of **C[10]T**, linear **L5T** and linear **L10T** (from top to bottom) in the neutral state (black lines) and upon chemical oxidation with one (red lines) and two (blue lines) equivalents of thianthrenium hexachloridoantimonate(V) ($ThiSbCl_5$) in 1,1,2,2-tetrachloroethane at room temperature. Adapted with permission from ref. [113]. Copyright 2011 Royal Society of Chemistry. b) Chemical structures of **C[10]T** in a neutral, cationic, bipolaron and polaron pair configuration. The thiophene ringes with aromatic and quinoid structures are coloured in blue and red, respectively, whereas a combination of both is shown in purple.[113]

Radical cation formation (red line) causes the emergence of broad bands with maxima located around 2025 nm and 1576 nm which can be assigned to the monomeric (**C[10]T**$^{\bullet+}$) and dimeric ((**C[10]T**)$_2^{\bullet+}$) radical cations, respectively. This hypothesis of an oxidation-induced aggregation process can be justified with the following finding: When the solution is exposed to higher temperatures the mentioned high energy band decreases in intensity while the lower energy band concomitantly grows. Further, this process is reversible.

The energy band centred around 500 nm is caused by high energy electronic transitions related to the high symmetry of **C[10]T** in comparison to linear counterparts. Further oxidation to the dicationic species (blue line) is accompanied by the appearance of two sharp absorption maxima located at 1334 nm and 683 nm (Figure 15a, top graph), which substantially differs from what would be expected for a bipolaron structure (*Chapter 2.1.3*) such as **L5T** (Figure 15a, middle graph) where the radical dication is characterized by one strong absorption band at 855 nm.

Therefore, macrocycle **C[10]T** exhibits a different electronic structure in the twofold oxidized state, namely a polaron pair configuration with two spatially clearly separated radical cations (Figure 15b). In contrast to these observations, the longer linear oligomer **L10T** also shows two absorptions (680 nm and 1705 nm) but with a highly increased broadening of both bands. Unlike in the cyclic analogue **C[10]T**, this indicates a noticeable interaction of the two polarons. Therefore, the formal spatial separation of the two positive charges in *e.g.*, different geometrical distortions of the chain in **L10T** (polaron pair configuration, *Chapter 2.1.3*) appears as a rather inappropriate description. Instead, most probably an unneglectable dependency of both charges has to be ascertained.

2.3 Oligothiophene-functionalized Rylene Bisimide Donor-Acceptor Dyads

2.3.1 Design and Key Features

As elucidated in *Chapter 1*, D-A dyads display a functional unit that mimics natural photosynthesis in its very simplest form with laboratory systems accessible and tailored by chemists. Within the scope of this thesis the literature reported systems of covalently linked electron-poor rylene bisimides with electron-rich oligothiophenes in imide position shall be discussed in more detail.[59]

The excellent photophysical properties and wide utilization of oligothiophenes in OLEDs, OFETs and OSCs has already been mentioned in *Chapter 2.1.1*. The electron-deficient counterpart to the oligothiophene based dyads described in *Chapter 4* and *5* are PBIs, which is a subgroup of rylene imides. Since the perylene was discovered by Kardos in 1913[191] rylene

dyes have received a great deal of attention not only in academic but also in industrial pigment research.[192] Imidization of these aromatic scaffolds allows for electronic modification of the chromophore, which in the end made perylene and naphthalene imides to one of the best ambient-stable n-type semiconductors on the market.[49, 193] Several rylene imide based D-A architectures are also subject to interesting and very promising research fields such as ambipolar materials [194], which can for example be applied in OFETs.[195-197] The attachment of various substituents onto PBIs can be achieved in different positions: Firstly, functionalization in imide position does not significantly alter the electronic properties of the molecule due to nodal planes at the imide nitrogen atom in the HOMO and LUMO.[198] Therefore, this substitution pattern is often used to adjust solubility or aggregation behavior[199] whereas absorption and emission properties remain mostly unchanged. Secondly, substitution in the bay- or ortho-position can alter the electrooptical properties as well as molecular geometry in a very pronounced way *e.g.*, by implementing donor π-systems in direct conjugation to the core, which in turn leads to D-A charge transfer (CT) interaction.[200] In contrast to the perylene the smaller naphthalene imides show a first reduction potential alternation upon *N*-substituent exchange.[201]

The covalent linkage of an oligothiophene (blue) to a perylene or naphthalene bisimide (red) results in molecular D-A dyads (Figure 16). A large variety of these kind of linear dyads were investigated in literature. [52-58]

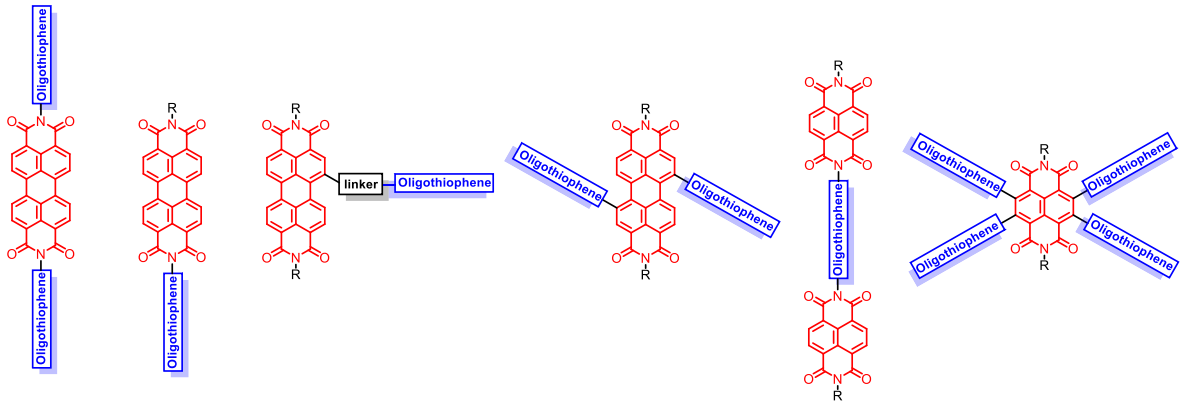

Figure 16. Selection of literature known oligothiophene (blue)-rylene bisimide (red) D-A systems.

Depending on the chain length and the location of the oligothiophene attachment onto the rylene imide the absorption of both subunits can be clearly distinguished from each other. The

mostly broad high energy oligothiophene region more or less overlaps with the lower energy highly fine structured perylene or naphthalene imide spectra (*Chapter 2.3.2*), which makes these molecular architectures panchromic light absorbers and therefore excellent candidates for light harvesting applications (*Chapter 1*). The specialty of a molecule with spectrally distinguishable subunits is the possibility to excite both segments selectively and monitor the subsequent photophysical processes.

Regarding photovoltaic application perspectives of D-A dyads, the overall goal is on the one hand a fast and efficient charge separation *via* photoinduced electron transfer (PET) upon optical excitation and on the other hand a slow charge recombination.[8] It is then possible for the formed CT states to dissociate into holes and electrons[13], which can then diffuse to the electrodes *e.g.* of a single-component OSC[14] device in order to generate electric current. A large variety of rylene imide-oligothiophene dyads is already known in literature and a small selection of linear dyads together with highly interesting processes upon photoexcitation shall be explained in this chapter. Thereby exclusively photophysical properties in solution will be discussed.

2.3.2 Photoinduced Processes

Upon photoexcitation of D-A dyads, photophysical processes such as intramolecular Förster resonance energy transfer (FRET) or photoinduced electron transfer (PET) can be observed depending on the constitution of the dyad.[202] Both phenomena together with TA spectroscopy as investigation method thereof, will be explained briefly below.

FRET, which was named after the discoverer Theodor Förster[203-204] is an electrodynamic phenomenon and it occurs between a donor unit in the excited state and an accepting fragment in the ground state (Figure 17a). As a result of FRET, the vice-versa situation with an excited acceptor and a donor in the ground state is received.[205] Spectrally speaking, upon photoexcitation of the donor, emission of the acceptor is observed (Figure 17b) and the amount of donor fluorescence is reduced to a minimum for an efficient FRET process (*vide infra*).

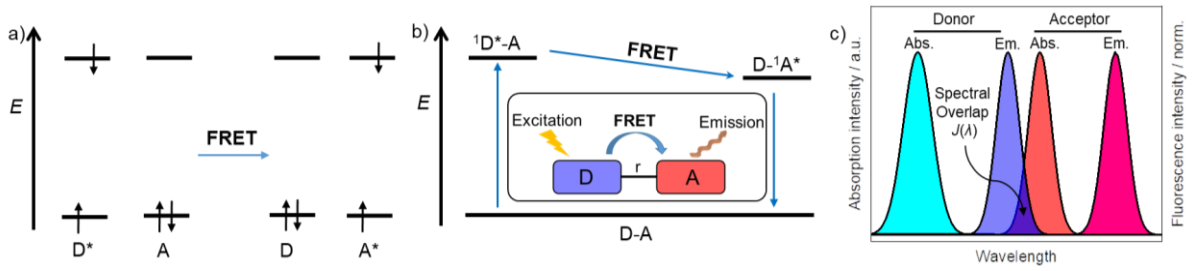

Figure 17. a) General qualitative energy diagram of a FRET process from an excited donor (D*) to an acceptor in the ground state (A) resulting in the vice-versa situation. b) Qualitative energy diagram of a covalently connected D-A system upon excitation of the donor (^{1}D*-A) and a subsequent FRET to the acceptor (D-^{1}A*). Inset: Sketched intramolecular FRET in a D-A dyad with a distance r between D and A segment. c) Sketched absorption and emission profiles of D (light blue and blue) and A (red and pink), respectively, as well as a highlighted spectral overlap $J(\lambda)$.

Theoretically, the FRET can be described as an oscillating dipole exchanging energy with another dipole possessing a similar resonance frequency.[206] The rate k_{FRET} of the energy transfer depends on the center-to-center distance of both fragments (r), the transition dipole orientations of D and A (κ), the degree of overlap of the donor emission spectrum normalized to unity with the acceptor absorption ($J(\lambda)$, Figure 17c), the quantum yield of the free donor Φ_D, the lifetime of the donor τ_D in absence of the acceptor and parameter n_{ref}, which is the refractive index of the solvent. The distance at which the efficiency of the FRET is 50% or half of the excited donor molecules decay by FRET and half decay by the usual radiative or non-radiative rates is the so called Förster distance R_0.

$$R_0 = 0.211(\kappa^2 n_{ref}^2 \Phi_D J(\lambda))^{\frac{1}{6}}. \quad (2)$$

$$k_{FRET} = \frac{1}{\tau_D}\left(\frac{R_0}{r}\right)^6. \quad (3)$$

By analyzing equation 3, it becomes apparent that the distance r of donor and acceptor units is the most decisive factor for k_{FRET}.

The orientation factor κ is 1 in case of a parallel orientation and 0 for a perpendicular orientation of the transition dipoles. Thus, in the last-named case no FRET should theoretically occur. Nevertheless, also for perpendicularly arranged D-A chromophores FRET can be observed.[207-208] In these closely spaced donor and acceptor moieties the dipoles are not small compared to the distance between them and the ideal dipole approximation utilized for the equations 2 and 3 is not an appropriate description of the molecular situation anymore.[209] In this case instead of using dipole approximations, transition densities have to be utilized to calculate accurate k_{FRET} values.[210] This procedure is comparably complicated and involves

deep knowledge about the definition and the development of these densities. Nevertheless, for a very closely spaced (< 10 Å) D-A pair in a non-perpendicular orientation with overlapping acceptor absorption and donor emission the FRET rate is most likely extremely high.
Due to the high distance dependency of the FRET this process is often used as a "spectroscopic ruler" especially for large macromolecules.[211-213] Here, a donor and an acceptor are attached on the molecule (mostly proteins) of interest and assuming no conformational changes occur during the process and only one D-A pair is involved in the process, the D-A distance can be calculated. Experimentally the FRET is often measured by the extent of donor emission quenching with and without the acceptor.[214]

Furthermore, in comparison to the ET (*vide infra*), FRET is mostly independent from the solvent as it is a through-space interaction. The FRET mechanism is in stark contrast to a Dexter-type energy transfer[215] where an orbital overlap of the D and A is a prerequisite for the process and as a result electrons are transferred. This type of energy transfer will not be explained further within the scope of this thesis and the interested reader is referred to the literature.[216]

Another interesting process D-A structures can undergo upon photoexcitation is electron tranfer (ET).[217] The ET process itself was first described in a quantitative way by Rudolph A. Marcus in the 1950s, where he originally based his theory on interactions of metal ions in solution.[218] Nevertheless, the derived concept also proved to be applicable to intramolecular ET processes in more complex inorganic and organic systems. Within the framework of this thesis the most important ideas, concepts and conclusions of this theory shall be sketched briefly.[219]

Two one dimensional harmonic profiles (Figure 18a) along a reaction coordinate represent the free energy surfaces of an initial (blue) and a final state (red) before and after the ET process between two redox centers. In a purely diabatic treatment (Figure 18a) in which donor and acceptor do not electronically communicate with each other and the charge is completely localized (mostly in intermolecular ET processes) or, more precisely, the electronic communication is small compared to the thermal energy k_BT, the following famous Marcus formula can be derived:

$$k_{\mathrm{ET}} = A \exp\left(-\frac{\left(\lambda_{\mathrm{E}} + \Delta G^{00}\right)^2}{4\lambda_{\mathrm{E}}\, k_{\mathrm{B}} T}\right). \qquad (4)$$

This Arrhenius-type equation describes the rate constant k_{ET} of the ET process. Here, A is a preexponential number depending among other factors on the nuclear motion frequency through the transition state (TS), k_B the Boltzmann constant and T the temperature. λ_E is the reorganization energy consisting of the sum of solvent (λ_o) and inner reorganization energy (λ_v) which takes into account the alteration of solvent molecules after ET and the changes in bond lengths and angles during the process, respectively.

Furthermore, in most cases the initial and final state are non-degenerated and the minimum of the harmonic potentials is not located at equal energy levels. In other words, a driving force ΔG^{00} for ET is present, which is also taken into account in equation (4). The energy barrier ΔG^* for the ET to proceed can be overcome either by applying optical or heat stimuli to the system (Figure 18a). The term "optically induced" referes to an absorption of a photon, which directly leads to the ET. In contrast, the below described "photoinduced" ET (PET) processes mean a preparation of an initial state by photoexcitation and a subsequent relaxation to the CSS. Although strictly speaking, the classical Marcus theory can only be applied for diabatic systems (which is a very limited group of compounds) kinetic calculations in ET are widely addressed for a huge variety of compounds with the above-mentioned equation. One very well-known consequence of the theory is the so-called Marcus parabola (Figure 18b) including an inverted region in which surprisingly a reduced ET rate is predicted for very exergonic reactions with the magnitude of the Gibbs energy $|\Delta G| > \lambda_E$, which is often found for back ET. The other Marcus "normal" region predicts a reduced k_{ET} for an endergonic ET. An optimum of the ET rate is reached when the activation energy $\Delta G^* = 0$ and the Gibbs energy equals the reorganization energy λ_E. The harmonic profiles for the initial (blue) and final (red) diabatic state in Figure 18b schematically represent the relative energy in each region of the parabola.

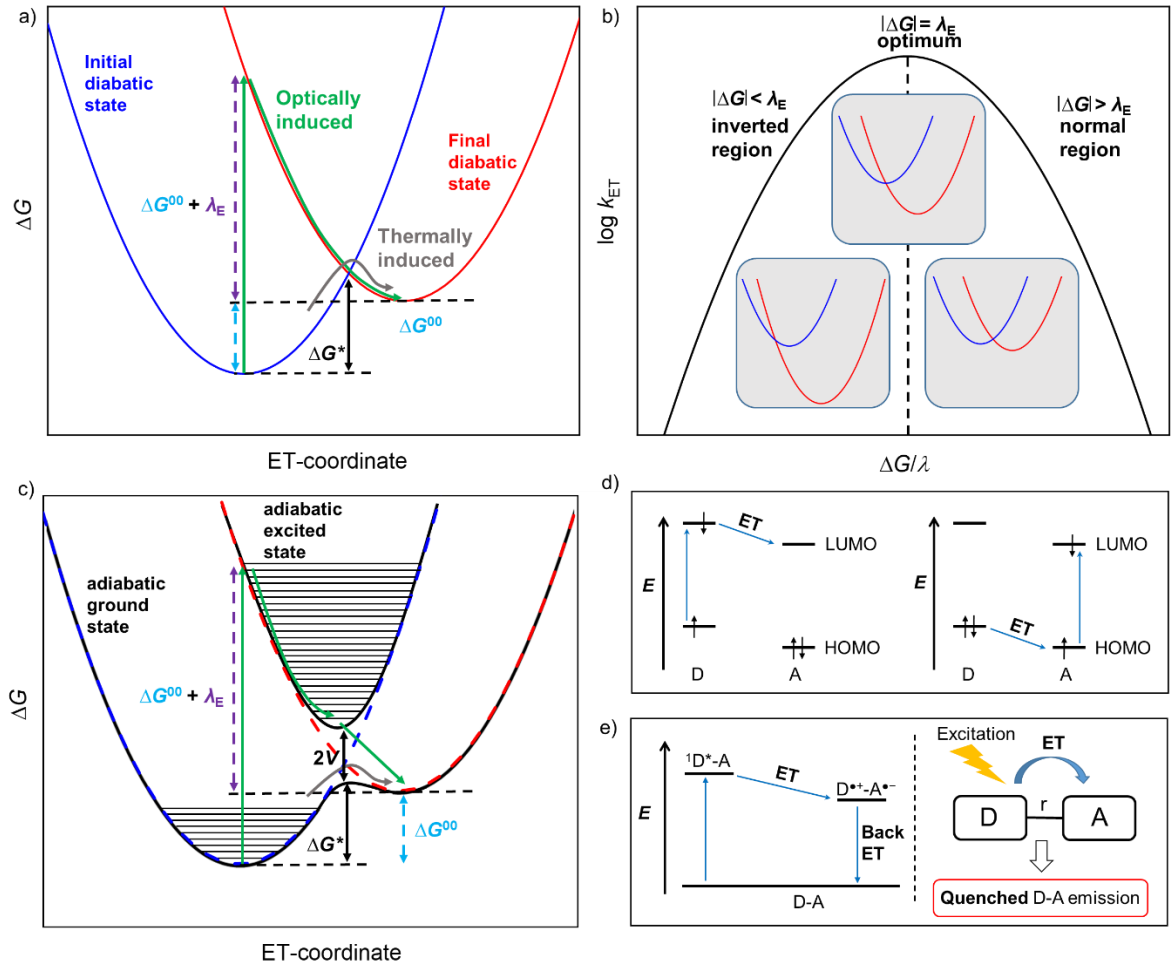

Figure 18. a) Diabatic free energy surfaces of the initial state (blue) and the final state (red) according to the Marcus theory as well as the pathway for thermally (grey)- and optically (green) induced ET.[219] b) Marcus parabola including inverted, optimum and normal region. For each region the corresponding diabatic free energy surfaces of the initial (blue) and final state (red) are sketched qualitatively. c) Adiabatic free energy surfaces (black solid lines) of the ground and excited state according to the Marcus-Hush theory combined with the diabatic free energy surfaces (blue and red dashed lines).[219] d) MO picture of an ET upon excitation of donor and acceptor (from left to right). e) Energy diagram of the states of a molecular dyad (D-A) involved in the ET after excitation of the donor and the sketched process upon photoexcitation with a distance r between D and A segment (from left to right).

Moving one step forward towards D-A systems where an electronic communication between both subunits is present, the Marcus-Hush theory[220-221] extends the classical Marcus theory to an adiabatic treatment by introducing an electronic coupling V, which can be conveniently calculated from optical data. If $V << \lambda_E$ the following equation (5) describes the calculation of the energy barrier ΔG^* in the adiabatic case:

$$\Delta G^* = \frac{\lambda_E}{4} - V + \frac{V^2}{\lambda_E}. \quad (5)$$

Of the resulting two adiabatic state free-energy surfaces (Figure 18c) the ground state now has two minima (black line) and both curves couple to the two diabatic lines (blue and red dash). One consequence in the adiabatic picture is the drastically reduced energy barrier (ΔG^*) for thermally induced ET (black). On the other hand, the optically induced ET (green) occurs from a Boltzmann vibrational state of one ground state minimum following the Franck-Condon principle to a vibrational level of the excited state. The relaxation to the vibrational modes of the second minimum of the ground state finalizes the ET. Interestingly, the finding of a CT band in the absorption spectrum upon optical excitation during that time triggered the deliberations outlined above. Often, this band corresponds to the lowest energy transition of the system in the near-infrared (NIR) region. The entire process is *i.a.* strongly D-A distance-dependent because a reduced orbital overlap between donor and acceptor causes a decay of the coupling element V and therefore a decrease in CT band intensity can be observed.[222] Overall, the described theories of Marcus and Hush provided very helpful frameworks for the calculation of ET rates.

As already outlined before, the term "PET" is reserved for the ET between photoexcited and ground state molecules or, in case of a covalently linked architecture, D and A moieties within a single molecule.[223] Thus, PET can be considered as a quenching pathway. The energy of the excited state as well as the redox potentials of D and A dictate the efficiency of the process. Intramolecular PET[224] can also be explained in a molecular orbital picture (Figure 18d). Here an excitation of the donor promotes the transition of an electron from the donor's HOMO in its LUMO which is then transferred to the empty LUMO of the acceptor. Excitation of the acceptor creates a hole in the acceptor HOMO which is then backfilled by an electron from the donor's higher energy HOMO. From an electronic state point of view, *e.g.* excitation of the donor in a D-A dyad's ground state produces the singlet excited ^{1}D*-A state, which upon ET converts to a CSS $D^{\bullet+}$-$A^{\bullet-}$ (Figure 18e). Its energy is calculated by using the Weller equation[225-226] and subsequently ΔG can be determined. By comparing of ΔG to λ_E a statement about the location of the ET within the Marcus parabola (Figure 18b) can be made. In other words, in order to clarify whether an ET is endergonic or exergonic, both mentioned values have to be provided.

The subsequent relaxation back to the ground state is most commonly a non-radiative process

and quenches the emission of often highly fluorescent individual D and A chromophores (Figure 18e, *vide infra*).

One of the most convenient methods to follow and evaluate such fast processes is TA spectroscopy.[227-228] Here, first a normal absorption spectrum is measured (without pump-pulse). Then the molecule is excited at a certain wavelength by a pump laser and the sample is afterwards probed by a white light continuum pulse with changing delays with regard to the pump laser excitation. The difference spectra obtained from these spectra as well as the steady-state (without pump-pulse) spectra is finally presented for several delay times to monitor the spectral evolution of the molecule in the femtosecond to nanosecond regime after excitation. In dyad chemistry most of the times either the donor or the acceptor gets selectively excited in order to differentiate subunit-dependent processes.

In TA spectra three main spectral characteristics, which partially overlap, can be observed (Figure 19a).

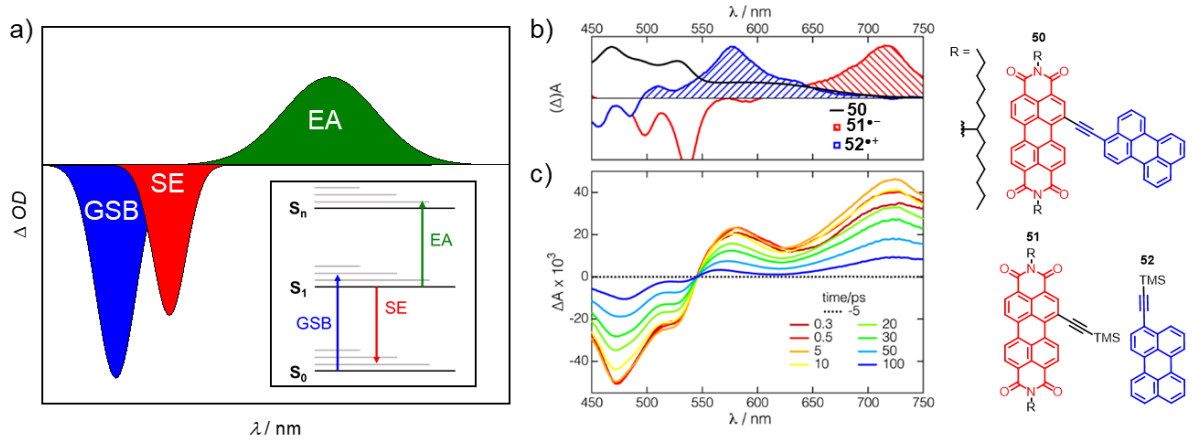

Figure 19. a) Qualitative spectral contributions of the GSB (blue), SE (red) and EA (green) in a TA spectrum. Inset: Energy states and possible transitions monitored in TA spectroscopy. b) Ground state absorption spectrum of **50** (black) and transient difference spectra of **51** anion (red) and **52** cation (blue). c) TA spectra of **50** in CH_2Cl_2. Adapted with permission from ref. [229]. Copyright 2017 American Chemical Society.

Firstly, negative signals corresponding to the ground state bleach (GSB) arise due to the fact that after excitation by the pump-pulse the number of molecules in the ground state (S_0) is decreased. Thus, the ground state absorption is larger in the unpumped than in the pumped case (after excitation) and a negative signal is observed. Secondly, another negative signal, the so-called stimulated emission (SE), occurs from radiative relaxation of excited molecules (S_1) to the ground state triggered by a photon of the probe pulse. Lastly, excited state absorption (EA),

a strongly positive signal in the TA spectra, occurs when excited molecules absorb a photon and the transition to higher energy levels (S_n) is allowed. The analysis of the delay-dependent evolution of these bands in highly valuable for the excited state character investigation. For example, in the case of compound **50** the received EA part of the TA spectra (Figure 19c) looks much alike a sum of the bands received for cation and anion by SEC or TA of the respective reference structures (**51** and **52**, Figure 19b) and can therefore be concluded to be a CSS. Generally, TA spectra are a sum of all aforementioned contributions (GSB, SE and EA) and therefore excited state dynamics can be nicely followed with this method.

With the fundamental theoretic background of the most prominent photophysical processes in D-A systems and TA spectroscopy as a very powerful analysis method thereof explained, the following section will describe a small selection of rylene bisimide dyads with covalently linked oligothiophenes in imide position where these phenomena can be observed.

The D-A dyad from Majima and co-workers[53] is composed of a quinquethiophene unit T5 which is connected in imide position with a diphenoxysubstituted-PBI segment *via* differently sized flexible alkyl linkers (**53** and **54**, Figure 20a).

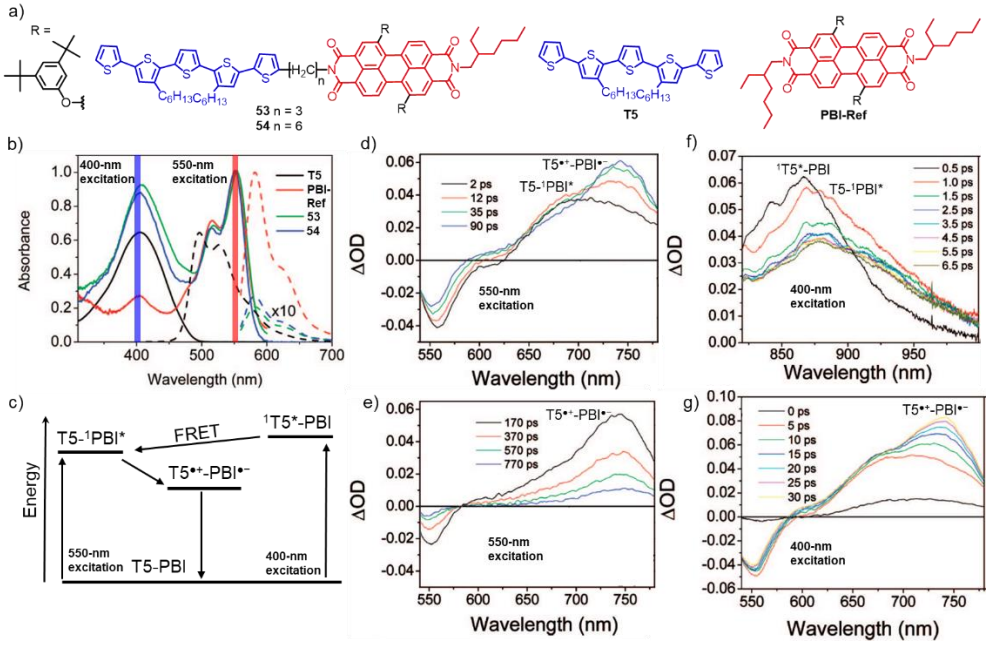

Figure 20. a) Chemical structures of the dyads **53** and **54** as well as reference compounds **T5** and **PBI-Ref**. b) UV/Vis (solid lines) and emission (dashed lines) spectra of **53** (green), **54** (blue), **T5** (black) and **PBI-Ref** (red) in benzonitrile. The excitation wavelengths utilized in TA spectroscopy are highlighted as vertical lines. c) Energy states diagram and photoinduced processes observed in dyads **C3** and **C6** after oligothiophene and PBI subunit excitation. TA spectra upon 550 nm (d/e) and 400 nm laser pulse excitation (f/g) in toluene including the respective assignment of the species in the graphs. Adapted with permission from ref. [53]. Copyright 2008 American Chemical Society.

In the UV/Vis spectrum (Figure 20b) it becomes apparent that both dyads in principle display a sum of the individual contributions of its reference structures **T5** and **PBI-Ref** (Figure 20a). This feature further confirms the electronic independency of both subunits in the dyads due to the aforementioned PBI imide substitution pattern (*Chapter 2.3.1*). The emission in benzonitrile is also immensely quenched to a quantum yield of below 0.1%. The compounds **53** and **54** show FRET and ET upon photoexcitation (Figure 20c). In the following section, all processes are exemplarily elucidated for **53**.

The D-A system **53** was selectively excited at two different wavelengths (400 nm and 550 nm) corresponding to the spectral region of the oligothiophene and the PBI, respectively, and the processes were monitored *via* TA spectroscopy. PBI excitation (Figure 20d, e) leads to the immediate rise of a GSB around 560 nm as well as SE at 630 nm, and additionally PBI S_1 EA at approximately 700 nm can be observed (**T5-^{1}PBI***). The absence of the T5 subunits'EA confirms exclusive excitation of the PBI chromophore. Within a few picoseconds an absorption band at 750 nm corresponding to the PBI radical anion emerges (**T5$^{\bullet+}$-PBI$^{\bullet-}$**, Figure 20d). It has to be noted at this point, that T5$^{\bullet+}$ absorption bands are reported to emerge at around 720 nm and 1270 nm,[105] which means that the first-named signal should overlap with the (more intense) PBI$^{\bullet-}$ band and the latter is out of the accessible spectral range. This is the reason why in the TA spectra only the PBI$^{\bullet-}$ bands can be unambiguously identified. After hundreds of picoseconds, clean relaxation to the ground state (**T5-PBI**) with no intermediate state formation can be seen (Figure 20e). Contrarily, upon oligothiophene excitation at 400 nm (Figure 20f, g) the spectral T5 subunit's S_1 EA signature with an absorption maximum around 860 nm (**^{1}T5*-PBI**) quickly converts within 1 ps to a band located at 880 nm corresponding to the PBI S_1 state (**T5-^{1}PBI***). The absence of the before mentioned PBI anion peak at 750 nm indicates that a charge separation mechanism is not involved in the deactivation process of **^{1}T5*-PBI**. Therefore, Figure 20e can clearly be interpreted as an FRET process from the oligothiophene T5 to the PBI subunit of **53**. Afterwards (Figure 20f), again a CSS is formed and the spectral signature of the PBI radical anion (peak at 750 nm) arises.

Collectively, the formation of a CSS in case of both excitations explains the low quantum yield determined for the dyads. The FRET from the donating T5 to the accepting PBI segment within 1 ps elucidates the PBI emission (Figure 20b) upon excitation at 400 nm.

With the above described TA spectra interpretation strategy in hand, the excited state dynamics also of other linear oligothiophene imide linked PBI D-A systems such as quartet bis-oligothiophene-PBI structure **55**[52], the highly flexible system **56**[230] or octithiophene-PBI dyads **57** and **58**[55] can be unraveled (Figure 21). All mentioned structures were part of a series but in order to ease the comparison only one molecule is exemplarily shown and analyzed. Two very important key parameters for the processes upon photoexcitation of D-A compounds are the rate of charge separation (k_{CS}) and recombination (k_{CR}), which are derived from the time scans of the bands of interest (*e.g.* **PBI$^{\bullet-}$**). The exponential fit of the rise and decay of these scans delivers the respective rate constants with sometimes more than one component of different percentages. In this case for better comparison an average value is calculated.

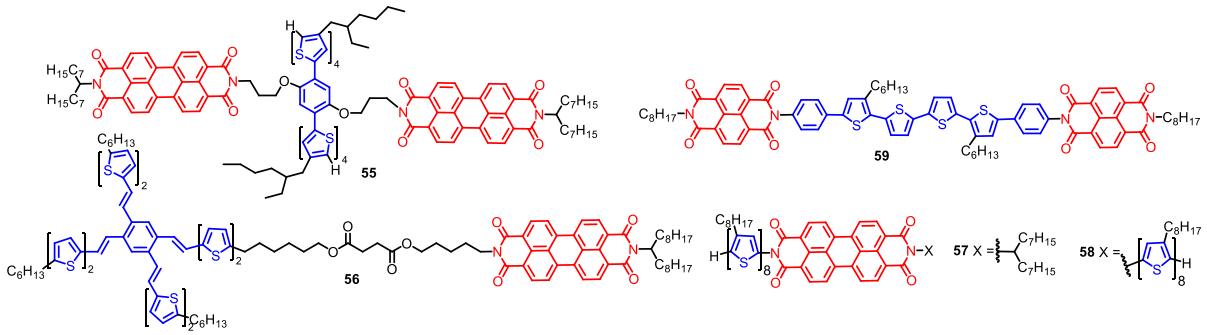

Figure 21. Chemical structures of oligothiophene imide linked PBI D-A (blue and red) systems **55**-**59**.

All systems **53-58** show a CSS formation upon acceptor excitation and a clean charge recombination to the ground state with no appearance of intermediate species. The respective rate constants k_{CS} of **53-58** in toluene overall indicate the formation of a CSS in the picosecond range (Table 2).

Table 2. Averaged rate constants of the charge separation (k_{CS}) and charge recombination (k_{CR}) upon photoexcitation of compounds **53-59** at the wavelength λ_{ex}.

compound	solvent	λ_{ex} / nm	k_{CS} / s^{-1}	k_{CR} / 10^{12} s^{-1}
53	toluene	550	$2.1 \cdot 10^{10}$	$2.7 \cdot 10^{9}$
55	toluene	527	$5.1 \cdot 10^{12}$	$2.1 \cdot 10^{10}$
56	benzonitrile	525	$1.5 \cdot 10^{8}$	–
57	toluene	527	$7.1 \cdot 10^{11}$	$2.3 \cdot 10^{9}$
58	toluene	527	$1.4 \cdot 10^{12}$	$2.8 \cdot 10^{9}$
59	CH_2Cl_2	420	$6.6 \cdot 10^{11}$	$1.7 \cdot 10^{11}$

Although measured in much more polar benzonitril, k_{CS} of **56** is 100-10000 times slower than the aforementioned rates, which can be explained with the long distance between D and A. The relaxation to the ground state occurs in the nanosecond region for all compounds (k_{CR}). Further oligothiophene imide linked PBI systems exist in literature, but these were not subject to excited state studies and can thus not be compared in this regard.[54, 231-232]

In the field of naphthalene bis(dicarboximide) (NBI) linked oligothiophenes the group of Kirk S. Schanze contributed two very detailed and well-illustrated investigations of the same compounds.[233-234] Here, oligothiophenes of different lengths were sandwiched between two naphthalene bisimides (the structure **59** is exemplarily shown in Figure 21). This end-capping also results in a completely quenched emission due to ET from the oligothiophenes to the NBIs. Calculation of the CSS energy level reveals a strong driving force for ET in the highly exergonic region, where charge separation and recombination proceed extremely fast within tens of picoseconds (Table 2). These experiments were followed by a detailed discussion of TA results and the exciton migration mechanisms in the excited state.

Chapter 3

Unusual Zig-Zag Effect in the Electrochemical Oxidation of Phenyl End-Capped α-Oligothiophenes

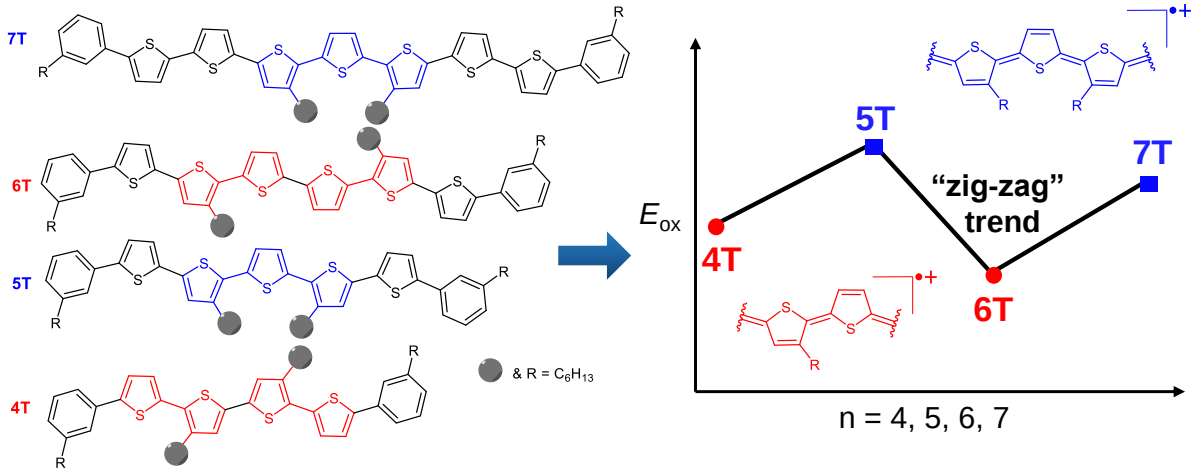

This chapter and the corresponding supporting information has been published:

K. Bold, M. Stolte, F. Würthner, *Org. Mater.* **2021**, *3*, 119-127.

Abstract: A series of phenyl end-capped α-oligothiophenes containing four to seven thiophene subunits (**4T-7T**) was synthesized utilizing palladium-catalyzed cross-coupling reactions. UV/Vis spectroscopic analysis revealed one broad absorption band that shifts bathochromically with increasing number of thiophene units. Structured emission spectra are observed with Stokes shift >4000 cm^{-1} and quantum yields of up to 53%. End-capping of the oligothiophene molecules by phenyl units does not only extend the effective conjugation but also prevents from α–α-homocoupling upon electrochemical oxidation. Accordingly,

reversible redox waves are observed in cyclic voltammetry with up to four reversible one-electron processes for the two longer congeners. Analyses of the first two oxidation processes in the framework of multiredox systems provide insight into the stabilization or destabilization of polaronic and bipolaronic states. An unusual zig-zag trend for the first (and to a lesser extend second) oxidation process could be explained by the sterical encumbrance of solubilizing hexyl chains in **5T** and **7T** molecules which counteract the formation of a fully planar quinoidal oligothiophene backbone.

3.1 Introduction

In the 1990s oligo- and polythiophenes advanced to the most important class of materials for organic electronics.[66] Different from other classes of compounds such as the acenes, pentacene being the most important representative,[236] or a variety of (semi-)conducting polymers such as polyacetylene or polyaniline, highly successful materials containing (oligo-)thiophene were developed both for small molecules and for polymers.[65] Further, this class of compounds proved to perform well and to be sufficiently stable in a large variety of applications including conducting polymers such as poly(3,4-ethylenedioxythiophene) (PEDOT)[237-238] as transparent conductive interlayer or low molecular weight oligothiophene-based organic semiconductors for applications in field effect transistors[239] and organic solar cells[240]. Whilst all successful oligo- and polythiophene molecules rely on the connection of the thiophene units in 2,5- (α) positions, either accessible by electropolymerization[241]or chemical synthesis,[242] the length and position of alkyl chains proved to be of significant importance for the ordering of the molecules in the solid state where interdigitation of alkyl chains plays a major role. Further, despite of the fact that the conformational equilibrium between *cis*- and *trans*-orientation of the neighboring thiophene units was noted already early,[243] it took until 2000 that Bäuerle and co-workers demonstrated by scanning tunneling microscopy studies how 180° turns of a polythiophene chain could be realized on highly oriented pyrolytic graphite (HOPG) surfaces by about eight thiophenes in *cis*-orientation.[136] In the same year the Bäuerle group could also synthesize the first fully conjugated (macro)cyclic π-conjugated oligothiophenes containing 12 to 18 thiophene units.[136] With their improved synthetic methodology, later on also larger cyclo[*n*]oligothiophenes became reality.[40]

Nevertheless, albeit with such impressive work the existence of conformational equilibria between *cis*- and *trans*-oriented conformers and the concomitant establishment of curvature due to significant amounts of the *cis* conformers has been demonstrated, the impact of the respective positioning of alkyl substituents with respect to each other on the *cis*/*trans* equilibria and on the π-conjugation remains not fully understood.[107] This problem relates to the fact that oligo- and polythiophenes are not rigid in the ground state but prevail as rotameric mixtures with low rotation barriers of only 1-2 kcal/mol.[124] Also it has been consistently reported that

the *cis*- and *trans*-conformers are nonplanar in solution. In contrast, the vast majority of oligothiophene single crystals reveal fully planar all-*trans* geometries (in few cases a *cis*-orientation has been observed in particular for the terminal bithiophene units)[156] which is obviously the result of packing forces. However, also in solution both the optically excited and the oxidized states are significantly more planar due to an increased quinoid character, i.e. double bond formation between the thiophene units.[113, 244] In this paper we will investigate some unusual effects that are revealed by electrochemical oxidation depending on the position of the solubilizing alkyl chains.

3.2 Results and Discussion

The oligothiophene series **4T**-**7T** was synthesized following stannylation reactions employing lithiated oligothiophenes **60**, **T5**, **63** or **65** and $Sn(C_4H_9)_3Cl$ as a tin source, and subsequent palladium-catalyzed Stille cross-coupling protocols with 1-bromo-3-hexylbenzene (Scheme 5).[102] All compounds were characterized by nuclear magnetic resonance (NMR) spectroscopy and high-resolution mass spectrometry (HRMS). Redox potentials were determined using cyclic voltammetry (CV) and differential pulse voltammetry (DPV) in CH_2Cl_2. Optical characterization was conducted using UV/Vis absorption and fluorescence spectroscopy in CH_2Cl_2 as well.

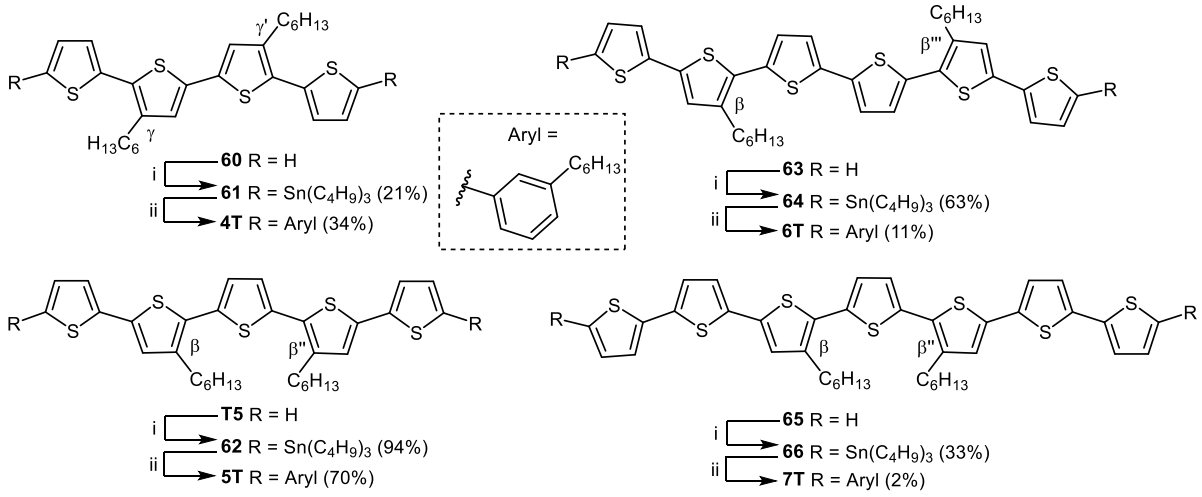

Scheme 5. Synthesis of the phenyl end-capped oligothiophene compounds **4T**-**7T**. i) $Sn(C_4H_9)_3Cl$, *n*-BuLi, TMEDA, THF or Et_2O. ii) 1-Bromo-3-hexylbenzene, $[Pd_2dba_3]$, P(*o*-tolyl)$_3$, toluene, 95 °C, overnight. dba = dibenzylideneacetone, TMEDA = tetramethylethylenediamine.

The basic α-oligothiophene backbone design involved modifications by two hexyl chains attached in three different regioisomeric relationships with each other.[245] Accordingly, the central terthiophene unit of **5T** and **7T** was equipped with two aliphatic chains in β,β″-positions, whereas in **6T** the aliphatic chains are located at the spatially more separated β,β‴-positions (Scheme 5). Contrarily, in compound **4T** the focal bithiophene center is equipped with two hexyl chains in γ,γ′-positions. The above-described positioning of the alkyl chains is of major importance for the structure-property relationship discussion below. Supported by the two alkyl chains of the terminal benzene units, all of these oligothiophenes exhibit sufficient solubility to enable the optical and electrochemical experiments conducted in this work. The end-capping by phenyl units proved to be successful to protect the central oligothiophene units against subsequent oxidative coupling reactions as typically observed for the most reactive free α-positions of oligothiophenes.[241]

Oligothiophenes **4T**–**7T** show one main broad and unstructured absorption band in CH_2Cl_2 corresponding to the lowest energy π–π* transition where an electron is promoted from the HOMO to the LUMO level.[107] The gradual increase of the number of thiophene subunits within the series from **4T** to **7T** leads to a bathochromic shift of the absorption maxima (λ_{abs}) from 413 nm for **4T** up to 444 nm for **7T** (Figure 22).

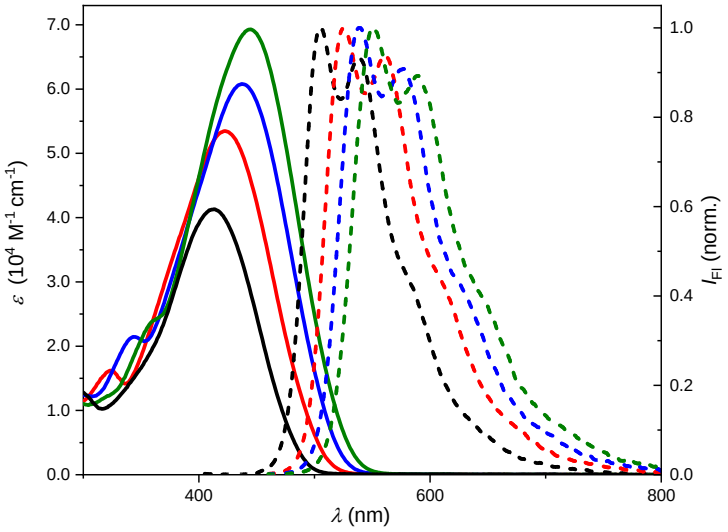

Figure 22. UV/Vis absorption (solid lines, $c_0 = 10^{-5}$ M) and normalized emission spectra (dashed lines, λ_{ex} = 400 nm, $c_0 = 10^{-7}$ M) of **4T** (black), **5T** (red), **6T** (blue) and **7T** (green) in CH_2Cl_2 at room temperature.

The common procedure to evaluate conjugation along π-conjugated oligomeric backbones, i.e. correlating the electronic band gap (here approximated by the absorption maxima λ_{max}) and the

inverse number of thiophene units,[246] reveals nothing special compared to other oligothiophene series studied in the past (Figure 25).[108-109, 111] This can be taken as an indication that the conformation of the oligothiophene chain with regard to the equilibrium of cis/trans rotamers and the average twist angle between the thiophene units are not unusual for **4T**–**7T** in their electronic ground states. In accordance with previous work, also the extinction coefficients are increased upon π-core extension from 41300 M^{-1} cm^{-1} for **4T** up to 69300 M^{-1} cm^{-1} for **7T** (Table 3).[247]

Table 3. Absorption, fluorescence and electrochemical data of **4T**-**7T** in CH_2Cl_2 at room temperature.

	4T	**5T**	**6T**	**7T**
$\lambda_{abs,max}$[a]/nm	413	422	437	444
$\varepsilon_{max}/10^3$ M^{-1} cm^{-1}	41.3	53.5	60.8	69.3
$\lambda_{em,max}$[b]/nm	505	526	538	551
$\Delta\tilde{\nu}_{Stokes}$ /cm^{-1}	4530	4740	4240	4370
Φ_{fl}[c]/ %	40	53	49	46
τ_{fl}[d]/ ns	0.74	0.88	0.79	0.77
$E_{ox,1}$[e]/V	0.33	0.41	0.16	0.24
$E_{ox,2}$[e]/V	0.58	0.59	0.34	0.43
$E_{ox,3}$[e]/V	–	–	0.96	0.88
$E_{ox,4}$[e]/V	–	–	1.21	1.12
$E_{ox,2} - E_{ox,1}$/V	0.25	0.18	0.18	0.19

[a]$c_0=10^{-5}$ M. [b]λ_{ex}= 400 nm, $c_0=10^{-7}$ M. [c]The fluorescence quantum yields were measured relative to perylene[248] as a reference at four different excitation wavelengths. [d]For lifetime measurements a pulsed laser diode with a wavelength of 403.8 nm was utilized. [e]$c_0=10^{-4}$ M, Bu_4NPF_6 was used as a conducting salt; all values are referenced against the ferrocenium/ferrocene (Fc^+/Fc redox couple)

However, compared to the respective non-end capped α-oligothiophenes,[107, 111] the two additional phenyl caps lead to an enhanced red shift of about 30–40 nm (1750–2700 cm^{-1}), which suggests that they extend the HOMOs and LUMOs as well as the transition dipole moments of the conjugated oligothiophene π-scaffolds. Indeed, **6T** exhibits an absorption maximum at 437 nm that almost corresponds to the one observed for a similar four alkyl-chain-solubilized octithiophene ($\lambda_{abs,max}$ = 439 nm) reported by Bäuerle and co-workers.[249]

In contrast to the broad and unstructured absorption spectra, the fluorescence spectra of **4T**-**7T** in CH_2Cl_2 show vibronic patterns with two clearly distinguishable emission maxima ($\lambda_{em,max}$) at a distance of about 50 nm (1580 cm^{-1}). The appearance of such vibronic patterns originating from aromatic C–C stretching modes suggests that **4T**-**7T** molecules are more rigid in their excited states (S_1) due to more quinoidal structures with pronounced double bond character

between the respective thiophene units.[111] The structural rearrangements of the excited states also cause large Stokes shifts ($\tilde{\nu}_{Stokes}$) of over 4200 cm^{-1} for all chromophores (Table 3). Further, the emission maxima are bathochromically shifted with increasing number of thiophene units from **4T** (505 nm) to **7T** (551 nm), thereby corroborating the delocalization along the π-conjugated oligothiophene backbone. However, similar to the absorption maxima, there is also nothing particularly unusual for the positions of the emission maxima ($\lambda_{em,max}$) upon plotting the band gap for the relaxed excited states against the inverse number of thiophene units (Figure 25). The fluorescence quantum yields (Φ_{fl}) increase from 40% (**4T**) to 53% (**5T**), while then decreasing with elongation of the π-system to 46% (**7T**), probably due to an increase of nonradiative deactivation pathways as suggested by the energy gap law (Table 3).[250] Fluorescence lifetimes (τ_{fl}) were determined by time-correlated single photon counting (TCSPC) with a diode laser at 403.8 nm and yielded for all oligothiophenes similar values between 0.7 and 1 ns (Table 3; for details see *Chapter 3.4*, Figure 25). Insight into the redox properties of this new series of end-capped oligothiophenes **4T**–**7T** was obtained *via* electrochemical investigations by CV and DPV in CH_2Cl_2. Electrochemical oxidation of α-oligothiophenes is often accompanied by irreversible α,α′-coupling reactions between the resulting radical cations, leading to longer oligomers and polymers.[244] The irreversibility of this oxidation process is observed, *e.g.* in CV experiments, where also additional waves upon radical coupling can be monitored. As shown by Bäuerle, such couplings can, however, be prohibited by either end-capping of the reactive terminal thiophene α–positions[111] or extension of the oligothiophene chain until the radical cation or dication is sufficiently stabilized.[251] For the here-investigated oligothiophenes **4T**–**7T** that are flanked by a hexylphenyl moiety at both ends, CV experiments in CH_2Cl_2 revealed only reversible oxidation processes (Figure 23a).

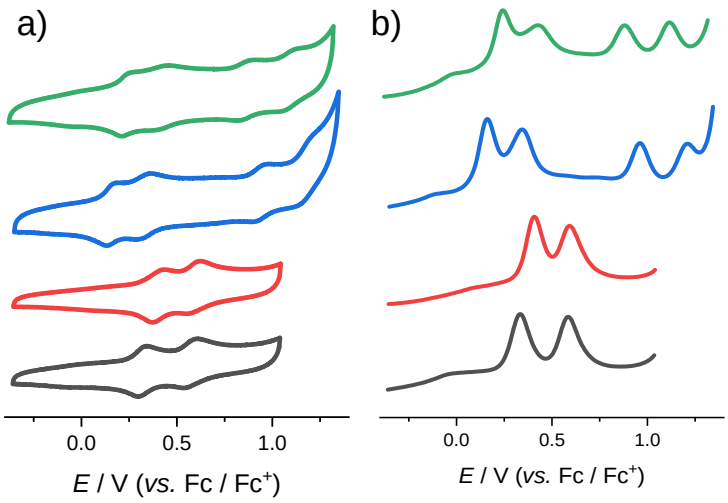

Figure 23. a) CV and b) DPV measurements of **4T** (black), **5T** (red), **6T** (blue) and **7T** (green) in CH_2Cl_2 solutions of Bu_4NPF_6 at room temperature ($c_0 = 10^{-4}$ M) relative to Fc^+/Fc.

While **4T** and **5T** show only two one-electron transfer steps leading to the radical cation and the dication, respectively, for **6T** and **7T** even the subsequent oxidation waves to the tri- and tetracationic species could be detected. This is in accordance with earlier work on oligothiophenes as the number of possible redox states increases with the number of thiophene units and therewith allows for a distribution of the positive charges without the creation of too large repulsive Coulomb forces.[107] Nevertheless, the reversible formation of the three- and fourfold charged species within the solvent window of CH_2Cl_2 is typically only observed for higher homologues such as structures bearing 10 thiophene subunits or more.[40] Accordingly, the observation of these states again corroborates the stabilizing influence of the terminal phenyl units in oligothiophenes **4T**–**7T**. Most interestingly, however, the first oxidation potentials ($E_{ox,1}$) do not gradually decrease with increasing number of thiophene units in our series **4T**–**7T**, but rather display an unexpected zig-zag trend that will be discussed in detail later.

With the better resolution of the peaks, DPV measurements (Figure 23b) clearly indicate the respective stabilization of cationic versus dicationic species of each oligothiophene. While the two subsequent oxidation processes in the case of **4T** are energetically clearly separated by 0.25 V from each other, with increasing oligothiophene length the waves become more closely spaced by only 0.18 V ($E_{ox,2} - E_{ox,1}$; Table 3). Similar behavior has been observed for other oligothiophene series, *e.g.* for Bäuerle's series of oligothiophenes bearing tetramethylene bridges at terminating thiophene units (**ECnT**) the difference in the redox potentials for the

first and second oxidation waves reduces from 0.34 V for **EC4T** *via* 0.29 (**EC5T**) to 0.19 V (**EC6T**).[111]

Whilst the properties of these radical cations and dications were mostly analyzed from the physics perspective on polaron–bipolaron theory,[111, 113] little attention has indeed been devoted to interrelate the difference in these subsequent redox processes to earlier work in chemistry. However, it is easily possible to interpret such two-stage organic redox systems as Weitz-type redox systems according to Hünig[252-253] as a chemical equilibrium between the reduced neutral state (**nT**), radical cation (**nT**$^{+}$), and dication (**nT**$^{2+}$) state:

$$\mathrm{nT} + \mathrm{nT}^{2+} \overset{K}{\rightleftarrows} 2\mathrm{nT}^{+}$$

$$\log K = \frac{\mathrm{n}\cdot F\cdot\left(E_{\mathrm{ox},2}-E_{\mathrm{ox},1}\right)}{R\cdot T} = \frac{\mathrm{n}\cdot\left(E_{\mathrm{ox},2}-E_{\mathrm{ox},1}\right)}{0.059}. \quad (6)$$

Here K can be understood as a comproportionation constant that defines the thermodynamic stability of the radical cation against disproportionation into the neutral and dicationic closed-shell species. For the 0.25 V separation observed for **4T**, the equilibrium constant K for one-electron oxidations (n=1) at room temperature (T=298 K) accordingly is 17000, which is reduced by more than one order of magnitude to K=1100 for **5T** and **6T**. This trend can be interpreted either as a decreased stabilization of the radical cation or as an increased stabilization of the dication upon chain extension. In contrast to classical Weitz- and Wurster-type redox systems[253] or organic mixed valence compounds,[219] the second interpretation is favored in the field of conductive polymers because it suggests that a second positive charge can only be accommodated at reasonably low redox potentials if the oligothiophene chain exhibits a sufficient length to overcome the Coulomb repulsion between the two positive charges.[107] A perfect example for such a case is given with a cyclic oligothiophene consisting of 10 thiophene units that forms with the second oxidation a polaron pair, i.e. this dication is a biradical with a pronounced electron paramagnetic resonance signal.[113] However, in other situations the second oxidation may involve the same orbital (singly occupied molecular orbital) in a fully conjugated system, leading to a bipolaron (dication without radical character). For classical Weitz-type redox systems as provided by viologens, $K > 10^6$ was calculated by equation (6) from a larger separation of the two, in this case, reductive waves of 0.40 V and interpreted as arising from the stabilization of the radical cation by full delocalization of the

first (negative) charge across both pyridinium units.[254] For the vinylogous situation where both pyridinium units are connected by a double bond, a smaller *K*-value of 1000 is calculated by equation (6) from the smaller separation of the two reduction processes by only 0.18 V,[255] quite similarly as observed in our series of oligothiophenes. This smaller *K*-value according to Hünig is explained by the reduced delocalization of the negative charge across the vinylogous bridge. This explanation could obviously also rationalize the related observations for oligothiophenes in our and earlier studies. Notably, for rigid fully planar π-scaffolds as given in the series of rylene bisimides, Bard, Müllen and co-workers could even observe the limiting case: thus, whilst a separation of the first and second reduction waves by 0.22 V for perylene bisimides affords a *K*-value of 5000, suggesting strong sharing of the negative charge in this radical anion by both imide units, for extended quaterrylene bisimides a single two-electron reduction process is observable for which digital simulation affords a *K*-value of only 5. Accordingly in this case the two negative charges might be considered as localized on the two respective terminal naphthalimide subunits with little interaction. Clearly, this stage has not yet been reached by the oligothiophenes investigated in our study.

Similar to the optical properties discussed before, two main aspects are expected to dictate the energetics of the first one-electron oxidation process in the **4T**-**7T** series. The degree of conjugation along the π-system related to the chain length and planarity, as well as the electron-donating influence of the substituents. Firstly, the end-capping by two phenyl moieties greatly enhanced the conjugation length in comparison to entirely unsubstituted α-oligothiophenes.[247] Secondly, the electron-donating effect of four aliphatic C_6H_{13}-chains should lead to lower oxidation potentials compared to the respective unsubstituted α-oligothiophenes. Indeed, a comparison of the electrochemical data of **4T** and **6T** ($E_{ox,1}$ = 0.33 V and 0.16 V, respectively; Table 3) with closely related α-sexithiophenes supports the view that the first oxidation is supported by the combination of the terminal phenyl groups and the alkyl substituents (Figure 24c).

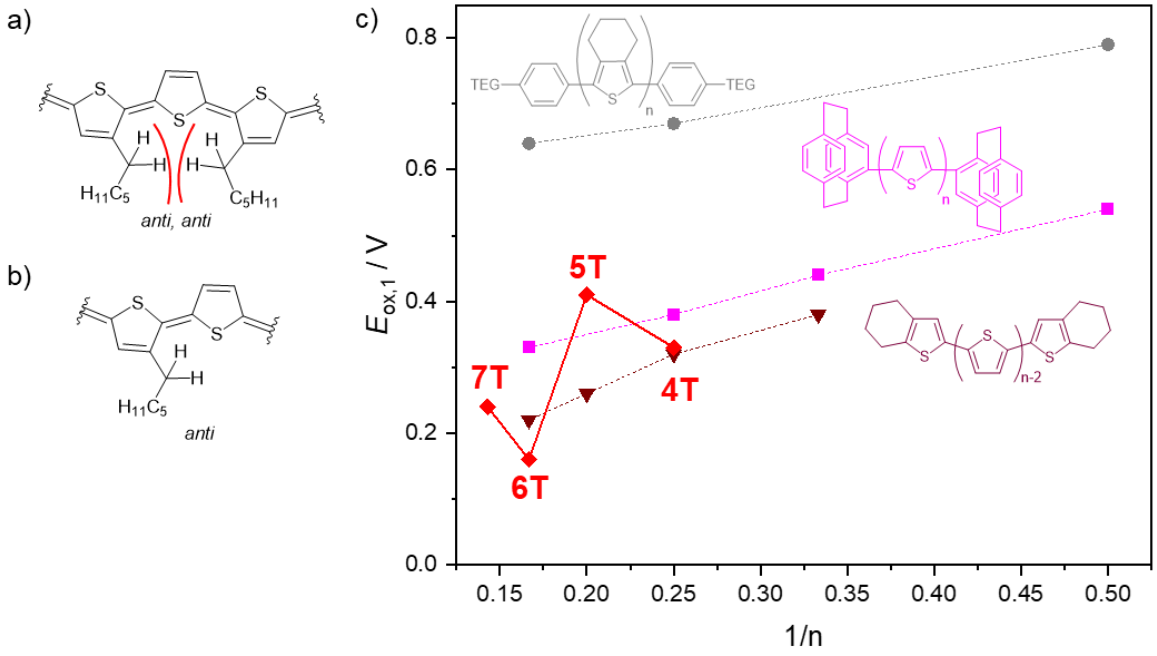

Figure 24. Graphic illustration of the first oxidation potential $E_{ox,1}$ vs. the inverse total number of thiophene units n for different end-capped oligothiophenes. The displayed compounds were synthesized by the groups of Ikeda[109] (grey), Audebert[108] (magenta) and Bäuerle[111] (purple). The red symbols represent the compounds **4T**-**7T** and the lines serve as guide to the eye. All measurements were conducted in CH_2Cl_2 solutions at room temperature. TEG = Tetraethylene glycol.

Surprisingly, however, a gradual decrease of $E_{ox,1}$ is not observed upon extension of the oligothiophene chain in the series **4T**-**7T**. Instead, a zig-zag trend of $E_{ox,1}$ is observed with values of 0.33 V (**4T**), 0.41 V (**5T**), 0.16 V (**6T**), and 0.24 V (**7T**). This observation is clearly opposed to the trends observed for other end-capped α-oligothiophene architectures illustrated in Figure 24c that were investigated by the groups of Bäuerle,[111] Audebert,[108] and Ikeda[109], which show a gradual decrease of the first one-electron oxidation potentials $E_{ox,1}$ with increasing number of thiophene subunits. This finding has also been supported by theoretical calculations for different unsubstituted α-oligothiophenes.[114]

The reason for the unusual behavior observed for our series **4T**-**7T** is presumably attributable to the aforementioned location of the solubilizing alkyl chains. Upon oxidation of the oligothiophene backbone, a more planar quinoidal structure with closer thiophene units (due to the double bond character) is adopted. Such planarization of the entire backbone is particularly needed for the shorter oligomers, *i.e.* **4T** and **5T**, to delocalize the charge along a significant number of thiophene units. However, steric encumbrance of the alkyl chains in **5T** and **7T** (Figure 24a) will countervail a complete planarization due to their close proximity,

thereby enforcing a larger contortion and concomitantly destabilization of the radical cationic state. Clearly, whilst also in the absorption and fluorescence spectra (Figure 22 and Figure 25) modest deviations in the bathochromic displacements compared to other oligothiophene series could be observed, *e.g.* the $\lambda_{abs,max}$ value increases unsteadily by 9 nm (**4T** to **5T**), 15 nm (**5T** to **6T**), and 7 nm (**6T** to **7T**) (Table 3), this effect is much more pronounced for the oxidation process where the stabilization of the radical cation calls for a higher degree of planarity.
An alternative option to the illustrated *trans*-*trans*-conformation for the oligothiophene backbone where the alkyl CH_2 groups suffer from close proximity in the case of **5T** and **7T** (Figure 24a) might be a preferential formation of a *trans*-*cis*-conformation for these oligothiophenes. However, due to the fact that Bäuerle and co-workers observed lower first oxidation potentials for an all-*cis* cyclo[10]oligothiophene and attributed this observation to a raised HOMO level in the *cis* conformation,[40] we favor the above explanation based on a less planarized conjugated chain.

Different from **5T** and **7T**, the aliphatic chains in **4T** point away from each other and in **6T** (Scheme 5) the hexyl chains are too far apart for any repulsive effects. A representation of the expected situation in a *trans*-conformation for molecule **4T** in their radical state is displayed in Figure 24b. Thus, for **4T** and **6T** the oxidation potential is not influenced by sterical encumbrance, enabling a better stabilization of the oxidized more quinoidal state that requires planarity and closer thiophene–thiophene distances due to the double bond character. Notably, a similar zig-zag trend is also observable for the second oxidation process (Table 3), which is, however, more difficult to analyze due to the above-discussed special effects originating from the interactions of the two polarons in multiredox systems. The impact of such sterical interactions should be taken into account in the design of oligothiophenes. Avoiding such sterical congestions can afford a better stabilization of the quinoid structure and concomitantly lower the oxidation potentials, whilst increasing such sterical congestions might be an approach to isolate multiple radical cations, *i.e.* to create polaron pair states. Such concepts are currently also applied to create organic biradicals[256] that are of interest for functional materials for singlet fission[257-258].

3.3 Conclusion

In conclusion, a new series of phenyl end-capped α-oligothiophenes **4T-7T** was synthesized and characterized by UV/Vis absorption and fluorescence spectroscopy as well as electrochemistry. Optical spectroscopy revealed a notable bathochromic shift of the absorption maxima compared to nonsubstituted α-oligothiophenes that is attributable to the conjugated phenyl substituents. Another more unexpected effect was found that is caused by the position of the alkyl chains. Thus, all electronic states that require planarization of the oligothiophene backbone will be disfavored by sterical encumbrance of close-by positioned alkyl chains. This effect was particularly pronounced for the formation of the radical cations upon electrochemical oxidation, leading to a zig-zag trend for the first one-electron oxidation potential in our series of molecules **4T-7T**. Accordingly, the alkyl chain positioning rather than the number of thiophene units determines the electro-chemical properties in this series of oligomers. This result could pave the way for an improved electronic fine-tuning of α-oligothiophenes as required for various applications in (opto-) electronic devices.

3.4 Supporting Information to Chapter 3

Materials and methods

All reactions were performed in standard glass equipment. All used chemicals were purchased from commercial suppliers and used without further purification. The reactions were carried out under nitrogen atmosphere. Diethylether, THF and toluene were purified and dried with the commercial purification system PureSolv MD from *Innovative Technology*. Stille coupling procedures were conducted in additionally degassed toluene.

Preparative column chromatography was performed with self-packed glass columns of several sizes filled with silica gel 60 M (particle size 0.04-0.063 mm, *Merck KGaA*). CH_2Cl_2 was freshly distilled prior to use. Size exclusion chromatography was performed with commercial glass columns using Bio-Beads® (S-X3-Beads, styrene divinylbenzene copolymer, Bead size 40–80 μm) from *Bio-Rad* as stationary phase and HPLC grade solvents as mobile phase. Purification by gel permeation chromatography was performed on a *Shimadzu* instrument (LC-20AD Prominence Pump, SPD-MA20A Prominence Diode Array Detector) with two preparative columns (*Japan Analytical Industries Co., Ltd).* Ethanol stabilised $CHCl_3$

(Chromasolv®, *Sigma Aldrich*) was used as eluent.

NMR spectra were recorded on a *Bruker* Avance III HD 400 MHz spectrometer using deuterated solvents. ^{13}C NMR spectra are broad band proton decoupled. Chemical shifts (δ) are listed in parts per million (ppm) and coupling constants (J) are listed in Hertz (Hz). The spectra are referenced internally to residual proton solvent resonances or natural abundance carbon resonances. Multiplicities are reported as s = singlet, d = doublet, dd = doublet of doublets, t = triplet, quin = quintet, m = multiplet with the chemical shift in the center of the signal.

High-resolution MALDI-TOF mass spectra were recorded with an MALDI TOF MS ultrafleXtreme mass spectrometer (*Bruker Daltonics GmbH*) using DCBT (2-[(2*E*)-3-(4-tert-butylphenyl)-2-methylprop-2-enylidene]malononitrile) as matrix. The melting points (m.p.) were determined using a Stuart SMP50 automatic melting point apparatus and are uncorrected.

UV/Vis absorption spectra of the solutions were recorded in cuvettes (SUPRASIL®, *Hellma® Analytics*) on a Jasco V-670 or V-770 spectrometer and fluorescence spectra on a FLS980-D2D2-ST fluorescence spectrometer (*Edinburgh Instruments*) and were corrected against the photomultiplier sensitivity and the lamp intensity. The fluorescence lifetimes were determined *via* time-correlated single photon counting (TCSPC) utilizing an EPL picosecond pulsed diode laser (λ_{ex} = 403.8 nm) with a pulse width of 141.7 ps with a FLS980-D2D2-ST spectrometer (*Edinburgh Instruments Ltd.*, UK) under magic-angle conditions (54.7°). The fitting of the data was carried out using the reconvolution fit routine supplied by *Edinburgh Instruments Ltd., Inc.*, taking the instrument response function (IRF) into consideration.

Cyclic and differential pule voltammetry experiments were carried out with a *BASi* Epsilon potentiostat connected to a microcell apparatus from *rhd instruments* involving a 1.6 mL sample container, a platinum counter- and pseudo-reference electrode as well as a glassy carbon working electrode.

Synthetic Procedure

The precursor molecules **60**[259], **T5**[87], **63**[260] and 3,3''-dihexyl-[2,2':5',2''-terthiophene]-5,5''-diyl)bis[1,1,1-tributylstannane][261] were synthesized according to the procedures reported in literature.

General procedure for stannylation reactions on oligothiophenes

To a stirred solution of oligothiophene (1.0 eq.) and tetramethyl-ethylenediamine (TMEDA) (2.1 eq.) in dry THF or Et_2O, *n*-butyllithium (1.6 M in *n*-hexane, 3.0 eq.) was added dropwise at 0 °C. The solution was stirred for 1 h at 0 °C. $Sn(C_4H_9)_3Cl$ (4.0 eq.) was added dropwise at 0 °C and the reaction mixture was stirred at room temperature (r.t.). The reaction was quenched with water and the aqueous layer was extracted three times with CH_2Cl_2. The combined organic layers were washed with brine, dried over $MgSO_4$, and the solvent was removed *in vacuo*. The residue was purified by (flash) column chromatography (deactivated silica gel) using *n*-hexane as eluent to give the desired compounds as pale yellow oils.

(3',4''-Di-*n*-hexyl-[2,2':5',2'':5'',2'''-quaterthiophene]-5,5'''-diyl)bis[1,1,1-tributylstannane] (61)

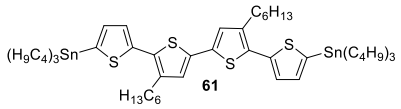

61

Oligothiophene **60** (60.5 mg, 121 µmol), TMEDA (38.0 µL, 255 µmol), *n*-BuLi (227 µL, 364 µmol), $Sn(C_4H_9)_3Cl$ (132 µL, 485 µmol), THF (10 mL). Addition of *n*-BuLi at −78 °C, stirring at r.t. for 4 h. Additional purification *via* size exclusion chromatography (CH_2Cl_2/MeOH = 9:1). **Yield**: 27.6 mg (25.6 µmol, 21%), yellow oil. **^{1}H NMR** (400 MHz, CD_2Cl_2, 295 K): δ/ppm = 7.25 (d, ^3J = 3.4 Hz, 2H), 7.13 (d, ^3J = 3.4 Hz, 2H), 7.01 (s, 2H), 2.75 (t, ^3J = 7.8 Hz, 4H), 1.70-1.55 (m, 16H), 1.44-1.30 (m, 24H), 1.22 -1.07(m, 12H), 0.91 (t, ^3J = 7.3 Hz, 24H). **^{13}C NMR** (101 MHz, CD_2Cl_2, 295 K): δ/ppm = 141.7, 140.3, 138.0, 136.2, 134.7, 130.3, 127.1, 126.8, 32.1, 30.9, 29.8, 29.6, 29.4, 27.7, 23.0, 14.3, 13.8, 11.2. **HRMS** (MALDI-TOF, positive mode, DCTB in $CHCl_3$): m/z = 1078.3651 (calcd. for $C_{52}H_{86}S_4Sn_2^+$: 1078.3656).

(3''',4'-Di-*n*-hexyl-[2,2':5',2'':5'',2''':5''',2''''-quinque-thiophene]-5,5''''-diyl)bis[1,1,1-tributylstannane] (62)

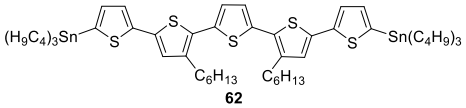

62

Oligothiophene **T5** (165 mg, 284 µmol), TMEDA (770 µL, 596 µmol), *n*-BuLi (533 µL, 852 µmol), $Sn(C_4H_9)_3Cl$ (310 µL, 1.14 mmol), Et_2O (15 mL). Stirring overnight at r.t. **Yield**: 308 mg (266 µmol, 94%), yellow oil. **^{1}H NMR** (400 MHz, CD_2Cl_2, 295 K): δ/ppm = 7.30 (d, ^3J = 3.4 Hz, 2H), 7.10 (s, 2H), 7.09 (d, ^3J = 3.4 Hz, 2H), 7.05 (s, 2H), 2.78 (t, ^3J = 7.8 Hz, 4H), 1.73-1.65 (m, 4H), 1.64-1.55 (m, 12H), 1.47-1.28 (m, 24H), 1.17 -1.11(m, 12H), 0.91 (t, ^3J = 7.3 Hz, 24H). **^{13}C NMR** (101 MHz, CD_2Cl_2, 295 K): δ/ppm = 142.7, 141.0, 137.6, 136.7, 136.1, 135.7, 129.3, 126.9, 126.2, 125.2, 32.1, 30.9, 29.9, 29.7, 29.3, 27.7, 23.1, 14.3, 13.8, 11.2. **HRMS** (MALDI-TOF, positive mode, DCTB in $CHCl_3$): *m/z* = 1160.3528 (calcd. for $C_{56}H_{88}Sn_2S_5^+$: 1160.3533).

(3'''',4'-Di-*n*-hexyl-[2,2':5',2'':5'',2''':5''',2'''':5'''',2'''''-sexithiophene]-5,5'''''-diyl)bis[1,1,1-tributylstannane] (64)

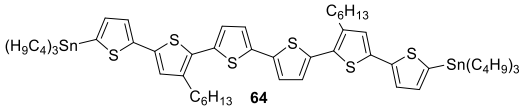

64

Oligothiophene **63** (428 mg, 646 µmol), TMEDA (320 µL, 1.36 mmol), *n*-BuLi (1.21 mL, 1.94 mmol), $Sn(C_4H_9)_3Cl$ (132 µL, 2.58 mmol), Et_2O (25 mL). Addition of *n*-BuLi at □78 °C, stirring at r.t. for 4 h. Additional purification via size exclusion chromatography ($CHCl_3$/MeOH = 9:1). **Yield**: 507 mg (409 µmol, 63%), yellow oil. **^{1}H NMR** (400 MHz, CD_2Cl_2, 295 K): δ/ppm = 7.30 (d, ^3J = 3.4 Hz, 2H), 7.16 (d, ^3J = 3.8 Hz, 2H), 7.09 (d, ^3J = 3.4 Hz, 2H), 7.07 (d, ^3J = 3.8 Hz, 2H), 7.05 (s, 2H),2.78 (t, ^3J = 7.8 Hz, 4H), 1.73-1.55 (m, 16H), 1.45-1.30 (m, 24H), 1.20-1.08 (m, 12H), 0.91 (t, ^3J = 7.3 Hz, 24H). **^{13}C NMR** (101 MHz, CD_2Cl_2, 295 K): δ/ppm = 142.6, 141.1, 137.7, 136.9, 136.7, 135.8, 135.6, 129.2, 126.9, 126.6, 125.2, 124.3, 32.1, 30.8, 29.9, 29.6, 29.3, 27.7, 23.0, 14.3, 13.8, 11.2. **HRMS** (MALDI-TOF, positive mode, DCTB in $CHCl_3$): *m/z* = 1242.3405 (calcd. for $C_{60}H_{90}S_6Sn_2^+$: 1242.3411).

(3''',4''-Di-*n*-hexyl-[2,2':5',2'':5'',2''':5''',2'''': 5'''',2''''':5''''',2'''''-septithiophene]-5,5'''''-diyl)bis[1,1,1-tributylstannane] (66)

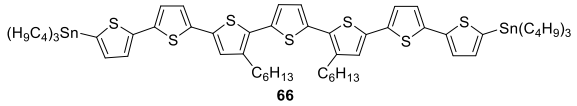

66

Oligothiophene **65** (620 mg, 832 µmol), TMEDA (262 µL, 1.75 mmol), *n*-BuLi (1.56 mL, 2.50 mmol), $Sn(C_4H_9)_3Cl$ (903 µL, 3.33 mmol), Et_2O (15 mL). Stirring overnight at r.t. Purification *via* column chromatography (deactivated silica gel, cyclohexane CH_2Cl_2 = 5:1). **Yield**: 362 mg (274 µmol, 33%), yellow oil. **^{1}H NMR** (400 MHz, CD_2Cl_2, 295 K): δ/ppm = 7.31 (d, ^3J = 3.4 Hz, 2H), 7.12 (s, 2H), 7.10 (s, 4H), 7.06 (s, 2H), 7.09 (d, ^3J = 3.4 Hz, 2H), 2.79 (t, ^3J = 7.8 Hz, 4H), 1.73-1.65 (m, 4H), 1.64-1.55 (m, 12H), 1.47-1.28 (m, 4H), 1.17-1.11(m, 12H), 0.91 (t, ^3J = 7.3 Hz, 24H). **^{13}C NMR** (101 MHz, CD_2Cl_2, 295 K): δ/ppm = 142.6, 141.1, 137.9, 137.0, 136.7, 136.1, 135.7, 135.2, 129.7, 127.0, 126.4, 125.3, 124.7, 124.5, 32.1, 30.9, 29.9, 29.7, 29.3, 27.7, 23.0, 14.3, 13.8, 11.2. **HRMS** (MALDI-TOF, positive mode, DCTB in $CHCl_3$): *m*/*z* = 1324.3282 (calcd. for $C_{64}H_{92}Sn_2S_7^+$: 1324.3288).

General procedure for Stille coupling reactions

Stannylated precursors (1.0 eq.), the respective bromo compounds (2.5 eq.), $[Pd_2(dba)_3]$ (5 mol%), tris(*o*-tolyl)phosphine (11 mol%) were dissolved in degassed toluene and stirred overnight at 95 °C. The solution was allowed to cool down to r.t. and the solvent was removed *in vacuo*.

3'''',4''-Di-*n*-hexyl-2,2':5',2'':5'',2''':5''',2'''':5'''',2''''': 5''''',2'''''-septithiophene (65)

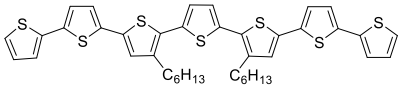

65

(3,3"-Dihexyl-[2,2':5',2"-terthiophene]-5,5"-diyl)bis[1,1,1-tributylstannane] (919 mg, 924 µmol), 5-bromo-2,2'-bithiophene (566 mg, 2.31 mmol), $[Pd_2dba_3]$ (42.3 mg, 46.2 µmol), P(*o*-tolyl)$_3$ (31.0 mg, 102 µmol), toluene (30 mL). Purification *via* column chromatography (gradient of cyclohexane/CH_2Cl_2 = 5:1 to cyclohexane/CH_2Cl_2 = 1:1). **Yield**: 604 mg (811 µmol, 88%), orange solid. **M.p.** = 162-163 °C. **^{1}H NMR** (400 MHz, CD_2Cl_2, 295 K): δ/ppm = 7.26 (dd, ^3J = 5.1 Hz, ^4J = 1.2 Hz, 2H), 7.21 (dd, ^3J = 3.7 Hz, ^4J = 1.2 Hz, 2H), 7.12

(d, ^3J = 3.8 Hz, 2H), 7.12 (s, 2H), 7.11 (d, ^3J = 3.8 Hz, 2H), 7.07 (s, 2H), 7.05 (d, ^3J = 5.1 Hz, 2H), 2.79 (t, ^3J = 7.9 Hz, 4H), 1.69 (quin, ^3J = 7.3 Hz, 4H), 1.46-1.30 (m, 12H), 0.90 (t, ^3J = 7.1 Hz, 6H). **^{13}C NMR** (101 MHz, CD_2Cl_2, 295 K): δ/ppm = 141.1, 137.3, 136.6, 136.2, 135.1, 129.8, 128.4, 127.2, 126.4, 125.1, 124.8. 124.7, 124.2, 32.1, 30.9, 29.9, 29.7, 23.0, 14.3. **HRMS** (MALDI-TOF, positive mode, DCTB in $CHCl_3$): m/z = 744.1169 (calcd. for $C_{40}H_{40}S_7^+$: 744.1175). **M.p.**: 162-163 °C.

5,5'''-Bis(3-*n*-hexylphenyl)-3',4''-di-*n*-hexyl-2,2':5',2'':5'',2'''-quaterthiophene (4T)

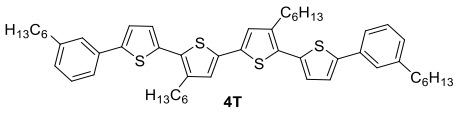

4T

Stannylated oligothiophene **61** (23.3 mg, 21.6 μmol), 1-bromo-3-hexylbenzene (13.1 mg, 54.1 μmol), [Pd_2dba_3*$CHCl_3$] (1.12 mg, 1.08 μmol), P(*o*-tolyl)$_3$ (0.73 mg, 2.38 μmol), toluene (10 mL). Purification *via* flash column chromatography (gradient of cyclohexane to cyclohexane/CH_2Cl_2 = 5:1) and gel permeation chromatography ($CHCl_3$). **Yield**: 6.1 mg (7.45 μmol, 34%), orange solid. **^{1}H NMR** (400 MHz, CD_2Cl_2, 295 K): δ/ppm = 7.42-7.47 (m, 4H), 7.31 (t, ^3J = 7.5 Hz, 2H), 7.31 (d, ^3J = 3.8 Hz, 2H), 7.16-7.12 (m, 4H), 7.06 (s, 2H), 2.80 (t, ^3J = 7.8 Hz, 4H), 2.65 (t, ^3J = 7.7 Hz, 4H), 1.75-1.60 (m, 8H), 1.45-1.29 (m, 24H), 0.94-0.87 (m, 12H). **^{13}C NMR** (101 MHz, CD_2Cl_2, 295 K): δ/ppm = 144.6, 144.3, 141.0, 135.5, 135.0, 134.2, 130.1, 129.2, 128.3, 127.1, 127.0, 126.0, 123.8, 123.2, 36.3, 32.1, 32.1, 32.0, 30.8, 30.1, 29.9, 29.6, 29.4, 23.0, 14.3. **HRMS** (MALDI-TOF, positive mode, DCTB in $CHCl_3$): m/z = 818.4042 (calcd. for $C_{52}H_{66}S_4^+$: 818.4047). **M.p.**: 86-87 °C. UV/Vis (CH_2Cl_2, c =50 μM): λ_{max} [nm] (ε_{max} [M^{-1} cm^{-1}]): 413 (44800). **Fluorescence** (CH_2Cl_2) λ_{em} [nm] (λ_{ex} [nm]): 505 nm (400 nm). **PLQY** (CH_2Cl_2): Φ_{fl} [%] = 40.

5,5''''-Bis(3-*n*-hexylphenyl)-3''',4'-di-*n*-hexyl-2,2':5',2'':5'',2''':5''',2''''-quinquethiophene (5T)

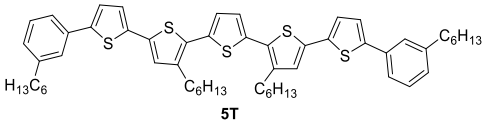

5T

Stannylated oligothiophene **62** (110 mg, 94.9 µmol,), 1-bromo-3-hexylbenzene (57.4 mg, 238 µmol), [Pd_2dba_3] (4.34 mg, 4.75 µmol), P(*o*-tolyl)$_3$ (3.18 mg, 10.4 µmol), toluene (30 mL). Purification *via* column chromatography (cyclohexane/CH_2Cl_2 = 5:1) reprecipitation from CH_2Cl_2 and MeOH. **Yield**: 60.0 mg (66.6 µmol, 70%), red solid. **^{1}H NMR** (400 MHz, CD_2Cl_2, 295 K): δ/ppm = 7.46-7.41 (m, 4H), 7.30 (t, ^3J = 7.5 Hz, 2H), 7.27 (d, ^3J = 3.8 Hz, 2H), 7.17 (d, ^3J = 3.8 Hz, 2H), 7.15-7.13 (m, 2H), 7.13 (s, 2H), 7.09 (s, 2H), 2.80 (t, ^3J = 7.8 Hz, 4H), 2.65 (t, ^3J = 7.7 Hz, 4H), 1.75-1.60 (m, 8H), 1.45-1.29 (m, 24H), 0.94-0.87 (m, 12H). **^{13}C NMR** (101 MHz, CD_2Cl_2, 295 K): δ/ppm = 144.3, 143.8, 141.1, 136.5, 136.1, 135.5, 134.1, 129.7, 129.2, 128.3, 127.0, 126.4, 126.0, 124.9, 124.2, 123.2, 36.3, 32.1 (2 signals), 31.9, 30.9, 29.9, 29.7, 29.4, 23.1, 23.0, 14.3 (2 signals). **HRMS** (MALDI-TOF, positive mode, DCTB in $CHCl_3$): *m*/*z* = 900.3919 (calcd. for $C_{56}H_{68}S_5^+$: 900.3925). **M.p.**: 112-113 °C. **UV/Vis** (CH_2Cl_2, *c* =50 µM): λ_{max} [nm] (ε_{max} [M^{-1} cm^{-1}]): 422 (54600). **Fluorescence** (CH_2Cl_2) λ_{em} [nm] (λ_{ex} [nm]): 526 (400). **PLQY** (CH_2Cl_2): Φ_{fl} [%] = 53.

5,5''''-Bis(3-*n*-hexylphenyl)-3'''',4'-di-*n*-hexyl-[2,2':5',2'':5'',2''':5''',2'''':5'''',2''''']-sexithiophene (6T)

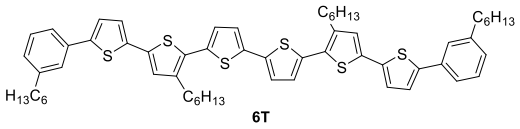

6T

Stannylated oligothiophene **64** (507 mg, 409 µmol), 1-bromo-3-hexylbenzene (246 mg, 1.02 mmol), [Pd_2dba_3] (18.7 mg, 20.4 µmol), P(*o*-tolyl)$_3$ (13.7 mg, 44.9 µmol), toluene (15 mL). Purification *via* filtration through a pad of celite using cyclohexane and subsequent size exclusion chromatography (CH_2Cl_2/MeOH = 9:1). **Yield**: 44.4 mg (45.1 µmol, 11%), red solid. **^{1}H NMR** (400 MHz, CD_2Cl_2, 295 K): δ/ppm = 7.46-7.41 (m, 4H), 7.30 (t, ^3J = 7.5 Hz, 2H), 7.27 (d, ^3J = 3.8 Hz, 2H), 7.19 (d, ^3J = 3.8 Hz, 2H), 7.17 (d, ^3J = 3.8 Hz, 2H), 7.15-7.13 (m, 2H), 7.10 (d, ^3J = 3.8 Hz, 2H), 7.09 (s, 2H), 2.80 (t, ^3J = 7.8 Hz, 4H), 2.65 (t, ^3J = 7.7 Hz,

4H), 1.75-1.60 (m, 8H), 1.45-1.29 (m, 24H), 0.94-0.87 (m, 12H). **^{13}C NMR** (101 MHz, CD_2Cl_2, 295 K): δ/ppm = 144.3, 143.9, 141.2, 137.0, 136.4, 135.5, 135.4, 134.1, 129.6, 129.2, 128.3, 127.0, 126.8, 126.0, 124.9, 124.4, 124.2, 123.2, 36.3, 32.1 (2 signals), 31.9, 30.8, 29.9, 29.6, 29.4, 23.0, 14.3 (2 signals). **HRMS** (MALDI-TOF, positive mode, DCTB in $CHCl_3$): m/z = 982.3796. (calcd. for $C_{60}H_{70}S_6^+$: 982.3802). **M.p.**: 134-135 °C. **UV/Vis** (CH_2Cl_2, c =50 μM): λ_{max} [nm] (ε_{max} [M^{-1} cm^{-1}]): 437 (62300). **Fluorescence** (CH_2Cl_2) λ_{em} [nm] (λ_{ex} [nm]):538 (400). **PLQY** (CH_2Cl_2): Φ_{fl} [%] = 49.

5,5''''''-Bis(3-*n*-hexylphenyl)-3'''',4''-di-*n*-hexyl-[2,2':5',2'':5'',2''':5''',2'''':5'''',2''''':5''''',2''''''-septithiophene (7T)

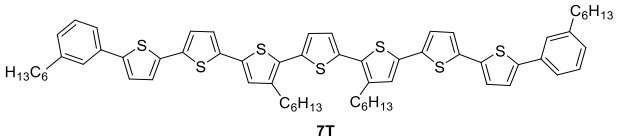

7T

Stannylated oligothiophene **66** (350 mg, 264 μmol), 1-bromo-3-hexylbenzene (159 mg, 661 μmol), [Pd_2dba_3] (12.1 mg, 13.2 μmol), P(*o*-tolyl)$_3$ (8.86 mg, 29.1 μmol), toluene (40 mL). Purification *via* flash column chromatography (gradient of cyclohexane to cyclohexane/CH_2Cl_2 = 10:1) and gel permeation chromatography ($CHCl_3$). Yield: 5.0 mg (4.69 μmol, 2%), red solid. **^{1}H NMR** (400 MHz, CD_2Cl_2, 295 K): δ/ppm = 7.46-7.41 (m, 4H), 7.30 (t, ^3J = 7.5 Hz, 2H), 7.27 (d, ^3J = 3.8 Hz, 2H), 7.19 (d, ^3J = 3.8 Hz, 2H), 7.15-7.12 (m, 8H), 7.08 (s, 2H), 2.80 (t, ^3J = 7.8 Hz, 4H), 2.65 (t, ^3J = 7.7 Hz, 4H), 1.75-1.60 (m, 8H), 1.45-1.29 (m, 24H), 0.94-0.87 (m, 12H). **^{13}C NMR** (101 MHz, CD_2Cl_2, 295 K): δ/ppm = 144.4, 144.0, 141.2, 136.6, 136.4, 136.2, 136.1, 135.1, 134.1, 129.9, 129.2, 128.4, 127.2, 126.5, 126.0, 125.0, 124.7 (2 signals), 124.2, 123.2, 36.3, 32.1, 32.1, 31.9, 30.9, 29.9, 29.7, 29.4, 23.05, 23.03, 14.3 (2 signals). **HRMS** (MALDI-TOF, positive mode, DCTB in $CHCl_3$): m/z = 1064.3674 (calcd. for $C_{64}H_{72}S_7^+$: 1064.3679). **M.p.**: 157-158 °C. **UV/Vis** (CH_2Cl_2, c =50 μM): λ_{max} [nm] (ε_{max} [M^{-1} cm^{-1}]): 444 (69300). **Fluorescence** (CH_2Cl_2) λ_{em} [nm] (λ_{ex} [nm]): 551 (400), **PLQY** (CH_2Cl_2): Φ_{fl} [%] = 46.

Comparison of Optical Bandgaps

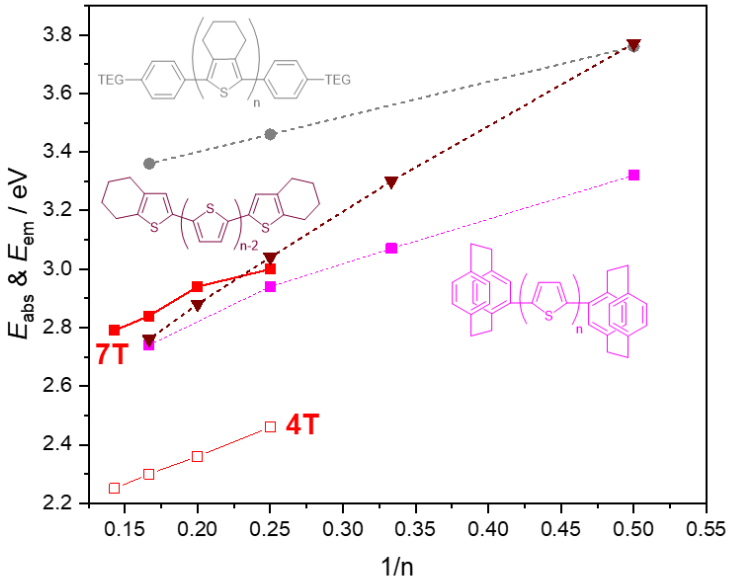

Figure 25. Graphic illustration of the optical bandgap (E_{abs}: full symbol; E_{em}: open symbol) deduced from the absorption/emission maxima vs. the inverse total number of thiophene units n for different end-capped oligothiophenes. The displayed compounds were synthesized by the groups of Ikeda (grey), Audebert (magenta) and Bäuerle (purple). The red symbols represent the compounds **4T**-**7T** and the lines serve as guide to the eye. All measurements were conducted in CH_2Cl_2 solutions at room temperature.

Fluorescence Lifetime Measurements

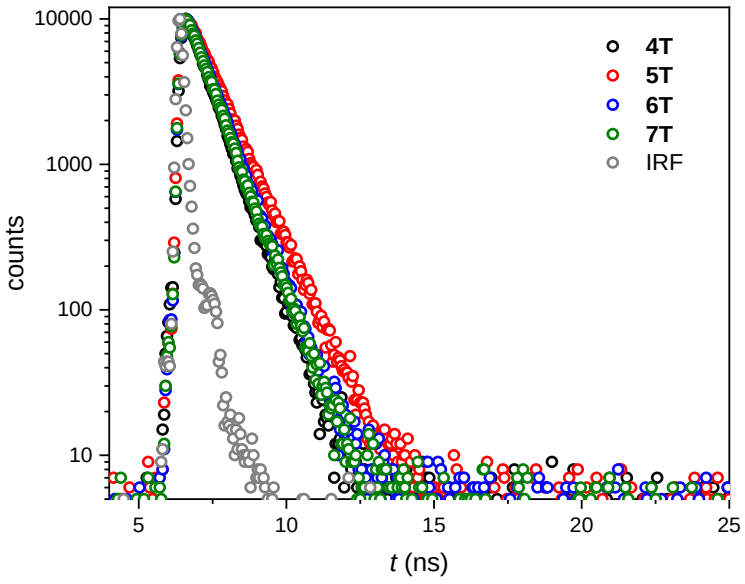

Figure 26. Fluorescence decay curves (λ_{ex} = 403.8 nm) of oligothiophenes **4T**-**7T** in CH_2Cl_2 at 295 K ($c_0 = 10^{-7}$ M) as well as the IRF.

NMR Spectra

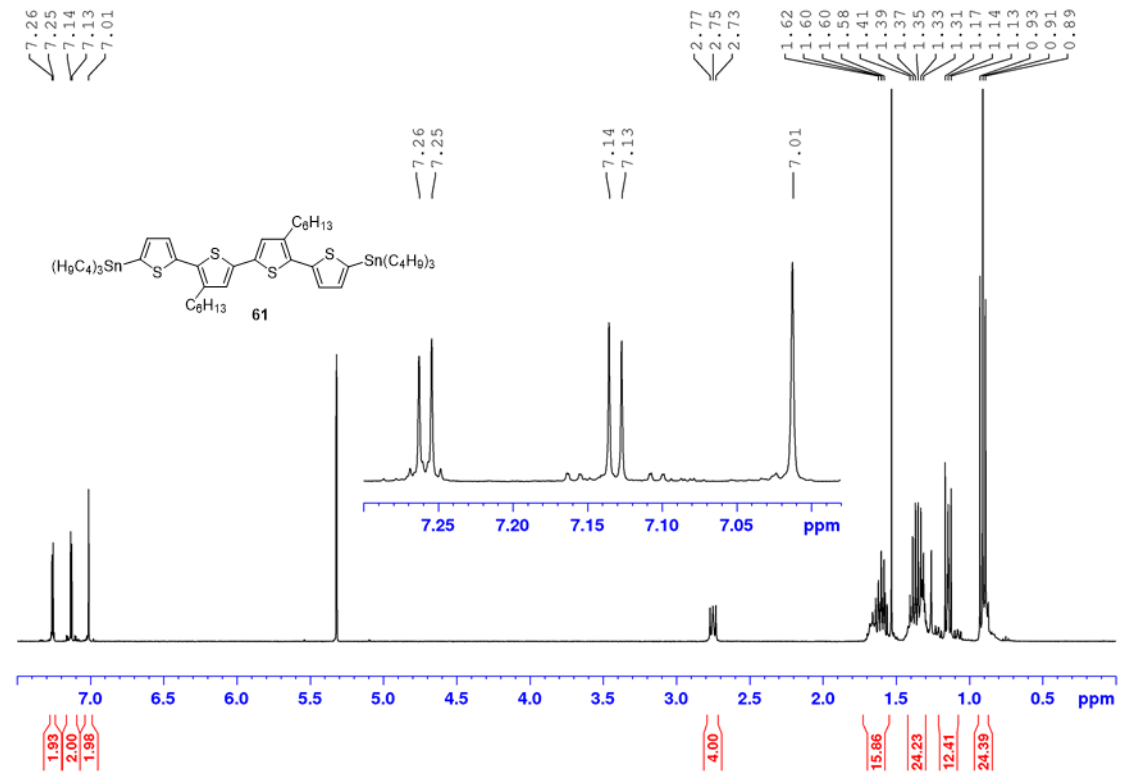

Figure 27. ^{1}H NMR spectrum (400 MHz) of **61** in CD_2Cl_2 at 298 K.

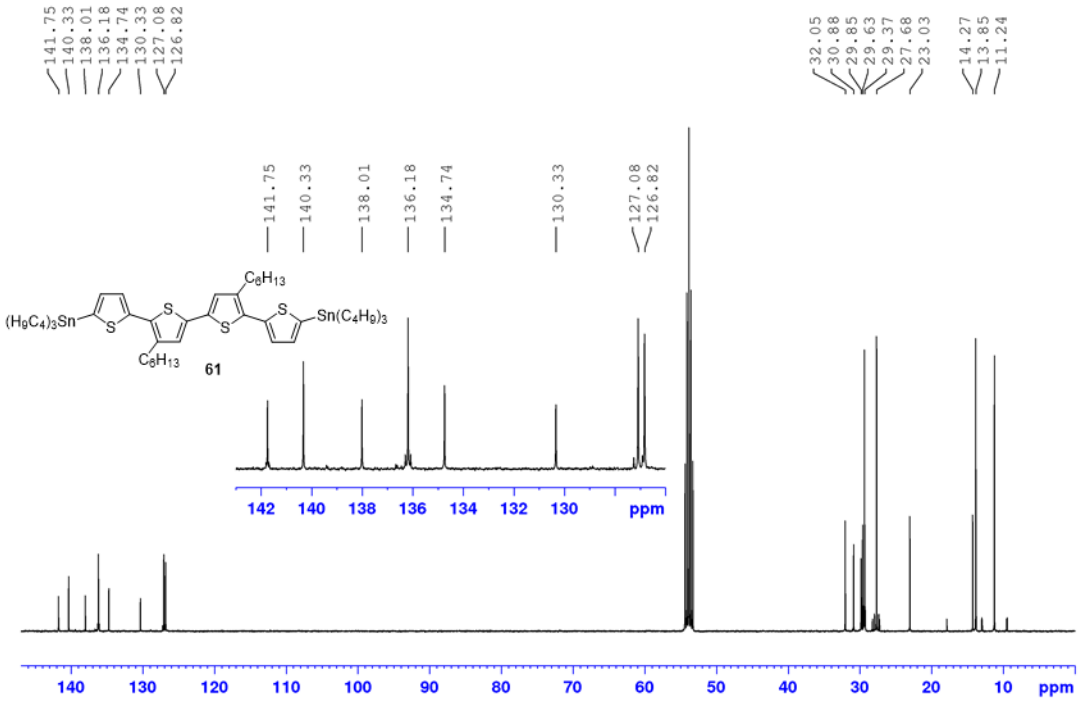

Figure 28. ^{13}C NMR spectrum (101 MHz) of **61** in CD_2Cl_2 at 298 K.

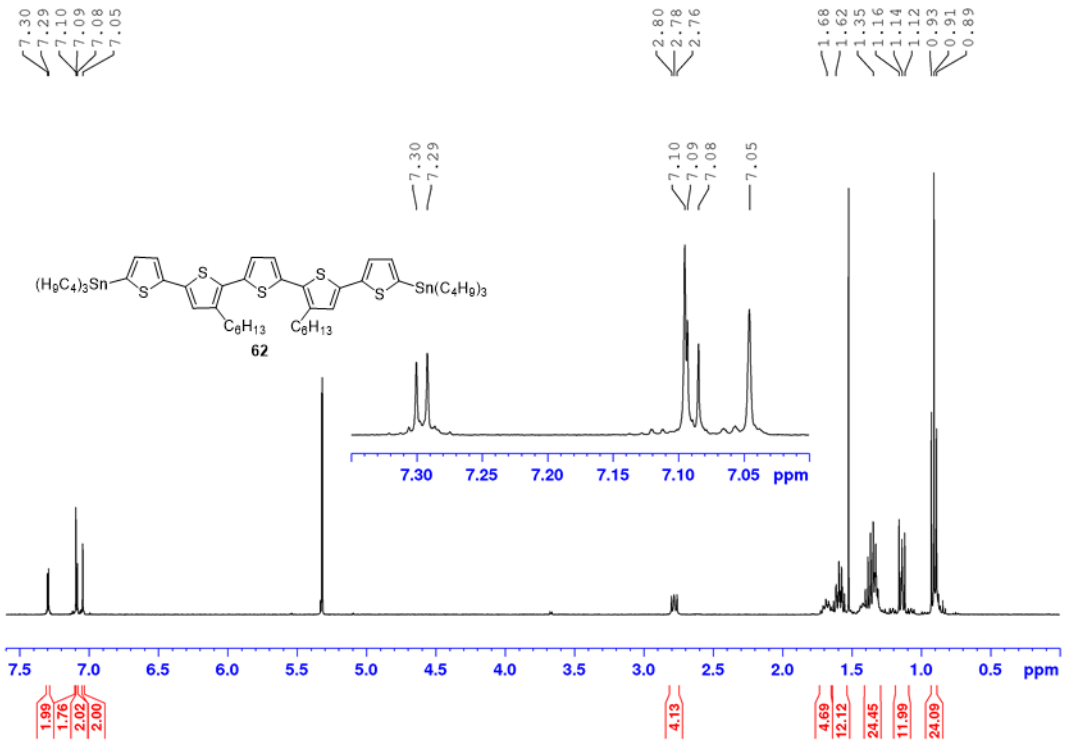

Figure 29. ^{1}H NMR spectrum (400 MHz) of **62** in CD_2Cl_2 at 298 K.

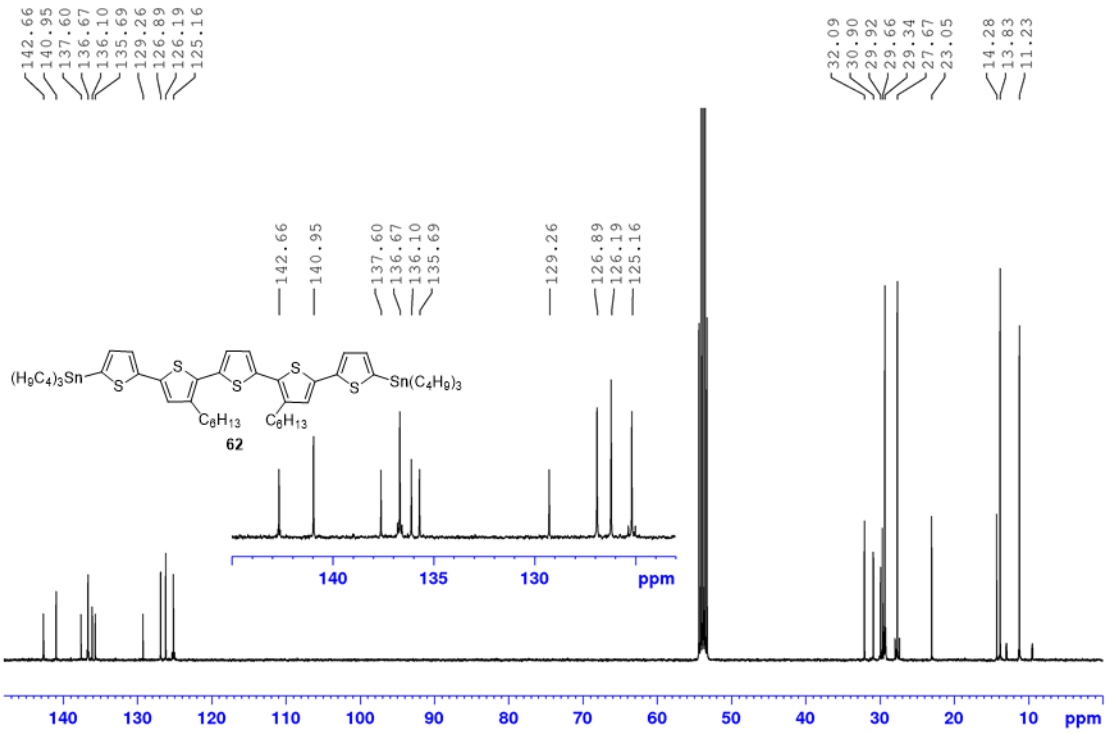

Figure 30. ^{13}C NMR spectrum (101 MHz) of **62** in CD_2Cl_2 at 298 K.

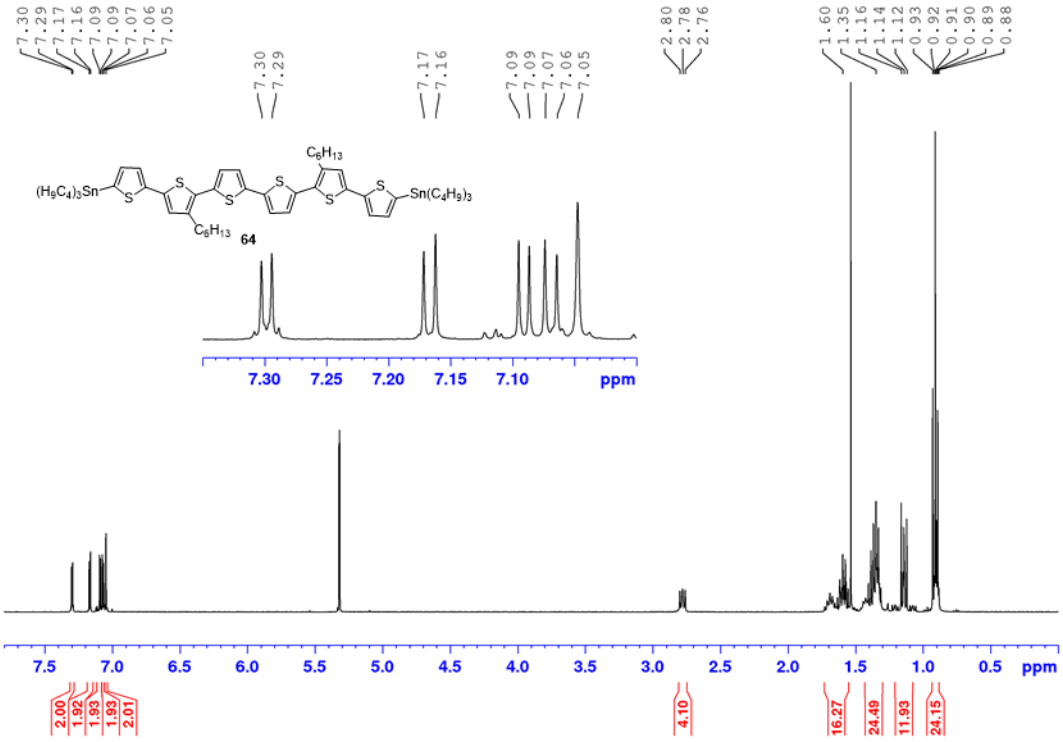

Figure 31. ^{1}H NMR spectrum (400 MHz) of **64** in CD_2Cl_2 at 298 K.

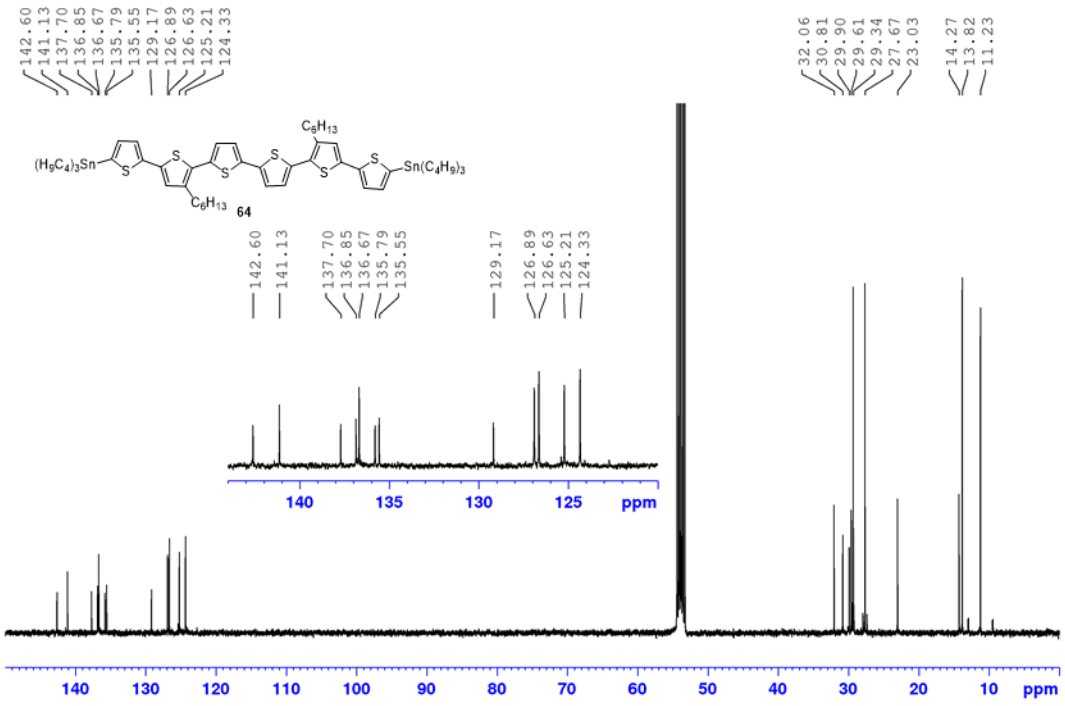

Figure 32. ^{13}C NMR spectrum (101 MHz) of **64** in CD_2Cl_2 at 298 K.

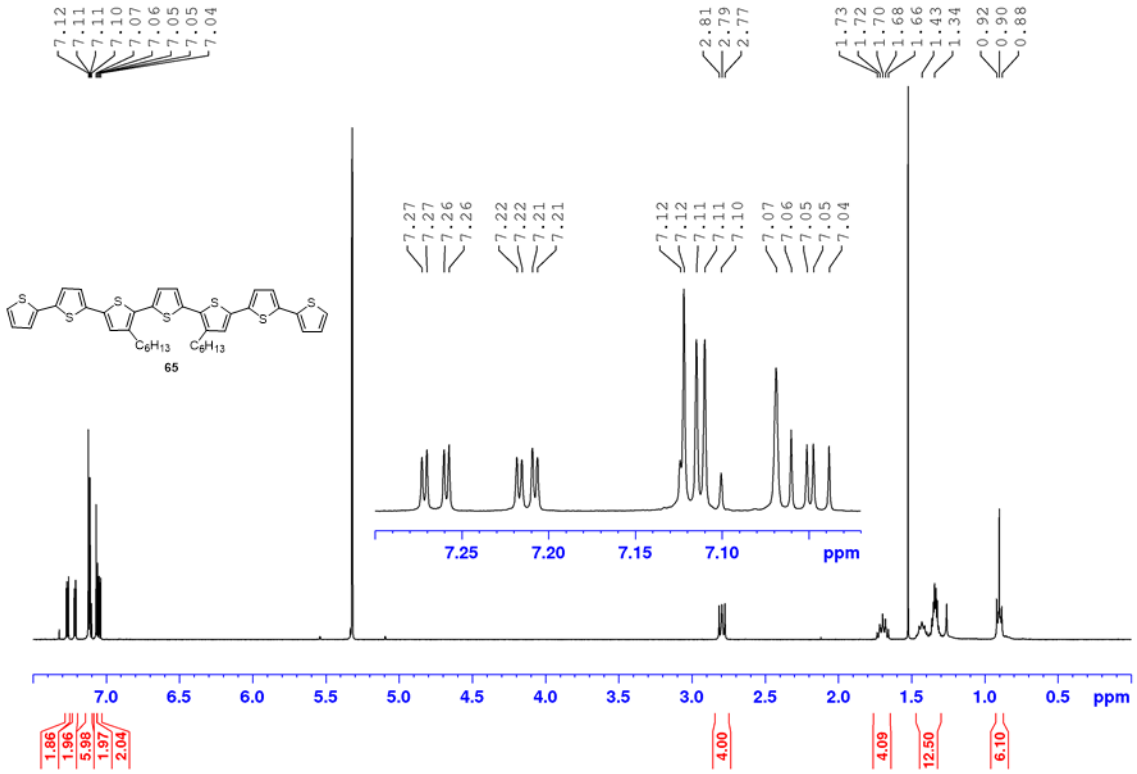

Figure 33. ^{1}H NMR spectrum (400 MHz) of **65** in CD_2Cl_2 at 298 K.

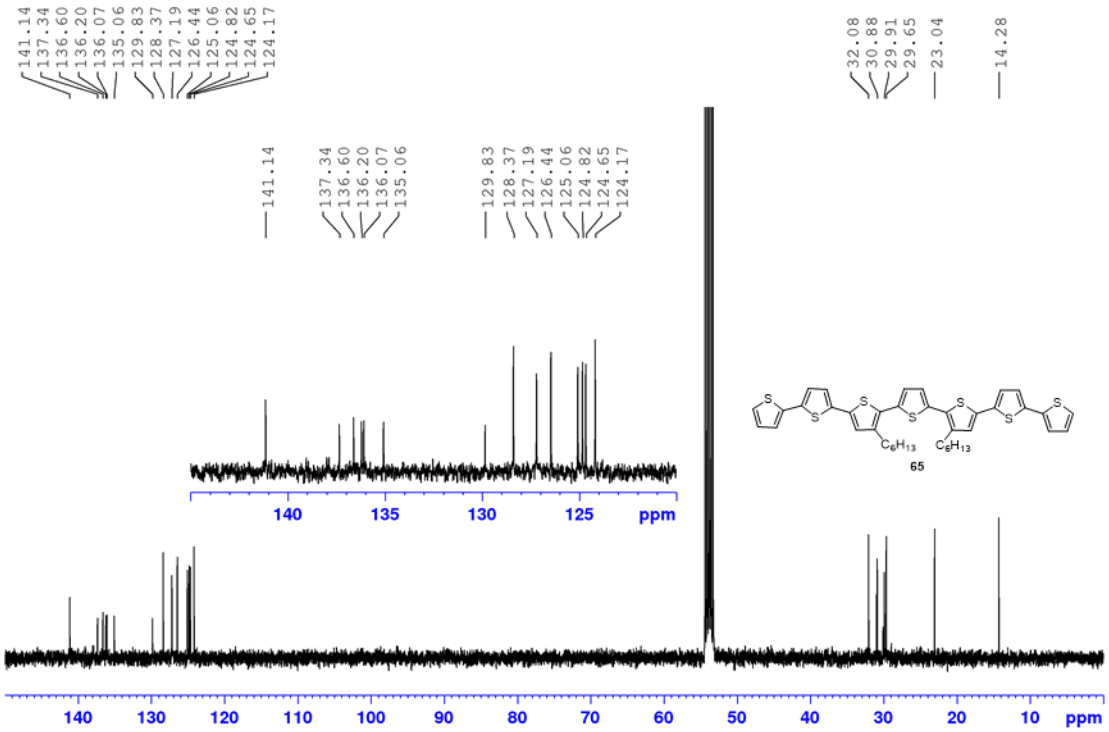

Figure 34. ^{13}C NMR spectrum (101 MHz) of **65** in CD_2Cl_2 at 298 K.

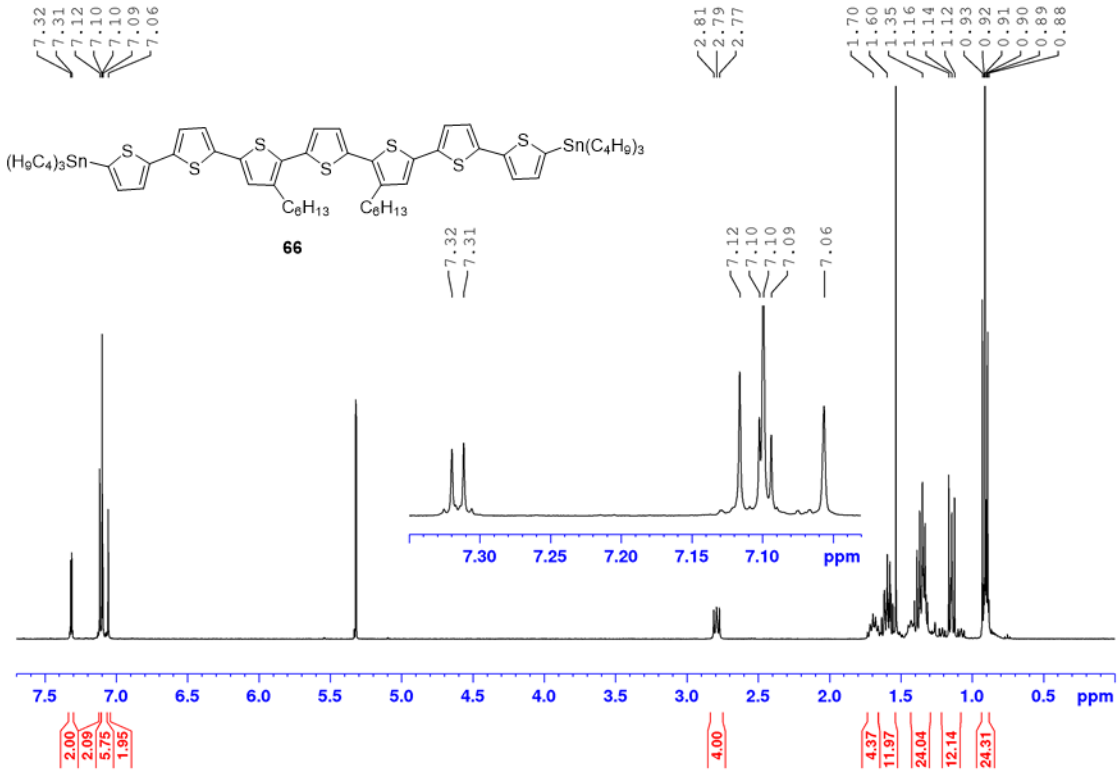

Figure 35. ^{1}H NMR spectrum (400 MHz) of **66** in CD_2Cl_2 at 298 K.

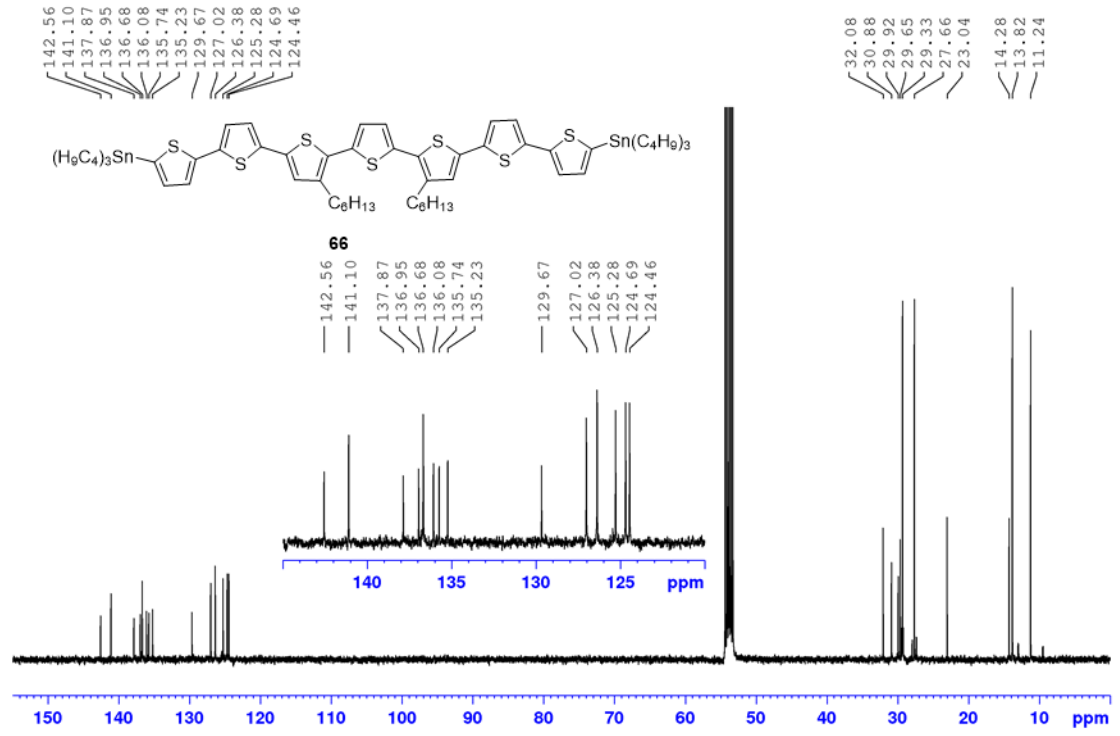

Figure 36. ^{13}C NMR spectrum (101 MHz) of **66** in CD_2Cl_2 at 298 K.

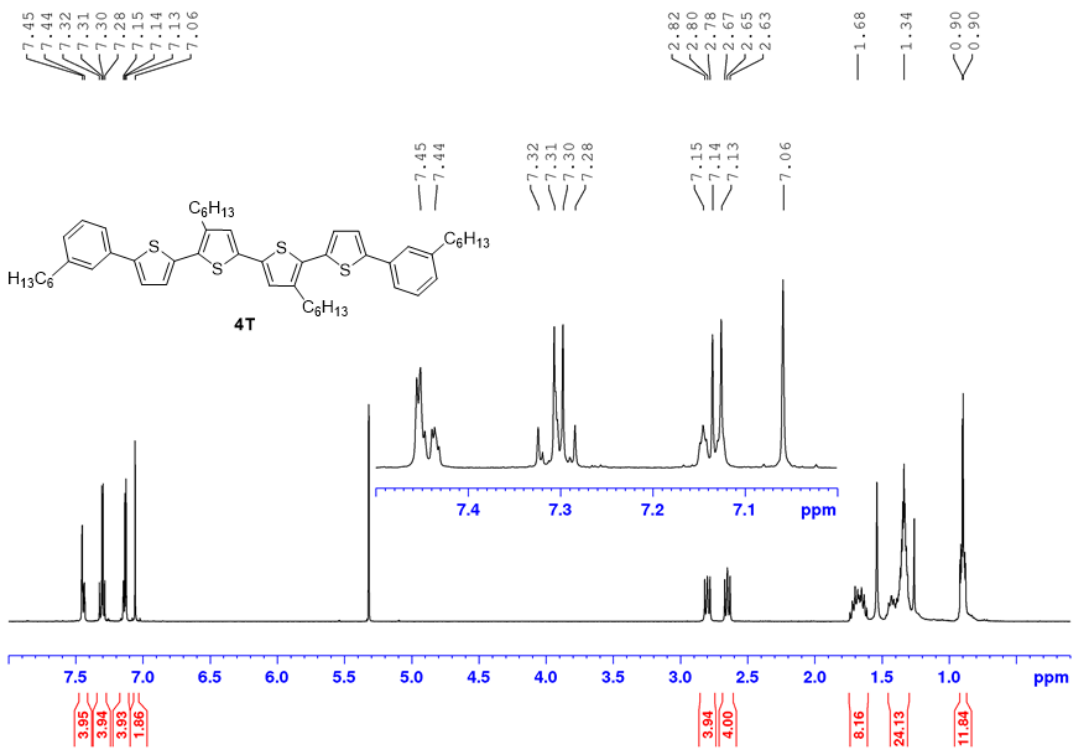

Figure 37. ^{1}H NMR spectrum (400 MHz) of **4T** in CD_2Cl_2 at 298 K.

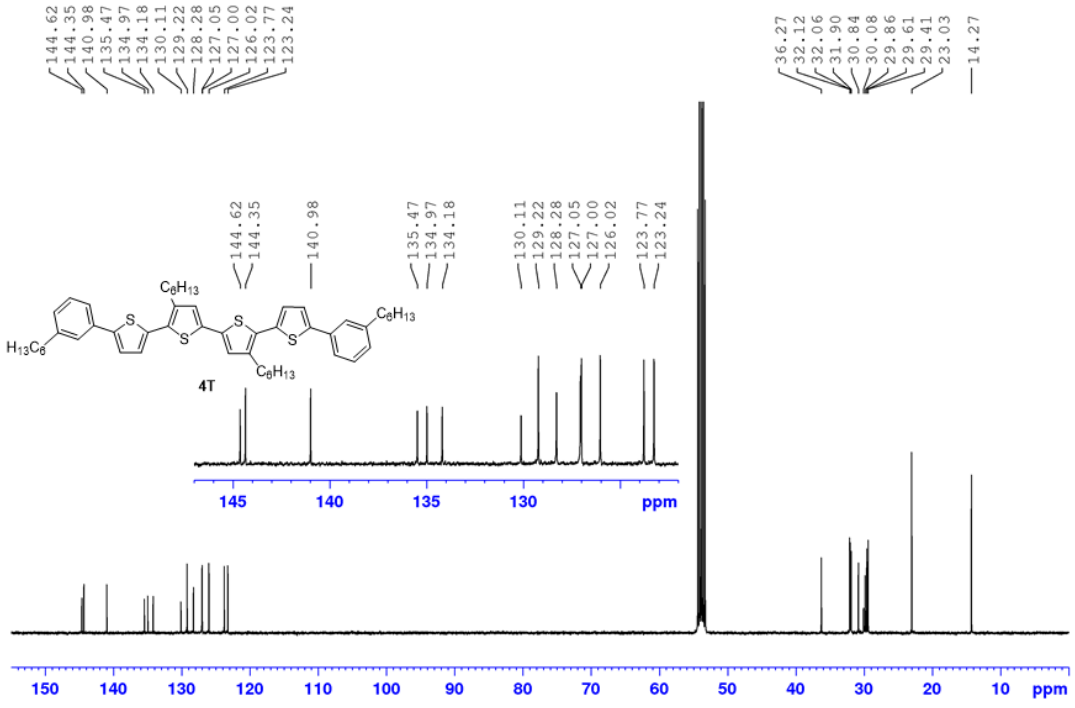

Figure 38. ^{13}C NMR spectrum (101 MHz) of **4T** in CD_2Cl_2 at 298 K.

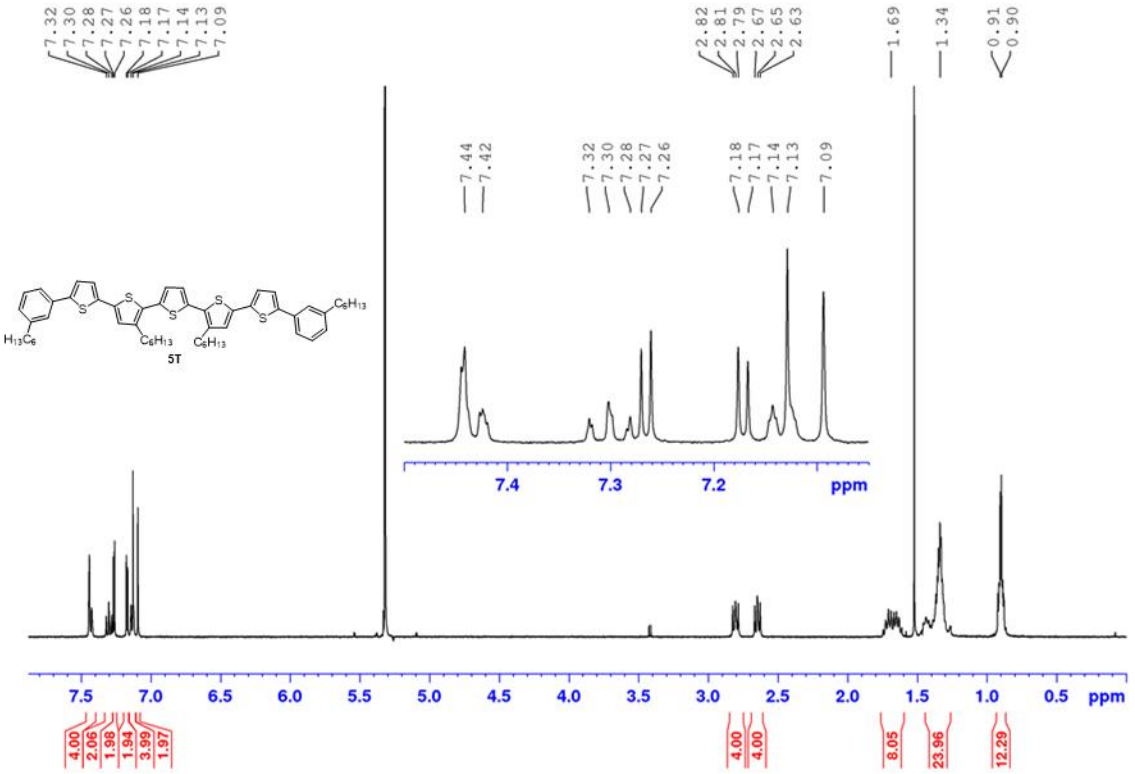

Figure 39. ^{1}H NMR spectrum (400 MHz) of **5T** in CD_2Cl_2 at 298 K.

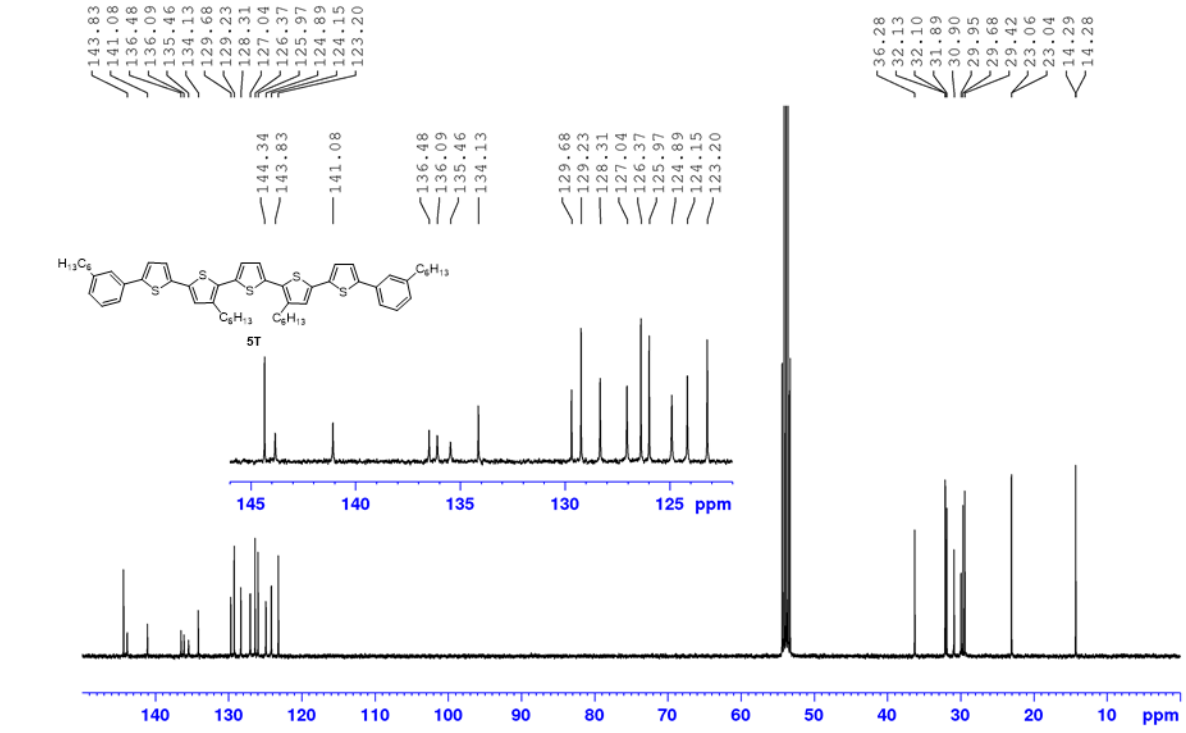

Figure 40. ^{13}C NMR spectrum (101 MHz) of **5T** in CD_2Cl_2 at 298 K.

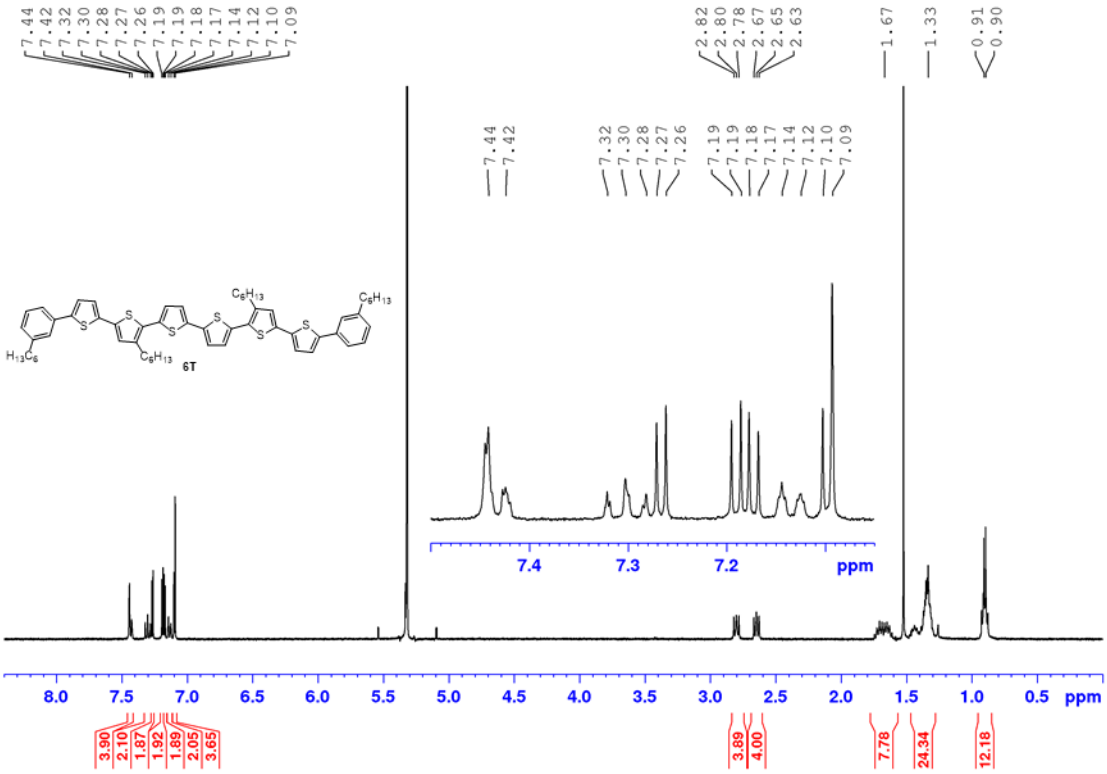

Figure 41. ^{1}H NMR spectrum (400 MHz) of **6T** in CD_2Cl_2 at 298 K.

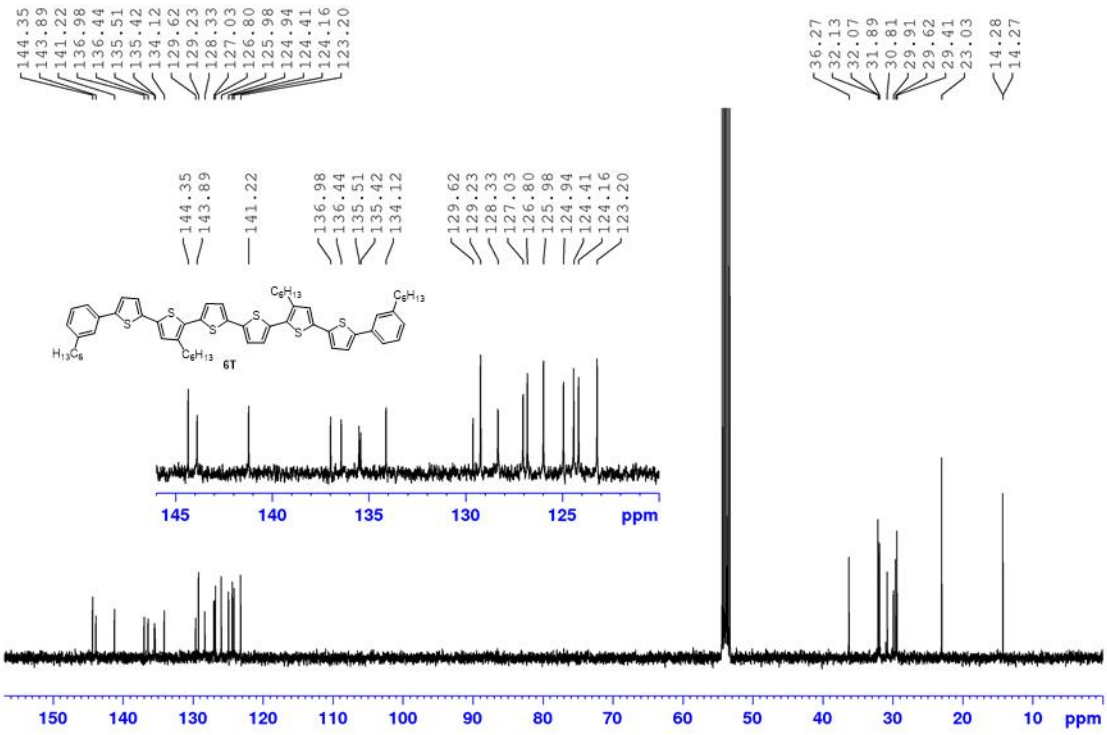

Figure 42. ^{13}C NMR spectrum (101 MHz) of **6T** in CD_2Cl_2 at 298 K.

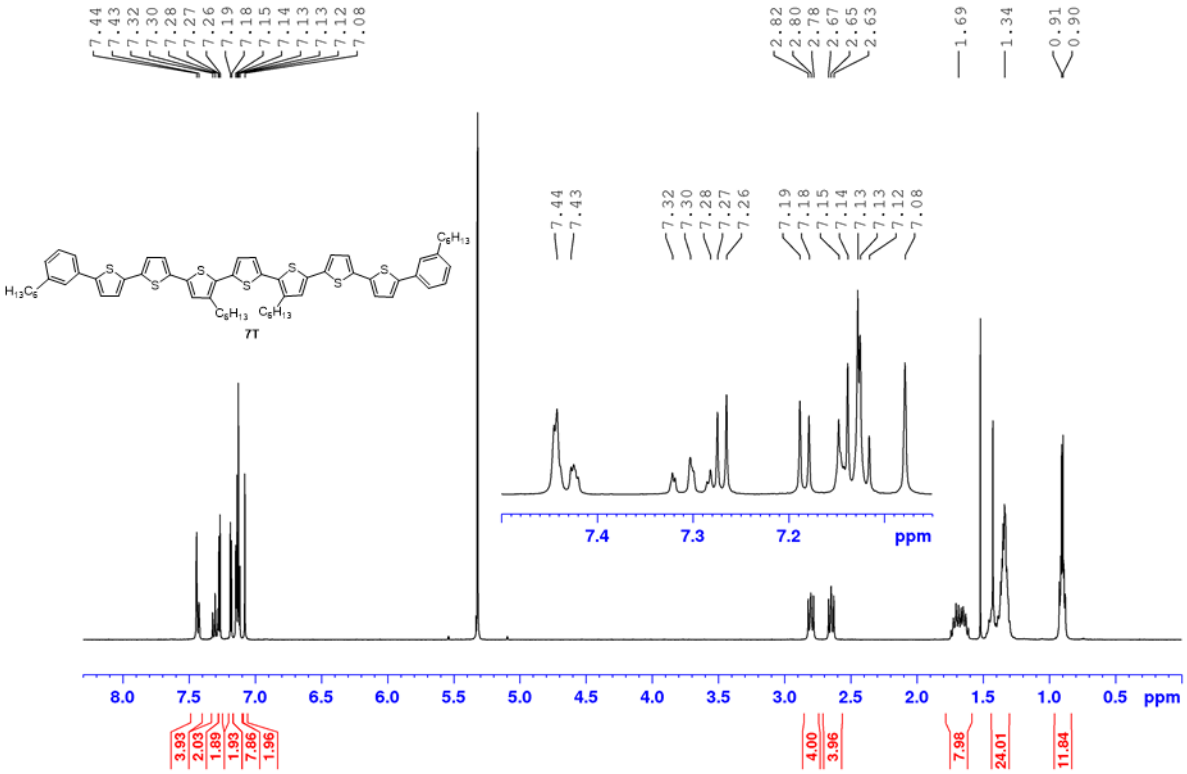

Figure 43. ^{1}H NMR spectrum (400 MHz) of **7T** in CD_2Cl_2 at 298 K.

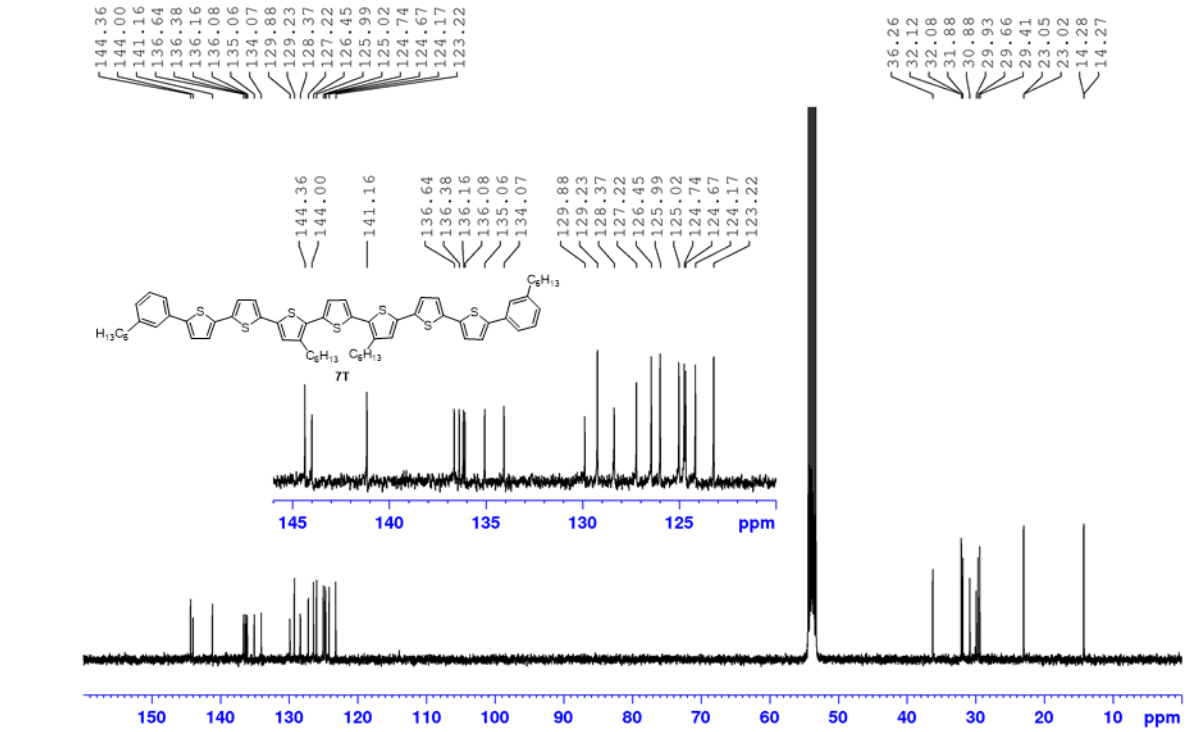

Figure 44. ^{13}C NMR spectrum (101 MHz) of **7T** in CD_2Cl_2 at 298 K.

Chapter 4

Macrocyclic Donor–Acceptor Dyads Composed of a Perylene Bisimide Surrounded by Oligothiophene Bridges

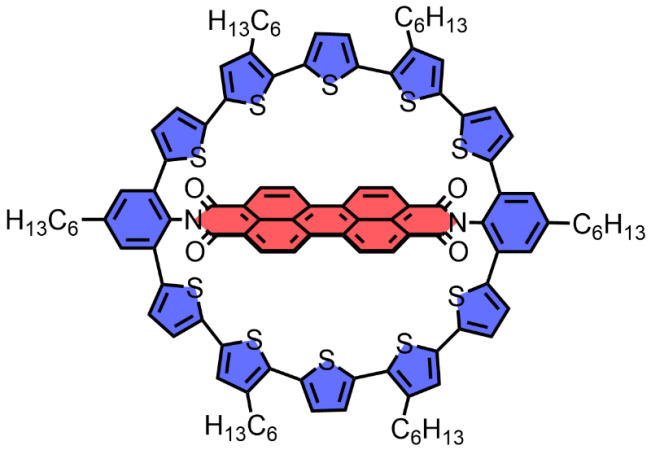

This chapter and the corresponding supporting information has been published:

K. Bold, M. Stolte, K. Shoyama, M. Holzapfel, A. Schmiedel, C. Lambert, F. Würthner, *Angew. Chem. Int. Ed.* **2022**, *61*, e202113598; *Angew. Chem.* **2022**, *134*, e202113598.

Abstract:[i] Two macrocyclic architectures comprising oligothiophene strands that connect the imide positions of a perylene bisimide (PBI) have been synthesized *via* a platinum-mediated cross- coupling strategy. The crystal structure of the double bridged PBI reveals all *syn*-

[i] Synthesis of **5T-PBI** using other reaction conditions has been described in: K. Bold, Master Thesis, Julius-Maximilians-Universität Würzburg, **2017**.

arranged thiophene units which completely enclose the planar PBI chromophore *via* a 12-membered macrocycle. The target structures were characterized by steady-state UV/Vis absorption, fluorescence and transient absorption spectroscopy, as well as cyclic and differential pulse voltammetry. Both D-A dyads show ultrafast Förster Resonance Energy Transfer and photoinduced electron transfer, thereby leading to extremely low fluorescence quantum yields even in the lowest polarity cyclohexane solvent.

4.1 Introduction

Cyclic molecular structures have always attracted chemists for a variety of reasons. These include purely aesthetic reasons,[263] the suitability of macrocycles as well pre-organized supramolecular host[264-267] and the usefulness of π-conjugated (macro-)cycles to shed light on aromaticity[268-272] or for enabling special physical properties[273-277] of interest. Emanating from the latter research field, the fascinating classes of cyclo[*n*]oligothiophenes,[40, 136, 148-149, 278] cyclo[*n*]paraphenylenes,[137] carbon nanobelts[279-280] as well as porphyrin nanorings[281-282] have been realized in the recent years. Some of them, such as Bäuerle's cyclo[*n*]oligothiophenes or Osuka's and Anderson's porphyrin nanorings, also exhibit fascinating properties, i.e. the formation of polaron pairs (biradicals) or the switching between aromatic and antiaromatic properties upon oxidation or photoexcitation, respectively.[113, 272, 275] By taking a look onto the light-harvesting complex 1 (LHC 1) of purple bacteria we may identify another roadmap for future research on macrocyclic functional π-scaffolds.[283-284] In this complex nature organizes a ring of 32 bacteriochlorophyll (BChl) *a* molecules in an elliptical ring structure around the reaction center with its special pair of BChl *b* molecules, thereby encoding the desirable functionality of light harvesting, energy transfer and electron transfer required for the primary steps of photosynthesis.[285] This example from nature may inspire chemists to further develop the chemistry on π-conjugated macrocycles consisting of a sequence of identical building blocks such as phenylene, thiophene, porphyrin, etc. towards dyads[16-18] including a second functional dye to realize a broader variety of functional properties. In this research article we pursue along this approach starting from the pioneering work of Bäuerle on cyclo[*n*]oligothiophenes.[40, 136] Like their linear counterparts, cyclo[*n*]oligothiophenes are electron-rich molecules belonging to the class of organic semiconductors.[65] By combining cyclo[*n*]oligothiophenes with electron-poor perylene bisimides (PBIs),[286] we envisioned to accomplish molecular dyads with the function of panchromatic light absorption and efficient charge separation on the nanoscale, similar as at the donor-acceptor interface of a photovoltaic bulk heterojunction.

4.2 Results and Discussion

4.2.1 Synthesis and Structural Characterization

Our synthesis of macrocycles **5T-PBI** and **(5T)$_2$-PBI** started with the imidization of perylene bisanhydride **67** with sterically hindered amines[287-288] **68** and **69** which could only be accomplished using microwave irradiation as well as elevated temperatures yielding PBIs **70** and **71** (Scheme 6). Subsequently, twofold and fourfold stannylation of the free thiophene *α*-positions was conducted using excess of deprotonation agent *n*-BuLi and tin source $Sn(C_4H_9)_3Cl$. Upon Sn-Pt exchange of **72** and **73** with $Pt(COD)Cl_2$ the precursors **74** and **75** could be obtained. At this point, it should be noted that the compounds **70**, **72** and **74** prevail as mostly inseparable *syn*/*anti* rotameric mixtures in solution. In case of **5T-PBI**, precursor molecules **74** exhibiting a *syn*-conformation are a prerequisite for the desired macrocyclization to proceed and accordingly elevated temperatures in order to overcome the calculated inversion barrier of 114 kJ mol^{-1} (for details see *Chapter 4.4*) were applied for the final reaction.[289-290] Inspired by other successful macrocyclization protocols utilizing this method in literature,[26, 291] especially the formation of cyclo-*para*phenylenes,[28, 138, 169] the macrocyclization of bay-bridged PBI- thiophene compounds[61-62] and the synthesis of giant cyclic oligothiophenes,[40]

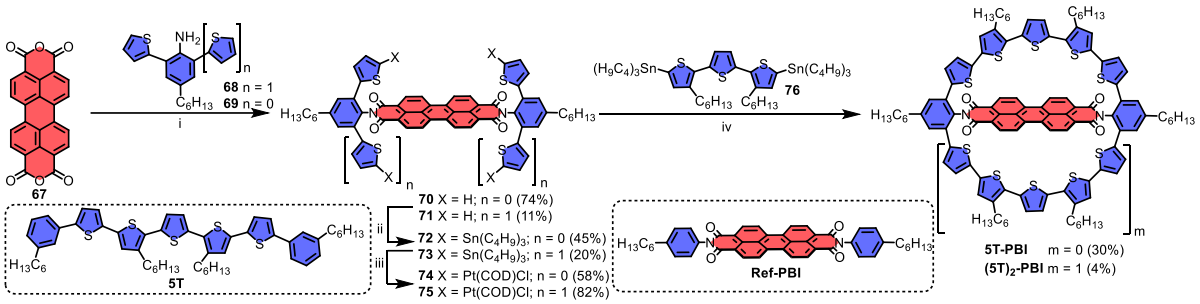

Scheme 6. Synthesis of the macrocyclic architectures **(5T)$_2$-PBI** and **5T-PBI**. Reagents and conditions: i) $Zn(OAc)_2$, imidazole, microwave irradiation. ii) $Sn(C_4H_9)_3Cl$, *n*-BuLi, THF, r.t., overnight. iii) $Pt(COD)Cl_2$, toluene, 95 °C. iv) Toluene, 75 °C, overnight, then dppf, CH_2Cl_2, r.t, 6 h, then *m*-xylene, 120 °C, overnight. Dppf = 1,1′-Ferrocenediyl-bis(diphenylphosphine); COD = 1,5-Cyclooctadiene.

we decided to apply this three step platinum-mediated cross-coupling reaction cascade to obtain target molecular dyads **5T-PBI** and **(5T)$_2$-PBI** in yields of 30% and 4%, respectively (Scheme 1; for details see *Chapter 4.4*). This decrease in yields can be explained by four vs. two couplings statistics and the enhanced strain energy of **(5T)$_2$-PBI** in comparison to **5T-PBI** (*vide infra*). Target molecules **5T-PBI** and **(5T)$_2$-PBI** were characterized by nuclear magnetic resonance (NMR) spectroscopy and high-resolution mass spectrometry (HRMS). In

comparison to their linear phenyl end-capped α-quinquethiophene counterpart **5T** (Scheme 6)[235] the thiophene units in the macrocyclic bridges in **5T-PBI** and **(5T)$_2$-PBI** adopt a more rigid all-*syn* configuration in solution. Two doublet and two singlet proton signals in the aromatic region of the ^{1}H NMR spectrum for both constrained oligothiophenes confirm the high symmetry (Figure 49). Interestingly, both sets of oligothiophene signals for **5T-PBI** and **(5T)$_2$-PBI** barely differ in the chemical shift suggesting a very similar chemical proton environment, which is also true for the PBI subunit proton signals when compared to **Ref-PBI** (Scheme 6).

For an unambiguous structural proof for the 12-membered macrocycle-formation as well as PBI enclosure, single crystals suitable for X-ray crystallography could be grown by slow vapor diffusion of methanol into a solution of **(5T)$_2$-PBI** in chlorobenzene. While the small set of signals in the aromatic region of the ^{1}H NMR (*Chapter 4.4*) suggested a very high degree of symmetry (D_{2h}) in solution, contrarily in the crystal of **(5T)$_2$-PBI** two different manifestations of the molecule are present, presumably due to packing effects in the solid state. One motif has a crystallographic inversion center (molecule A in Figure 45a), whereas the other (molecule B in Figure 45a) shows rather deformed oligothiophene bridges. Two of these non-symmetric structures B flank one molecule A with high symmetry in the unit cell (Figure 45a). The attached aliphatic chains are not depicted in Figure 45 but are included in Figure 50 in *Chapter 4.4*.

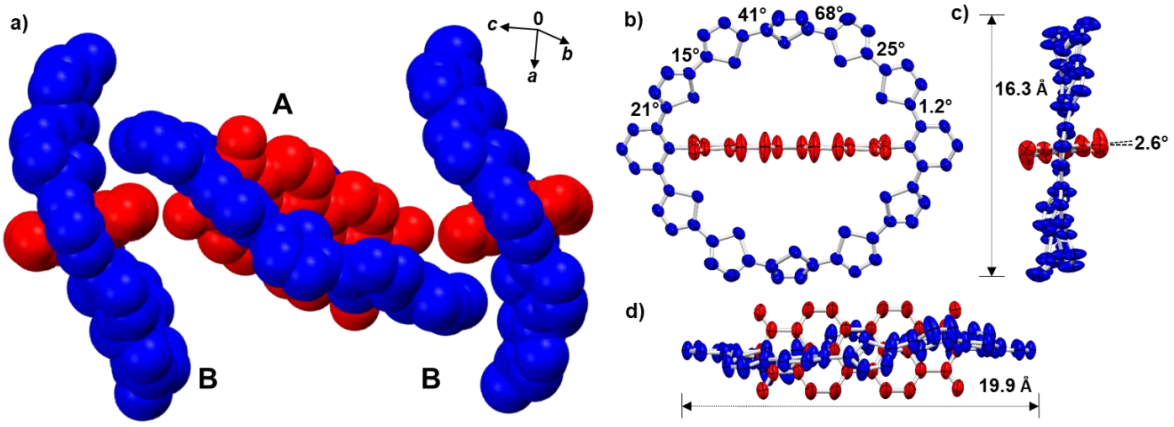

Figure 45. Crystal structure of **(5T)$_2$-PBI** with ellipsoids set to 50% probability and PBI coloured in red and macrocycle in blue. a) Space-filling model of the unit cell consisting of three molecules with structures A and B and their molecular packing in the crystal structure. b) Front, c) side and d) top view onto the molecule A of **(5T)$_2$-PBI** with crystallographic inversion center. The hydrogen atoms, solvent molecules as well as the alkyl chains are omitted for clarity.

Figure 45b-d provide further analysis for molecule A whilst molecule B, embedded solvent molecules and structural disorder in the unit cell is analyzed in Figure 51 in *Chapter 4.4*. In the side and top view of the molecule (Figure 45c, d) the thiophene chain describes an S-shape with respect to the PBI subunit.

As proven by the crystal structure as well as corroborated from DFT calculations (Figure 53) both oligothiophene bridging units show an overall highly twisted structure with neighboring thiophene units rotated from 15° to 68° (Figure 45b). These values are indeed larger than those observed for linear α-oligothiophene chains[156, 292] and similarly sized cyclic oligothiophenes.[113, 151] Interestingly, the central thiophene units of each bridge show the highest torsion of the ten subunits, thereby interrupting the π-conjugation. The oligothiophene ring with an outer diameter of 16.3 Å adapts an all-*syn* conformation with all sulphur atoms pointing towards the central PBI chromophore. The averaged interatomic S-S distance amounts to 3.37 Å which is 9% below the sum of their van der Waals radii (3.70 Å). Together with the slightly extended interring thiophene-thiophene bond lengths (1.453(3) Å to 1.477(3) Å) the above discussed factors add up to a strained macrocycle which also leads to electronic consequences (*vide infra*). Due to the fact that the central PBI chromophore only exhibits a small twist between the two naphthalene subunits of about 3° it can be concluded that the oligothiophene bridges compensate for the major part of the macrocyclic strain energy of 30.6 kJ mol^{-1} for **(5T)$_2$-PBI** which is slightly more than two times higher as for **5T-PBI** (13.9 kJ mol^{-1}, for details see *Chapter 4.4*). In comparison to similarly sized macrocycles such as [12]cycloparaphenylene (117 kJ mol^{-1})[137] or α-cyclo[12]oligothiophene (7.5 kJ mol^{-1})[136] the macrocycle **(5T)$_2$-PBI** can be considered as moderately strained.

4.2.2 Redox Properties

Both oligothiophene-bridged macrocycles were electrochemically characterized by cyclic voltammetry (CV), differential pulse voltammetry (DPV) and spectroelectrochemistry (SEC, for **5T-PBI**) in CH_2Cl_2 with Bu_4NPF_6 as supporting electrolyte (Figure 46). In the CV reversibility of all involved redox processes can be monitored.

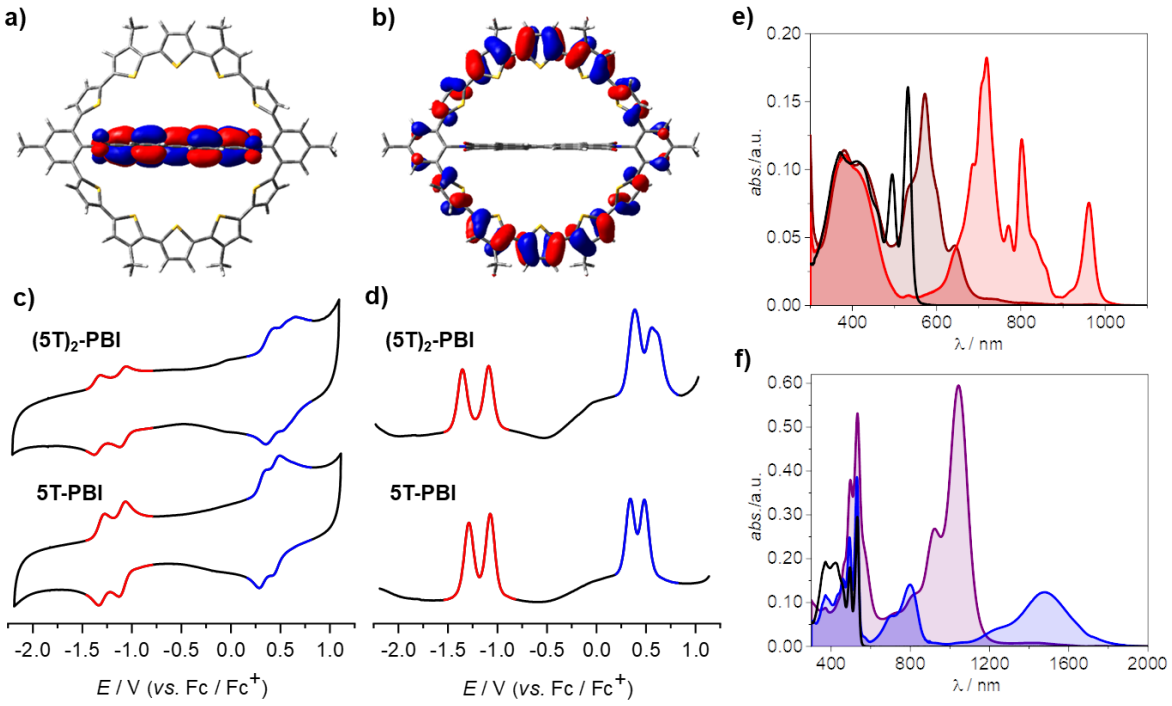

Figure 46. a) LUMO and b) HOMO of **(5T)$_2$-PBI** based on geometry optimized structures from DFT calculations. The quantum mechanics calculations were carried out on the level of B3LYP density functional with the 6-31G(d) basis set as implemented in Gaussian 16. c) CV and d) DPV measurements of **5T-PBI** and **(5T)$_2$-PBI** as well as UV/Vis/NIR absorption spectra of **5T-PBI** (black line) upon electrochemical reduction to e) **5T-PBI$^{\bullet-}$**(red line), **5T-PBI^{2-}** (maroon line) and electrochemical oxidation to f) **5T$^{\bullet+}$-PBI** (blue line) and **5T^{2+}-PBI** (violet line) in CH_2Cl_2 solutions with Bu_4NPF_6 at room temperature ($c_0 = 10^{-4}$ M).

Two reversible reduction waves for both structures, **5T-PBI** and **(5T)$_2$-PBI**, mark the formation of an anionic ($E_{red,1}$ = −1.07 V/−1.09 V, Table 4) and dianionic ($E_{red,2}$ = −1.29 V/−1.35 V) PBI chromophore, respectively. Compared to **Ref-PBI** ($E_{red,1}$ = −0.99 V/$E_{red,2}$ = −1.19 V, Figure 55) these reduction events are at about 0.1 V more negative potential which might be due to a macrocyclic ring-strain induced destabilization of the anionic states that are characterized by a reduced length of the PBI unit along its long axis.[293] The localization and shapes of the lowest unoccupied and highest occupied molecular orbital (LUMO/HOMO) of the neutral **(5T)$_2$-PBI** (Figure 46a, b) suggest very little electronic communication between electron donor oligothiophene chain and PBI acceptor segment which is also true for **5T-PBI** (Figure 57). Due to the nodes which are located at the imide nitrogen atoms, conjugation of PBI to the residues is interrupted. Likewise, due to the *meta*-connectivity, the two oligothiophene units are rather independent π-conjugated units. This interpretation is supported by the almost invariant redox properties as well as by time-dependent density functional theory (TDDFT) calculations (Table 6), where the oscillator

strengths for HOMO-LUMO transitions were determined to be close to zero, which agrees well with the observed UV/Vis absorption spectra (*vide infra*), that show now charge transfer (CT) band.

Table 4. Photophysical and electrochemical properties of macrocycles **5T-PBI**, **(5T)$_2$-PBI** as well as **Ref-PBI** and **5T**[235] in CH_2Cl_2 at room temperature.

	λ_{max}[a] /nm	ε_{max}[a] /M^{-1} cm^{-1}	$E_{ox,1}$[b] / V	$E_{ox,2}$[b] / V	$E_{red,1}$[b] / V	$E_{red,2}$[b] / V
Ref-PBI	526	72100	–[c]	–[c]	−0.99	−1.19
5T[235]	422	53500	0.41	0.59	–[c]	–[c]
5T-PBI	531	64800	0.34	0.48	−1.07	−1.29
(5T)$_2$-PBI	536	54000	0.39	0.56	−1.09	−1.35

[a] $c_0 = 10^{-6}$ M. [b] $c_0 = 10^{-4}$ M, Bu_4NPF_6 was used as electrolyte; all half-wave potentials are referenced against the ferrocenium/ferrocene (Fc^+/Fc) redox couple. [c] Not observed.

While all reduction waves correspond to one-electron processes of the PBI subunit, the waves for the oxidations of both macrocycles have to be differentiated. For **5T-PBI** the oxidation waves also reflect one-electron processes ($E_{ox,1}$ = +0.34 V and $E_{ox,2}$ = +0.48 V), whereas two bridge moieties are simultaneously oxidized in **(5T)$_2$-PBI**. Accordingly, the two oxidation potentials $E_{ox,1}$ = +0.39 V and $E_{ox,2}$ = +0.56 V each represent the transfer of two electrons (Figure 56). Therefore, due to the installation of a second semi-oligothiophene circle in **(5T)$_2$-PBI** tri-and tetracationic states are accessible. With a better resolution of the peaks in DPV (Figure 46) a broadening of the second oxidation wave of **(5T)$_2$-PBI** can be observed. Thus, upon formation of (**(5T)$_2$-PBI**)$^{2+}$ the increased quinoidal character of the oligothiophene chain calls for an almost stepwise oxidation to the tricationic (**(5T)$_2$-PBI**)$^{3+}$ and tetracationic (**(5T)$_2$-PBI**)$^{4+}$ state due to severe Coulomb interactions between the charges in both bridging units. This can be interpreted as an electronic intramolecular cation-cation communication between the bridged thiophene chains.[294-296] The described oxidation features of **(5T)$_2$-PBI** do not resemble those of structurally closely related and fully conjugated α-cyclo[10]thiophene of Bäuerle and co-workers[113] where four reversible oxidation waves with a very low energy first oxidation potential of 0.03 V were found but rather the cyclophane type alkylene bridged quinquethiophene structures of Sakai *et al.*[296] In accordance with the observed electronic phenomena for **(5T)$_2$-PBI** also in this structure both oligothiophenes show two reversible

oxidation events of which the high energy oxidation process splits in to two CV waves. Thus, the multi-oxidation process for **(5T)$_2$-PBI** involving four electrons presumably occurs stepwise. Furthermore, the oxidations are in the same range compared to the linear all-*anti* oligothiophene analogue **5T** ($E_{ox,1}$ = +0.41 V/$E_{ox,2}$ = +0.59 V)[235]. Besides small contortion related reduction or oxidation potential changes of about 0.1 V and the above mentioned cation-cation interaction the electronic properties of **5T-PBI** and **(5T)$_2$-PBI** are nearly a sum of the reference structures **Ref-PBI** and **5T**. Thus, as envisioned, by connecting both PBI's imide positions with oligothiophene chains a covalently linked donor-acceptor dyad with independent subunits has been be achieved.

This lack of electronic communication between donor and acceptor is further illustrated in the SEC (Figure 46e, f). Upon electrochemical reduction of **5T-PBI** the PBI segment is independently reduced and spectral changes occur only for this part of the spectrum (450-550 nm) while the oligothiophene region (300-450 nm) mainly remains unchanged. In contrast, electrochemical oxidation leads to the selective emerging of oligothiophene cation and dication related bands. The spectral signature for anion and dianion of **5T-PBI** depicted in Figure 46e compares well to similar literature known bay-unsubstituted reference PBI structures.[293] Typical spectral PBI signatures comprising three sharp bands at 719 nm, 802 nm and 962 nm corresponding to the anion **5T-PBI$^{\bullet-}$** (Figure 46e, red line) which decrease upon further reduction and give rise of a band at 572 nm (maroon line) belonging to the dianion **5T-PBI^{2-}**. Onefold oxidation of **5T-PBI** leads to the simultaneous formation of two peaks at 795 nm and 1480 nm indicating the formation of the cationic species **5T$^{\bullet+}$-PBI** (Figure 46f, blue line). Further oxidation to the dicationic species **5T^{2+}-PBI** causes submerging of the aforementioned cationic signals and emerging of a strong signal at 1043 nm (Figure 46f, violet line). Also the cationic and dicationic band shapes (Figure 46f) look much alike linear quinquethiophene analogues in similar solvents[111, 113] but both respective near-IR peaks (1480 nm and 1043 nm) undergo a red shift of about 200 nm (1031 cm^{-1} and 2108 cm^{-1}) due to the two additional phenyl units and the consequent enhanced conjugation length. This band shape similarity of both macrocyclic subunits in comparison with the free donor and acceptor analogues underlines the fact that both π-systems have to be regarded as electronically decoupled.

4.2.3 Optical Properties

Spectroscopic investigations of **5T-PBI** and **(5T)$_2$-PBI** were performed in CH_2Cl_2 (Figure 47). The UV/Vis spectra show a superposition of a high energy oligothiophene absorption below 450 nm as well as the characteristic S_0–S_1 transition of the PBI at around 530 nm with well-resolved vibronic progression. In contrast to **Ref-PBI** (λ_{max} = 26 nm, ε_{max} = 72100 M^{-1} cm^{-1}) the absorption maxima of the macrocyclic PBIs in **5T-PBI** and **(5T)$_2$-PBI** experience a slight bathochromic shift of 6 nm (215 cm^{-1}) and 11 nm (390 cm^{-1}) with an additional decrease of their respective molar extinction coefficients (ε_{max}, Table 4). Similar red-shifted absorbances were recently reported by Nuckolls and co-workers for highly bent PBIs.[297]

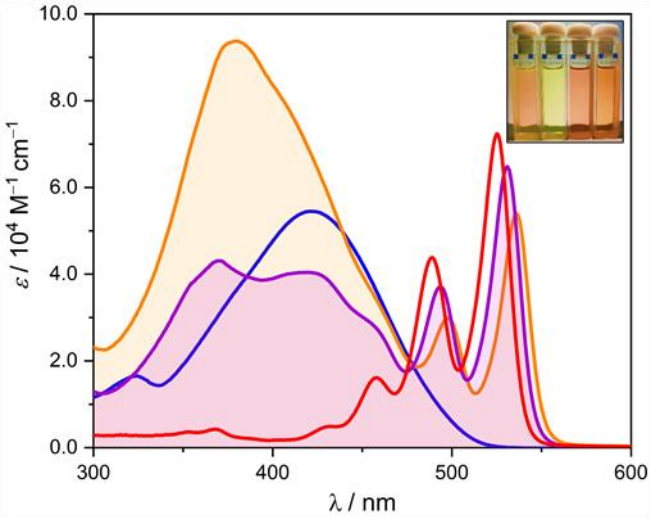

Figure 47. UV/Vis absorption spectra ($c_0 = 10^{-6}$ M) of **5T-PBI** (purple line), **(5T)$_2$-PBI** (orange line), **5T** (blue line) and **Ref-PBI** (red line) in CH_2Cl_2 at room temperature. Inset: Photograph of **Ref-PBI**, **5T**, **5T-PBI** and **(5T)$_2$-PBI** (from left to right) in CH_2Cl_2.

Compared to the structureless absorption of the phenyl end-capped α-oligothiophene **5T** counterpart's[235] π-π* transition (Figure 47), rigidification of the oligothiophene bridge within the *syn*-macrocyclic architectures leads to distinct vibronic fine structures in the higher energy region of the UV/Vis spectrum for **5T-PBI** and **(5T)$_2$-PBI**. While only one oligothiophene absorption maximum can be found for the latter macrocycle (λ_{Thio} = 380 nm, $\varepsilon_{max,Thio}$ = 93900 M^{-1} cm^{-1}) the monobridged analogue shows two distinct maxima at 369 nm and 420 nm, respectively. According to the absorption spectrum of **(5T)$_2$-PBI** both bridges are not in full conjugation but rather have to be considered as photophysically independent. Further, the spectral signatures with most intense absorption bands at rather high energy

indicate a loss in π-conjugation due to the rotational twists of the oligothiophene backbone. While **Ref-PBI** exhibits fluorescence quantum yields (Φ_{fl}) close to unity in many solvents[298] and **5T** is a strong emitter with 53%[235] as well, both donor-acceptor dyads **5T-PBI** and **(5T)$_2$-PBI** show no emission in polar solvents such as CH_2Cl_2 (for a comparison of reference structures and macrocycles see Figure 58), which favor photoinduced electron transfer (PET, *vide infra*).

Even in cyclohexane only extremely low Φ_{fl} below 0.1% were determined (Table 7, Figure 59). Due to the distinguishable spectral regions of the oligothiophene bridge donor and PBI core acceptor both subunits can be excited separately. Upon selective excitation of the PBI acceptor at 480 nm in cyclohexane, typical PBI emission with mirror-image behavior can be observed for **5T-PBI**, whereas **(5T)$_2$-PBI** shows similar but broadened vibronic patterns (Figure 59). Donor chain excitation at 340 nm and 310 nm for both macrocycles **5T-PBI** and **(5T)$_2$-PBI** affords likewise a PBI emission which is attributed to a fast Förster Resonance Energy Transfer to the PBI acceptor unit.

4.2.4 Transient Absorption

For a full understanding of the excited state dynamics, transient absorption (TA) spectra were measured upon excitation at 530 nm in CH_2Cl_2 (Figure 60 and Figure 61). The thereof derived evolution associated difference spectra (EADS) reveal a similar behavior for **5T-PBI** and **(5T)$_2$-PBI** (Figure 48). Thus, with the rise time of the IRF (instrument response function < ca. 80 fs) a ground state bleaching (GSB) at 530 nm and stimulated emission (SE) at 580 nm is observed, confirming the exclusive excitation of the PBI chromophore in the macrocycles. These spectra of the PBI´s S_1 state are followed by two subsequent similar transient absorption spectra that show a superposition of the PBI radical anion and oligothiophene radical cation covering the spectral range from 500 nm to 850 nm (Figure 46e and f). This is best viewed by comparison of the EADS with a radical anion and cation spectra received from SEC (Figure 62). The first EADS is assigned to a hot state that converts to the cold state by molecular and solvent relaxation within ca. 1 ps. The ultrafast population of this cold charge transfer state consisting of a PBI radical anion and oligothiophene radical cation is followed by a fast charge recombination (Figure 48) within 8 ps for the singly bridged and 12 ps for the doubly bridged derivative, respectively. The species giving rise to the first EADS possess lifetimes of 0.2 ps and 0.4 ps, respectively, thus are limited by the charge separation process

with k_{CS} = (0.4 ps)$^{-1}$ and (0.2 ps)$^{-1}$ for **5T-PBI** and **(5T)$_2$-PBI**, respectively. Thus, the rate of the **(5T)$_2$-PBI**'s charge separation is two times faster which is presumably due to the second oligothiophene bridge which increases the charge separation probability and therefore also the rate.

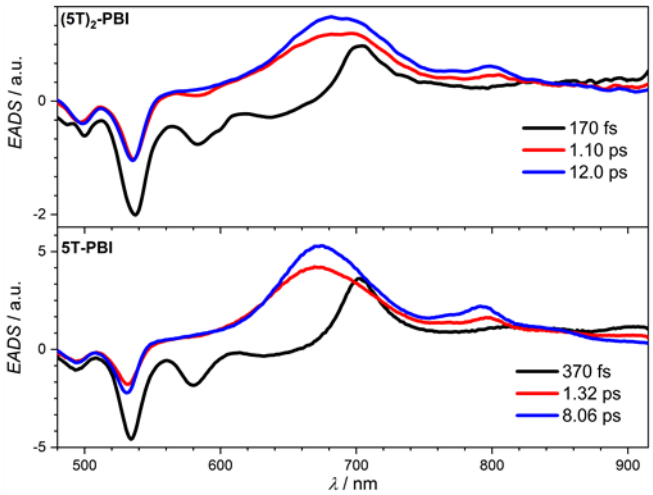

Figure 48. Evolution associated difference spectra (EADS) and lifetimes from a global fit analysis of the transient spectra of macrocycles **5T-PBI** and **(5T)$_2$-PBI** obtained by excitation at 530 nm in CH_2Cl_2 ($c_0 = 10^{-4}$ M) at room temperature.

In closely related but less rigid and non-cyclic PBI dyads functionalized with oligothiophenes the charge separation process of a rather more rigid PBI-octithiophene dyad[55] takes up to 13 times longer than for the macrocycles **5T-PBI** and **(5T)$_2$-PBI**. To the best of our knowledge, the unique cyclic molecules **5T-PBI** and **(5T)$_2$-PBI** allow for one of the fastest PET in an imide functionalized PBI-oligothiophene dyad known in literature which is probably due the rigid structure and the extremely close proximity of donor and acceptor subunits.[52-53, 230]

4.3 Conclusion

In summary we synthesized two novel types of dyads comprising a central accepting PBI core which is bridged by one or two oligothiophene donor chains. Single crystal X-ray analysis provided unambiguous proof for the complete enclosure of the PBI acceptor by the 12-membered donor macrocycle. Rigidification and bending of each quinquethiophene semicircle leads to distinct high energy bands in the absorption spectra of both macrocycles in comparison to the linear phenyl-end-capped oligothiophene analogue. The imide functionalization of the PBI with oligothiophene(s) ensures the intended electronic and photophysical independency of the PBI and oligothiophene units. Upon photo-excitation both macrocyclic dyads showed

an ultrafast photoinduced electron transfer from the oligothiophene to the perylene bisimide subunit to afford a charge separated state for which both the radical anionic PBI and the radical cationic oligothiophene could be assigned by the comparison of the transient absorption spectra with those obtained by spectroelectrochemistry.

4.4 Supporting Information to Chapter 4

General Methods

All reactions were performed in standard glass equipment. All used chemicals were purchased from commercial suppliers (*abcr/carbolution chemicals, Acros Organics, Alfa Asear, Merck, Sigma Aldrich, TCI* and *VWR*) and applied without further purification. CH_2Cl_2, THF and toluene were purified and dried with the commercial purification system PureSolv MD from *Innovative Technology*. Preparative column chromatography was performed with self-packed glass columns of several sizes filled with silica gel 60 M (particle size 0.040-0.063 mm, *Merc*k). The solvents CH_2Cl_2 and methanol were freshly distilled prior to use.
Flash column chromatography was performed on a PuriFLash XS-420 from *Interchim* using columns of the sizes 0012, 0025 and 0040. Silica gel deactivation was achieved by flushing the columns with a solvent mixture of cyclohexane/trimethylamine = 20:1 for two column volumes and subsequent purging with pure cyclohexane for five to ten column volumes prior to the actual purification method.

High-resolution MALDI-TOF mass spectra were measured with a ultrafleXtreme mass spectrometer from *Bruker Daltonics GmbH* using *trans*-2-[3-(4-*tert*-butylphenyl)-2-methyl-2-propenylidene]malononitrile (DCTB) as a matrix material. High-resolution ESI-TOF mass spectroscopy was carried out using a microTOF focus instrument from *Bruker Daltonics GmbH*. For melting point measurements an *Olympus* BX41 polarisation microscope with a temperature regulator TP84 from *Linkam Scientific* was used. The reported values are uncorrected. The purification by gel permeation chromatography was performed on a *Shimadzu* instrument (LC-20AD Prominence Pump, SPD-MA20A Prominence Diode Array Detector) with two preparative columns (*Japan Analytical Industries Co., Ltd).* Ethanol stabilized $CHCl_3$ (Chromasolv®, *Sigma Aldrich*) was used as eluent.

^{1}H and ^{13}C NMR spectra were recorded on *Bruker* Avance III HD 400 or 600 MHz instruments using deuterated solvents. ^{13}C NMR spectra are broad band proton decoupled. Chemical shifts (δ) are listed in parts per million (ppm). Coupling constants (J) are stated in Hertz (Hz). The spectra are referenced internally to residual proton solvent resonances or natural abundance carbon resonances. Multiplicities are reported as s = singlet, brs = broad singlet, d = doublet, dd = doublet of doublets, t = triplet, dt = doublet of triplets, q = quartet, quin = quintet, sex = sextet, m = multiplet with the chemical shift in the center of the signal.

UV/Vis absorption spectra were recorded for solutions in cuvettes (SUPRASIL®, Hellma® Analytics) on a Jasco V-670 or V-770 spectrometer and fluorescence spectra on a FLS980-D2D2-ST fluorescence spectrometer (*Edinburgh Instruments*) and were corrected against the photomultiplier sensitivity and the lamp intensity.

CV and DPV experiments were carried out with a *BASi* Epsilon potentiostat connected to a microcell apparatus from *rhd instruments* involving a 1.6 mL sample container, a platinum counter- and pseudo-reference electrode as well as a glassy carbon working electrode.

Single crystal X-ray diffraction data were collected at the P11 beamline at DESY. The diffraction data were collected by a single 360° scan ϕ sweep at 100 K. The diffraction data were indexed, integrated, and scaled using the XDS program package.[299] In order to compensate low completeness due to single-axis measurement, two data sets were merged using the XPREP program from *Bruker*.[300] The structures were solved using SHELXT, expanded with Fourier techniques and refined using the SHELX software package.[301] Hydrogen atoms were assigned at idealized positions and were included in the calculation of structure factors. All non-hydrogen atoms in the major disorder part of main residues were refined anisotropically. In the crystal structures some of the side chains were disordered and modelled with restraints and constraints using standard SHELX commands RIGU, DELU, ISOR, SADI, SAME, DFIX, DANG, FLAT, SIMU, CHIV and EADP. The solvent molecules in the solvent accessible voids also had disorder and were restrained and/or constrained by a similar set of instructions.

The transient absorption spectrometer setup is based on a femtosecond laser "Solstice" from *Newport-Spectra Physics* with a fundamental wavelength of 800 nm which provides 100 fs long pulses with a repetition rate of 1 kHz. This laser source was used to pump a NOPA to generate the excitation pulses at 530 nm with a pulse length of around 50 fs. The FWHM-bandwidth of the excitation pulse was 8.5 nm and the pulse energy was set to 20 nJ (**(5T)$_2$-PBI**) and 15 nJ (**5T-PBI**). Wire grid polarizers were used to set the pump pulse polarization to 54.7° in relation to the horizontal polarized white light continuum to achieve magic angle conditions. Another part of the laser beam was guided to a TOPAS-C from *Light-Conversion* to obtain a wavelength from 1260 nm (**(5T)$_2$-PBI**) and 1000 nm (**5T-PBI**) which was used to generate the probing white light continuum within a moving CaF_2 (**(5T)$_2$-PBI**) or sapphire crystal (**5T-PBI**). To achieve the probe range from 450 nm to 915 nm a dielectrically coated quartz glass short pass filter with 950 nm, thickness 3 mm, from *Edmund-Optics* were used. The sample was dissolved in spectroscopic grade CH_2Cl_2 from ACROS organics and the solution was filled in a quartz glass cuvette with an optical path length of 0.2 mm (**(5T)$_2$-PBI**) and 2 mm (**5T-PBI**). The optical density at the excitation wavelength was set to 0.055 for **(5T)$_2$-PBI** and 0.50 for **5T-PBI**. The IRF was ca. 80 fs as measured for stimulated Raman signals of the solvent. Further details on this spectrometer setup are provided in ref. [302].

Spectroelectrochemical experiments were performed on a Cary 5000 UV/Vis/NIR Spectrometer from *Agilent* in combination with a sample compartment consisting of a custom-made cylindrical PTFE cell with a sapphire window and an adjustable three in one electrode (6 mm platinum disc working electrode, 1 mm platinum counter and Ag/AgCl leak free reference electrode) in reflection mode. The optical path was adjusted to 100 µm with a micrometer screw. Potentials were applied with a reference potentiostat PAR 283 from *Princeton Applied Research.* Upon applying a new potential to the solution an equilibration time of 20 seconds between each measurement was employed.

DFT and TD-DFT calculations were performed by Gaussian 16[303] using B3LYP/6-31G(d) level of theory.

Stannylated precursor compound **76**[261] and **Ref-PBI**[298] were synthesized according to literature known procedures. The synthesis of **5T** was recently reported.[235]

Synthetic Procedure

4-Hexyl-2-(thiophen-2-yl)aniline (69)

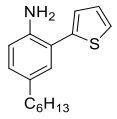

69

A solution of 2-bromo-4-hexylaniline (3.71 g, 14.5 mmol, 1.00 eq.), 2-thienylboronic acid (5.00 g, 39.1 mmol, 2.70 eq.) and $Pd(PPh_3)_2Cl_2$ (1.52 g, 2.17 mmol, 15 mol%) in degassed dioxane (50 mL) was stirred for 30 min at room temperature. Subsequently, 20 mL of aqueous K_2CO_3 (1 M) was added and the reaction mixture was refluxed overnight. The suspension was allowed to cool down to room temperature and water (20 mL) was added. The aqueous layer was extracted three times with CH_2Cl_2 (50 mL each) and the combined organic fractions were washed with brine, dried over $MgSO_4$ and the solvent was removed under reduced pressure. The crude compound was purified by column chromatography (CH_2Cl_2/*n*-hexane = 1:1) to give compound **69**. **Yield**: 3.56 g, 13.7 mmol, 95%, yellow oil. **^{1}H NMR** (400 MHz, CD_2Cl_2): δ/ppm = 7.35 (dd, ^3J = 5.2 Hz, ^4J = 1.2 Hz, 1H), 7.20 (dd, ^3J = 3.5 Hz, ^4J = 1.2 Hz, 1H), 7.12 (q, ^3J = 3.6 Hz, 1H), 7.08 (dd, ^4J = 2.1 Hz, ^5J = 0.4 Hz, 1H), 6.95 (dd, ^3J = 8.1 Hz, ^4J = 2.0 Hz, 1H), 6.69 (d, ^3J = 8.1 Hz, 1H), 3.92 (brs, 2H), 2.50 (t, ^3J = 7.8 Hz, 2H), 1.60-1.51 (m, 2H), 1.38 - 1.26 (m, 6H), 0.88 (t, ^3J = 6.9 Hz, 3H). **^{13}C NMR** (101 MHz, $CDCl_3$): δ/ppm = 141.8, 141.5, 133.3, 130.8, 129.1, 127.6, 125.8, 125.2, 120.0, 116.1, 35.1, 31.9, 31.8, 29.1, 22.8, 14.3. **HRMS** (ESI-TOF, positive mode, MeCN/CHCl3 1:1): *m*/*z* calculated for $C_{16}H_{22}NS$ $[M+H]^+$: 260.1467, found: 260.1465. **R_f**: 0.63 using CH_2Cl_2/n-hexane = 1:1 as eluent.

4-Hexyl-2,6-di(thiophen-2-yl)aniline (68)

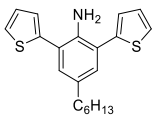

68

A solution of 4-hexylaniline (2.47 g, 7.38 mmol, 1.00 eq.), 2-thienyl boronic acid (2.83 g, 22.1 mmol, 3.00 eq.) and $Pd(PPh_3)_2Cl_2$ (777 mg, 1.11 mmol, 15 mol%) in degassed dioxane (40 mL) was stirred for 30 min at room temperature. Subsequently, 20 mL of aqueous K_2CO_3

(1 M) was added and the reaction mixture was heated to reflux for three days. The suspension was allowed to cool down to room temperature and water (20 mL) was added. The aqueous layer was extracted three times with CH_2Cl_2 (50 mL each) and the combined organic fractions were washed with brine, dried over $MgSO_4$ and the solvent was removed under reduced pressure. The crude product was purified by column chromatography (gradient of *n*-hexane/CH_2Cl_2 = 4:1 to 3:1) to give the title compound **68**. **Yield**: 1.93 g, 5.67 mmol, 77%, brown oil. **^{1}H NMR** (400 MHz, CD_2Cl_2): δ/ppm = 7.38 (dd, ^3J = 5.2 Hz, ^4J = 1.2 Hz, 2H), 7.24 (dd, ^3J = 3.5 Hz, ^4J = 1.2 Hz, 2H), 7.14 (dd, ^3J = 5.2 Hz, ^4J = 3.5 Hz, 2H), 7.08 (s, 2H), 4.28 (brs, 2H), 2.52 (t, ^3J = 7.6 Hz, 2H), 1.69 (quin, ^3J = 7.3 Hz, 2H), 1.40 - 1.25 (m, 6H), 0.88 (t, ^3J = 6.9 Hz, 3H). **^{13}C NMR** (101 MHz, $CDCl_3$): δ/ppm = 141.3, 140.0, 132.5, 131.0, 127.7, 126.3, 125.5, 120.6, 35.0, 31.9, 31.8, 29.2, 22.8, 14.3. **HRMS** (ESI-TOF, positive mode, MeCN/CHCl3 1:1): *m*/*z* calculated for $C_{20}H_{24}NS_2$ $[M+H]^+$: 342.1345, found: 342.1348. **R_f**: 0.46 using CH_2Cl_2/n-hexane = 1:1 as eluent.

***N*,*N*'-Di(4-hexyl-2-(thiophen-2-yl)phenyl)-3,4:9,10-tetracarboxylic acid bisimide (70)**

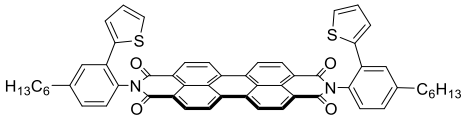

70

A suspension of perylene-3,4:9,10-tetracarboxylic dianhydride (300 mg, 765 µmol, 1.00 eq.), aniline derivate **69** (794 mg, 3.06 mmol, 4.00 eq.) and $Zn(OAc)_2$ (42.0 g, 229 µmol, 0.30 eq) in imidazole (3.0 g, 44.1 mmol) was stirred for 4 h at 120 °C under microwave irradiation. The crude solid was collected with CH_2Cl_2, adsorbed on celite and the solvent was removed under reduced pressure. The crude product-celite mixture was purified by flash column chromatography (gradient of CH_2Cl_2/*n*-hexane = 0:1 to 1:0) to give compound **70**. **Yield**: 492 mg, 562 µmol, 74%, red solid. **^{1}H NMR** (400 MHz, CD_2Cl_2): δ/ppm = 8.73 (d, ^3J = 8.0 Hz, 4H), 8.69 (d, ^3J = 8.0 Hz, 4H), 7.60 (d, ^4J = 2.0 Hz, 2H), 7.38 (dd, ^3J = 8.0 Hz, ^4J = 2.1 Hz, 2H), 7.26 (d, ^3J = 7.9 Hz, 2H), 7.15 (dd, ^3J = 3.6 Hz, ^4J = 1.2 Hz, 2H), 7.12 (dd, ^3J = 5.1 Hz, ^4J = 1.2 Hz, 2H), 6.90 (q, ^3J = 3.6 Hz, 2H), 2.77 (t, ^3J = 7.6 Hz, 4H), 1.76 (quin, ^3J = 7.5 Hz, 4H), 1.41 - 1.34 (m, 12H), 0.93 (t, ^3J = 7.0 Hz, 6H). **^{13}C NMR** (101 MHz, $CDCl_3$): δ/ppm = 163.9, 144.6, 139.7, 135.1, 133.2, 132.1, 131.0, 130.2, 129.6, 129.3, 127.3, 126.1,

126.0, 123.5, 123.4, 35.9, 31.9, 31.3, 29.3, 22.8, 14.3. **HRMS** (ESI-TOF, positive mode, MeCN/CHCl3 1:1): *m*/*z* calculated for $C_{56}H_{46}N_2NaO_4S_2$ $[M+Na]^+$: 897.2791, found: 897.2736. **M.p.**: >300 °C. **R_f**: 0.32 using CH_2Cl_2 as eluent.

N,*N*'-Tetra(4-hexyl-2-(thiophen-2-yl)phenyl)-3,4:9,10-tetracarboxylic acid bisimide (71)

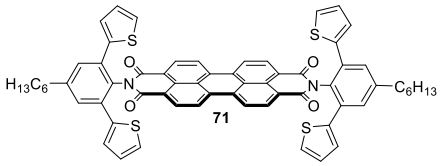

A suspension of perylene-3,4:9,10-tetracarboxylic dianhydride (50.0 mg, 127 µmol, 1.00 eq.), aniline derivate **68** (348 mg, 1.02 mmol, 8.00 eq.) and $Zn(OAc)_2 \cdot 2H_2O$ (42.0 mg, 229 µmol, 1.30 eq) in imidazole (600 mg, 8.81 mmol) was stirred for 14 h at 135 °C under microwave irradiation. The crude solid was collected with CH_2Cl_2, ultrasonicated, adsorbed on celite and the solvent was removed under reduced pressure. The crude product-celite mixture was purified by flash column chromatography (gradient of CH_2Cl_2/*n*-hexane = 1:1, CH_2Cl_2) to give compound **71**. **Yield**: 14.6 mg, 14.1 µmol, 11%, red solid. **^{1}H NMR** (400 MHz, CD_2Cl_2): δ/ppm = 8.57 (d, ^3J = 8.1 Hz, 4H), 8.69 (d, ^3J = 8.1 Hz, 4H), 7.55 (s, 4H), 7.13 (dd, ^3J = 3.6 Hz, ^4J = 1.1 Hz, 8H), 6.89 (dd, ^3J = 3.6 Hz, 4H), 2.80 (t, ^3J = 7.8 Hz, 4H), 1.80 (quin, ^3J = 7.1 Hz, 4H), 1.50 - 1.35 (m, 12H), 0.93 (t, ^3J = 7.0 Hz, 6H). **^{13}C NMR** (101 MHz, CD_2Cl_2): δ/ppm = 164.0, 144.9, 139.8, 135.0, 134.6, 132.0, 131.4, 130.0, 129.0, 127.5, 127.0, 126.8, 126.5, 123.5, 123.2, 36.0, 32.1, 31.6, 29.6, 23.0, 14.3. **HRMS** (MALDI-TOF, positive mode, DCTB in $CHCl_3$): *m*/*z* calculated for $C_{64}H_{50}N_2O_4S_4$ $[M]^+$: 1038.2653, found: 1038.2648. **M.p.**: >300 °C. **R_f**: 0.40 using CH_2Cl_2 as eluent.

_N,N_'-Di(4-hexyl-2-(5-(tributylstannyl)thiophen-2-yl)phenyl)-3,4:9,10-tetracarboxylic acid bisimide (72)

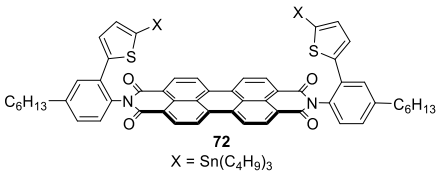

To a solution of perylene bisimide **70** (480 mg, 549 µmol, 1.00 eq.) in dry THF (100 mL) *n*-butyllithium (5.14 mL, 1.6 M in *n*-hexane, 15.0 eq.) was added dropwise under stirring at room temperature and the solution was further stirred for 2 h. Subsequently, $Sn(C_4H_9)_3Cl$ (2.53 mL, 9.32 mmol, 17.0 eq.) was added dropwise at room temperature and the solution was further stirred overnight. The reaction was quenched with water (50 mL), extracted three times with CH_2Cl_2 (50 mL each), and the combined organic layers were washed with brine, dried over $MgSO_4$ and the solvent was removed under reduced pressure. The crude residue was purified *via* flash column chromatography (deactivated silica gel, gradient of CH_2Cl_2/*n*-hexane = 0:1 to 1:0) to give the desired compound **72**. **Yield**: 355 mg, 244 µmol, 45%, deep red solid. **^{1}H NMR** (400 MHz, CD_2Cl_2): δ/ppm = 8.73 (d, ^3J = 8.0 Hz, 4H), 8.69 (d, ^3J = 8.0 Hz, 4H), 7.52 (d, ^4J = 2.0 Hz, 2H), 7.38 (dd, ^3J = 8.0 Hz, ^4J = 2.1 Hz, 2H), 7.32 (d, ^3J = 3.5 Hz, 2H), 7.27 (d, ^3J = 8.0 Hz, 2H), 6.98 (d, ^3J = 3.5 Hz, 2H), 2.77 (t, ^3J = 7.8 Hz, 4H), 1.77 (quin, ^3J = 7.8 Hz, 4H), 1.42 - 1.35 (m, 12H), 1.27 - 1.21 (m, 12H), 1.04 (sex, ^3J = 7.4 Hz, 12H), 0.93 (t, ^3J = 7.0 Hz, 6H), 0.80 (t, ^3J = 8.1 Hz, 12H), 0.64 (t, ^3J = 7.4 Hz, 18H). **^{13}C NMR** (101 MHz, $CDCl_3$): δ/ppm = 164.0, 145.3, 144.9, 138.4, 135.8, 135.1, 133.5, 131.8, 130.3 (2 signals), 130.0, 128.9, 127.4, 126.8, 123.8, 123.7, 36.1, 32.2, 31.7, 29.6, 29.0, 27.4, 23.1, 14.3, 13.6, 10.9. **HRMS** (ESI-TOF, positive mode, MeCN/CHCl3 1:1): *m*/*z* calculated $C_{80}H_{98}N_2NaO_4S_2Sn_2$ $[M+Na]^+$: 1477.4904, found: 1477.4821. **M.p.**: 116-118 °C. **R_f**: 0.55 using CH_2Cl_2 as eluent.

_N,N_'-Tetra(4-hexyl-2-(5-(tributylstannyl)thiophen-2-yl)phenyl)-3,4:9,10-tetracarboxylic acid bisimide (73)

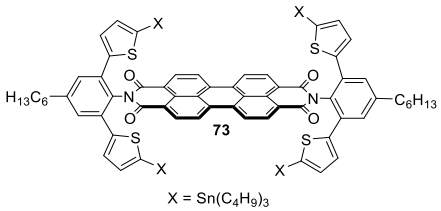

To a solution of perylene bisimide **71** (108 mg, 104 µmol, 1.00 eq.) in dry THF (22 mL) *n*-butyllithium (1.30 mL, 1.6 M in *n*-hexane, 20.0 eq.) was added dropwise under stirring at room temperature and the solution was further stirred for 1 h. Subsequently, $Sn(C_4H_9)_3Cl$ (676 µL, 2.49 mmol, 24.0 eq.) was added dropwise at room temperature and the solution was further stirred overnight. The reaction was quenched with water (15 mL), extracted three times with CH_2Cl_2 (50 mL each), and the combined organic layers were washed with brine, dried over $MgSO_4$ and the solvent was removed under reduced pressure. The crude residue was purified *via* flash column chromatography (deactivated silica gel, gradient of *n*-hexane/ CH_2Cl_2 = 1:0 to 1:1) to yield the desired compound **73**. **Yield**: 45.1 mg, 20.5 µmol, 20%, deep red solid. **^{1}H NMR** (400 MHz, CD_2Cl_2): δ/ppm = 8.65 (d, ^3J = 7.9 Hz, 4H), 8.62 (d, ^3J = 7.9 Hz, 4H), 7.55 (s, 4H), 7.27 (d, ^3J = 3.4 Hz, 4H), 6.94 (d, ^3J = 3.4 Hz, 4H), 2.79 (t, ^3J = 7.7 Hz, 4H), 1.79 (quin, ^3J = 7.2 Hz, 4H), 1.52-1.46 (m, 4H), 1.41-1.36 (m, 8H), 1.32 - 1.24 (m, 24H), 1.06 (sex, ^3J = 7.4 Hz, 24H), 0.93 (t, ^3J = 7.0 Hz, 6H), 0.82 (t, ^3J = 8.1 Hz, 24H), 0.67 (t, ^3J = 7.2 Hz, 36H). **^{13}C NMR** (150 MHz, CD_2Cl_2): δ/ppm = 164.2, 145.3, 144.8, 138.5, 135.7, 135.3, 134.8, 132.1, 130.2, 130.1, 128.1, 127.9, 127.0, 123.8, 123.6, 36.1, 32.2, 31.6, 29.7, 29.0, 27.4, 23.0, 14.3, 13.7, 11.0. **HRMS** (MALDI-TOF, positive mode, DCTB in $CHCl_3$): *m*/*z* calculated $C_{112}H_{154}N_2NaO_4S_4Sn_4$ $[M+Na]^+$: 2221.6772, found: 2221.6771. **M.p.**: 183-185 °C. **R_f**: 0.73 using CH_2Cl_2/cyclohexane = 2:1 as eluent.

N,*N*'-Di(4-hexyl-2-(5-(chloro(1,5-cyclooctadiene)platinum)thiophen-2-yl)phenyl)-3,4:9,10-tetracarboxylic acid bisimide (74)

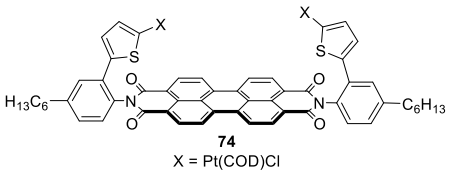

A solution of **72** (50.0 mg, 34.4 µmol, 1.0 eq.) and $Pt(COD)Cl_2$ (28.3 mg, 75.5 µmol, 2.2 eq.) in degassed toluene (10 mL) was stirred for 2 h at 95 °C. The solvent was removed under reduced pressure and the crude product was purified *via* flash column chromatography (gradient of CH_2Cl_2/acetone = 1:0 to 20:1) to yield compound **74**. **Yield**: 31.0 mg, 20.0 µmol, 58%, deep red solid. **^{1}H NMR** (400 MHz, $C_2D_2Cl_4$): δ/ppm = 8.70 (brs, 8H), 7.59 (d, ^3J = 1.9 Hz, 2H), 7.32 (dd, ^3J = 1.9 Hz, ^3J = 8.0 Hz, 2H), 7.24 (^3J = 8.0 Hz), 7.08 (d, ^3J = 3.7 Hz, 2H), 6.77 (d, ^3J = 3.7 Hz, 2H), 5.60-5.52 (m, 4H), 4.96-4.89 (m, 4H), 2.75 (t, ^3J = 7.7 Hz, 4H), 2.47-2.12 (m, 16H), 1.74 (quin, ^3J = 7.3 Hz, 4H), 1,38-1.26 (m, 12H), 0.93 (t, ^3J = 7.0 Hz, 6H). **^{13}C NMR** (101 MHz, $C_2D_2Cl_4$): δ/ppm = 163.6, 144.3, 141.1, 138.5, 134.7, 133.3, 131.9, 130.3, 129.7, 129.4, 129.2, 128.1, 126.3, 126.0, 123.2, 120.2, 112.9, 90.1, 35.7, 31.6, 31.5, 31.2, 30.8, 29.1, 28.3, 22.6, 14.2. **HRMS** (MALDI-TOF, positive mode, DCTB in $CHCl_3$): *m*/*z* calculated for $C_{72}H_{68}Cl_2N_2O_4Pt_2S_4$ $[M]^+$:1548.3293, found: 1548.3288. **M.p.**: >300 °C. **R_f**: 0.29 using CH_2Cl_2/acetone = 20:1 as eluent.

N,*N*'-Tetra(4-hexyl-2-(5-(chloro(1,5-cyclooctadiene)platinum)thiophen-2-yl)phenyl)-3,4:9,10-tetracarboxylic acid bisimide (75)

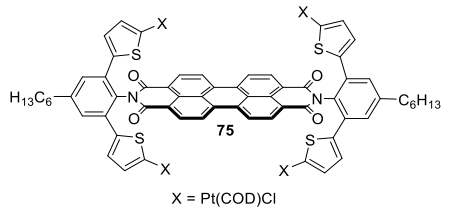

A solution of **73** (49.6 mg, 22.6 µmol, 1.0 eq.) and $Pt(COD)Cl_2$ (169 mg, 452 µmol, 20.0 eq.) in degassed toluene (25 mL) was stirred overnight at 80 °C. The solvent was removed under reduced pressure and the crude product was purified *via* flash column chromatography (gradient of CH_2Cl_2/MeOH = 1:0 to 99:1) to yield compound **75**. **Yield**: 44.4 mg, 217 µmol,

82%, deep red solid. **^{1}H NMR** (400 MHz, $C_2D_2Cl_4$): δ/ppm = 8.66 (brs, 8H), 7.48 (brs, 4H), 7.10 (brs, 4H), 6.77 (brs, 4H), 5.55 (brs, 8H), 4.85 (brs, 8H), 2.77-2.70 (m, 4H), 2.44-2.36 (m, 8H), 2.32-2.24 (m, 4H), 2.15-2.10 (m, 4H), 1.78-1.71 (m, 4H), 1.39-1.34 (m, 12H), 0.96-0.91 (m, 6H). **^{13}C NMR** (150 MHz, $C_2D_2Cl_4$): δ/ppm = 163.7, 141.2, 138.4, 134.5, 134.2, 132.1, 130.2, 126.5, 123.4, 120.2, 116.7, 116.5, 116.3, 112.9, 100.3, 99.4, 90.0, 35.7, 31.5, 30.8, 29.6, 29.2, 28.3, 22.6, 14.2. **HRMS** (MALDI-TOF, positive mode, DCTB in $CHCl_3$): *m*/*z* calculated $C_{96}H_{94}Cl_4N_2O_4Pt_4S_4$ $[M]^+$: 2386.3441, found: 2386.3437. **M.p.**: >300 °C. **R_f**: 0.44 using CH_2Cl_2/MeOH = 20:1 as eluent.

5T-PBI

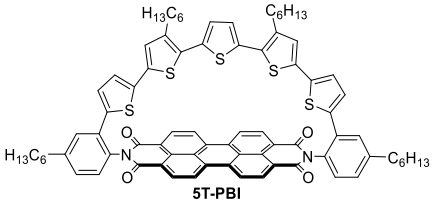

5T-PBI

To a stirred solution of **74** (31.0 mg, 20.0 µmol, 1.00 eq.) in degassed toluene (40 mL) was added dropwise the stannylated oligothiophene **76** (21.9 mg, 37.8 µmol, 1.10 eq.) in degassed toluene (1.0 mL) *via* a syringe pump over 15 h and the reaction mixture was stirred overnight at 75 °C. The solvent was removed *in vacuo* and the crude residue was washed with *n*-hexane. The crude product was redissolved in degassed CH_2Cl_2 (40 mL) and 1,1'-bis(diphenylphosphino)ferrocene (24.4 mg, 75.5 µmol, 2.20 eq.) was added. The solution was stirred for 6 h at room temperature. The solvent was removed *in vacuo* and the residue was dissolved in degassed *m*-xylene (40 mL) and stirred overnight at 120 °C. The solvent was removed under reduced pressure and the crude product was purified *via* flash column chromatography (CH_2Cl_2/cyclohexane = 1:1 to 1:0) and gel permeation chromatography ($CHCl_3$) to give the desired compound. **Yield**: 7.71 mg, 5.99 µmol, 30%, red orange solid. **^{1}H NMR** (600 MHz, CD_2Cl_2): δ/ppm = 8.70 (s, 8H), 7.79 (d, ^4J = 1.8 Hz, 2H), 7.45 (d, ^3J = 4.0 Hz, 2H), 7.36 (dd, ^3J = 8.0 Hz, ^4J = 1.8 Hz, 2H), 7.30 (d, ^3J = 8.0 Hz, 2H), 7.19 (d, ^3J = 4.0 Hz, 2H), 7.03 (s, 2H), 6.88 (s, 2H), 2.80 (t, ^3J = 7.7 Hz, 4H), 2.58 (t, ^3J = 7.9 Hz, 4H), 1.79 (quin, ^3J = 7.6 Hz, 4H), 1.35-1.42 (m, 8H), 1.22-1.31 (m, 20H), 0.94 (t, ^3J = 7.0 Hz, 6H), 0.83 (t, ^3J = 7.0 Hz 6H). **^{13}C NMR** (150 MHz, CD_2Cl_2): δ/ppm = 164.2, 145.0, 141.5, 138.1, 137.8, 135.7, 135.5, 135.1, 132.2, 132.0, 130.7, 130.1, 129.5, 129.3, 129.2, 128.6, 127.7, 127.0, 126.9, 126.8, 124.1, 123.8, 123.6, 36.2, 32.2, 32.0, 31.7, 30.7, 29.6, 29.5, 23.1, 22.9, 14.3, 14.2. **HRMS** (MALDI-TOF, positive mode, DCTB in $CHCl_3$): *m*/*z* calculated $C_{80}H_{74}N_2O_4S_5$ $[M]^+$: 1286.4252, found: 1286.4247. **UV/Vis** λ_{max} (ε_{max}): CH_2Cl_2: 531 nm (64.8 × 10^3 L mol^{-1} cm^{-1}). **Fluorescence** λ_{max} (λ_{ex}): Cyclohexane: 528 nm (480 nm). **PLQY**: Φ_{fl} = <0.1%. **R$_f$**: 0.32 using CH_2Cl_2 as eluent.

(5T)$_2$-PBI

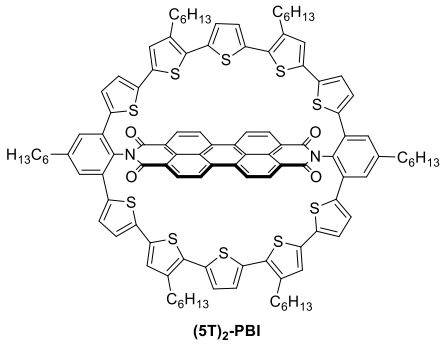

(5T)$_2$-PBI

To a stirred solution of **75** (44.4 mg, 18.5 µmol, 1.00 eq.) in degassed toluene (25 mL) was added dropwise the stannylated oligothiophene **76** (40.7 mg, 40.9 µmol, 2.20 eq.) in degassed toluene (1.0 mL) *via* a syringe pump over 15 h and the reaction mixture was stirred overnight at 75 °C. The solvent was removed *in vacuo* and the crude residue was washed with *n*-hexane. The crude product was redissolved in degassed CH_2Cl_2 (25 mL) and 1,1'-bis(diphenylphosphino)ferrocene (45.3 mg, 81.7 µmol, 4.40 eq.) was added. The solution was stirred for 6 h at room temperature. The solvent was removed *in vacuo* and the residue was dissolved in degassed *m*-xylene (25 mL) and stirred overnight at 120 °C. The solvent was removed under reduced pressure and the crude product was purified *via* flash column chromatography (cyclohexane / CH_2Cl_2 = 1:0 to 1:1) and gel permeation chromatography ($CHCl_3$) to give the desired compound. **Yield**: 1.26 mg, 676 nmol, 4%, red orange solid. **^{1}H NMR** (400 MHz, CD_2Cl_2): δ/ppm = 8.84 (d, ^3J = 8.4 Hz, 4H), 8.74 (d, ^3J = 7.9 Hz, 4H), 7.73 (s, 4H), 7.43 (d, ^3J = 3.9 Hz, 4H), 7.20 (d, ^3J = 3.9 Hz, 4H), 7.04 (s, 4H), 6.90 (s, 4H), 2.85 (t, ^3J = 7.8 Hz, 4H), 2.60 (t, ^3J = 7.6 Hz, 8H), 1.84 (quin, ^3J = 7.3 Hz, 4H), 1.50-1.27 (m, 44H), 0.95 (t, ^3J = 7.1 Hz, 6H), 0.88 (t, ^3J = 6.7 Hz, 12H). **^{13}C NMR** (150 MHz, CD_2Cl_2): δ/ppm = 164.6, 145.1, 141.3, 138.3, 138.1, 135.9, 135.7, 134.9, 134.0, 132.3, 130.3, 129.7, 129.2, 128.9, 127.2, 127.1, 126.5, 125.8, 124.5, 123.8, 123.7, 36.2, 32.2, 32.0, 31.6, 30.7, 30.1, 29.7, 29.5, 23.1, 23.0, 14.3, 14.2. **HRMS** (MALDI-TOF, positive mode, DCTB in $CHCl_3$): *m*/*z* calculated for $C_{112}H_{106}N_2O_4S_{10}$ $[M+H]^+$: 1862.5360, found: 1862.5354. **UV/Vis** λ_{max} (ε_{max}): CH_2Cl_2: 380 nm (93.9×10^3 L mol^{-1} cm^{-1}). **Fluorescence** λ_{max} (λ_{ex}): Cyclohexane: 528 nm (480 nm). **PLQY**: Φ_{fl} = <0.1% **R$_f$**: 0.81 using CH_2Cl_2/cyclohexane = 2:1 as eluent.

^{1}H NMR Spectra Comparison

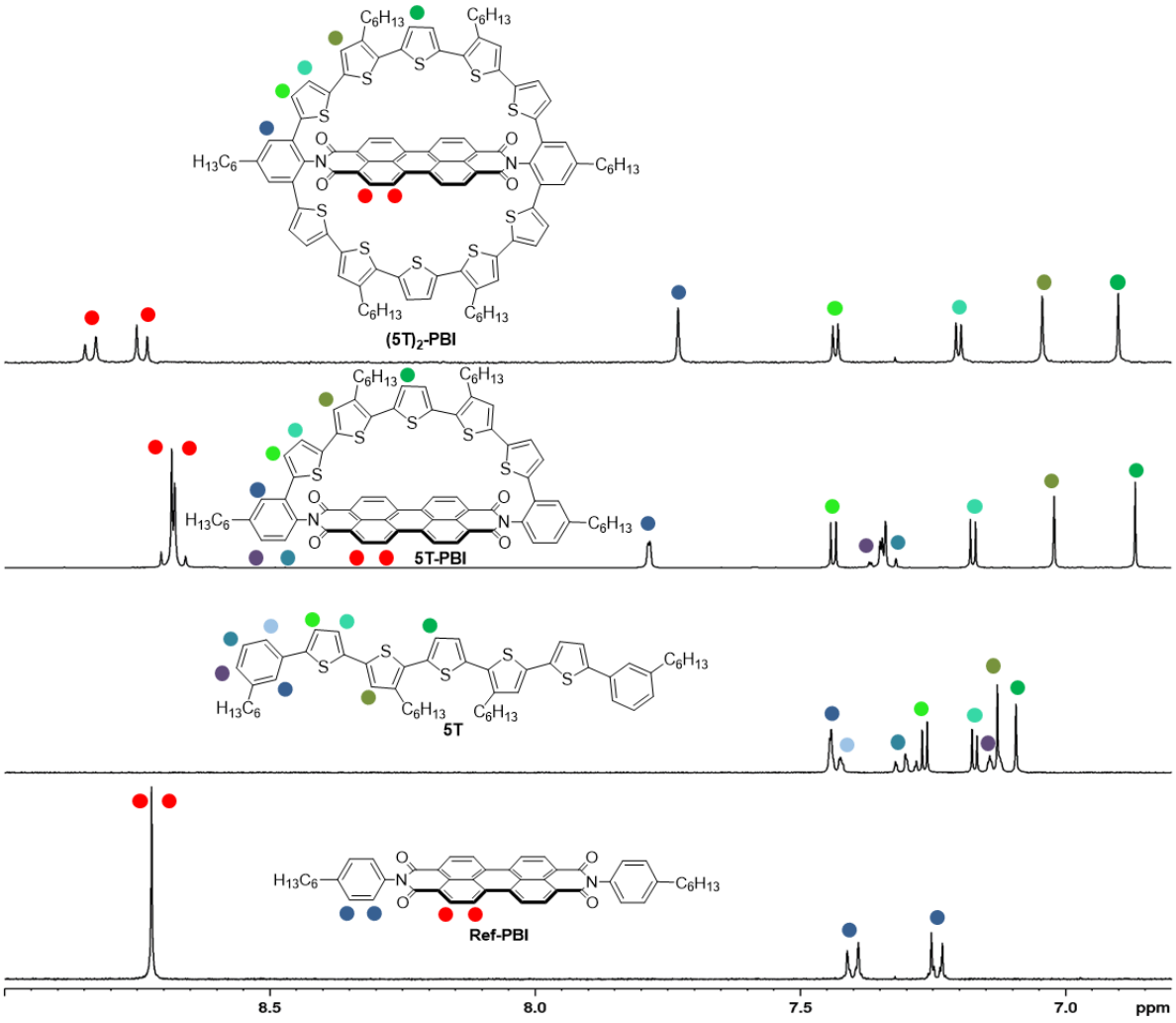

Figure 49. Aromatic region of the ^{1}H NMR spectra (400 MHz) of **Ref-PBI**, **5T**[235], **5T-PBI** and **(5T)$_2$-PBI** (from bottom to top) in CD_2Cl_2 at 298 K.

Single Crystal X-ray Analysis

Table 5. Crystal data and structure refinement for **(5T)$_2$-PBI**

CCDC Number	2102595	
Empirical formula	$C_{120.64}H_{113.21}Cl_{1.44}N_2O_4S_{10}$	
Formula weight	2026.55 g·mol^{-1}	
Temperature	100(2) K	
Wavelength	0.61992 Å	
Crystal system	Triclinic	
Space group	P-1	
Unit cell dimensions	a = 15.385(10) Å	α = 74.973(5)°
	b = 17.342(3) Å	β = 89.82(2)°
	c = 31.216(5) Å	γ = 85.158(16)°
Volume	8014(5) Å^3	
Z	3	
Density (calculated)	1.260 mg/m^3	
Absorption coefficient	0.203 mm^{-1}	
F(000)	3202.4	
Crystal size	0.100 × 0.100 × 0.100 mm^3	
Theta range for data collection	0.589 to 27.653°.	
Index ranges	$22 \leq h \leq 22$, $25 \leq k \leq 24$, $45 \leq l \leq 46$	
Reflections collected	264918	
Independent reflections	43791 [R_{int} = 0.0914]	
Completeness to theta = 21.836°	98.8%	
Absorption correction	None	
Refinement method	Full-matrix least-squares on F^2	
Data / restraints / parameters	43791 / 4155 / 2852	
Goodness-of-fit on F^2	1.109	
Final R indices [I > 2sigma(I)]	R_1 = 0.0848, wR_2 = 0.2698	
R indices (all data)	R_1 = 0.1117, wR_2 = 0.3036	
Extinction coefficient	n/a	
Largest diff. peak and hole	0.624 and −0.664 e·Å^{-3}	

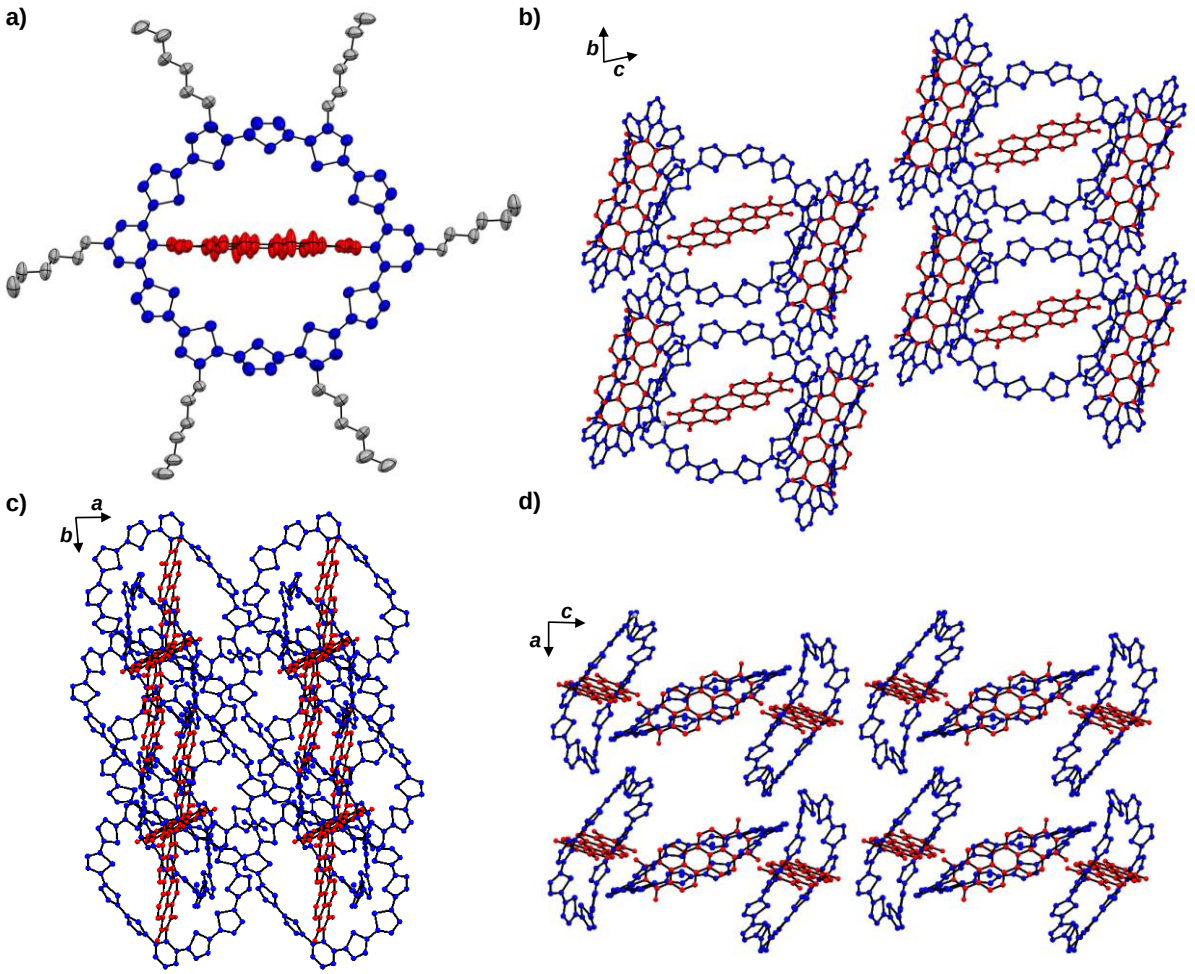

Figure 50. a) Front view of a single **(5T)$_2$-PBI** centrosymmetric molecule A (ORTEP drawing in 50% probability for thermal ellipsoids). PBI chromophore is coloured in red, macrocycle in blue and solubilizing alkyl chains in grey. Crystal packing seen approximately along the *a*-, *c*-, and *b*-axes for b), c) and d), respectively. Heavily disordered aliphatic chains as well as solvent molecules were omitted for clarity.

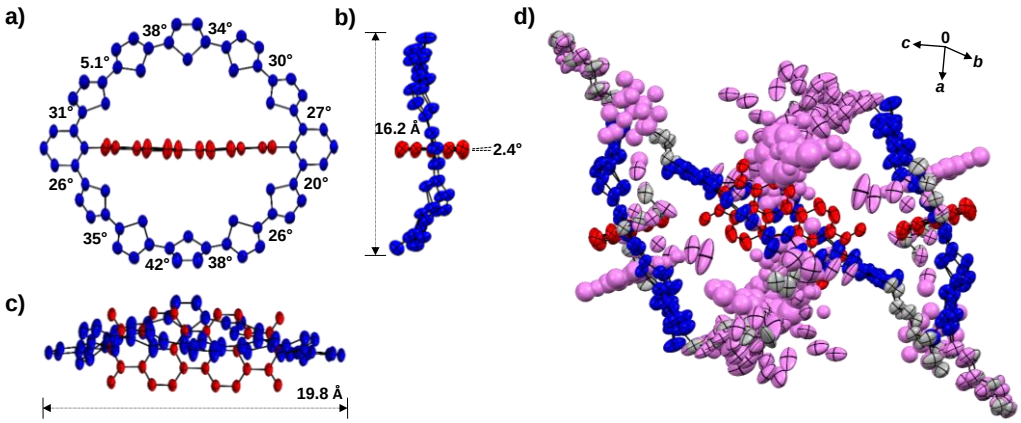

Figure 51. a) Front, b) side and c) top view onto the unsymmetric molecule B of **(5T)$_2$-PBI**. Heavily disordered aliphatic chains as well as solvent molecules were omitted for clarity. d) Unit cell including all structural disorder (violet) and aliphatic chains (grey). The ellipsoids are set to 50% probability.

DFT Calculations

Rotational Barrier:

To estimate the rotational barrier (Figure 52) of the imide substituent of **8**, calculations were conducted only on one half-segment, namely the naphthalene imide part (Figure 52b). In order to estimate the energy cost of this rotation a dihedral angle scan of α in 0.5° intervals was performed (Figure 52a). Here, the change of the total energies ΔE depending on the torsion angle α is plotted. This angle α, which was modified during the scan, is highlighted in Figure 52c. The initial α of 90° between the phenyl substituent and the naphthalene monoimide core was readily reduced until complete rotation of the substituent. In the starting geometry (Figure 52c) the sulphur atom points away from the naphthalene imide core, whereas during the rotation this subunit undergoes a conformational change at α = 59° (Figure 52d) towards the core due to the repulsive hydrogen-core interaction. Further rotation up to –26° leads to an outer plane uplifting of the nitrogen atom (Figure 52e) and an almost perpendicular angle between the thiophene and the phenyl group. This geometry also resembles the structure with the highest total energy level during the entire rotation process and therefore the closest structure to the "real" transition state (TS). This geometry was the basis for the TS calculation of which the result is shown in Figure 52f. The energy difference between this TS geometry and the fully relaxed monoimide is 114 kJ mol^{-1} and can therefore be considered as the rotational barrier or the Gibbs free energy of activation $\Delta G^{\ddagger}$. To determine the half life time of the rotation event the reaction rate k_{rot} according to Eyring has to be determined first (Eq. 7)

$$k_{\mathrm{rot}} = \frac{k_{\mathrm{B}}T}{h} \cdot e^{-\frac{\Delta G^{\ddagger}}{RT}}. \qquad (7)$$

Here k_B is the Boltzmann constant, T the temperature R the universal gas constant and h the Planck constant. For T = 298.15 K (room temperature) and 348.15 K (macrocyclization reaction temperature) the resulting k_{rot} values are $6.60 \cdot 10^{-8}$ s^{-1} and $5.70 \cdot 10^{-5}$ s^{-1}, respectively.

The half life time $t_{1/2}$ (Eq. 8) can be calculated by the following equation:

$$t_{1/2} = \frac{\ln(2)}{4k_{\mathrm{rot}}}. \qquad (8)$$

The results of $t_{1/2}$ = 30 days at room temperature (25 °C) and around 51 min at 75 °C show the importance of elevated temperatures during the final macrocyclization reaction towards **5T-PBI**. [304]

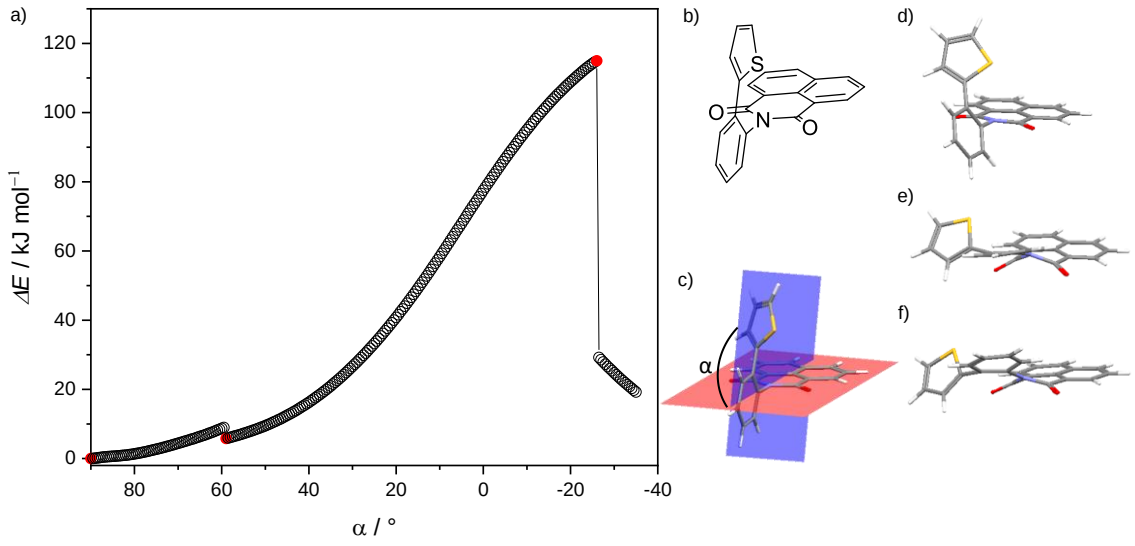

Figure 52. a) Plot of the change in total energy Δ*E* against the dihedral angle α. b) Chemical structure of the molecular fragment used for the calculations. c) Geometry optimized structure of the starting geometry for the rotational scan and the starting angle α incorporated by the planes of the naphthalene (red) and phenylene (blue) subunit. d) Geometry with α = 59 °e) Highest energy geometry with α = –26°. f) Geometry of the TS. All calculations were conducted with DFT at the B3LYP/6-31G(d) level of theory.

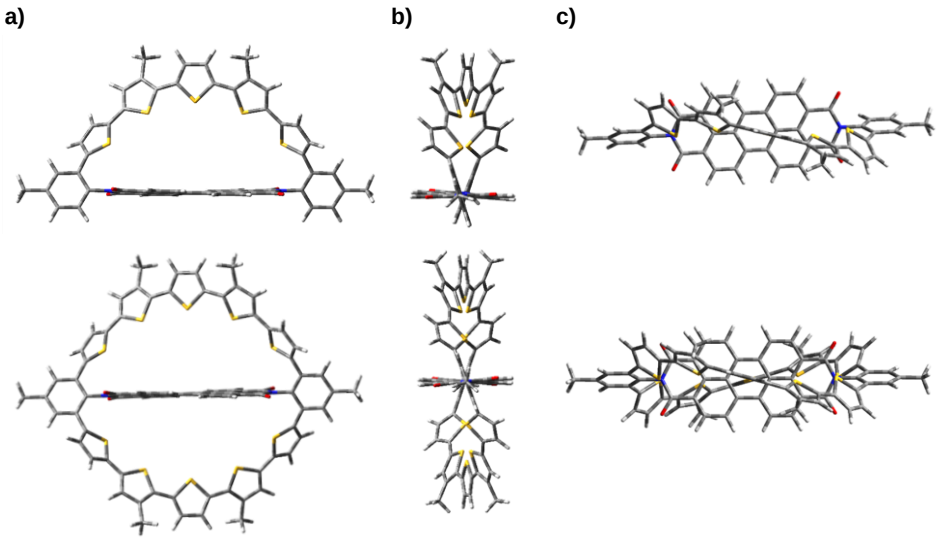

Figure 53. Side view (a), view along the *N*,*N*´-axis (b) and top view (c) onto the PBI π-surface of geometry optimized structures of **5T-PBI** and **(5T)$_2$-PBI** (from top to bottom). The quantum mechanics calculations were carried out on the level of B3LYP density functional with the 6-31G(d) basis set as implemented in Gaussian 16. Aliphatic chains were replaced by methyl groups. Color code: carbon = light grey, hydrogen = white, nitrogen = blue, oxygen = red, sulfur = yellow.

Strain energies:

The strain energies of the macrocycles **(5T)$_2$-PBI** and **5T-PBI** were calculated as follows: The connecting C-C bonds between two thiophene units of the bridges were removed virtually from the optimized geometries of **(5T)$_2$-PBI** and **5T-PBI** and the obtained radicals were saturated by thiophene capping molecules to retain the local environment of the two ends. Geometry optimization leads to the lowest energy conformation of the resulting structures and complete macrocyclic induced strain release of both subunits. Figure 54 shows the optimized geometries of these open macrocycles **11** and **12** as well as capping bithiophene **13**.

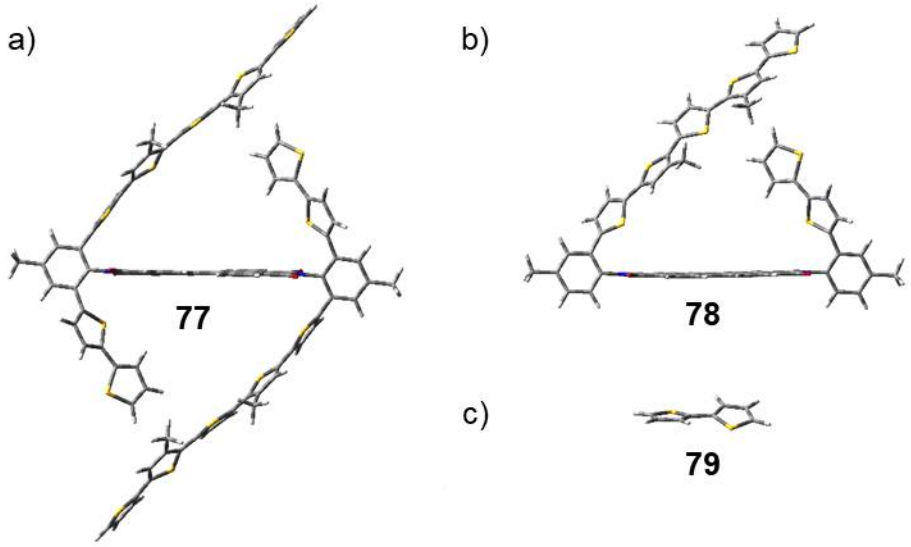

Figure 54. Front view of the optimized geometries of the non-cyclic structures **77** and **78** as well as bithiophene **79**. The quantum mechanics calculations were carried out on the level of B3LYP density functional with the 6-31G(d) basis set as implemented in Gaussian 16. Aliphatic chains were replaced by methyl groups. Color code: carbon = light grey, hydrogen = white, nitrogen = blue, oxygen = red, sulfur = yellow.

The strain energies of the respective macrocycles (E_{Strain}) were determined by comparing the lowest energy conformation of the respective macrocycles ($E_{\mathbf{5T\text{-}PBI}}$ or $E_{\mathbf{(5T)2\text{-}PBI}}$) to the homodesmic reaction product[305] of the linear structures **77** and **78** (E_{77} or E_{78}) and the bithiophene cap **79** (E_{79}):

$$E_{Strain,\ \mathbf{(5T)2\text{-}PBI}} = (E_{\mathbf{5T2\text{-}PBI}} + 2E_{79}) - E_{77} = 30.6\ \text{kJ mol}^{-1}. \quad (9)$$

$$E_{Strain,\ \mathbf{5T\text{-}PBI}} = (E_{\mathbf{5T\text{-}PBI}} + E_{79}) - E_{78} = 13.9\ \text{kJ mol}^{-1}. \quad (10)$$

Table 6. First excited state (S_1) energy predictions of **5T-PBI** and **(5T)$_2$-PBI** with TDDFT at the B3LYP/6-31G(d) level of theory (H = HOMO, L = LUMO).

Compound	**Excitation Energy** / eV	**Wavelength** / nm	**Osc. Strength**	**Contribution**
5T-PBI	1.18	1051	0.0000	H → L (100%)
(5T)$_2$-PBI	1.32	937	0.0001	H → L (100%)

Electrochemistry

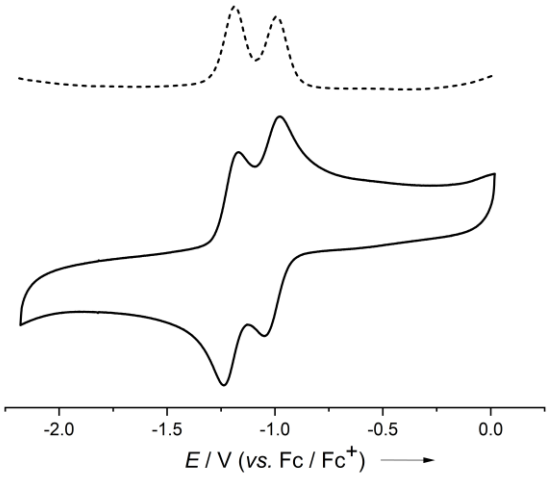

Figure 55. Cyclic voltammogram (solid line) initiated in the forward (positive-going) scan direction (marked by an arrow) at a scan rate of 100 mV s^{-1} and differential pulse voltammogram (dashed line) of **Ref-PBI** in CH_2Cl_2 with Bu_4NPF_6 at room temperature ($c_0 = 10^{-4}$ M).

In order to demonstrate the involvement of four electrons in the entire oxidation process of **(5T)$_2$-PBI** we decided to utilize the baseline (recorded prior to the actual measurement) corrected DPV data which was compared to those of **5T-PBI**. It is evident that for respective reduction of both macrocyclic PBI subunits two electrons are transferred. By comparing the PBI's DPV reduction to the oligothiophene's oxidation wave integrals the relative amount of transported charges can be assigned (Figure 56).

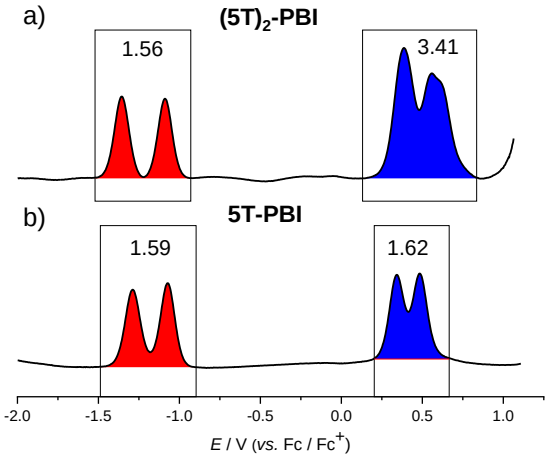

Figure 56. DPV measurements of a) **(5T)$_2$-PBI** and b) **5T-PBI** in CH_2Cl_2 solutions with Bu_4NPF_6 at room temperature (c_0 = 10^{-4} M). The wave integrals for PBI reduction and oligothiophene oxidation are highlighted in red and blue, respectively. The straight black lines mark the integration limits and the values above the waves represent the absolute integral in arbitrary units. The graphs are baseline corrected to ease the integration.

The ratio of both signals in reduction and oxidation determined by integration for **5T-PBI** is 1.62/1.59 = 1.02 ≈ 1 and for **(5T)$_2$-PBI** 3.41/1.56 = 2.19 ≈ 2, respectively. The ratios prove that approximately double the amount of charges was transferred in the oxidation process of **(5T)$_2$-PBI** in comparison to the reduction. For **5T-PBI** an equal amount of charges are involved in reduction and oxidation.

Molecular Orbital DFT Calculations

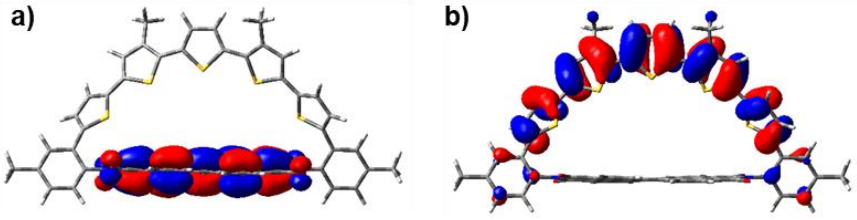

Figure 57. a) LUMO and b) HOMO of **5T-PBI** based on geometry optimized structures from DFT calculations. The quantum mechanics calculations were carried out on the level of B3LYP density functional with the 6-31G(d) basis set as implemented in Gaussian 16.

Spectroscopy in CH_2Cl_2

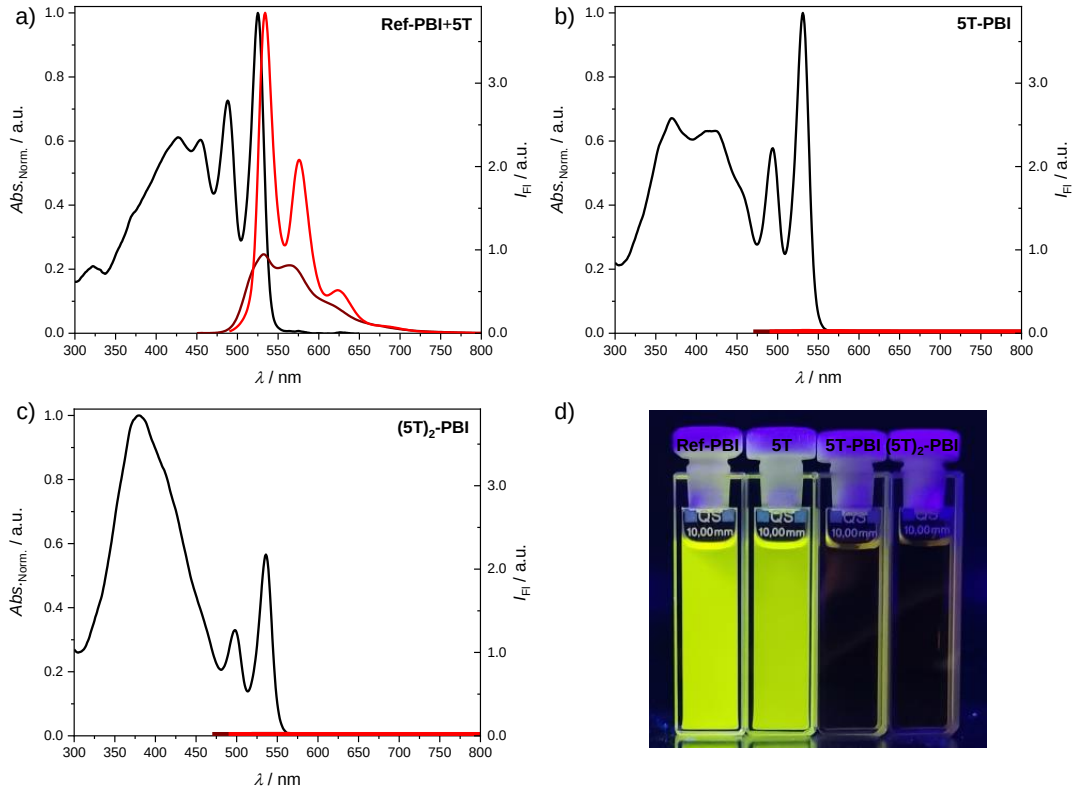

Figure 58. Normalized UV/Vis spectra (black lines) and emission spectra with the excitation wavelengths λ_{ex} = 400 nm (maroon lines) and λ_{ex} = 480 nm (red lines) of a) a 1:1 mixture of **Ref-PBI + 5T**, b) **5T-PBI** and c) **(5T)$_2$-PBI**. All UV/Vis and emission ($c_0 = 10^{-7}$ M) measurements were carried out in CH_2Cl_2 at room temperature. d) Photograph of **Ref-PBI**, **5T**[235], **5T-PBI** and **(5T)$_2$-PBI** (from left to right) in CH_2Cl_2 under 365 nm UV light irradiation.

Spectroscopy in Cyclohexane

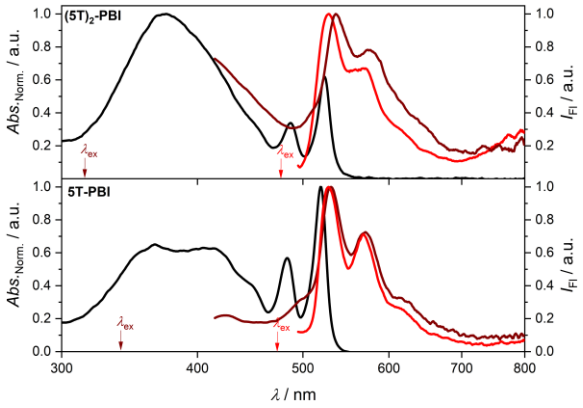

Figure 59. Normalized UV/Vis absorption (black solid) and emission (red: λ_{ex} = 480 nm, maroon: λ_{ex} = 340/310 nm) spectra of **5T-PBI** (bottom) and **(5T)$_2$-PBI** (top) in cyclohexane at room temperature ($c_0 = 10^{-7}$ M). The wavelengths for excitation to obtain the fluorescence spectra are highlighted by arrows.

Table 7. Spectroscopic properties of **5T-PBI** and **(5T)$_2$-PBI** in cyclohexane at room temperature.

	$\lambda_{abs,max}$ [a] / nm	$\lambda_{em,max}$ [a], [b] / nm	$\lambda_{em,max}$ [a], [c] / nm	$\Delta\tilde{\nu}_{Stokes}$ (PBI) [a] / cm^{-1}	Φ_{fl} [a],[d] / %
5T-PBI	519	531	528	329	<< 0.1
(5T)$_2$-PBI	374	536	528	145	<< 0.1

[a] $c_0 = 10^{-7}$ M. [b] λ_{ex} = 340/310 nm. [c] λ_{ex} = 480 nm [d] The fluorescence quantum yields of the PBI were measured relative to *N,N'*-bis(2,6-diisopropylphenyl)-1,6,7,12-tetraphenoxy-perylenebis(dicarboximide)[248] (96% in $CHCl_3$) as a reference at four different excitation wavelengths in the spectral region of the PBI absorption band.

Transient Absorption Spectra

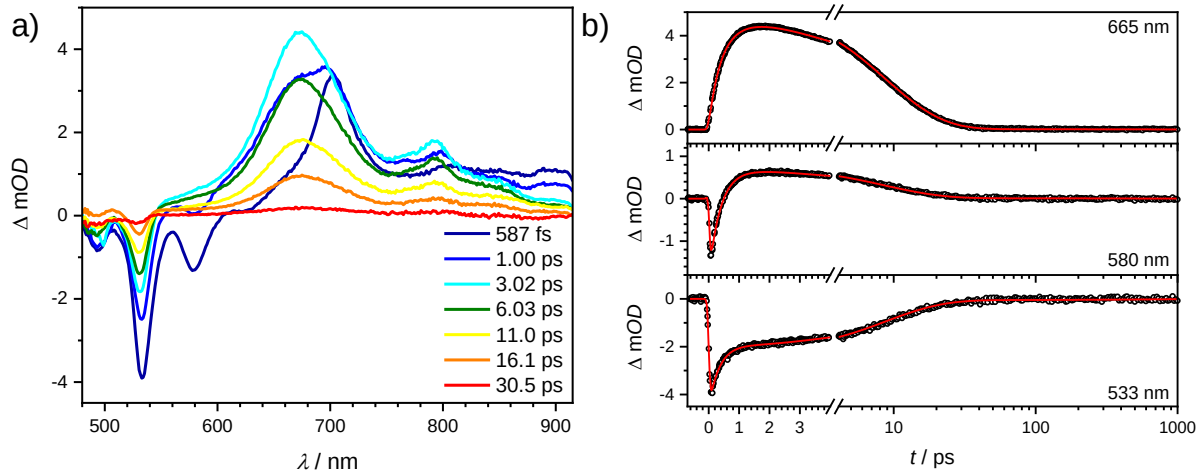

Figure 60. a) Transient absorption spectra of **5T-PBI** in CH_2Cl_2 after excitation at 530 nm and b) time scans and fit (red line) at selected wavelengths.

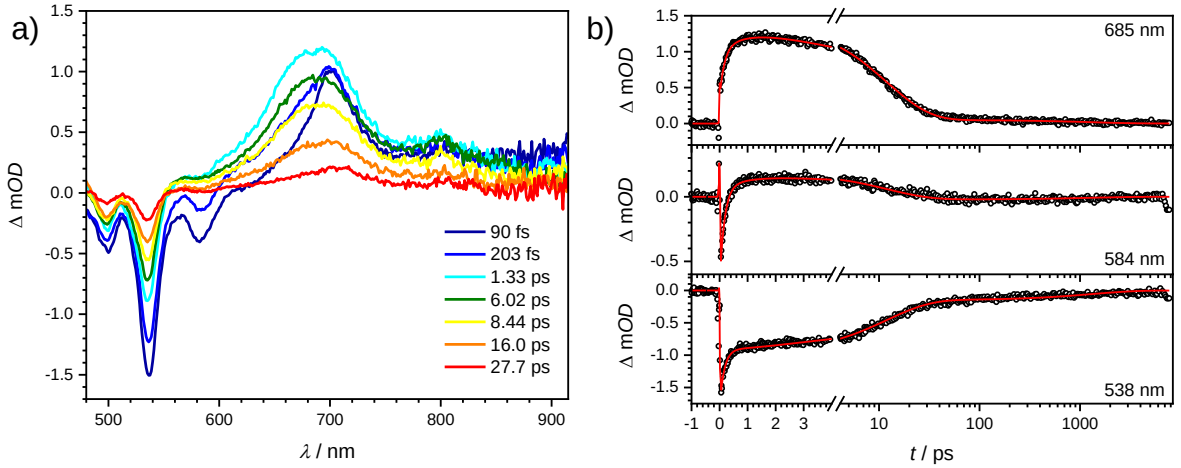

Figure 61. a) Transient absorption spectra of **(5T)$_2$-PBI** in CH_2Cl_2 after excitation at 530 nm and b) time scans and fit (red line) at selected wavelengths.

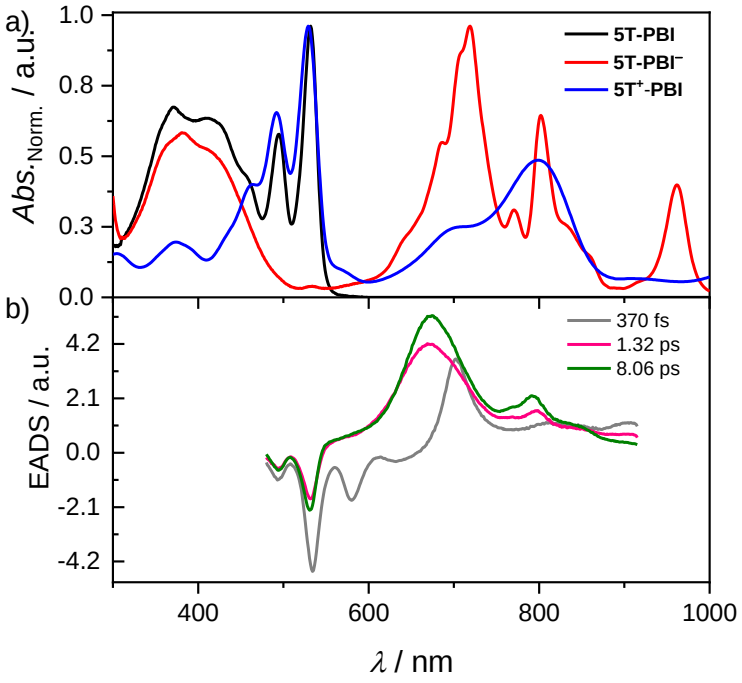

Figure 62. a) Normalized UV/Vis/NIR absorption spectra of **5T-PBI** (black line) upon electrochemical reduction to **5T-PBI**$^{\bullet-}$ (red line) and electrochemical oxidation to **5T**$^{\bullet+}$**-PBI** (blue line) in CH_2Cl_2 solutions with Bu_4NPF_6 at room temperature ($c_0 = 10^{-4}$ M). b) Evolution associated difference spectra (EADS) and lifetimes from a global fit analysis of the transient spectra of **5T-PBI** obtained by excitation at 530 nm in CH_2Cl_2 ($c_0 = 10^{-4}$ M) at room temperature.

NMR Spectra

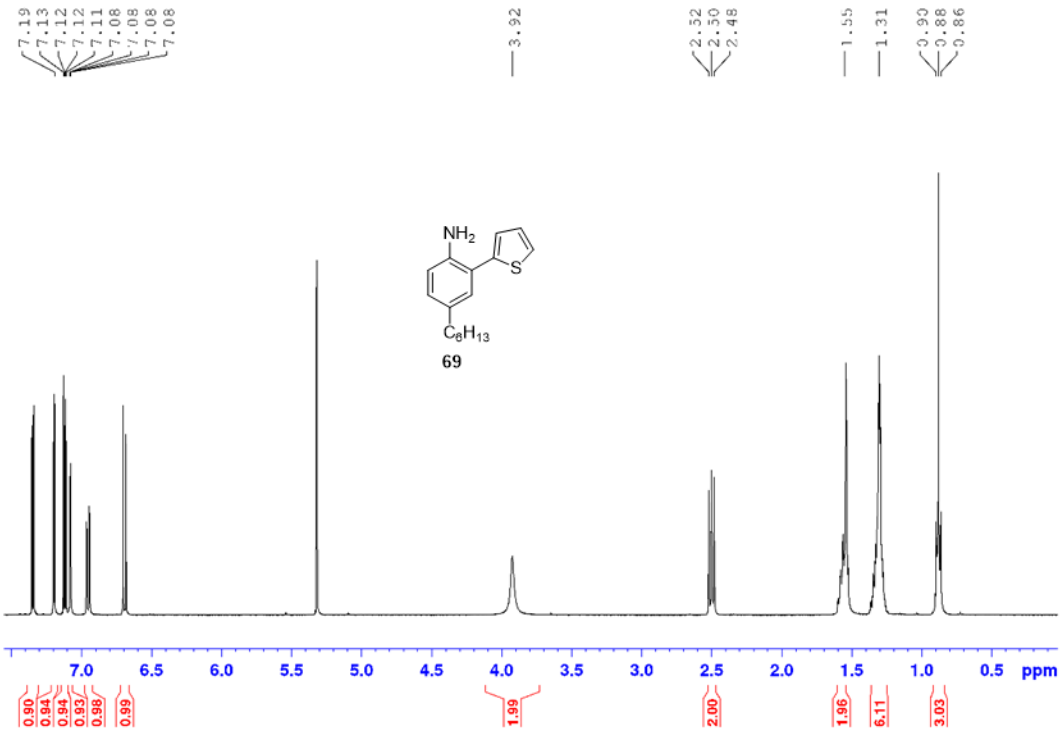

Figure 63. ^{1}H NMR spectrum (400 MHz) of **69** in CD_2Cl_2 at 298 K.

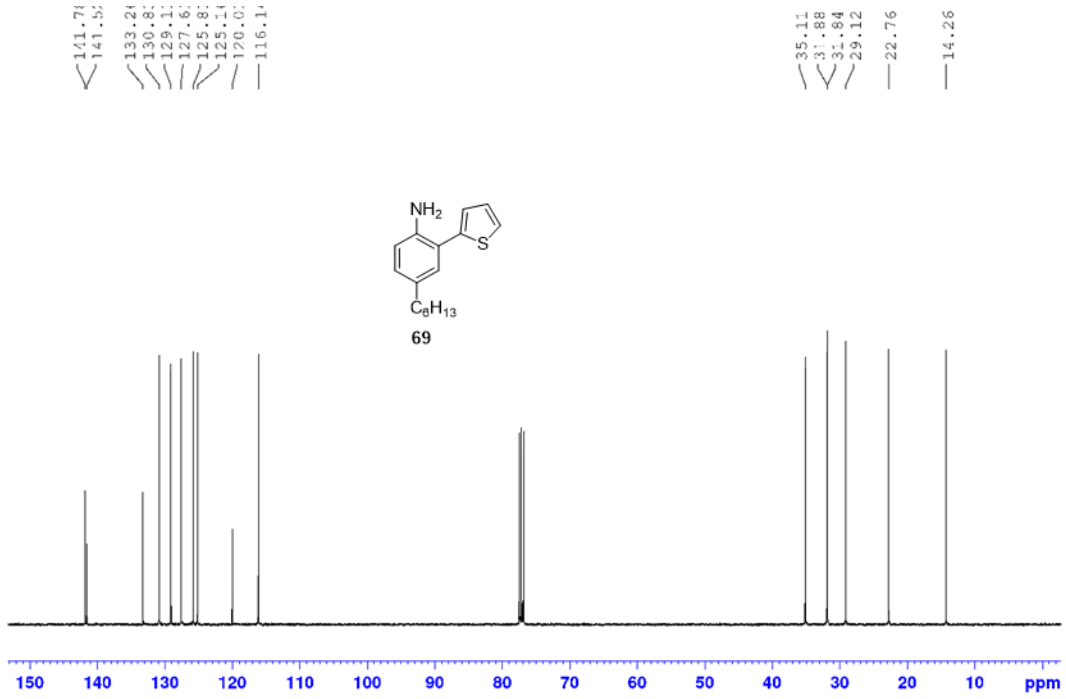

Figure 64. ^{13}C NMR spectrum (101 MHz) of **69** in $CDCl_3$ at 298 K.

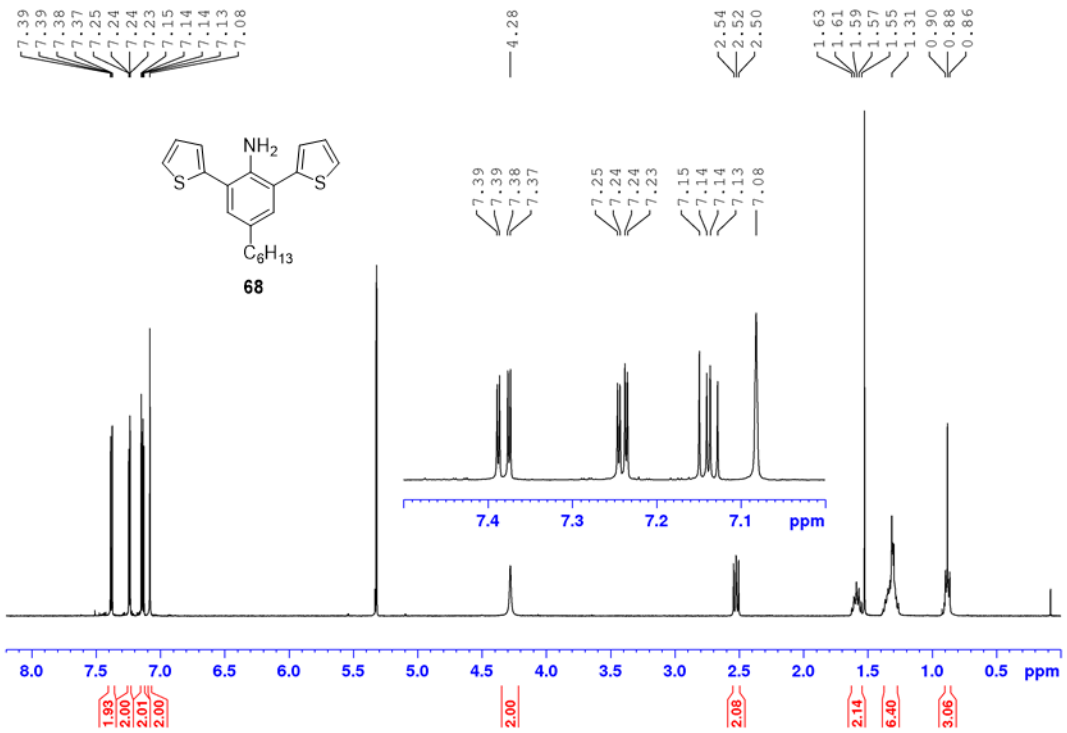

Figure 65. ^{1}H NMR spectrum (400 MHz) of **68** in CD_2Cl_2 at 298 K.

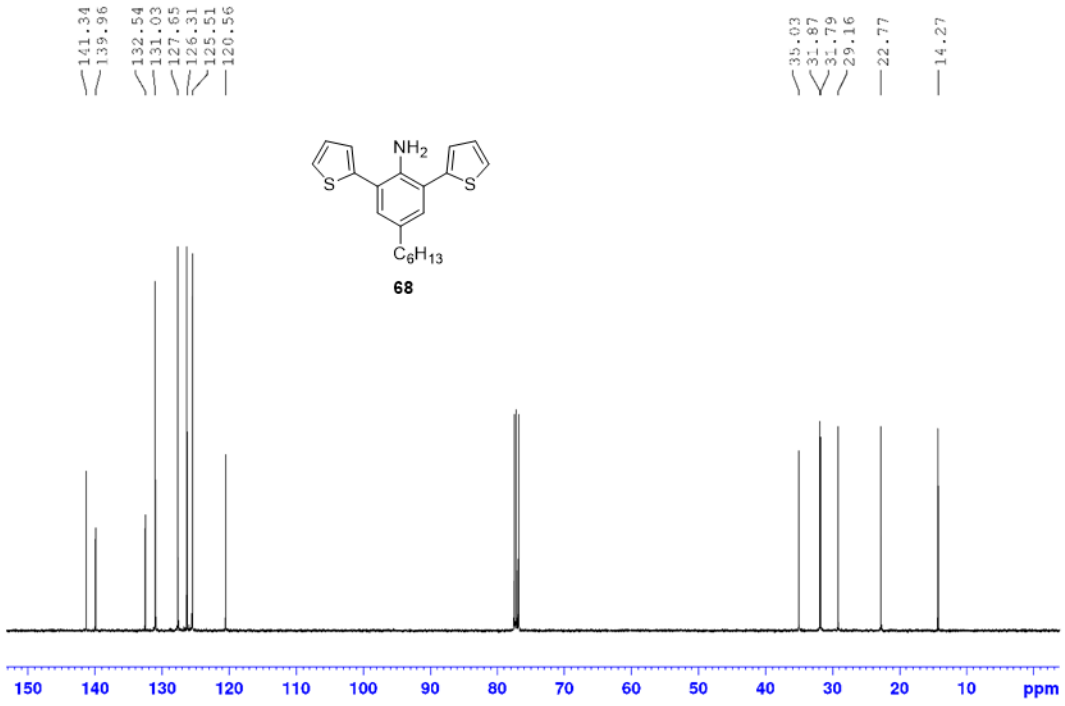

Figure 66. ^{13}C NMR spectrum (101 MHz) of **68** in $CDCl_3$ at 298 K.

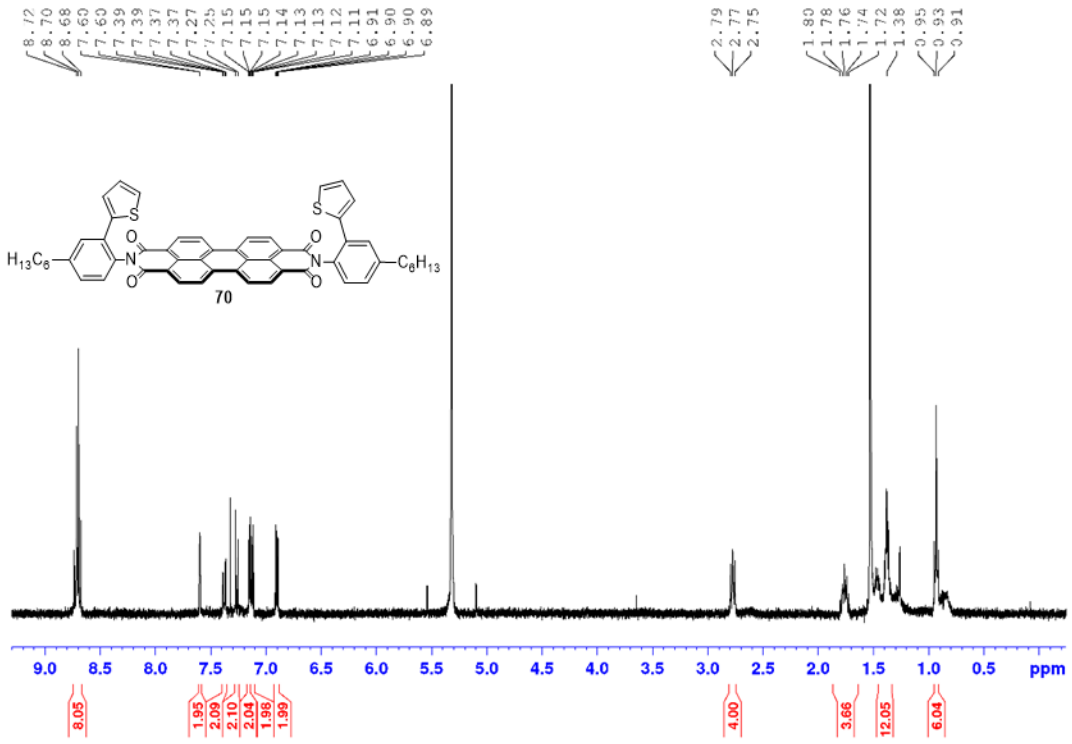

Figure 67. ^{1}H NMR spectrum (400 MHz) of **70** in CD_2Cl_2 at 298 K.

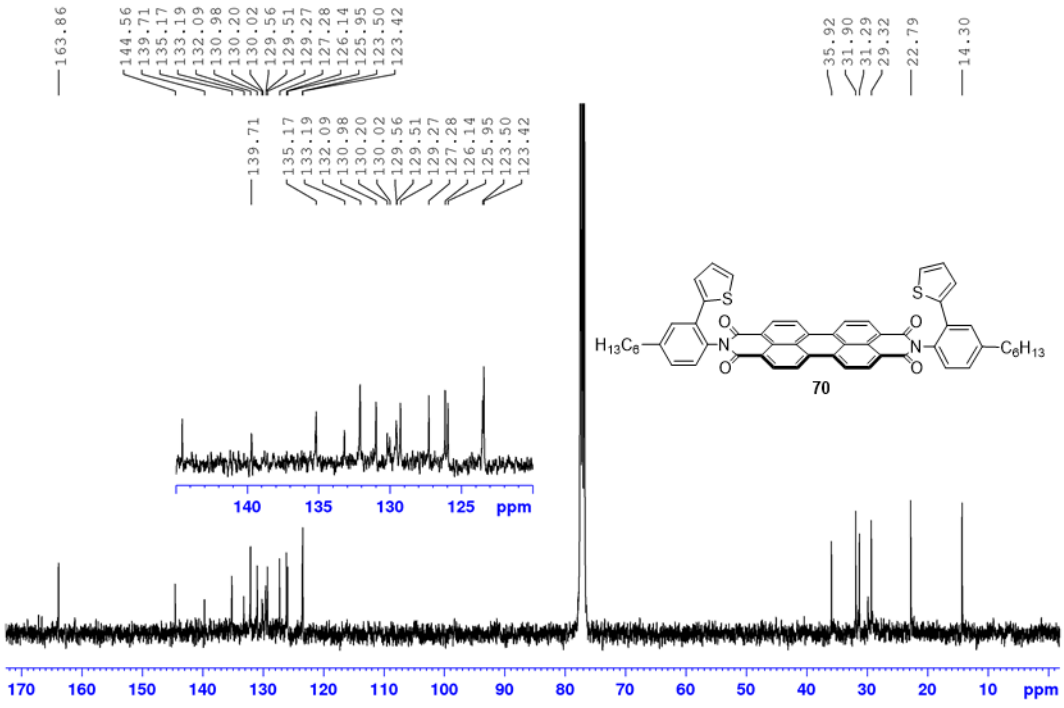

Figure 68. ^{13}C NMR spectrum (101 MHz) of **70** in $CDCl_3$ at 298 K.

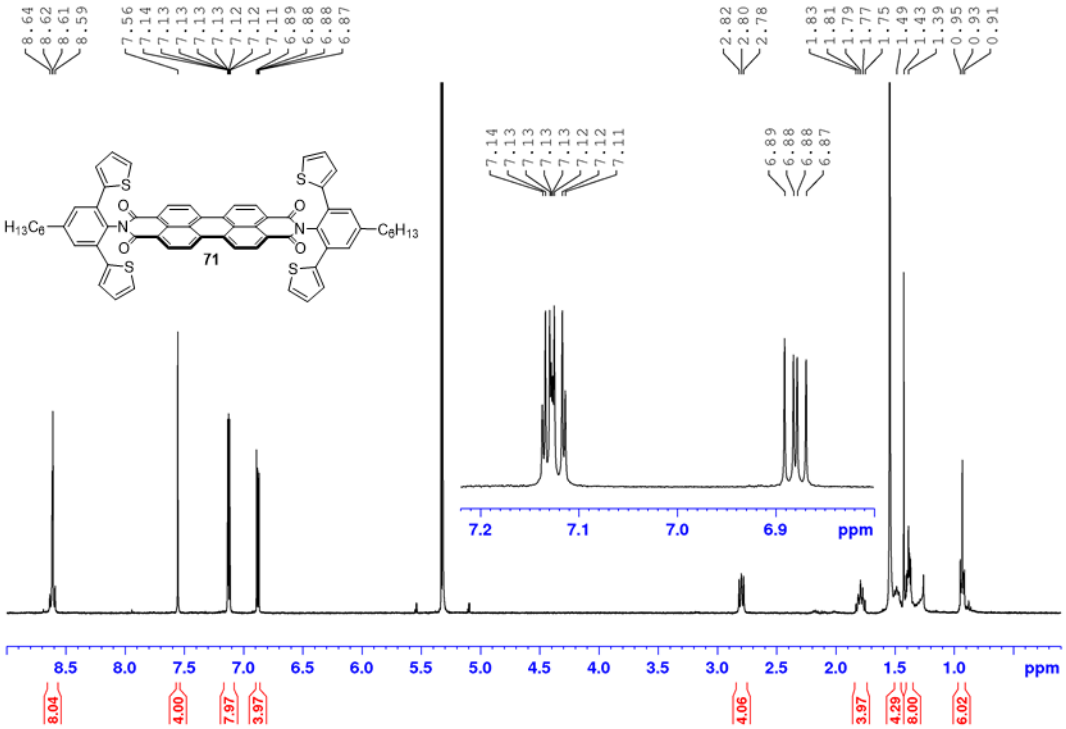

Figure 69. ^{1}H NMR spectrum (400 MHz) of **71** in CD_2Cl_2 at 298 K.

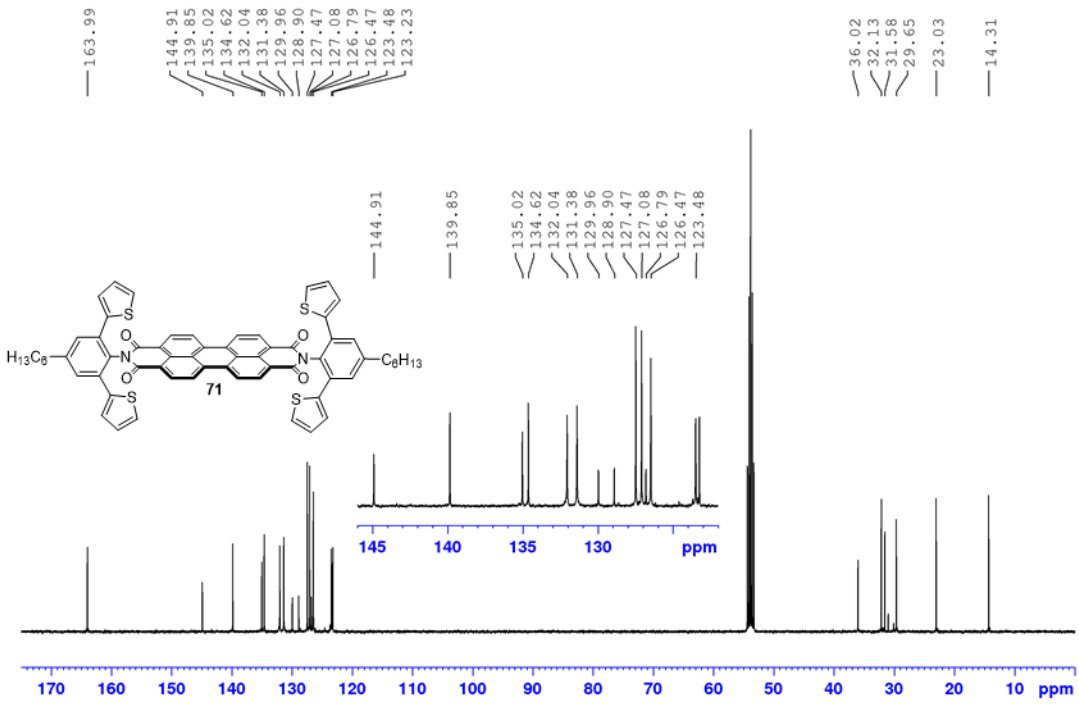

Figure 70. ^{13}C NMR spectrum (101 MHz) of **71** in CD_2Cl_2 at 298 K.

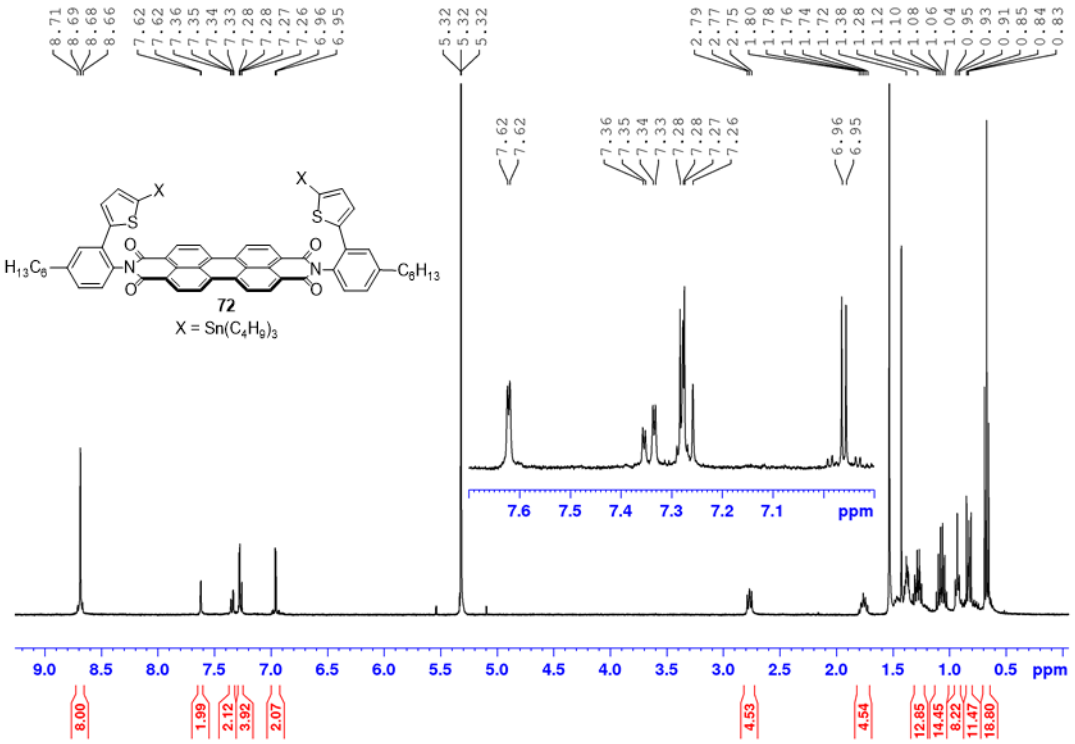

Figure 71. ^{1}H NMR spectrum (400 MHz) of **72** in CD_2Cl_2 at 298 K.

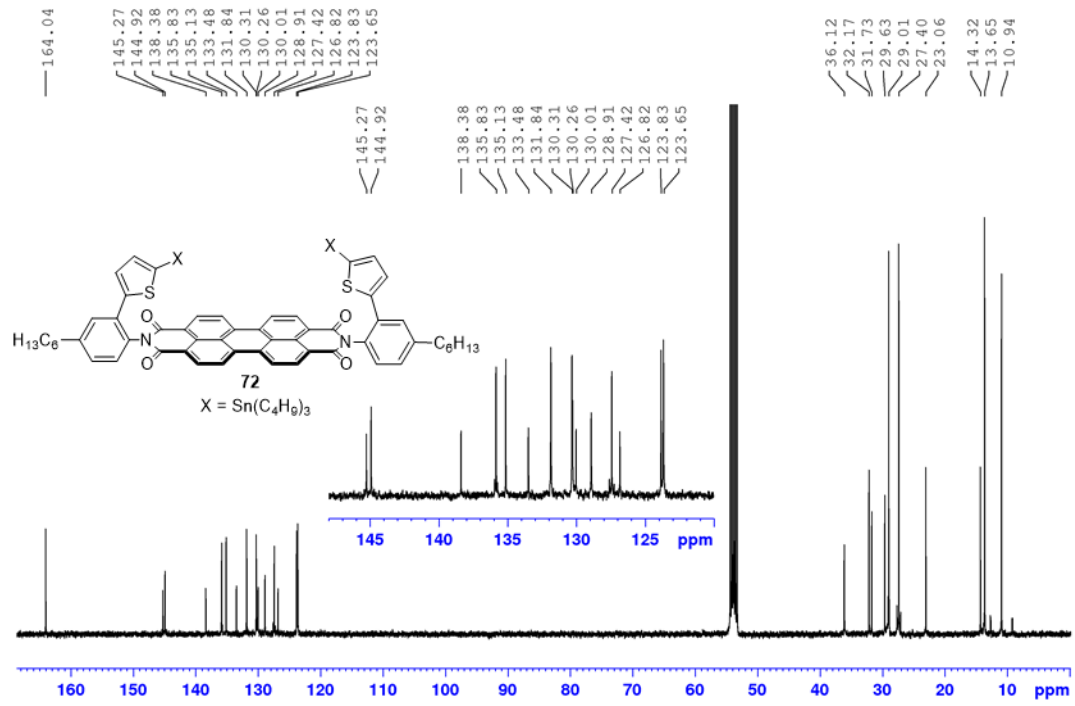

Figure 72. ^{13}C NMR spectrum (101 MHz) of **72** in CD_2Cl_2 at 298 K.

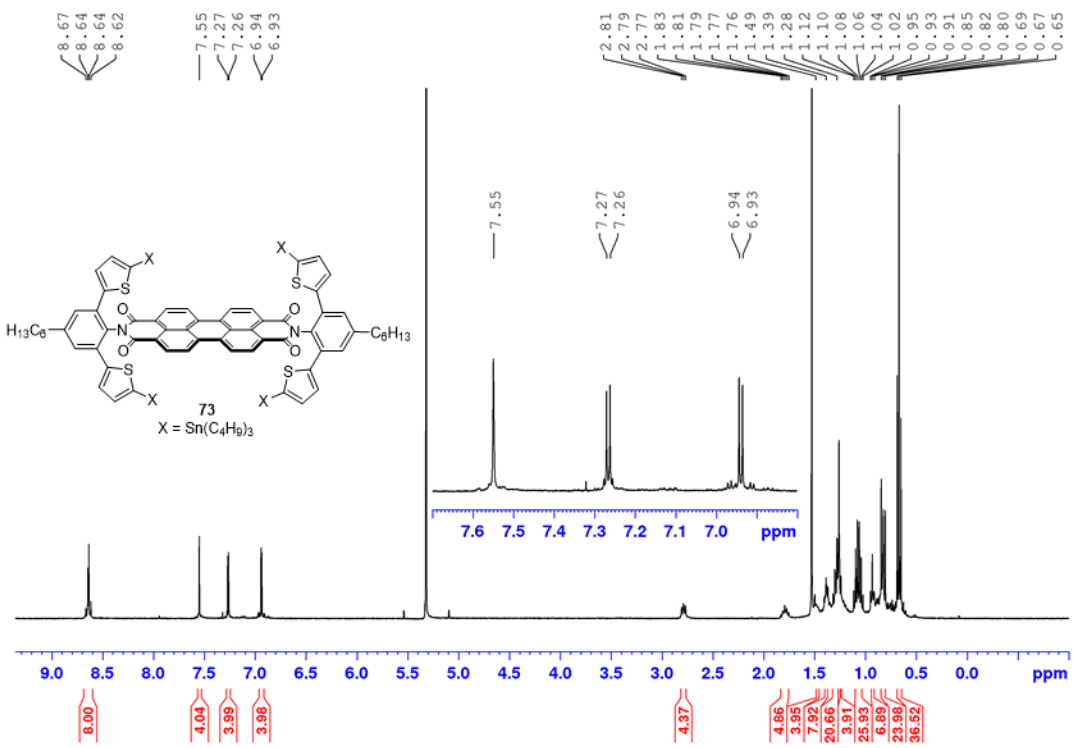

Figure 73. ^{1}H NMR spectrum (400 MHz) of **73** in CD_2Cl_2 at 298 K.

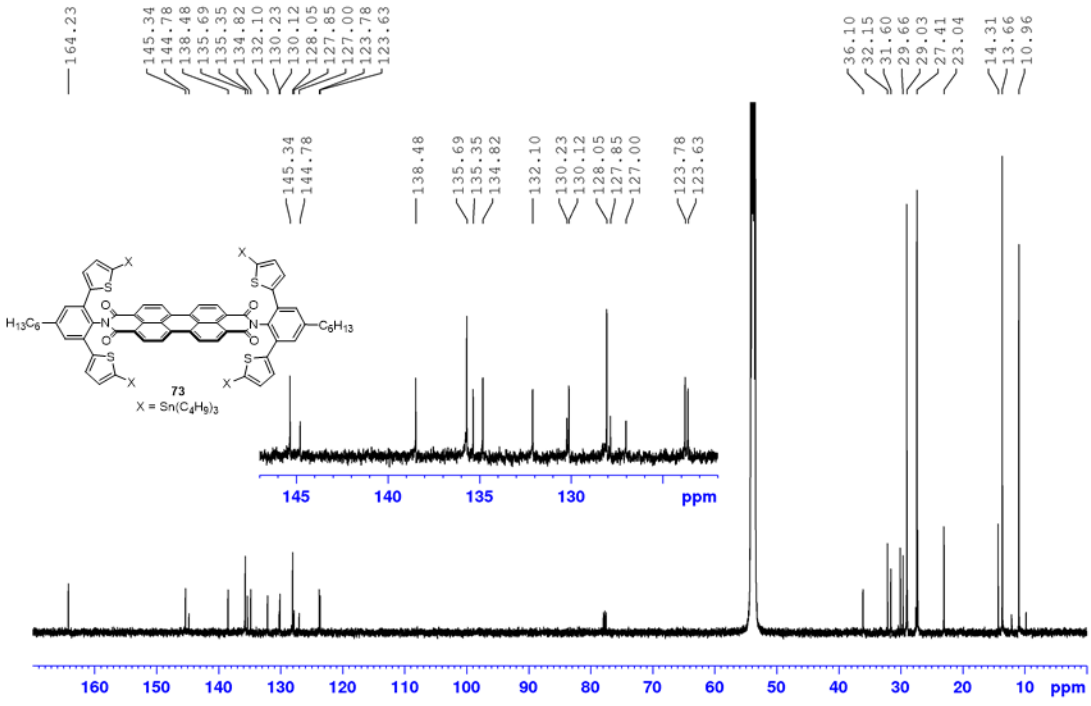

Figure 74. ^{13}C NMR spectrum (150 MHz) of **73** in CD_2Cl_2 at 298 K.

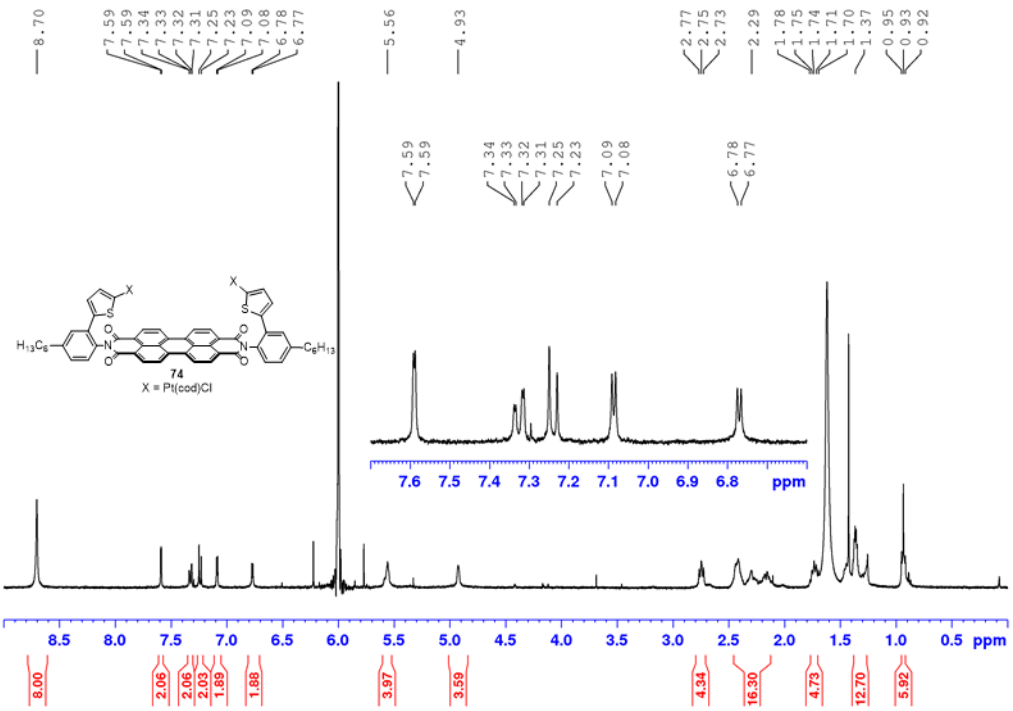

Figure 75. ^{1}H NMR spectrum (400 MHz) of **74** in $C_2D_2Cl_4$ at 298 K.

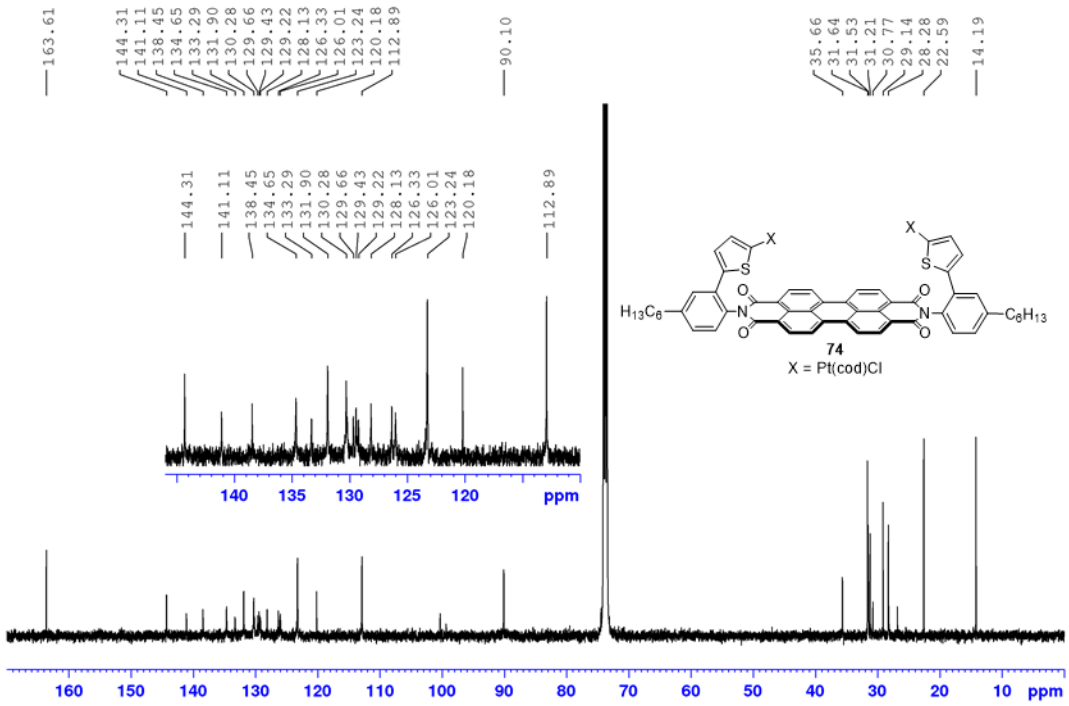

Figure 76. ^{13}H NMR spectrum (101 MHz) of **74** in $C_2D_2Cl_4$ at 298 K.

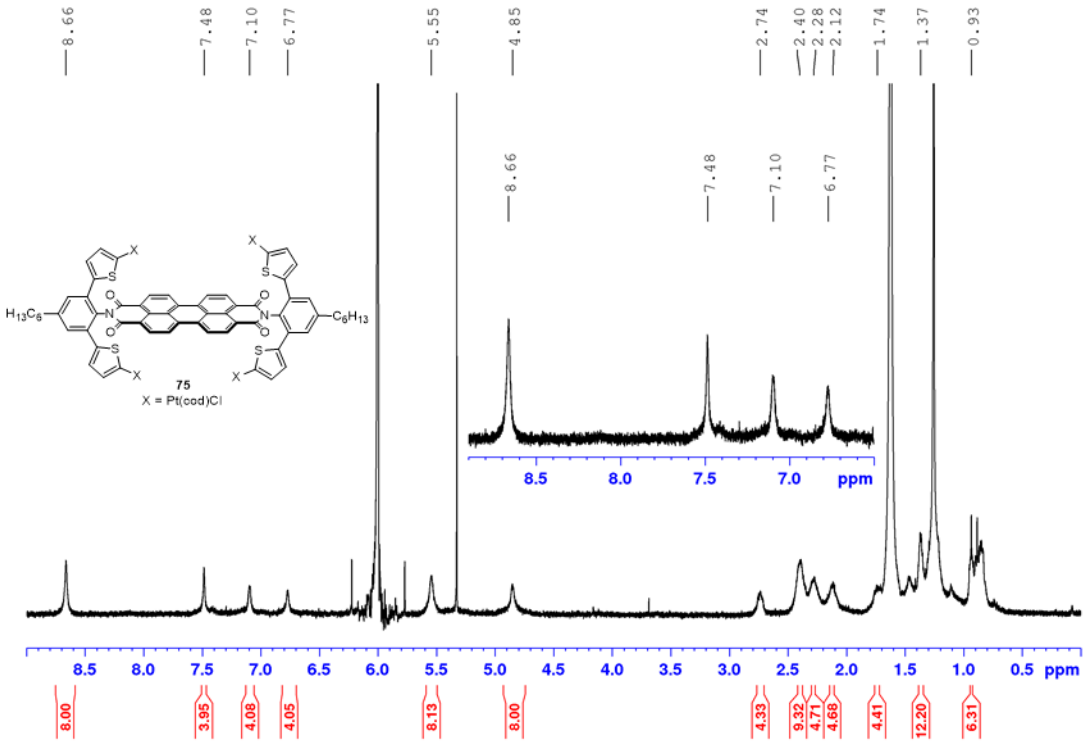

Figure 77. ^{1}H NMR spectrum (400 MHz) of **75** in $C_2D_2Cl_4$ at 298 K.

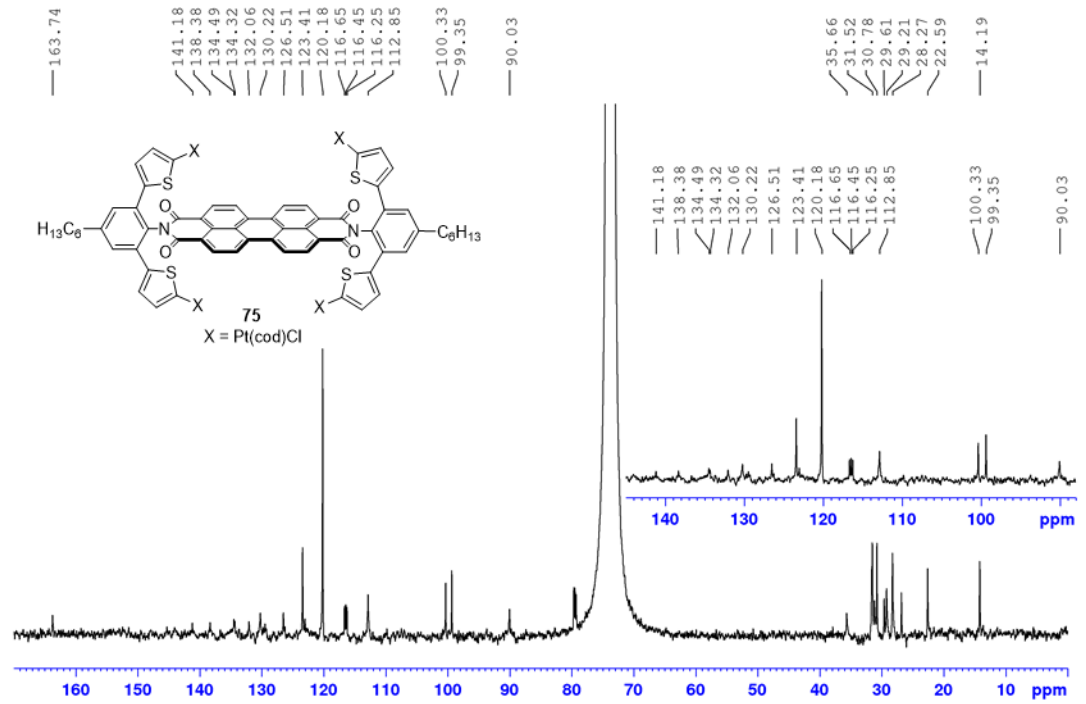

Figure 78. ^{13}C NMR spectrum (150 MHz) of **75** in $C_2D_2Cl_4$ at 298 K. Residual signals of $CHCl_3$ (79.5 ppm), H-grease (31.1 pm) and cyclohexane (26.8 ppm).

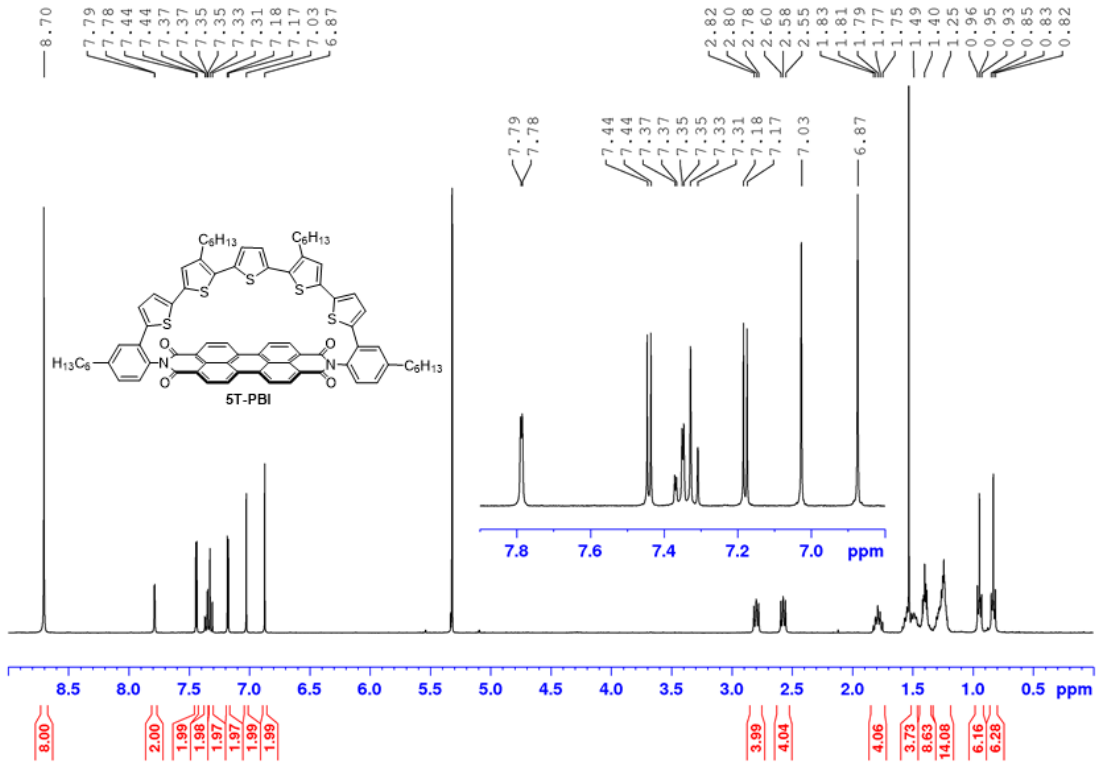

Figure 79. ^{1}H NMR spectrum (600 MHz) of **5T-PBI** in CD_2Cl_2 at 298 K.

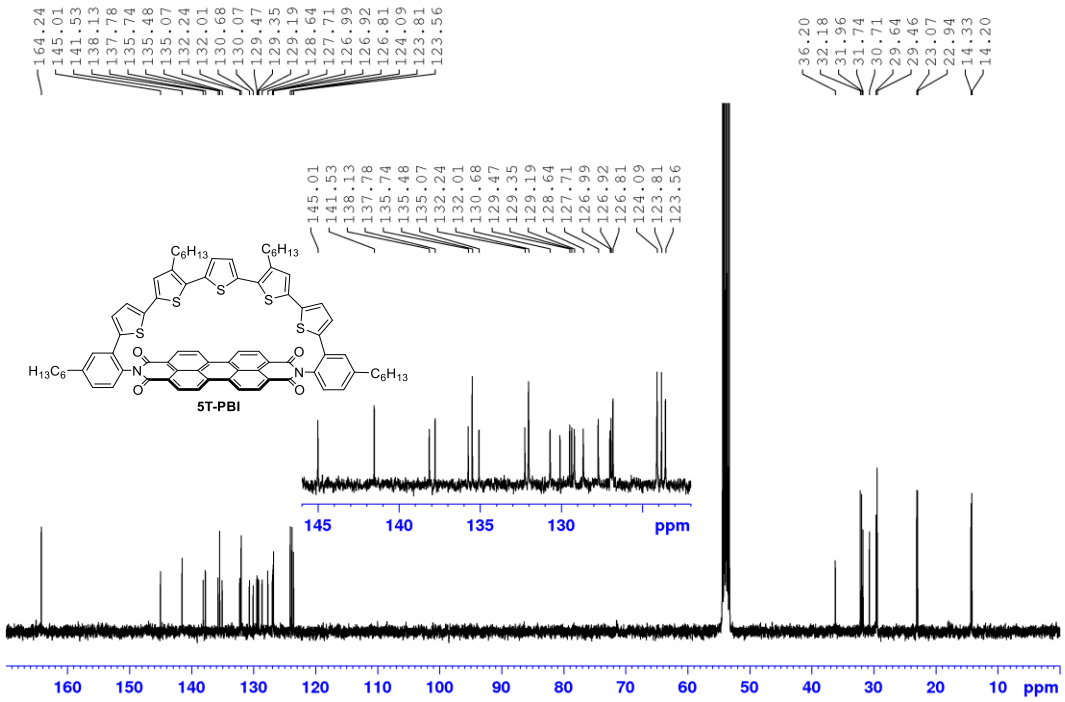

Figure 80. ^{13}C NMR spectrum (150 MHz) of **5T-PBI** in CD_2Cl_2 at 298 K.

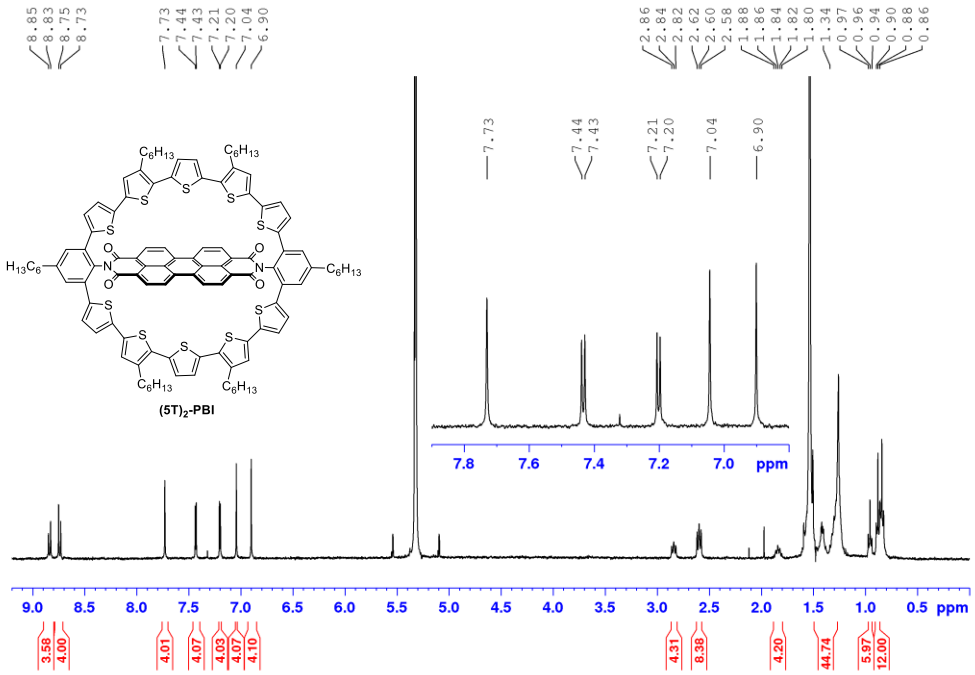

Figure 81. ^{1}H NMR spectrum (400 MHz) of **(5T)$_2$-PBI** in CD_2Cl_2 at 298 K.

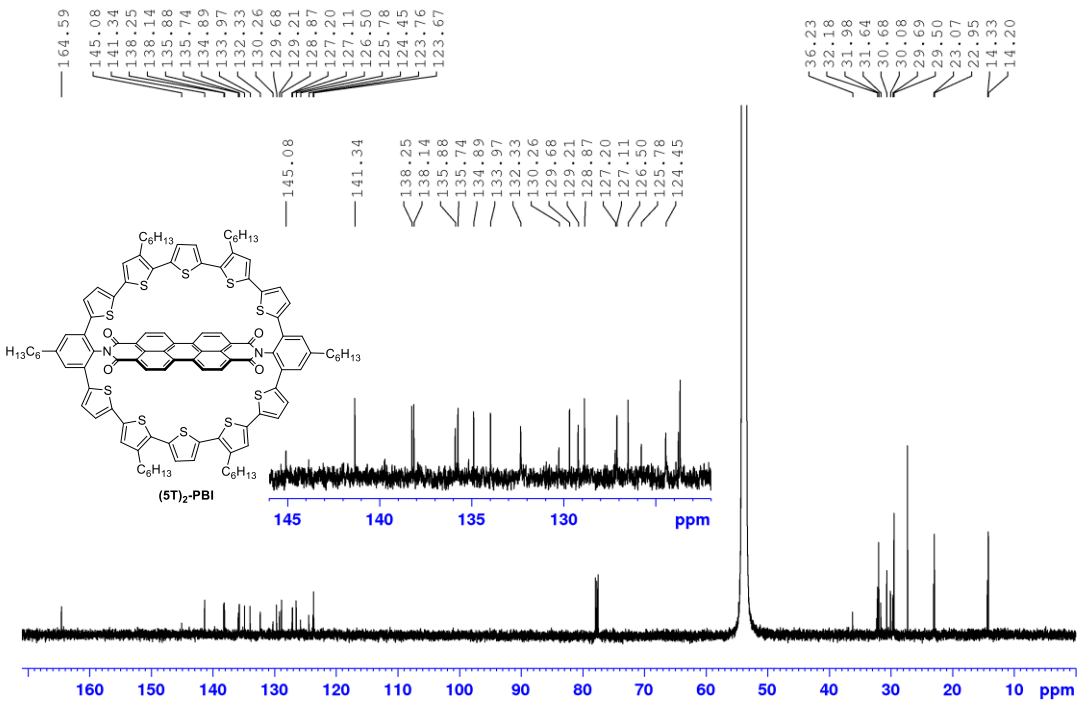

Figure 82. ^{13}C NMR spectrum (150 MHz) of **(5T)$_2$-PBI** in CD_2Cl_2 at 298 K.

Mass Spectra

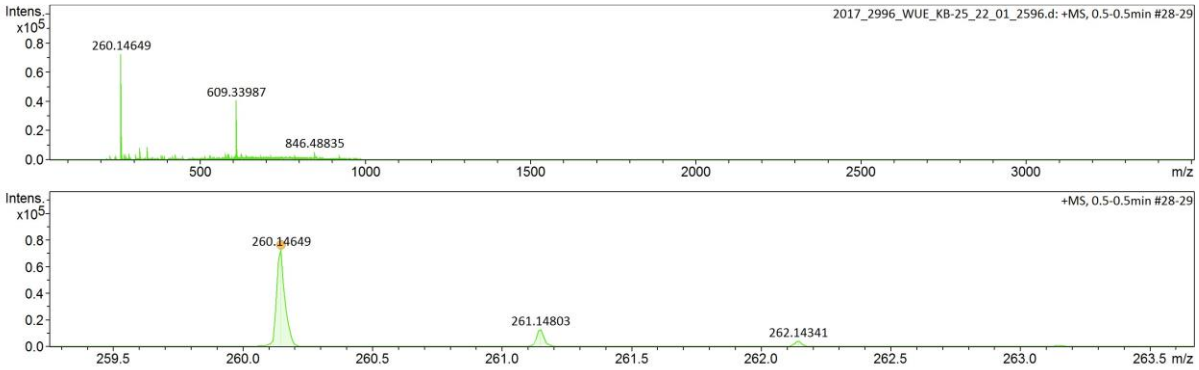

Meas. m/z	#	Ion Formula	m/z	err [ppm]	mSigma	# mSigma	Score	rdb	e⁻ Conf	N-Rule
260.14649	1	C16H22NS	260.14675	1.00	7.6	1	100.00	6.5	even	ok

Figure 83. HRMS (ESI-TOF, pos. mode, acetonitrile/chloroform 1/1) spectra of **69**.

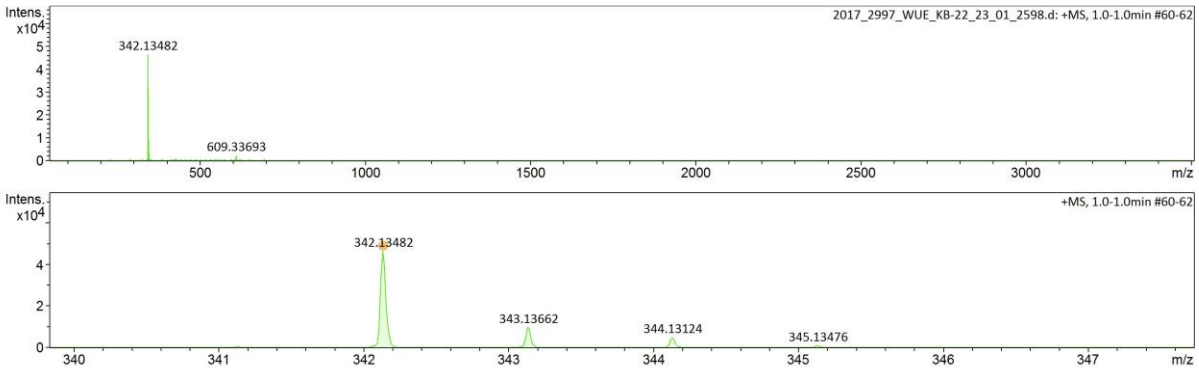

Meas. m/z	#	Ion Formula	m/z	err [ppm]	mSigma	# mSigma	Score	rdb	e⁻ Conf	N-Rule
342.13482	1	C20H24NS2	342.13447	-1.04	15.9	1	100.00	9.5	even	ok

Figure 84. HRMS (ESI-TOF, pos. mode, acetonitrile/chloroform 1/1) spectra of **68**

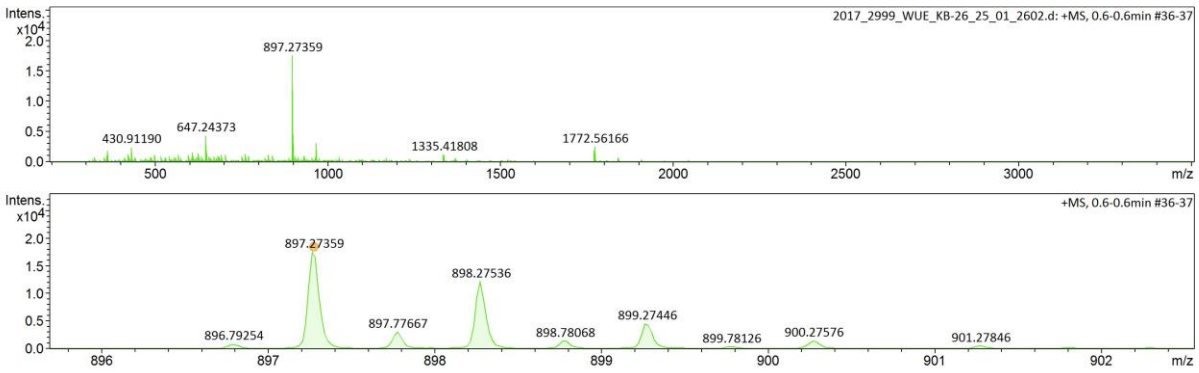

Meas. m/z	#	Ion Formula	m/z	err [ppm]	mSigma	# mSigma	Score	rdb	e⁻ Conf	N-Rule
897.27359	1	C56H46N2NaO4S2	897.27912	6.16	33.5	1	100.00	34.5	even	ok

Figure 85. HRMS (ESI-TOF, pos. mode, acetonitrile/chloroform 1/1) spectra of **70**.

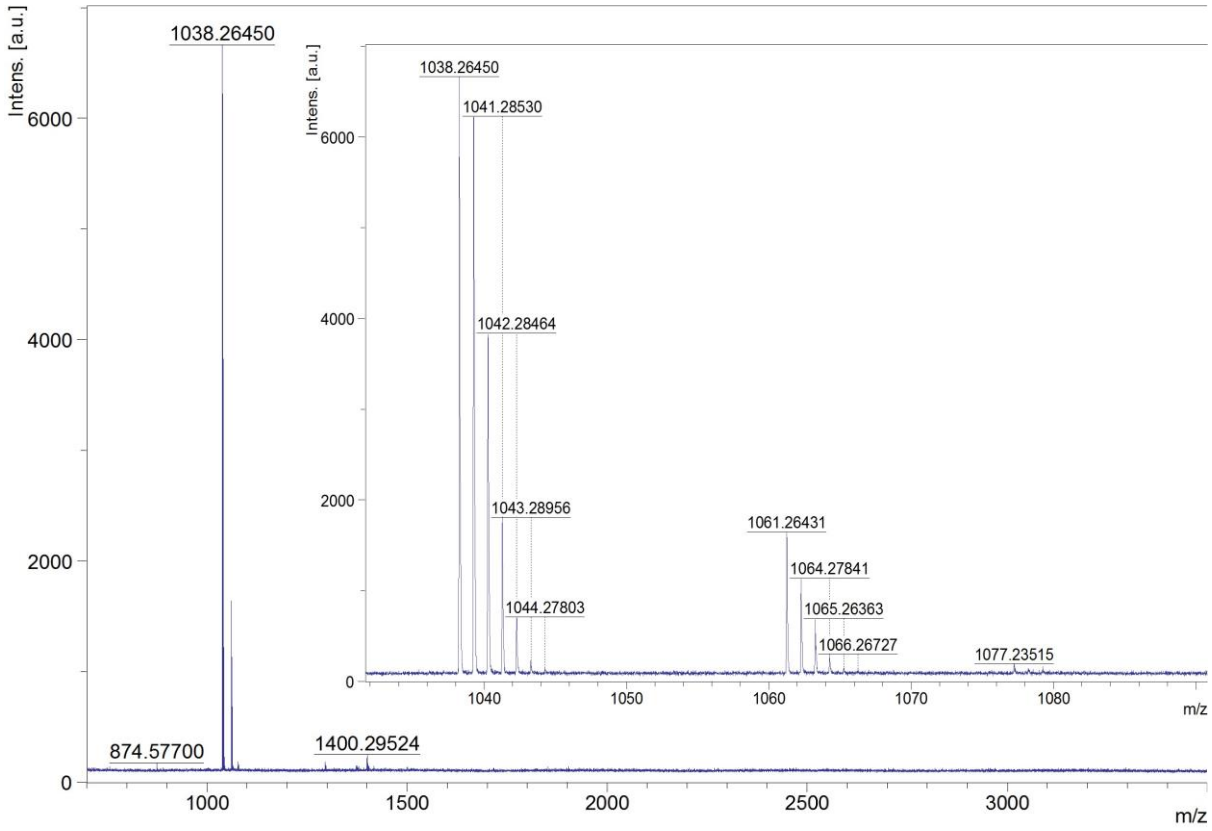

Formula	Mass	Error	mSigma	DblEq	N rule	Electron	Configuration
C 64 H 50 N 2 O 4 S 4	1,038.2648	0.2864	91.7609	41.00	ok	odd	

Figure 86. HRMS (MALDI-TOF, pos. mode, DCTB in $CHCl_3$) spectra of **71**.

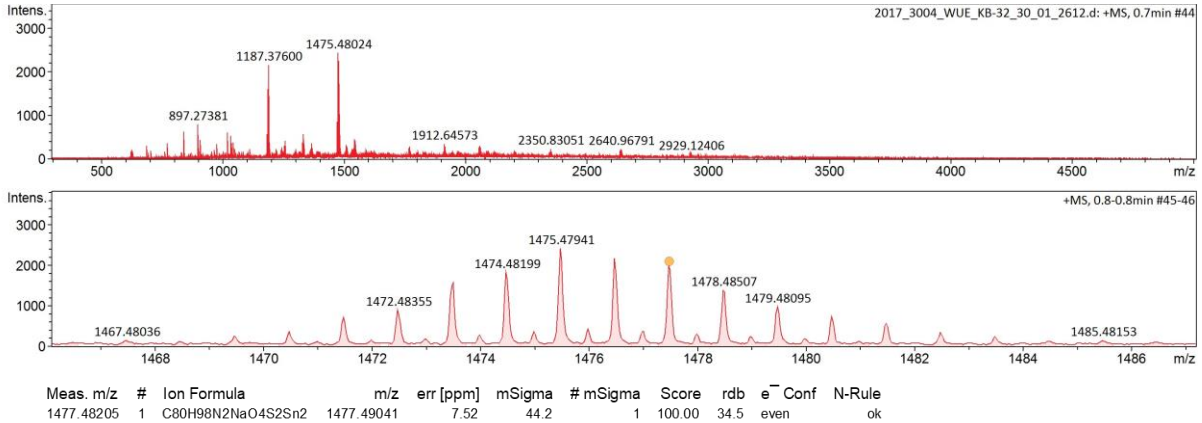

Figure 87. HRMS (MALDI-TOF, pos. mode, DCTB in $CHCl_3$) spectra of **72**.

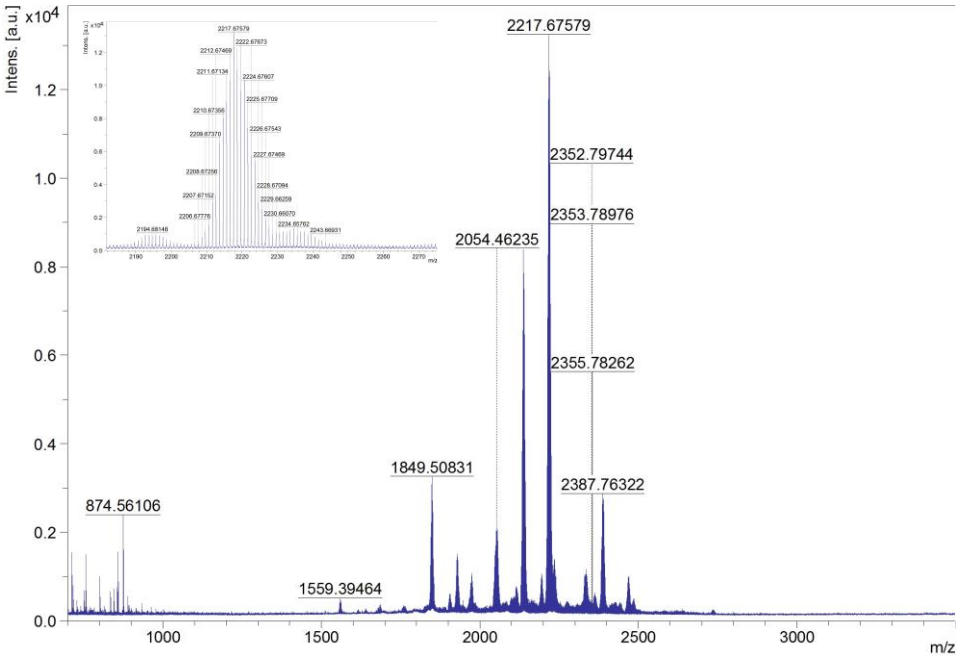

Formula	Mass	Error	mSigma	DblEq	N rule	Electron Configuration
C 112 H 154 N 2 Na O 4 S 4 Sn 4	2,221.6771	0.2617	50.9627	40.50	ok	even

Figure 88. HRMS (MALDI-TOF, pos. mode, DCTB in $CHCl_3$) spectra of **73**.

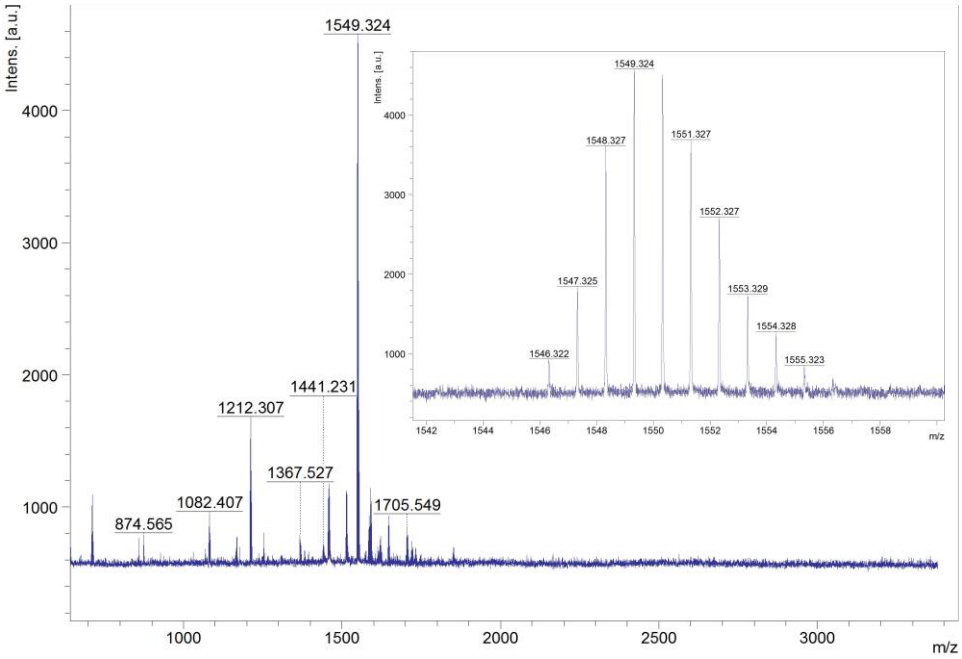

Formula	Mass	Error	mSigma	DblEq	N rule	Electron Configuration
C 72 H 68 Cl 2 N 2 O 4 Pt 2 S 2	1,548.3288	1.4653	34.7120	39.00	ok	odd

Figure 89. HRMS (MALDI-TOF, pos. mode, DCTB in $CHCl_3$) spectra of **74**.

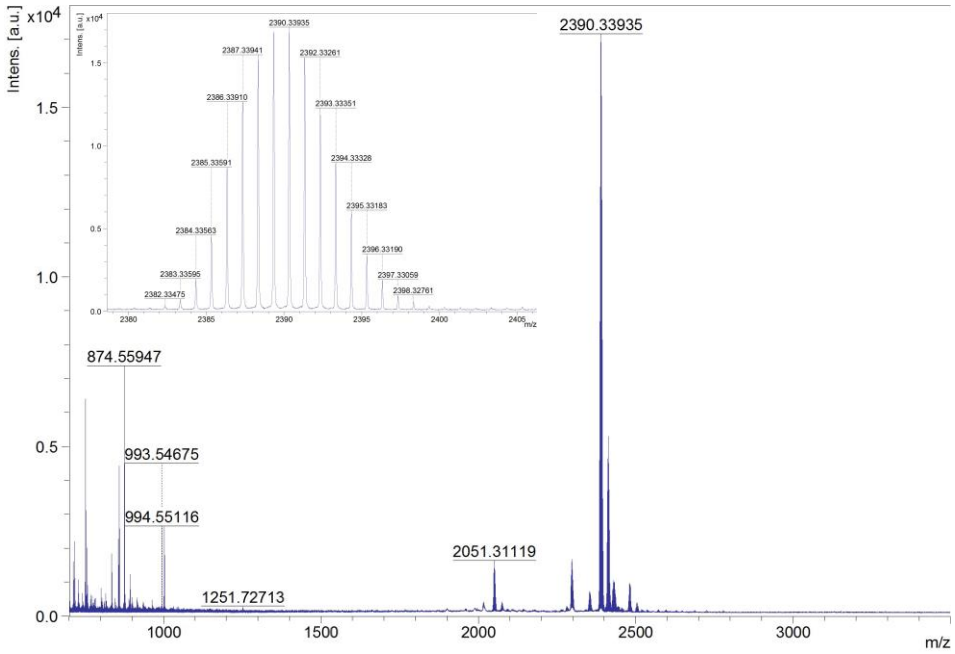

Formula	Mass	Error	mSigma	DblEq	N rule	Electron Configuration
C 96 H 94 Cl 4 N 2 O 4 Pt 4 S 4	2,386.3437	1.9164	28.3167	49.00	ok	odd

Figure 90. HRMS (MALDI-TOF, pos. mode, DCTB in $CHCl_3$) spectra of **75**.

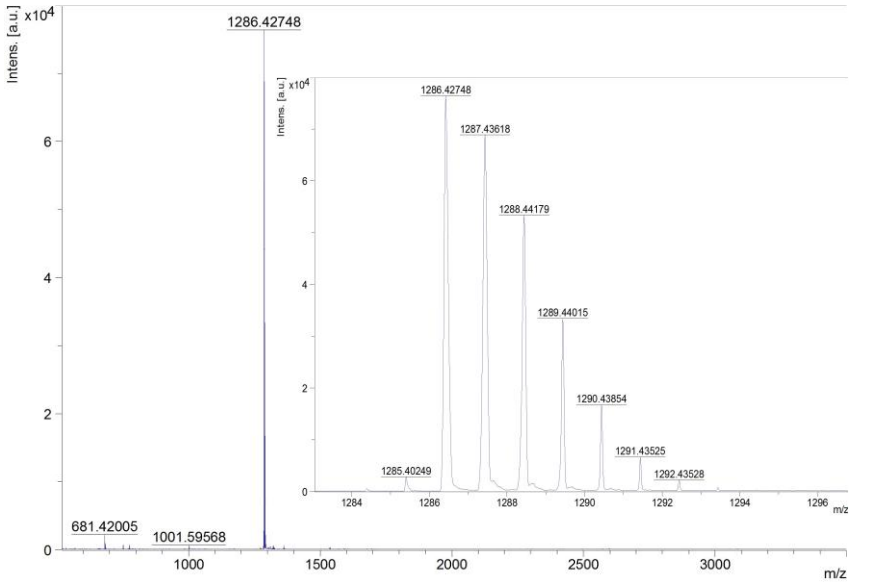

Formula	Mass	Error	mSigma	DblEq	N rule	Electron Configuration
C 80 H 74 N 2 O 4 S 5	1,286.4247	2.1853	48.1584	45.00	ok	odd

Figure 91. HRMS (MALDI-TOF, pos. mode, DCTB in $CHCl_3$) spectra of **5T-PBI**.

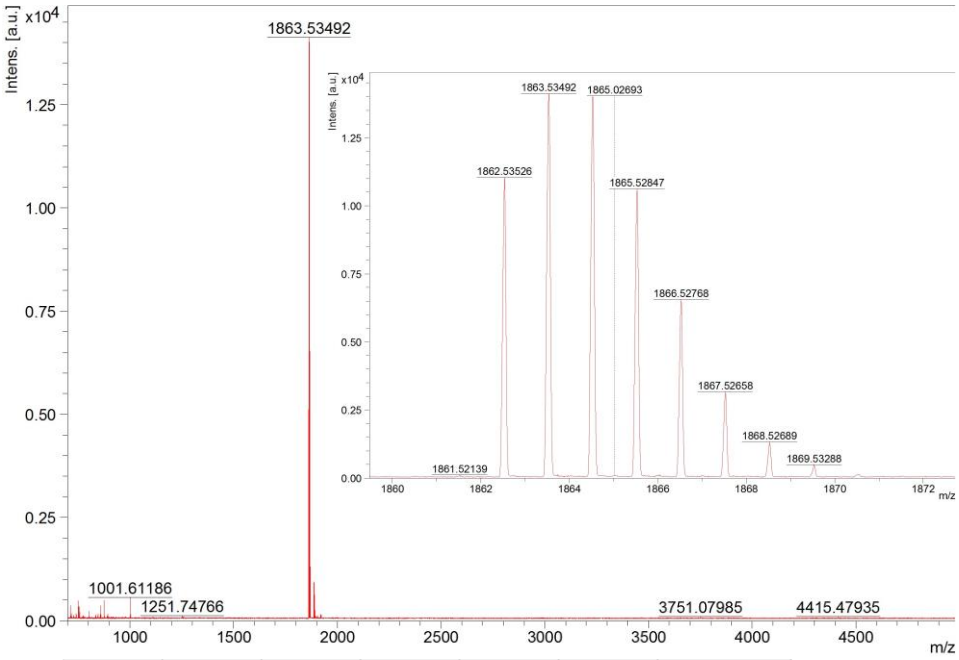

Formula	Mass	Error	mSigma	DblEq	N rule	Electron Configuration
C 112 H 106 N 2 O 4 S 10	1,862.5354	0.0846	13.9310	61.00	ok	odd

Figure 92. HRMS (MALDI-TOF, pos. mode, DCTB in $CHCl_3$) spectra of **(5T)$_2$-PBI**.

Cartesian Coordinates Received from DFT Calculations

Final geometry:

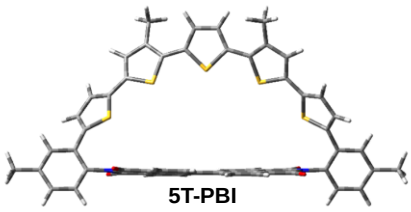

Total energy: −4708.34654570 Hartrees

C1	3.03793	−2.59722	2.21716	O28	−5.52174	−2.27285	2.66874	C55	6.87597	2.00511	1.63107
C2	1.64301	−2.59102	2.32188	O29	5.52174	−2.27316	−2.66847	C56	7.67722	0.8626	1.38696
C3	0.81874	−2.53261	1.19643	O30	5.84107	−2.60739	1.88907	C57	7.22032	0.06359	0.36112
C4	1.4289	−2.50466	−0.09766	C31	−7.13426	−2.33641	0.48187	C58	−4.80312	4.38252	−1.34348
C5	2.85508	−2.48696	−0.19483	C32	7.13427	−2.33647	−0.48159	C59	−3.59797	5.12841	−1.23609
C6	3.64911	−2.53461	0.97678	C33	−7.81236	−3.47701	0.90766	C60	−2.60521	4.43015	−0.5588
C7	0.64763	−2.48895	−1.29659	C34	−9.19984	−3.49023	0.98946	S61	−3.18705	2.84542	−0.06646
C8	1.30977	−2.42627	−2.52422	C35	−9.94245	−2.35436	0.63971	C62	−4.75964	3.12371	−0.78143
C9	2.7053	−2.38632	−2.60999	C36	−9.24962	−1.21768	0.22289	C63	−7.67723	0.86244	−1.38706
C10	3.48044	−2.41977	−1.46358	C37	−7.84539	−1.17377	0.13051	C64	−6.87598	2.00492	−1.6313
C11	5.12971	−2.52176	0.90181	C38	7.8454	−1.17378	−0.13036	C65	−5.79213	2.10932	−0.7826
C12	4.95609	−2.3587	−1.58978	C39	9.24962	−1.2177	−0.22274	S66	−5.78344	0.77147	0.35016
C13	−0.64762	−2.4888	1.29689	C40	9.94245	−2.35443	−0.63942	C67	−7.22033	0.06355	−0.36113
C14	−0.81874	−2.53275	−1.19613	C41	9.19985	−3.49034	−0.98904	C68	11.45122	−2.36271	−0.71633
C15	−1.42889	−2.50465	0.09796	C42	7.81236	−3.47711	−0.90724	C69	−11.45122	−2.36264	0.71662
C16	−2.85507	−2.48694	0.19513	C43	−1.24452	4.82243	−0.26151	C70	−3.44439	6.50534	−1.82535
C17	−3.64911	−2.53472	−0.97648	C44	−0.6942	6.0856	−0.14136	C71	3.44439	6.50555	1.82457
C18	−3.03793	−2.59748	−2.21685	C45	0.6942	6.08561	0.14062	H72	3.66218	−2.64162	3.10319
C19	−1.64301	−2.59129	−2.32157	C46	1.24451	4.82247	0.26092	H73	1.20964	−2.6331	3.31404
C20	−1.30977	−2.42597	2.52451	S47	−2E−6	3.60724	−2.19E−4	H74	0.74462	−2.39399	−3.44804
C21	−2.7053	−2.38601	2.61028	S48	3.18705	2.84542	0.06611	H75	3.20198	−2.32509	−3.57243
C22	−3.48044	−2.4196	1.46387	C49	2.6052	4.43022	0.55826	H76	−3.66218	−2.64198	−3.10288
C23	−4.95609	−2.35852	1.59007	C50	3.59797	5.12856	1.23547	H77	−1.20964	−2.63349	−3.31372
C24	−5.1297	−2.52187	−0.90151	C51	4.80311	4.38268	1.34295	H78	−0.74462	−2.39358	3.44832
N25	5.69287	−2.39261	−0.38695	C52	4.75964	3.12381	0.78105	H79	−3.20197	−2.32467	3.57271
N26	−5.69287	−2.39256	0.38723	S53	5.78344	0.77143	−0.35026	H80	−9.70934	−4.38847	1.3294
O27	−5.84107	−2.60761	−1.88876	C54	5.79212	2.10941	0.78235	H81	−9.80626	−0.31753	−0.02188

H82	9.80626	−0.31752	0.02192	H90	−8.54406	0.60024	−1.98366	H98	−4.19681	6.67771	−2.60146
H83	9.70934	−4.38862	−1.32888	H91	−7.06087	2.70655	−2.43718	H99	−3.57113	7.29188	−1.06931
H84	−1.27685	6.99381	−0.23005	H92	11.8663	−1.36326	−0.55423	H100	−2.4547	6.64125	−2.2745
H85	1.27685	6.99384	0.2292	H93	11.88313	−3.0292	0.0412	H101	2.45468	6.64152	2.27369
H86	5.69048	4.77359	1.83033	H94	11.79922	−2.71766	−1.69351	H102	4.19679	6.67802	2.60067
H87	7.06086	2.70684	2.43687	H95	−11.88312	−3.02921	−0.04083	H103	3.57114	7.29201	1.06844
H88	8.54405	0.60047	1.9836	H96	−11.79921	−2.71748	1.69384	H104	7.23797	−4.35917	−1.17207
H89	−5.69049	4.77337	−1.83089	H97	−11.8663	−1.3632	0.55441	H105	−7.23797	−4.35903	1.17259

Final geometry:

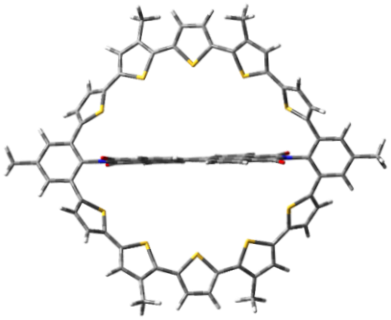

$(5T)_2$-PBI

Total energy: −7544.84772028 Hartrees

C1	−2.87541	−0.1459	−2.4185	C16	2.86074	−8.53E−4	3.54E−4	C31	7.14501	−9.15E−4	0.00118
C2	−1.47734	−0.11289	−2.4281	C17	3.57065	−0.08012	1.2233	C32	−7.14501	−9.07E−4	−0.00117
C3	−0.73419	−0.03066	−1.24907	C18	2.87541	−0.1454	2.41853	C33	7.84001	−1.16251	−0.38835
C4	−1.43174	−9.19E−4	−1.74E−4	C19	1.47733	−0.11238	2.42813	C34	9.24373	−1.13577	−0.38239
C5	−2.86075	−8.51E−4	−3.51E−4	C20	1.47791	0.11055	−2.42777	C35	9.96045	−9.39E−4	−7E−4
C6	−3.57065	−0.08037	−1.22328	C21	2.87598	0.14371	−2.41783	C36	9.24425	1.13565	0.37661
C7	−0.73449	0.02878	1.24889	C22	3.57092	0.0785	−1.22242	C37	7.84039	1.16153	0.38735
C8	−1.47791	0.11106	2.42775	C23	5.05045	0.11861	−1.24623	C38	−7.84039	1.16146	−0.38759
C9	−2.87598	0.14421	2.4178	C24	5.05019	−0.11994	1.24746	C39	−9.24425	1.13558	−0.37685
C10	−3.57092	0.07876	1.22241	N25	−5.70186	−6.34E−4	−7.02E−4	C40	−9.96045	−9.3E−4	6.94E−4
C11	−5.05019	−0.12019	−1.24743	N26	5.70186	−6.39E−4	7.05E−4	C41	−9.24373	−1.13569	0.38261
C12	−5.05046	0.11886	1.24621	O27	5.69476	−0.25372	2.27538	C42	−7.84001	−1.16243	0.38858
C13	0.73448	0.02852	−1.24889	O28	5.69523	0.25261	−2.27397	C43	1.22471	7.15537	0.34199
C14	0.73418	−0.0304	1.24908	O29	−5.69523	0.25308	2.27392	C44	0.68348	8.41835	0.18565
C15	1.43174	−9.2E−4	1.77E−4	O30	−5.69476	−0.25418	−2.27532	C45	−0.68348	8.41831	−0.18728

C46	−1.2247	7.1553	−0.34339	H79	3.43747	0.21748	−3.34298	S112	−3.18486	−5.18585	0.2713
S47	6E−6	5.94003	−5.89E−4	H80	9.77799	−2.03737	−0.66802	C113	−4.69643	−6.71364	1.68105
S48	−3.18507	5.18631	−0.2682	H81	9.77885	2.03988	0.653	C114	−2.56191	−6.76285	0.73664
C49	−2.56335	6.7643	−0.73195	H82	−9.77885	2.03975	−0.65342	C115	−3.49898	−7.4569	1.49284
C50	−3.50241	7.45976	−1.48446	H83	−9.77799	−2.03723	0.66842	H116	−5.54409	−7.10119	2.23708
C51	−4.70022	6.71681	−1.67111	H84	1.25924	9.32651	0.31252	C117	−1.22403	−7.15421	0.34565
C52	−4.70178	5.46349	−1.09621	H85	−1.25924	9.32644	−0.31432	C118	−3.29629	−8.82662	2.0841
S53	−5.83467	3.14739	0.00229	H86	−5.54922	7.10543	−2.22432	C119	−0.68316	−8.41722	0.18858
C54	−5.73053	4.44675	−1.16919	H87	−6.81885	4.9788	−2.96792	S120	−4E−6	−5.93894	5.77E−4
C55	−6.7179	4.30612	−2.12337	H88	−8.32748	2.87053	−2.60616	H121	−2.27248	−8.95757	2.45049
C56	−7.53183	3.16197	−1.9292	H89	5.54922	7.10586	2.22294	H122	−3.9813	−8.98913	2.92232
C57	−7.17784	2.39868	−0.83818	H90	8.3275	2.87105	2.60558	H123	−3.48544	−9.62226	1.35092
C58	4.70022	6.71713	1.6698	H91	6.81887	4.97939	2.96692	C124	0.68315	−8.41726	−0.18694
C59	3.50241	7.46005	1.48301	H92	−11.8803	0.98948	0.14757	H125	−1.25877	−9.32531	0.31674
C60	2.56336	6.76444	0.73063	H93	−11.84543	−0.35164	−1.00192	C126	1.22402	−7.15428	−0.34426
S61	3.18508	5.18637	0.26717	H94	−11.88147	−0.68382	0.73229	H127	1.25876	−9.32537	−0.31492
C62	4.70179	5.4637	1.09513	H95	11.84539	−0.35117	1.00214	C128	2.5619	−6.763	−0.73532
C63	7.53184	3.16235	1.92857	H96	11.88148	−0.68421	−0.73191	C129	3.49898	−7.4572	−1.49138
C64	6.71791	4.30654	2.12251	H97	11.88032	0.98938	−0.148	S130	3.18486	−5.18591	−0.27029
C65	5.73054	4.44698	1.16831	H98	3.98979	8.9957	2.90703	C131	4.69643	−6.71398	−1.67973
S66	5.83467	3.14739	−0.00291	H99	3.48722	9.6251	1.33627	C132	3.29628	−8.82704	−2.08237
C67	7.17784	2.39885	0.8377	H100	2.27909	8.96231	2.44228	C133	4.69947	−5.46172	−1.10258
C68	−11.471	−0.01081	−0.02763	H101	−2.27908	8.96185	−2.44402	H134	5.54409	−7.10164	−2.23568
C69	11.471	−0.01082	0.02767	H102	−3.98978	8.99514	−2.90878	H135	3.9813	−8.98971	−2.92055
C70	3.30144	8.83101	2.07198	H103	−3.48722	9.62483	−1.33813	H136	3.48543	−9.62253	−1.34903
C71	−3.30144	8.83061	−2.07369	C104	−7.17616	−2.39754	0.84346	H137	2.27248	−8.95806	−2.44874
H72	−3.43668	−0.21978	−3.34378	S105	−5.83728	−3.15041	−4.7E−5	C138	5.72783	−4.4446	−1.17614
H73	−0.97535	−0.16284	−3.38696	C106	−7.52518	−3.15549	1.93967	C139	6.71052	−4.29944	−2.13438
H74	−0.97615	0.16097	3.38672	C107	−5.72783	−4.44436	1.17702	S140	5.83726	−3.1504	6.57E−4
H75	−3.43747	0.21818	3.34294	C108	−6.71051	−4.299	2.13524	C141	7.52519	−3.15589	−1.93903
H76	3.43667	−0.21908	3.34383	H109	−8.31749	−2.86059	2.61905	H142	6.80748	−4.96831	−2.98242
H77	0.97535	−0.16213	3.38699	C110	−4.69947	−5.4615	1.10365	C143	7.17615	−2.39771	−0.84298
H78	0.97615	0.16026	−3.38675	H111	−6.80745	−4.9677	2.98342	H144	8.31751	−2.86114	−2.61847

Final geometry:

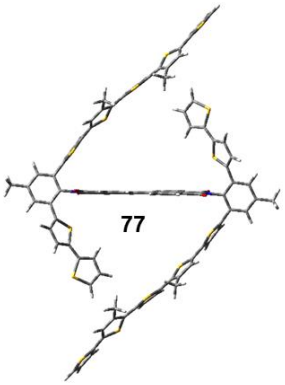

Total energy: −9754.49276862 Hartrees

C1	0.95871	−2.71421	−2.56024	N25	1.70772	−5.44122	−0.14375	C49	−6.2809	−4.83962	0.15355
C2	0.51661	−1.38751	−2.56859	N26	−1.70777	5.44126	−0.14377	C50	−5.86642	−5.43159	1.34004
C3	0.24216	−0.69402	−1.3882	O27	−1.57246	5.48079	2.13996	C51	−4.60028	−6.06716	1.21144
C4	0.4409	−1.36277	−0.1387	O28	−1.84329	5.39108	−2.42724	C52	−4.03002	−5.98035	−0.03904
C5	0.87715	−2.72411	−0.13926	O29	1.57249	−5.48071	2.13999	S53	−1.45717	−6.82406	0.62588
C6	1.1322	−3.38817	−1.36398	O30	1.84306	−5.39107	−2.42724	C54	−2.75963	−6.49492	−0.50441
C7	0.21252	−0.70384	1.11108	C31	−2.03734	6.84718	−0.14897	C55	−2.35039	−6.75894	−1.79412
C8	0.40472	1.42547	2.29081	C32	2.03742	−6.8471	−0.14899	C56	−1.00953	−7.22358	−1.88072
C9	0.81396	−2.76296	2.28128	C33	−1.00602	7.7706	−0.39203	C57	−0.37949	−7.31839	−0.66523
C10	1.05364	−3.41505	1.08438	C34	−1.29934	9.13746	−0.38794	C58	−12.32501	−0.51891	1.22699
C11	1.58437	−4.79821	−1.39089	C35	−2.59432	9.60371	−0.13747	C59	−11.06539	−1.17284	1.33167
C12	1.46155	−4.8392	1.10759	C36	−3.59832	8.66518	0.09794	C60	−10.74404	−1.88072	0.17949
C13	−0.24255	0.69396	−1.3882	C37	−3.35116	7.28051	0.09949	S61	−12.03979	−1.75496	−1.00756
C14	−0.21281	0.70382	1.11108	C38	1.00619	−7.77062	−0.39214	C62	−5.42538	6.55805	1.37624
C15	−0.44122	1.36274	−0.13871	C39	1.29968	−9.13744	−0.38829	C63	−6.43032	5.55739	1.39935
C16	−0.87741	2.7241	−0.13927	C40	2.59475	−9.60357	−0.13795	S64	−4.86363	4.95543	−0.55699
C17	−1.0538	3.41507	1.08437	C41	3.59862	−8.66496	0.09763	C65	−4.47902	6.3794	0.39232
C18	−0.81411	2.76299	2.28127	C42	3.35128	−7.28031	0.0994	C66	2.89148	−11.08473	−0.11626
C19	−0.40493	1.42548	2.29081	C43	−9.56894	−2.65015	−0.16738	C67	−2.89088	11.08491	−0.11536
C20	−0.51706	1.38743	−2.56858	C44	−9.14967	−3.03108	−1.4309	C68	−10.20018	−1.05286	2.55991
C21	−0.9591	2.71415	−2.56024	C45	−7.99508	−3.84264	−1.43564	C69	−6.64122	−5.44927	2.63239
C22	−1.1325	3.38814	−1.36399	C46	−7.48542	−4.10944	−0.17662	H70	1.16789	−3.23723	−3.48728
C23	−1.58457	4.79822	−1.39089	S47	−8.48308	−3.32469	1.04094	H71	0.39292	−0.90131	−3.52885
C24	−1.46159	4.83925	1.10758	S48	−5.06813	−5.05809	−1.1052	H72	0.23029	−0.95679	3.25192

H73	0.94793	−3.31063	3.20801	H106	5.37196	−7.37136	2.09158	C139	0.37957	7.31819	−0.66532
H74	−0.948	3.31068	3.20800	H107	7.22765	−5.52308	2.13432	H140	0.50861	7.46162	−2.81243
H75	−0.23048	0.9568	3.25192	S108	12.03952	1.75412	−1.00799	C141	−14.2592	−0.18225	−0.4033
H76	−0.39344	0.9012	−3.52884	C109	12.32566	0.5195	1.22724	C142	−14.77335	−0.09534	−1.68033
H77	−1.16832	3.23715	−3.48728	C110	10.74416	1.88044	0.17943	S143	−15.41243	0.4595	0.75702
H78	−0.49585	9.84259	−0.58281	C111	11.06599	1.17332	1.33193	C144	−16.07116	0.4863	−1.73296
H79	−4.61693	9.00367	0.26397	H112	12.72519	−0.10265	2.02228	H145	−14.22464	−0.42141	−2.55759
H80	0.49628	−9.84265	−0.58319	C113	9.56885	2.6495	−0.16754	C146	−16.54515	0.8429	−0.50036
H81	4.61727	−9.00334	0.26362	C114	10.20118	1.05398	2.56052	H147	−16.62456	0.6399	−2.65295
H82	−9.66794	−2.72943	−2.33492	C115	9.1488	3.02909	−1.4312	H148	−17.49017	1.30623	−0.25098
H83	−7.54371	−4.22903	−2.34315	S116	8.48375	3.32533	1.04074	C149	−7.09219	3.43258	0.14921
H84	−4.1323	−6.60533	2.02995	H117	9.16831	0.79055	2.30769	C150	−6.74985	2.25473	−0.47981
H85	−2.99969	−6.63404	−2.65442	H118	10.59084	0.27683	3.22515	S151	−8.77987	3.38925	0.63507
H86	−0.50912	−7.46306	−2.81222	H119	10.17122	1.98934	3.13348	C152	−7.8214	1.31988	−0.56121
H87	−12.7242	0.1038	2.02177	C120	7.99418	3.84061	−1.43609	H153	−5.74932	2.05814	−0.85046
H88	−5.37169	7.37131	2.09184	H121	9.6665	2.72647	−2.33522	C154	−8.97783	1.78498	0.00314
H89	−7.22762	5.52323	2.13422	C122	7.48528	4.10873	−0.17703	H155	−7.73402	0.33675	−1.01094
H90	2.54746	−11.54272	0.82023	H123	7.54223	4.226	−2.34374	H156	−9.93316	1.28411	0.0865
H91	2.38488	−11.606	−0.93604	C124	6.28096	4.83926	0.1531	C157	7.09187	−3.43193	0.14986
H92	3.96499	−11.27884	−0.20335	C125	5.8669	5.4319	1.3394	C158	6.74945	−2.25402	−0.479
H93	−2.54828	11.54226	0.82197	S126	5.06784	5.05724	−1.10541	S159	8.77952	−3.38849	0.63583
H94	−2.3829	11.6066	−0.93401	C127	4.60081	6.06757	1.21084	C160	7.82091	−1.31904	−0.5602
H95	−3.96423	11.27922	−0.20399	C128	6.64206	5.45013	2.63153	H161	5.74892	−2.05748	−0.8497
H96	−10.58985	−0.27564	3.22445	C129	4.03016	5.98018	−0.03942	C162	8.97735	−1.78411	0.00416
H97	−10.16968	−1.98803	3.13314	H130	4.13313	6.6062	2.02922	H163	7.73347	−0.33586	−1.00981
H98	−9.16748	−0.78914	2.30662	H131	6.22671	6.19884	3.31321	H164	9.93261	−1.28315	0.08767
H99	−7.69823	−5.68883	2.4736	H132	6.60284	4.48178	3.147	C165	6.27316	−4.59751	0.42265
H100	−6.22605	−6.19808	3.31406	H133	7.69891	5.69019	2.47241	C166	−6.27337	4.59802	0.42223
H101	−6.60138	−4.48086	3.14771	C124	2.75969	6.49463	−0.50469	C167	−12.98258	−0.70718	0.03077
C102	4.47904	−6.37912	0.39237	C135	2.35011	6.75795	−1.79443	C168	14.25936	0.18208	−0.40348
S103	4.8634	−4.95483	−0.55655	S136	1.45757	6.82449	0.62578	C169	14.77352	0.09539	−1.68053
C104	5.4255	−6.55791	1.37619	C137	1.00926	7.22264	−1.88093	S170	15.41245	−0.46018	0.7567
C105	6.4303	−5.55712	1.3995	H138	2.99917	6.63254	−2.65484				

Final geometry:

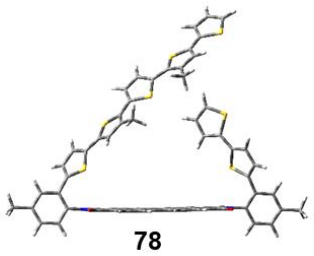

78

Total energy: −5813.16854119 Hartrees

C1	0.21155	5.03336	2.21321	O30	−2.22478	6.44743	2.06756	S59	2.44593	−4.58372	−0.62241
C2	1.42403	4.3359	2.22778	C31	8.6396	−0.43938	−0.13325	C60	3.6336	−3.8418	0.42892
C3	2.0176	3.86163	1.05631	C32	−3.59053	6.97454	−0.21385	C61	6.94679	−3.52268	−1.2948
C4	1.35849	4.10387	−0.1908	C33	9.88077	0.18714	−0.05074	C62	5.65099	−4.07457	−1.1208
C5	0.11958	4.81776	−0.19664	C34	11.05342	−0.55958	−0.09127	C63	4.97143	−3.55382	−0.03913
C6	−0.44424	5.27602	1.01895	C35	11.00642	−1.95356	−0.22507	S64	5.9607	−2.35792	0.77846
C7	1.90607	3.6475	−1.43197	C36	9.75415	−2.56705	−0.29641	C65	7.27767	−2.56862	−0.36002
C8	1.20926	3.9224	−2.61034	C37	8.5529	−1.83822	−0.25025	C66	−7.16559	9.40098	−0.10837
C9	−0.00184	4.62223	−2.60752	C38	−4.8202	6.36513	0.09139	C67	12.27721	−2.76794	−0.29075
C10	−0.55118	5.06888	−1.41836	C39	−5.96416	7.18511	0.11192	C68	0.94795	−3.77677	3.08035
C11	−1.72666	6.0215	1.03876	C40	−5.91534	8.55409	−0.15391	C69	−4.40575	−4.5542	2.61568
C12	−1.841	5.79954	−1.44974	C41	−4.6737	9.12323	−0.46657	H70	−0.23502	5.39283	3.13415
C13	3.28697	3.11894	1.06327	C42	−3.52652	8.33858	−0.49216	H71	1.89801	4.16683	3.18726
C14	3.17326	2.90128	−1.42458	C43	−0.08954	−5.10065	0.33072	H72	1.59838	3.58987	−3.5652
C15	3.82789	2.65121	−0.1766	C44	−0.40973	−6.06761	−0.60532	H73	−0.53109	4.82287	−3.53296
C16	5.0511	1.91085	−0.1679	C45	−1.79094	−6.34613	−0.69512	H74	5.39752	1.32374	−3.49768
C17	5.60316	1.43389	−1.38161	C46	−2.57609	−5.59999	0.16703	H75	3.29151	2.5948	−3.55544
C18	4.95879	1.69592	−2.57805	S47	−1.55614	−4.51321	1.10046	H76	3.60335	3.19085	3.19476
C19	3.7619	2.41939	−2.59539	S48	−4.95993	−6.31628	−1.01777	H77	5.7026	1.90716	3.16819
C20	3.98478	2.84527	2.2414	C49	−4.01626	−5.62925	0.30212	H78	12.0136	−0.05443	−0.02079
C21	5.18015	2.11902	2.24136	C50	−4.85019	−5.19765	1.32704	H79	9.69342	−3.64926	−0.37128
C22	5.71477	1.64724	1.05511	C51	−6.22224	−5.45155	1.04622	H80	−6.92213	6.71874	0.32363
C23	6.96356	0.84936	1.09407	S52	−4.31141	3.6417	−0.55495	H81	−4.60403	10.18466	−0.69135
C24	6.85936	0.64647	−1.39696	C53	−5.76734	2.99678	1.47194	H82	0.3429	−6.58438	−1.19108
N25	−2.35424	6.22396	−0.20857	C54	−5.74329	4.41494	1.4386	H83	−2.20337	−7.10041	−1.35668
N26	7.44781	0.37892	−0.14211	C55	−4.98482	4.93834	0.41593	H84	−7.0128	−5.21296	1.75115
O27	7.36814	0.23635	−2.42707	C56	3.07108	−3.57779	1.65875	H85	−6.28506	2.42199	2.2326
O28	7.54641	0.58686	2.13497	C57	1.71112	−3.97014	1.79506	H86	−6.24043	5.04186	2.17084
O29	−2.44515	6.02502	−2.48681	C58	1.21604	−4.55588	0.63765	H87	3.63232	−3.12977	2.47304

H88	7.61429	−3.79672	−2.1045	H100	−5.22573	−4.55195	3.34057	C112	−4.82908	1.00199	0.18352
H89	5.23052	−4.83559	−1.76987	H101	−3.55968	−5.08281	3.06759	C113	−3.79324	0.388	−0.48724
H90	−8.06577	8.783	−0.03602	H102	−2.56255	8.78133	−0.72349	S114	−6.0057	−0.19485	0.70245
H91	−7.15561	10.07583	0.75726	H103	9.91891	1.26833	0.03849	C115	−3.93059	−1.02678	−0.57539
H92	−7.25694	10.02679	−1.00375	C104	−7.72916	−6.46649	−0.74549	H116	−2.94695	0.93729	−0.88609
H93	12.80193	−2.60718	−1.24134	C105	−7.96477	−7.33151	−1.79389	C117	−5.06873	−1.49043	0.02613
H94	12.97116	−2.49086	0.51127	S106	−9.24963	−5.83759	−0.12837	H118	−3.20742	−1.67441	−1.05885
H95	12.07162	−3.83918	−0.20335	C107	−9.3456	−7.49723	−2.09577	H119	−5.41881	−2.51124	0.10583
H96	1.64092	−3.63127	3.91512	H108	−7.16852	−7.84793	−2.31954	C120	−6.46746	−6.06139	−0.16475
H97	0.29539	−2.89495	3.04075	C109	−10.16093	−6.76199	−1.27984	C121	−5.03165	2.41035	0.46483
H98	0.31486	−4.63877	3.31385	H110	−9.71559	−8.1437	−2.88408				
H99	−4.09834	−3.51132	2.46583	H111	−11.24095	−6.70331	−1.28355				

Final geometry:

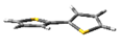

79

Total energy: −1104.81669881 Hartrees

C1	0.00000	3.21057	−0.05036	H7	−2.27318	0.80799	0.4783	C13	0.00000	−3.21057	−0.05036
C2	−1.26892	2.7657	0.19851	C8	0.14867	−0.71017	0.06763	H14	2.11707	−3.42706	0.33872
C3	−1.35485	1.34567	0.26702	C9	1.35485	−1.34567	0.26702	H15	−0.3497	−4.22987	−0.14378
S4	1.11645	1.89317	−0.22313	S10	−1.11645	−1.89317	−0.22313	C16	−0.14867	0.71017	0.06763
H5	0.3497	4.22987	−0.14378	C11	1.26892	−2.7657	0.19851				
H6	−2.11707	3.42706	0.33872	H12	2.27318	−0.80799	0.4783				

Chapter 5

Macrocyclic Donor−Acceptor Dyads Composed of Oligothiophene Half-Cycles and Perylene Bisimides

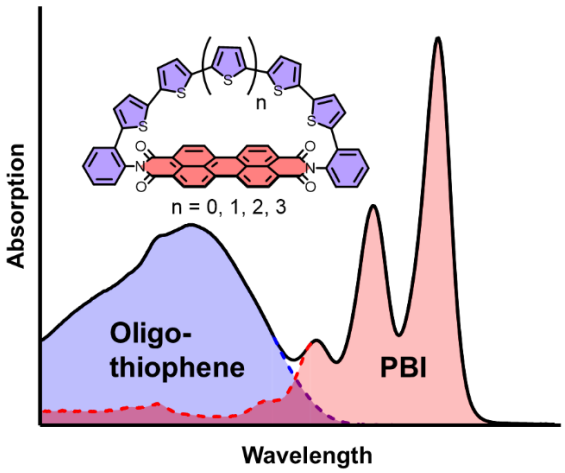

This chapter and the corresponding supporting information has been published:

K. Bold, M. Stolte, K. Shoyama, A.-M. Krause, A. Schmiedel, M. Holzapfel, C. Lambert, F. Würthner, *Chem. Eur. J.* **2022**, e202200355.

Abstract: A series of donor-acceptor (D-A) macrocyclic dyads consisting of an electron-poor perylene bisimide (PBI) π-scaffold bridged with electron-rich α-oligothiophenes bearing four, five, six and seven thiophene units between the two phenyl-imide substituents has been

synthesized and characterized by steady-state UV/Vis absorption and fluorescence spectroscopy, cyclic and differential pulse voltammetry as well as transient absorption spectroscopy. Tying the oligothiophene strands in a conformationally fixed macrocyclic arrangement leads to a more rigid π-scaffold with vibronic fine structure in the respective absorption spectra. Electrochemical analysis disclosed charged state properties in solution which are strongly dependent on the degree of rigidification within the individual macrocycle. Investigation of the excited state dynamics revealed an oligothiophene bridge size-dependent fast charge transfer process for the macrocyclic dyads upon PBI subunit excitation.

5.1 Introduction

Ensuing from the fascination of chemists towards π-conjugated macrocycles, great synthetic and scientific progress has been made in the last two decades. After early attempts of Vögtle and co-workers in the 1990s[167] to synthesize [*n*]cycloparaphenylenes ([*n*]CPPs), it was the groups of Jasti and Bertozzi who reported the synthesis of the first nanohoops in 2008 utilizing a remarkably similar strategy.[137] This was followed by two more decisive synthetic cornerstones in this research field by the groups of Itami[168] and Yamago[169]. Interestingly, much earlier back in 2000 Bäuerle and co-workers already reported the first synthesis of another class of conjugated macrocycles, namely cyclo[*n*]oligothiophenes (C[*n*]Ts).[136, 148-149, 278] Further development of these early synthetic successes lead to giant C[*n*]Ts comprising up to 35 thiophene rings in excellent yields.[40] Since then, a variety of versatile and efficient synthetic protocols were developed to bend initially planar π-conjugated chains into macrocyclic arrangements.[26]

The implementation of donor-acceptor (D-A) motifs into π-conjugated macrocycles received great attention in recent years.[41, 45-46, 307-310] Numerous structures were developed to alter the electrooptical properties by adjusting the respective HOMO and LUMO levels of D and A. This electronic fine-tuning is achieved by careful selec¬tion of subunit structures comprising different electron accepting and donating capabilities, respectively. The bithiophene bay-bridged perylene bisimide (PBI) macrocycles of Nuckolls and co-workers [61-64] displays one great example for such a tailored D-A system. Also non-cyclic covalent donor-acceptor linkages[16-18] of *e.g.* PBI-oligothiophene dyads were described within the past two decades.[59] Installation of thiophene moieties in the PBI's bay position leads to a bathochromic shift of the absorption compared to the unsubstituted PBI as well as fluorescence quenching due to charge transfer (CT) processes.[56] However, the introduction of oligothiophenes at the imide position more or less ensures electronic decoupling of both segments from each other due to nodal planes in the HOMO and LUMO of the PBI at the nitrogen atom.[53, 55] Therefore, the absorption properties of such dyads are often constituted of a sum of the respective subunit spectra. Furthermore, these dyads often show panchromic light absorption and an efficient photoinduced electron transfer (PET) leading to the fast formation of a charge separated state which often quenches the fluorescence of initially highly emissive individual chromophores.

This fast tailored charge separation by concomitantly decelerated or impeded charge recombination could offer interesting prospects towards the understanding and general design of organic photovoltaic devices.[8] By exploiting the advances of macrocyclic π-systems and imide linked PBI-oligothiophene dyads research we envisioned to combine both fields (Figure 93) and enlarge the toolbox of a substance class introduced by our group in a recent report.[262]

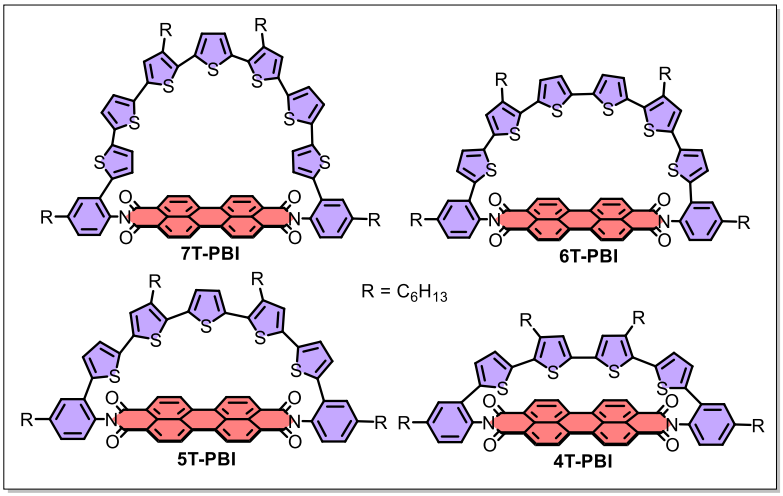

Figure 93. Molecular structures discussed in this chapter.

Besides this previously reported macrocycle **5T-PBI** (Scheme 7) we synthesized three novel differently sized oligothiophene semicircles whose ends are connected by an accepting PBI moiety. As demonstrated for a series of PBIs with a different number of thiophene donor units in PBI bay position[311], changing the semicircle size in our strained macrocyclic scaffolds could potentially also fine tune the exited state dynamics. By changing the oligothiophene chain length in those dyads, we also intended to influence the macrocyclic geometry and therefore especially highlight strain induced structural changes.

5.2 Results and Discussion

5.2.1 Synthesis and Structural Characterization

The synthesis started with the platinated thiophene-PBI precursor **74** comprising the accepting PBI moiety (red) and two of the donating thiophene units (blue) which was obtained after three consecutive synthetic steps which were recently reported by our group.[262] By combining this precursor with the stannylated α-oligothiophene bridge structures bearing two (**80**) to five (**62**)

thiophene subunits in a three step Pt-mediated cross coupling reaction macrocycles **4T-PBI**, **5T-PBI**[262], **6T-PBI** and **7T-PBI** could be synthesized in moderate yields of 14%, 30%, 13% and 3% (Scheme 7) after thorough purification *via* flash column- and gel permeation chromatography. To overcome competing polymerization, the stannylated oligothiophenes **80**, **76**, **81** and **62** were added dropwise over 15 h to a solution of **74** in toluene at 75 °C. In this way, *pseudo* high-dilution conditions favor the intramolecular complex formation over intermolecular side reactions. We utilized toluene in step i (Scheme 7) to apply elevated temperatures and exploit the templating effect of this solvent, as previously shown by our group for the synthesis of PBI cyclophanes.[312] More detailed information about the synthetic procedures as well as a possible reaction mechanism for the macrocyclization cascade reactions can be found in *Chapter 5.4*.

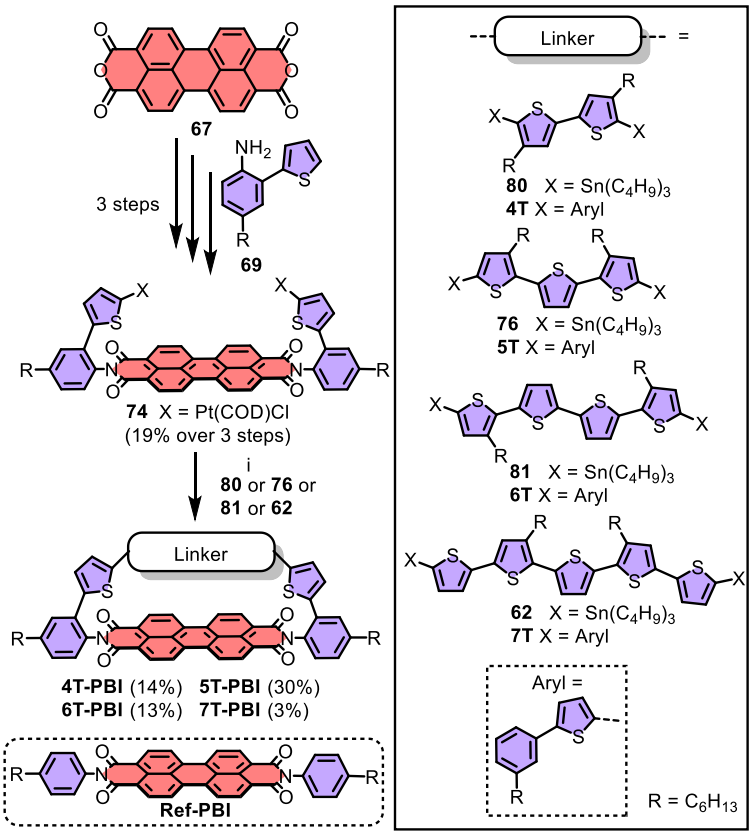

Scheme 7. Synthesis of the macrocyclic architectures **4T-PBI**, **5T-PBI**[262], **6T-PBI** and **7T-PBI**. Reagents and conditions: i) toluene, 75 °C, overnight, then dppf, CH_2Cl_2, r.t, 6 h, then *m*-xylene, 120 °C, overnight. COD = 1,5-Cyclooctadiene. Dppf = 1,1′-Ferrocenediyl-bis(diphenylphosphine).

The stannylated α-oligothiophene backbones **80**, **76**, **81** and **62** as well as the reference compounds **4T**-**7T**[235] could readily be synthesized following literature known Pd-catalyzed

cross coupling protocols.[102] Aliphatic hexyl chains at the phenyl-imide substituents and thiophene bridge of the final macrocyclic architectures **4T-PBI** to **7T-PBI** ensure sufficient solubility even in nonpolar cyclohexane. All new target molecules **4T-PBI**, **6T-PBI** and **7T-PBI** were structurally characterized by nuclear magnetic resonance (NMR) as well as optical spectroscopy (UV/Vis absorption, fluorescence) and high-resolution mass spectrometry (HRMS).

In comparison to the corresponding reference oligothiophene compounds **4T-7T**[235] where rotamer mixtures prevail in solution, the oligothiophene donor chains within the macrocyclic architectures **4T-PBI**, **5T-PBI**[262] and **6T-PBI** adopt a more static all-*syn* conformation, as already proven by the crystal structure of the previously reported double oligothiophene-bridged dyad **(5T)$_2$-PBI**.[262] This structural rigidification as well as additional structural features can be investigated by ^{1}H NMR spectroscopy (Figure 94).

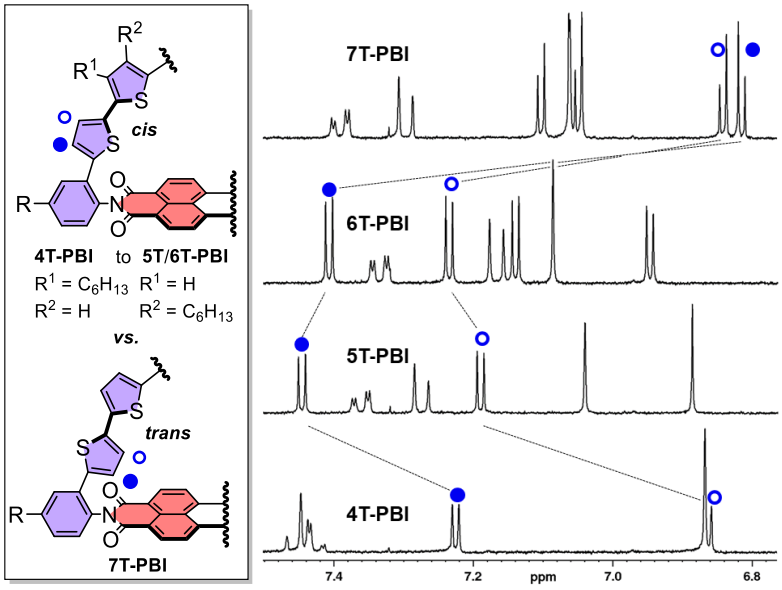

Figure 94. Excerpt of the ^{1}H NMR spectra of **4T-PBI**, **5T-PBI**[262], **6T-PBI** and **7T-PBI** (from bottom to top) in CD_2Cl_2 at room temperature.

The doublet proton signals of the thiophene closest to the phenyl moiety for **4T-PBI** experience an increased separation also in comparison to those of the linear oligothiophene counterpart **4T** due to a particularly strong upfield shift of the proton localized atop the PBI's aromatic shielding cone (Figure 103). This behaviour becomes less pronounced upon incorporation of additional thiophene units in the macrocyclic donor bridges (**5T-PBI** and **6T-PBI**, Figure 104-

105), indicating less strain[40] and enlarged distances to the PBI. Interestingly, both doublet proton signals for **7T-PBI** undergo a very strong shielding in comparison to the other macrocycles (Figure 94). This corroborates a *trans*-conformation of these two outer thiophenes towards their neighbour thiophene unit (see below) where both protons are pointing directly into the PBI shielding zone. This observation is confirmed by ROESY NMR spectroscopy, which shows cross signals of one highfield shifted doublet to one PBI proton signal (Figure 108). On the other hand, the chemical shift of the PBI proton signals do not change to a great extend within the series and also compared to **Ref-PBI** (Figure 107).

In order to fully unravel the structural features of our new macrocyclic architectures single crystals of the smallest macrocycle were grown by slow vapour diffusion of *n*-hexane in a dibromomethane solution of **4T-PBI**. The molecule crystallizes in a $P\bar{1}$ space group *via* the self-assembly of a close π-stacked PBI dimer unit where the intermolecular distance between the two PBI planes is 3.44 Å with only marginal longitudinal (~1 Å) and lateral (~2 Å) displacement (Figure 95a-b).

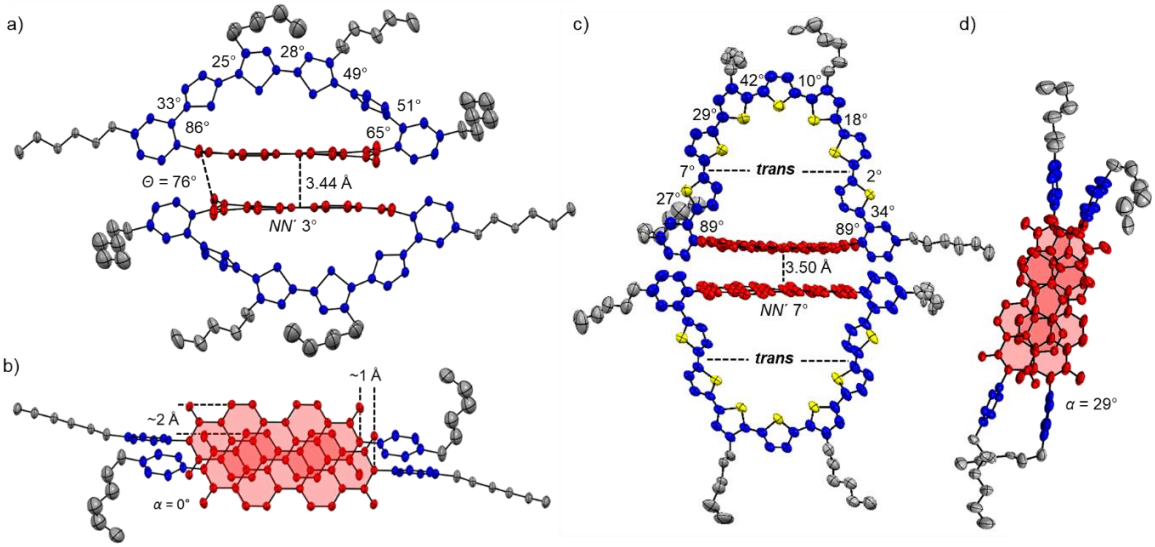

Figure 95. Crystal structure of a)-b) **4T-PBI** and c)-d) **7T-PBI** with ellipsoids set to 50% and 15% probability, respectively. a)/c) Side view onto the dimer structures of **4T-PBI** and **7T-PBI**. b)/d) Top view onto the π-stacked chromophore arrangement of **4T-PBI** and **7T-PBI** within the dimer while omitting the thiophene bridge. The hydrogen atoms, solvent molecules as well as the disorder of the alkyl chains are omitted for clarity.

A similar supramolecular assembly in low polar solvents could not be observed based on concentration- and temperature-dependent UV/Vis studies within the accessible solvent polarity and concentration range. While the individual thiophene units are tilted to a very high degree (Figure 95a; 25°-51°) with respect to each other in order to accommodate for the

induced overall macrocyclic strain of 19.6 kJ mol^{-1} (according to DFT calculations, see Table 12), the PBI displays only a marginal bending of 3° along the *N*,*N*´-axis in the solid state.

Strikingly, the angles that both imide-phenyl units comprise with the PBI segment (86° and 65°) are non-equivalent due to the arrangement of the molecules in the crystal. The attached hexyl chain on one side is extremely tilted which strongly affects the respective phenyl segment. This one sided twist is merely present in the solid state, whereas based on the ^{1}H NMR spectrum (Figure 94) in solution the hexyl chains as well as the oligothiophene backbone do not show any evidence of a symmetry-breaking effect of the bridge architecture as only three proton signals of the thiophene bridge are observed (Figure 103). However, the fact that one thiophene unit is almost stacked on top of the PBI π-plane seems to display the situation more realistically in solution where a strong shielding of the thiophene proton doublets in ^{1}H NMR compared to the other macrocycles **5T-PBI** and **6T-PBI** was observed (Figure 94).

Single crystals of the largest macrocycle could be obtained by slow vapour diffusion of methanol in a chlorobenzene solution of **7T-PBI**. This crystal structure likewise reveals a stacked dimer structure, however with a rotationally displaced arrangement of the two PBI (α = 35°, Figure 95c-d). Furthermore, the thiophene moiety next to the phenyl unit is rotated into a *trans* like arrangement to the neighbouring thiophenes as already noted in solution by the strong upfield shift of both thiophene doublets in the ^{1}H NMR of about 0.5 ppm (compared to **6T-PBI**, Figure 94), due to a different chemical environment as for the other protons in the bridge (see discussion above). This *trans*-twist of two thiophenes leads to a significant structural relaxation as the calculated strain energies for **7T-PBI** (22.5 kJ mol^{-1}) is reduced by almost one third in comparison to a theoretical all-*syn* analogue **7T-PBI-T** (30.6 kJ mol^{-1}, for details see *Chapter 5.4*). It should be noted at this point that the PBI subunit contortion is highly overestimated by the DFT calculation especially for **4T-PBI** (Figure 116). The induced macrocyclic strain is most likely almost exclusively compensated by the respective oligothiophene bridges in all macrocycles as the PBI proton signals remain mainly unaffected.

5.2.2 Redox Properties

The complete series of oligothiophene-bridged macrocycles as well as the reference compounds were electrochemically characterized by cyclic voltammetry (CV), differential

pulse voltammetry (DPV) as well as spectroelectrochemistry (SEC, Figure 109-112) in CH_2Cl_2 with tetrabutylammonium hexafluorophosphate (Bu_4NPF_6) as supporting electrolyte. In the CV (Figure 96a) reversibility of all involved redox processes can be monitored. Two reversible reduction waves corresponding to the anionic and dianionic PBI chromophore at around –1.00 V ($E_{red,1}$) and –1.20 V ($E_{red,2}$) were detected for all macrocycles (Table 9), which are in very good agreement to **Ref-PBI** (–0.99 V/–1.19 V)[262]. In contrast, the oxidation events differ greatly within the series. Thus, whilst the first one-electron oxidation process is high for the smallest macrocycle **4T-PBI** ($E_{ox,1}$ = +0.54 V, Table 9) the oxidation of the other macrocycles **5T-PBI**[262] up to **7T-PBI** can be accomplished at remarkably lower oxidation potentials of only $E_{ox,1}$ = +0.32 V to +0.38 V. Furthermore, in these rigid macrocyclic bridges the required energies for cation formation are disparately higher in the case of **4T-PBI** ($E_{ox,1}$ = +0.54 V) and **6T-PBI** ($E_{ox,1}$ = +0.38 V) compared to linear analogues **4T** ($E_{ox,1}$ = +0.33 V) and **6T** ($E_{ox,1}$ = +0.16 V).

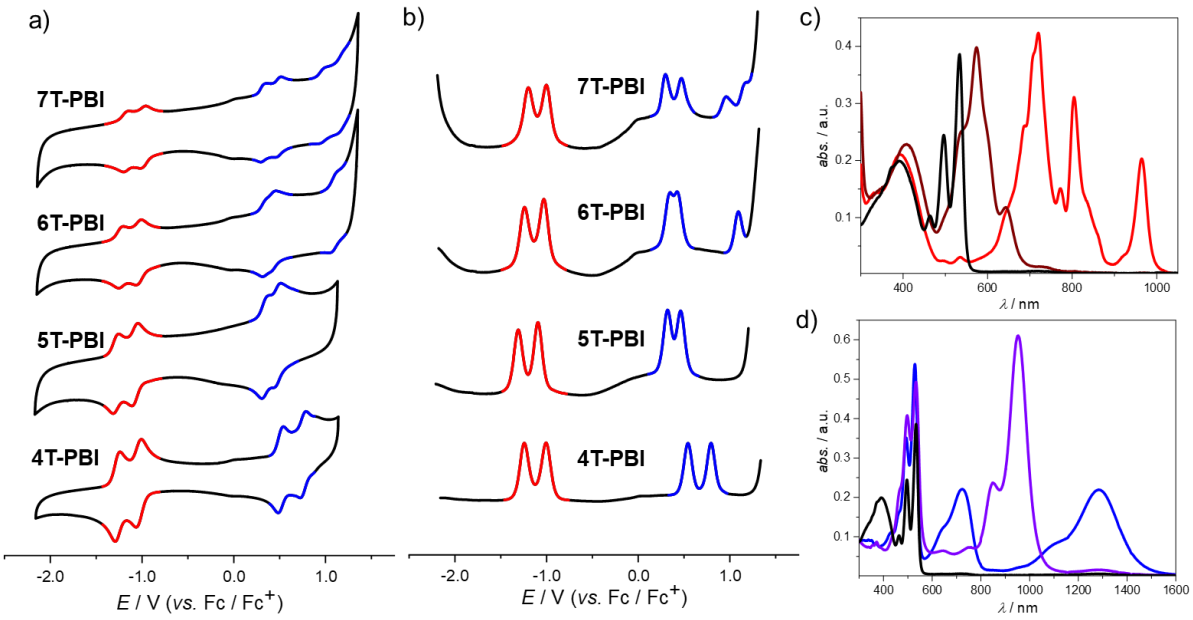

Figure 96. a) CV and b) DPV measurements of **4T-PBI**, **5T-PBI**[262], **6T-PBI** and **7T-PBI** (from bottom to top) as well as c) UV/Vis/NIR absorption spectra of **4T-PBI** (black line) upon electrochemical reduction to **4T-PBI**$^{\bullet-}$ (red line), **4T-PBI**$^{2-}$ (maroon line) and d) electrochemical oxidation to **4T**$^{\bullet+}$**-PBI** (blue line) and **4T**$^{2+}$**-PBI** (violet line). All measurements were carried out in CH_2Cl_2 solutions with Bu_4NPF_6 at room temperature ($c_0 = 10^{-4}$ M).

Due to the special aliphatic decoration and the concomitant cation destabilization in the linear oligothiophenes **5T** ($E_{ox,1}$ = +0.41 V) and **7T** ($E_{ox,1}$ = +0.24 V), which was described previously[235] the mentioned potential difference is non-existent for **5T-PBI** ($E_{ox,1}$ = +0.34 V)

in all-*cis* configuration and less pronounced for **7T-PBI** ($E_{ox,1}$ = +0.32 V). Even greater differences within the macrocyclic series can be observed by comparing the second oxidation potentials of **4T-PBI** ($E_{ox,2}$ = +0.80 V) with the other macrocycles **5T-PBI**[262] to **7T-PBI** ($E_{ox,2}$ = +0.46 V to +0.50 V). Here, especially the potential difference ($E_{ox,2} - E_{ox,1}$, Table 9) between the cationic and dicationic states shall be highlighted, which is best viewed in the DPV spectra with a higher resolution of the individual waves (Figure 96b). This potential difference is largest in **4T-PBI** (0.26 V) and smallest in **6T-PBI** (0.08 V) indicating a highly stabilized dicationic state in the latter case.[107] Presumably owing to the aforementioned *trans* orientation of two thiophenes in **7T-PBI** the potential difference almost resembles the one observed for the free **7T** with +0.19 V.[235] Notably, **6T-PBI** and **7T-PBI** show more than two reversible oxidation processes within the CH_2Cl_2 solvent window which is in accordance with observations made for the linear oligothiophenes **6T** and **7T**, where also the formation of tri- and tetracationic species could be observed.[235]

Table 8. Electrochemical properties of macrocycles **4T-PBI**, **5T-PBI**[262], **6T-PBI** and **7T-PBI** in CH_2Cl_2 at room temperature ($c_0 = 10^{-4}$ M).[a]

	4T-PBI	**5T-PBI**[262]	**6T-PBI**	**7T-PBI**
$E_{ox,1}$/ V	+0.54	+0.34	+0.38	+0.32
$E_{ox,2}$/ V	+0.80	+0.48	+0.46	+0.50
$E_{ox,3}$/ V	–	–	+1.12	+0.98
$E_{ox,4}$/ V	–	–	–	+1.19
$E_{ox,2} - E_{ox,1}$/ V	0.26	0.14	0.08	0.18
$E_{red,1}$/ V	−0.99	−1.07	−1.00	−0.98
$E_{red,2}$/ V	−1.24	−1.29	−1.21	−1.18

[a] Bu_4NPF_6 was used as electrolyte and all half-wave potentials are referenced against the ferrocenium/ferrocene (Fc^+/Fc) redox couple.

In order to unravel the electronic nature of the macrocycles upon electrochemical reduction and oxidation, SEC measurements of the series of macrocycles were conducted in CH_2Cl_2 (Figure 96c, d, Figure 97a, b). Reduction of **4T-PBI** (Figure 96c, black line) revealed typical spectral signatures of a PBI radical anion (**PBI**$^{\bullet-}$, red line) comprising three clearly distinguishable bands at 720 nm, 804 nm and 964 nm corresponding to **4T-PBI**$^{\bullet-}$ (red line) which decrease upon further reduction and give rise to a new absorption band at 573 nm

belonging to the dianion **4T-PBI**$^{2-}$ (maroon line).[293]

Spectral shapes of anion and dianion do not change to a great extend within the series of macrocycles because of the decoupled states between D and A as well as the almost identical reduction potentials observed in the CV (Figure 109a, b to Figure 112a, b). However, single oxidation of **4T-PBI** leads to the simultaneous formation of two absorption bands at 723 nm and 1285 nm, indicating the formation of the cationic species **4T**$^{\bullet+}$**-PBI** (Figure 96d, blue line). The lack of one thiophene moiety in the bridge causes a hypsochromic shift of 72 nm (1252 cm^{-1}) and 195 nm (1025 cm^{-1}) for both maxima, respectively, in comparison to **5T-PBI** oxidation (Figure 97a). As expected, within the macrocycle series up to **6T-PBI** these cation species spectra undergo a broadening as well as a bathochromic shift to 840 nm and 1633 nm, respectively (Figure 97a). Further oxidation to the dicationic species **4T**$^{2+}$**-PBI** (purple line) produces a strong absorption band at 953 nm (Figure 96d) which is shifted bathochromically for **5T**$^{2+}$**-PBI**[262] (Figure 97b). The appearance of one single peak in the dicationic state for **4T**$^{2+}$**-PBI** and **5T**$^{2+}$**-PBI** indicates the formation of a bipolaron (spinless dication) species causing minimal structural distortion of the bridge.[113] Interestingly, in the cases of **6T**$^{2+}$**-PBI** and **7T**$^{2+}$**-PBI** the rise of a second band at 585 nm and 598 nm with a higher intensity for the latter species can be monitored, respectively (Figure 97b, Figure 113). Presumably in these cases, a growing percentage of a polaron pair configuration with more structural contortion is formed as already described for a larger cyclic oligothiophene of ten subunits by Bäuerle and co-workers.[113] The polaron-pair state indicates localization of the charges in separated distorted segments of the sufficiently long oligothiophene π-system.

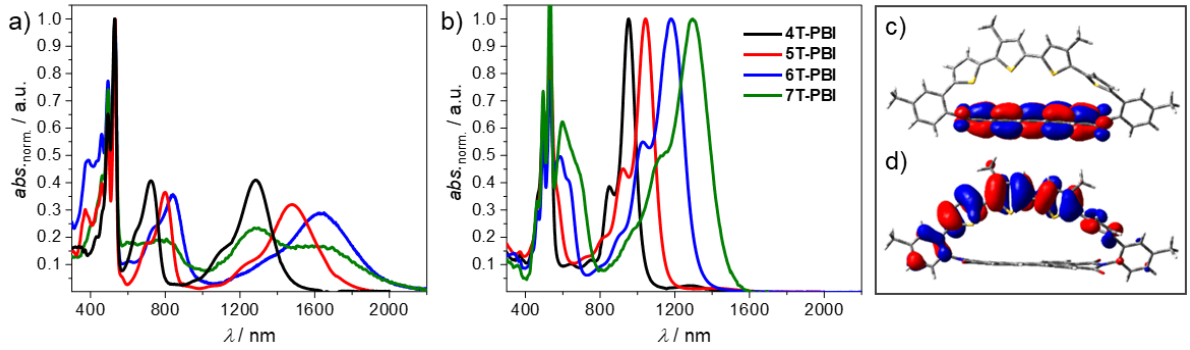

Figure 97. Normalized UV/Vis/NIR absorption spectra of the a) cations and b) dications of **4T-PBI** (black), **5T-PBI**[262] (red), **6T-PBI** (blue) and **7T-PBI** (green), respectively. All measurements were carried out in CH_2Cl_2 solutions with Bu_4NPF_6 at room temperature ($c_0 = 10^{-4}$ M). c) LUMO and d) HOMO of **4T-PBI** based on the molecular geometry received from X-ray analysis. The hexyl chains were omitted for clarity. The quantum mechanics calculations were carried out on the level of B3LYP density functional with the 6-31G(d) basis set as implemented in Gaussian 16.

The localization and shapes of the lowest unoccupied and highest occupied molecular orbital (LUMO/HOMO) of the neutral **4T-PBI** (Figure 97c/d) suggest as expected very little electronic communication between the electron-rich oligothiophene chain and electron-poor PBI acceptor segment. This idea is supported for all macrocycles by time-dependent density functional theory (TDDFT) calculations (Table 13), where the oscillator strengths for HOMO-LUMO transitions were determined to be negligible, which agrees well with the observed UV/Vis absorption spectra (*vide infra*), that show no indication for any charge transfer (CT) band. Optimized molecular geometries in the gas phase and respective HOMOs and LUMOs for **4T-PBI** to **7T-PBI** can be found in *Chapter 5.4* (Figure 117).

5.2.3 Steady State Optical Properties

UV/Vis spectroscopic investigations of the macrocycles **4T-PBI** to **7T-PBI** and **Ref-PBI**[262] were performed in CH_2Cl_2 (Figure 98). In comparison to the **Ref-PBI** with an absorption maximum ($\lambda_{abs,max}$) at 526 nm, all absorption maxima of the macrocycles exhibit a slight bathochromic shift of the PBI's S_0-S_1 absorption band (529-533 nm) by about 3 nm to 7 nm (107 cm^{-1} to 249 cm^{-1}) as well as a pronounced additional absorption band below 450 nm that can be attributed to their oligothiophene bridges.

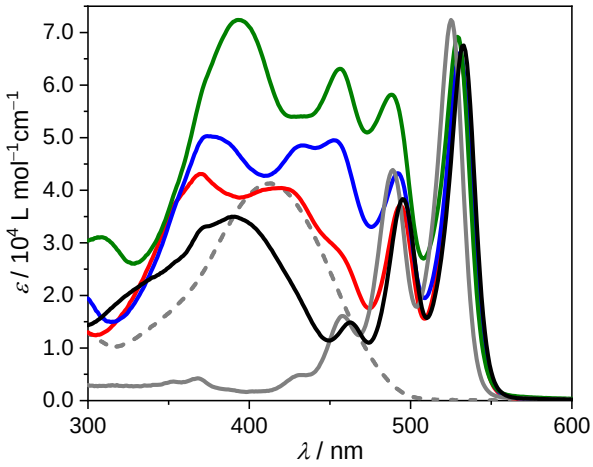

Figure 98. UV/Vis spectra of **4T-PBI** (black), **5T-PBI** (red line)[262], **6T-PBI** (blue), **7T-PBI** (green), **Ref-PBI** (solid grey) and **4T** (dashed grey)[235] in CH_2Cl_2 at room temperature (c_0=10^{-5} M).

In comparison to the structureless π-π* transition of their respective linear counterparts **4T-7T**[235], rigidification of the oligothiophene bridge within the macrocyclic arrangements leads to structured absorption spectra of **4T-PBI** to **7T-PBI** below 450 nm, which partially superimposes with the PBI´s S_0-S_1 transition (Figure 98). Unlike other PBI-oligothiophene

dyad systems[53, 55] the UV/Vis spectra of **4T-PBI** to **7T-PBI** are not simply a summation of the reference donor and acceptor spectrum. Depending on the donor bridge size, different dihedral angles and cisoid/transoid arrangements between the thiophene units lead to distinct conjugation lengths in each oligothiophene bridge. Concomitantly, partial breaking of conjugation may cause band splitting in the absorption spectra which is most pronounced in case of **6T-PBI**. With increasing oligothiophene length the corresponding lowest energy absorption band of the oligothiophene bridges undergo a bathochromic shift from 390 nm (**4T-PBI**) up to approximately 455 nm (**7T-PBI**). Thus, the degree of spectral overlap with the PBI´s S_0-S_1 transition becomes more and more pronounced. While the spectral regions of oligothiophene and PBI absorption in the case of **4T-PBI** are clearly distinguishable from each other, the absorption bands of the oligothiophene subunit in **7T-PBI** overlap strongly with the vibronic $A_{0\text{-}1}$ and $A_{0\text{-}2}$ transitions of the PBI. Accordingly, despite of the still pronounced $A_{0\text{-}0}$ band of PBI the lowest energy optically excited state may be located at the oligothiophene subunit for the longest bridge, in particular if we take the increased structural relaxation of oligothiophenes in their excited state into account.[185]

As has often been observed for donor-acceptor dyads, no fluorescence could be detected in solvents with higher polarity such as CH_2Cl_2 or $CHCl_3$, whereas **Ref-PBI** exhibits a quantum yield (Φ_{fl}) close to unity.[298] The electron donating oligothiophene subunit almost quantitatively quenches the PBI emission *via* photoinduced electron transfer (PET) resulting in Φ_{fl} values of less than 1% (Table 9) within the macrocycle series even in low polar cyclohexane. Also in cyclohexane, structured absorption spectra of the macrocycles (Figure 114, black solid lines) comprise features from both, the oligothiophene donor bridge at lower and the acceptor PBI at higher wavelengths. As the macrocyclic architectures **4T-PBI** to **7T-PBI** are composed of spectrally distinguishable oligothiophene and PBI subunits, we investigated the emission features of these systems upon excitation at two different wavelengths (λ_{ex}) at 350 nm and 480 nm. While for λ_{ex} = 480 nm primarily the PBI acceptor is excited, at 350 nm mainly the oligothiophene donor is excited. For a full comparison, the emission spectra of non-cyclic reference compounds **4T-7T** can be found in *Chapter 5.4* (Figure 115). Upon almost exclusive excitation of the oligothiophene unit of the macrocycles **4T-PBI** to **6T-PBI** at 350 nm (Figure 114, maroon solid lines) Förster Resonance Energy Transfer (FRET) from donor to acceptor moiety occurs and predominantly PBI emission can

be detected, as indicated by the characteristic vibronic emission profile of the PBI. Thus, these fluorescence spectra almost resemble those recorded upon selective excitation of the PBI at 480 nm (Figure 114, red solid lines). In contrast, upon oligothiophene excitation of the longer analogue in **7T-PBI** the FRET proceeds back and forth between donor and acceptor unit which may be due to an energetically low lying oligothiophene S_1 state (see above) and thus a superimposed emission of donor and acceptor can be monitored. This observation is confirmed by excitation at λ_{ex} = 480 nm leads to an emission spectrum, where both subunits seem to contribute.

Table 9. Photophysical properties of macrocycles **4T-PBI**, **5T-PBI**[262], **6T-PBI** and **7T-PBI** in solution (CH_2Cl_2 and cyclohexane) at room temperature.

	4T-PBI	**5T-PBI**[262]	**6T-PBI**	**7T-PBI**
$\lambda_{abs,max}$ [a]/ nm	533	531	531	529
ε_{max}[a] / 10^3 M^{-1} cm^{-1}	67.5	64.8	67.2	69.2
$\lambda_{abs,max}$ [b]/ nm	522	519	519	564
$\lambda_{em,max}$[b, c]/ nm	530	523	533	527
$\lambda_{em,max}$[b, d]/ nm	530	523	527	527
$\Delta\tilde{\nu}_{Stokes}$ [b]/ cm^{-1}	218	329	220	221
Φ_{fl}[b], [e]/ %	<1.0	<1.0	<1.0	<1.0

[a] CH_2Cl_2, $c_0 = 10^{-5}$ M. [b] Cyclohexane, $c_0 = 10^{-7}$ M. [c] λ_{ex} = 350 nm. [d] λ_{ex} = 480 nm [e] The fluorescence quantum yields of the PBI subunit were measured relative to *N,N'*-bis(2,6-diisopropylphenyl)-1,6,7,12-tetraphenoxy-perylene-3,4:9,10-bis(dicarboximide) as a reference[248] at four different excitation wavelengths in the spectral region of the PBI subunit.

5.2.4 Time-resolved Transient Absorption

For a better understanding of the fluorescence quenching process in the four macrocycles **4T-PBI** to **7T-PBI**, transient absorption (TA) spectroscopy was performed in CH_2Cl_2 solutions at 530 nm excitation with ca. 30 fs pulses which populate the S_1 state of the PBI moiety. TA spectra were obtained by probing the excited states by a delayed white light continuum between 490 nm and 910 nm. The thereby obtained transient spectra (see Figure 118-120) were deconvoluted by a global analysis employing a consecutive kinetic model which yielded evolution associated difference spectra (EADS). These EADS are associated with specific lifetimes and are presented for **4T-PBI** to **7T-PBI** in Figure 99. For all macrocycles the first EADS (black spectrum) shows a negative signal at 530 nm which is caused by a ground state

bleaching (GSB) of the PBI chromophore. Stimulated emission (SE) of the PBI is observed as a negative signal at 580 nm and also overlapping with the GSB at 530 nm (Figure 99).

The three dyads with more extended oligothiophene chains (**5T-PBI** to **7T-PBI**) exhibit very similar EADS and photoinduced dynamics that will be discussed here in more detail for **7T-PBI**. Thus, the first EADS of **7T-PBI** has a lifetime of 0.3 ps that refers to the S_1 state of the PBI. It is followed by a second EADS (red spectrum) where the SE is replaced by an excited state absorption (EA) which extends from ca. 500 nm to 850 nm with maxima at 700 nm and 800 nm. This EADS is very similar to that of PBI radical anion,[229] (also compare blue line in Figure 112a), and proves the formation of a charge separated state (CSS). The lifetime of the foregoing EADS (0.3 ps) thus is limited by the charge separation (CS) process with $k_{CS} = (0.3\ \text{ps})^{-1}$. The following blue EADS is very similar to the red EADS. Therefore, the former is interpreted to be a hot CSS which transforms by molecular and solvent relaxation processes to the cold CSS with $k = (1.2\ \text{ps})^{-1}$.

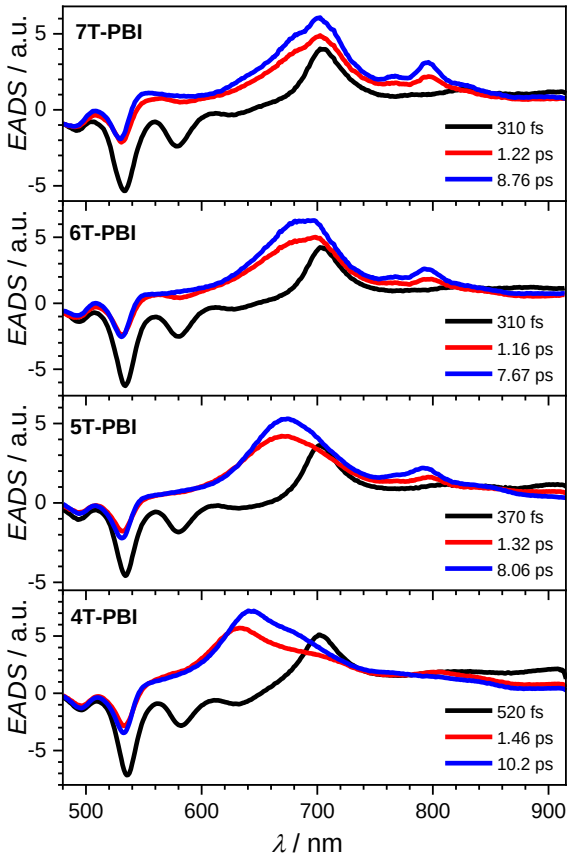

Figure 99. EADS and respective lifetimes from a global fit analysis of the transient spectra of macrocycles **4T-PBI**, **5T-PBI**[262], **6T-PBI** and **7T-PBI** obtained by excitation at 530 nm in CH_2Cl_2 ($c_0 = 10^{-4}$ M).

The lifetime of the cold CSS (8.8 ps) then refers to charge recombination with k_{CR} = (8.8 ps)$^{-1}$ to the ground state since no other components were found in the analysis of the TA spectra. While the spectral shape of the EADS of the singlet PBI state is the same for all four macrocycles, the rate of CS gradually decreases from (0.3 ps)$^{-1}$ to (0.5 ps)$^{-1}$ within that series. Nevertheless, these CS processes are among the fastest for PBI-oligothiophene dyads known in literature.[52-53, 230, 262] A TA control experiment with a 1:1 mixture of linear **4T**[235] and **Ref-PBI**[262] under the same conditions as utilized for the macrocycles reveals exclusive formation of the PBI's S_1 state with a lifetime of 3.5 ns (Figure 123) which underlines that the fast charge separation process is due to the covalent linkage of the two chromophores in **4T-PBI** to **7T-PBI**.

In a more detailed analysis we note that the spectral shape of the blue EADS changes gradually from **7T-PBI** to **5T-PBI** (Figure 99), that is, the maximum at 700 nm blue-shifts to 640 nm and a small band at 800 nm decreases in intensity. This is interpreted as a gradual decrease of the extent of charge separation from **7T-PBI** to **5T-PBI**, which is confirmed by a comparison of the respective "cold" EADS with the sum of anion and cation spectra obtained from SEC in Figure 126. Thus, while for **7T-PBI** comparison with aforementioned SEC spectra suggest full CS, for the other dyads the degree of CS is reduced. Most notably, for the smallest oligothiophene bridged **4T-PBI** we interpret the spectra as being due to the formation of a CT state with only partial negative charge (δ^-) at the PBI and partial positive charge (δ^+) at the thiophene bridge. Interestingly, the lifetime of the CT state of **4T-PBI** (10.2 ps) is not much different from that of the full CSS of **7T-PBI** (8.8 ps). This shows that in the present cases the spectral signatures of the CS/CT states are much more sensitive to the extent of charge distribution than the kinetics.

Whilst the detection of the PBI radical anion is straightforward due to their intense and characteristic bands in the visible and NIR region,[229] the detection of the corresponding radical cations of oligothiophenes are more challenging. To prove the positive charge residing on the oligothiophene bridge we probed the excited states of **5T-PBI** in the NIR upon excitation at 400 nm (Figure 122, Figure 124b). A broad band between 1200-1450 nm is in good agreement with SEC measurements of the radical cation species (Figure 125). Thus, while the TA spectra in the visible range indicates partial negative charge on the PBI moiety

(Figure 121, Figure 124a), the NIR part of the TA spectra prove a full positive charge located at the oligothiophene subunit. In other words, the centre of a dipole moment difference vector representing the charge transfer is located nearer to the oligothiophene. In that way, TA spectroscopy in comparison with SEC can give rather detailed insight into the charge distribution of such CT states. In the UV/Vis region, excitation at 400 nm reveals similar EADS spectra for **5T-PBI** (Figure 124a) in comparison to an excitation of the same compound at 530 nm[262]. Here, presumably due to the extremely close proximity of donor and acceptor an unresolvable fast energy transfer from the oligothiophene bridge to the PBI chromophore in the lower femtosecond region occurs. Thus, independent of oligothiophene or PBI excitation wavelength (400 nm or 530 nm) the TA spectra remain similar.

Due to the limited solubility of the macrocycles as well as additional solvent artefacts in cyclohexane no TA could be recorded in this nonpolar solvent to gain additional insights in the PET in solvents of low polarity.

5.3 Conclusion

In this study we synthesized as series of novel macrocyclic perylene bisimide dyads comprising quarter-, quinque-, sexi- and septithiophene bridges that connect both imide positions. The final macrocyclization reaction was realized by applying a three step Pt-catalyzed cross coupling procedure. These unique molecular architectures containing a planar PBI acceptor and tether-like donor moieties, which are electronically independent due to their connectivity, were compared to their corresponding linear reference subunit systems revealing differences regarding absorption, emission and electrochemical properties. X-ray analysis in line with NMR spectroscopy provided valuable structural insights into the smallest and largest macrocycle showing large torsional angles among the thiophene rings and a dimer arrangement with π-π-stacked PBI subunits in the solid state. Due to a highly efficient photoinduced electron transfer process these donor-acceptor systems are almost non-fluorescent even in low polar solvents such as cyclohexane. According to the spectral signatures in the excited state investigated by transient absorption spectroscopy, the larger oligothiophene bridge sizes support full charge separation into oligothiophene radical cations and PBI radical anions whilst a charge transfer state with incomplete separation is observed for the dyad with the smallest quarterthiophene bridge.

5.4 Supporting Information to Chapter 5

General methods

All reactions were performed in standard glass equipment. All used chemicals were purchased from commercial suppliers (*abcr/carbolution chemicals*, *Acros Organics*, *Alfa Asear*, *Merck*, *Sigma Aldrich*, *TCI* and *VWR*) and applied without further purification. The synthesis of stannylated oligothiophenes **80**[313], **76**[261] and **81**[233] is literature known. The preparation of compound **74** and **5T-PBI**[262] as well as reference oligothiophenes **4T-7T** and stannylated compound **62**[235] were reported recently.

THF, CH_2Cl_2, and toluene were purified and dried with the commercial purification system PureSolv MD from *Innovative Technology*. The solvent *m*-xylene was dried over molecular sieves prior to use.

Flash column chromatography was performed on a PuriFLash XS-420 from *Interchim* using columns of the size 0025. The purification by gel permeation chromatography was performed on a *Shimadzu* (LC-20AD Prominence Pump, SPD-MA20A Prominence Diode Array Detector) with two preparative columns (*Japan Analytical Industries Co., Ltd).* Ethanol stabilised $CHCl_3$ (Chromasolv®, *Sigma Aldrich*) was used as eluent.

MALDI-TOF mass spectra were measured with an ultrafleXtreme from *Bruker Daltonics GmbH* using *trans*-2-[3-(4-*tert*-butylphenyl)-2-methyl-2-propenylidene]malono-nitrile (DCTB) as a matrix material.

^1H and ^{13}C NMR spectra were recorded on a *Bruker* Avance III HD 400 MHz using deuterated solvents. ^{13}C NMR spectra are broad band proton decoupled. Chemical shifts (δ) are listed in parts per million (ppm) and are reported relative to tetramethyl silane (TMS). Coupling constants (J) are stated in Hertz (Hz). The spectra are referenced internally to residual proton solvent resonances or natural abundance carbon resonances. Multiplicities are reported as s = singlet, brs = broad singlet, d = doublet, dd = doublet of doublets, t = triplet, dt = doublet of triplets, q = quartet, quin = quintet, sex = sextet, m = multiplet with the chemical shift in the center of the signal.

UV/Vis absorption spectra were recorded with solutions of the compounds in cuvettes (SUPRASIL®, *Hellma® Analytics*) on a Jasco V-670 or V-770 spectrometer and fluorescence spectra on a FLS980-D2D2-ST fluorescence spectrometer (*Edinburgh Instruments*) and were corrected against the photomultiplier sensitivity and the lamp intensity.

Spectroelectrochemical experiments were performed on a Cary 5000 UV/Vis/NIR spectrometer from *Agilent* in combination with a sample compartment consisting of a custom-made cylindrical PTFE cell with a sapphire window and an adjustable three in one electrode (6 mm platinum disc working electrode, 1 mm platinum counter and Ag/AgCl leak free reference electrode) in reflection mode. The optical path was adjusted to 100 µm with a micrometer screw. Potentials were applied with a reference potentiostat PAR 283 from *Princeton Applied Research.* Upon applying a new potential to the solution an equilibration time of 20 seconds between each measurement was employed.

The transient absorption spectrometer setup for the excitation at 530 nm is based on a femtosecond laser "Solstice" from *Newport-Spectra Physics* with a fundamental wavelength of 800 nm which provides 100 fs long pulses with a repetition rate of 1 kHz. This laser source was used to pump a NOPA to generate the excitation pulses at 530 nm with a pulse length <50 fs. The FWHM-bandwidth of the excitation pulse was 8.5 nm and the pulse energy was set to 20 nJ. Wire grid polarizers were used to set the pump pulse polarization to 54.7° in relation to the horizontal polarized white light continuum to achieve magic angle conditions. Another part of the laser beam was guided to a TOPAS-C from *Light-Conversion* to obtain a wavelength from 1000 nm, which was used to generate the probing white light continuum within a sapphire crystal. To achieve the probe range from 455 nm to 915 nm a dielectrically coated quartz glass short pass filter with 950 nm, thickness 3 mm, from *Edmund-Optics* were used. The sample was dissolved in spectroscopic grade CH_2Cl_2 from ACROS organics and the solution was filled in a quartz glass cuvette with an optical path length of 2 mm. The optical density at the excitation wavelength was set to 0.34 for **4T-PBI**, 0.50 for **5T-PBI**[262], 0.32 for **6T-PBI** and 0.30 for **7T-PBI**. The IRF was 60-100 fs as measured for stimulated Raman signals of the solvent. Further details on this spectrometer setup are provided in ref. [302].

For the transient absorption spectrometer setup excitation at 400 nm the same laser source was used to pump a TOPAS to generate the excitation pulses at 400 nm with a pulse length <150 fs.

The FWHM-bandwidth of the excitation pulse was 1.7 nm and the pulse energy was set to 20 nJ. Wire grid polarizers were used to set the pump pulse polarization to 54.7° in relation to the horizontal polarized white light continuum to achieve magic angle conditions. Another part of the laser beam was guided to a TOPAS-C from *Light-Conversion* to obtain a wavelength from 800 nm, which was used to generate the probing white light continuum within a 15 mm sapphire crystal. To achieve the probe range from 771 nm to 1501 nm a coloured glass filter with 850 nm from *Edmund-Optics* were used. The sample was dissolved in spectroscopic grade CH_2Cl_2 from ACROS organics and the solution was filled in a quartz glass cuvette with an optical path length of 0.2 mm. The optical density at the excitation wavelength was set to 0.34 for **5T-PBI**. The IRF was 70 fs as measured for stimulated Raman signals of the solvent.

Cyclic and differential pulse voltammetry experiments were carried out with a *BASi* Epsilon potentiostat connected to a microcell apparatus from *rhd instruments* involving a 1.6 mL sample container, a platinum counter- and pseudo-reference electrode as well as a glassy carbon working electrode. The compounds were dissolved in CH_2Cl_2 and Bu_4NPF_6 was added as supporting electrolyte.

Single crystal X-ray diffraction data of **4T-PBI** were collected at 100 K on a Bruker D8 Quest Kappa Diffractometer using CuK_α-radiation (λ = 1.54178 Å) from an Incoatec IμS microsource with Montel multi layered mirror with a Photon II CPAD detector. The structure was solved using direct methods, expanded with Fourier techniques and refined with the SHELX software package.[301] All non-hydrogen atoms were refined anisotropically. Hydrogen atoms were included in the structure factor calculation on geometrically idealized positions. The compound **4T-PBI** crystallizes as red plates that scatter very weakly. Multiple attempts were made to grow better diffracting crystals. Crystals that are better suitable for single X-Ray diffraction studies were grown from dibromomethane/*n*-hexane. However, the data yielded problems due to weak diffraction and disorder in the atom position of the side-chains and of the solvent. A large amount of disorder in the side chains and in the solvent was observed which made it difficult to model the chains and the solvent. Therefore restrains were applied to the atoms in the disorder. Alerts originated from the large amount of disorder in the side chains and in the solvent.

Single crystal X-ray diffraction data of **7T-PBI** were collected at the P11 beamline at DESY. The diffraction data were collected by a single 360° scan ϕ sweep at 100 K. The diffraction data were indexed, integrated, and scaled using the XDS program package.[299] The structures were solved using SHELXT,[314] expanded with Fourier techniques and refined using the SHELX software package.[315] Hydrogen atoms were assigned at idealized positions and were included in the calculation of structure factors. All non-hydrogen atoms in the main residue were refined anisotropically. The diffraction data had a resolution of ca. 1.5 Å (defined by the resolution shell with intensity $I > 2\sigma$). For refinement diffraction data until 1.1 Å were used. In the crystal structure, the four crystallographic isomers found in the asymmetric unit cell were restrained by the SAME command of SHELX due to low resolution of diffraction data. All the alkyl substituents had heavy disorder and were modelled with constraints and restraints using standard SHELX commands RIGU, DELU, ISOR, SADI, DFIX, DANG, EADP, FLAT, CHIV, and SIMU. A similar set of commands were used to model solvents found in solvent accessible voids.

The diffraction of this crystal was not satisfactory for normal criteria of small molecule crystallography. This is due to the large molecular structure and thus large unit cell similar to those of macromolecular crystals. Nevertheless, diffraction data were good enough to elucidate the packing motif of this molecule and therefore solved with a resolution of ca. 1.6 Å. Diffraction data down to 1.1 Å were used for refinement and this treatment caused A-levelsome Alerts in the Checkcif routine. Due to cutoff of diffractions below 1.1 Å the data / parameter ratio needed to as low as 5.62. The weighted R factor (wR_2) was high (0.47) due to inclusion of weakly diffracting data between 1.6 and 1.1 Å. Due to the low data / parameter ratio and disorder of solvent molecules (chlorobenzene and methanol) the shift/error during the last step of refinement was as large as 0.65.

DFT and TD-DFT calculations were performed by Gaussian 16[303] using B3LYP/6-31G(d) level of theory.

Synthetic Procedure

Typical procedure for macrocyclization reactions

A stirring solution of Pt-complex **74** (50.0 mg, 32.3 μmol, 1.0 eq.) in degassed toluene (40 mL) was stirred and stannylated oligothiophene compounds (35.5 μmol, 1.1 eq.) in degassed toluene (1.0 mL) were added dropwise *via* a syringe pump over 15 h. Then the reaction mixture was stirred overnight at 75 °C. The solvent was removed *in vacuo* and the crude residue was washed with *n*-hexane. The crude product was redissolved in degassed CH_2Cl_2 (40 mL) and 1,1'-bis(diphenylphosphino)ferrocene (39.4 mg, 71.0 μmol, 2.2 eq.) was added. The solution was stirred for 6 h at room temperature. The solvent was removed *in vacuo* and the residue was redissolved in degassed *m*-xylene (40 mL) and stirred overnight at 120 °C. The solvent was removed under reduced pressure and the crude product was purified *via* flash column chromatography (CH_2Cl_2/*n*-hexane = 1:1 to 1:0) and gel permeation chromatography ($CHCl_3$) to give the desired compounds.

4T-PBI

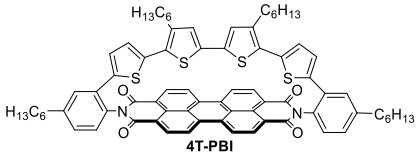

Yield: 5.29 mg, 4.39 µmol, 14%, red solid. **^{1}H NMR** (400 MHz, CD_2Cl_2): δ/ppm = 8.68 (d, ^3J = 8.2 Hz, 4H), 8.64 (d, ^3J = 7.9 Hz, 4H), 7.69 (d, ^4J = 1.5 Hz, 2H), 7.51 (d, ^3J = 8.0 Hz, 2H), 7.47 (dd, ^3J = 8.0 Hz, ^4J = 1.9 Hz, 2H), 7.25 (d, ^3J = 3.8 Hz, 2H), 6.88 (d, ^3J = 3.8 Hz, 2H), 6.88 (s, 2H), 2.85 (t, ^3J = 7.7 Hz, 4H), 2.48 (t, ^3J = 7.7 Hz, 4H), 1.83 (quin, ^3J = 7.3 Hz, 4H), 1.22-1.51 (m, 28H), 0.98 (t, ^3J = 7.1 Hz, 6H), 0.87 (t, ^3J = 6.8 Hz, 6H). **^{13}C NMR** (101 MHz, CD_2Cl_2): δ/ppm = 164.3, 145.1, 142.0, 139.3, 135.8, 135.4, 132.2, 131.8, 130.1, 129.7, 129.2, 128.3, 127.0, 126.9, 126.8, 124.0, 132.8, 36.2, 32.2, 31.9, 31.8, 30.8, 29.6, 29.4, 29.2, 23.0, 22.9, 14.3, 14.2. **HRMS** (MALDI-TOF, positive mode, DCTB in $CHCl_3$): *m/z* calculated for $C_{76}H_{72}N_2O_4S_4$ $[M]^+$: 1204.4375, found: 1204.4369. **UV/Vis** λ_{max} (ε_{max}): CH_2Cl_2: 533 nm (67.5 × 10^3 L mol^{-1} cm^{-1}). **Fluorescence** λ_{max} (λ_{ex}): Cyclohexane: 530 nm (480 nm), 530 nm (400 nm). **PLQY**: Φ_{fl} = <1%. **R_f**: 0.22 using CH_2Cl_2 as eluent.

6T-PBI

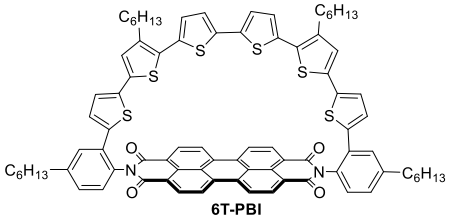

Yield: 5.85 mg, 4.27 µmol, 13%, orange solid. **^{1}H NMR** (400 MHz, CD_2Cl_2): δ/ppm = 8.79 (d, ^3J = 8.21 Hz, 4H), 8.74 (d, ^3J = 7.9 Hz, 4H), 7.74 (d, ^4J = 1.9 Hz, 2H), 7.41 (d, ^3J = 4.0 Hz, 2H), 7.34 (dd, ^3J = 8.0 Hz, ^4J = 1.9 Hz, 2H), 7.23 (d, ^3J = 3.9 Hz, 2H), 7.17 (d, ^3J = 8.0 Hz, 2H), 7.14 (d, ^3J = 3.8 Hz, 2H), 7.08 (s, 2H), 6.94 (d, ^3J = 3.8 Hz, 2H), 2.80 (t, ^3J = 7.9 Hz, 4H), 2.70 (t, ^3J = 7.9 Hz, 4H), 1.78 (quin, ^3J = 7.2 Hz, 4H), 1.60 (quin, ^3J = 7.2 Hz, 4H),1.45-1.25 (m, 24H), 0.94 (t, ^3J = 7.1 Hz, 6H), 0.86 (t, ^3J = 7.1 Hz, 6H). **^{13}C NMR** (101 MHz, CD_2Cl_2): δ/ppm = 164.3, 145.0, 141.4, 138.8, 138.1, 136.3, 135.8, 135.5, 135.0, 133.3, 132.3, 130.4,

130.2, 130.1, 129.7, 129.5, 129.4, 127.9, 127.4, 127.3, 126.3, 124.1, 124.1, 124.0, 123.7, 36.1, 32.2, 32.0, 31.7, 30.6, 29.6, 29.5, 23.1, 23.0, 14.3, 14.2. **HRMS** (MALDI-TOF, positive mode, DCTB in $CHCl_3$): *m/z* calculated for $C_{84}H_{76}N_2O_4S_6$ $[M]^+$: 1368.4129, found: 1368.4124. **UV/Vis** λ_{max} (ε_{max}): CH_2Cl_2: 531 nm (67.2×10^3 L mol^{-1} cm^{-1}). **Fluorescence** λ_{max} (λ_{ex}): Cyclohexane: 527 nm (480 nm), 533 nm (400 nm). **PLQY**: Φ_{fl} = <1%. **R_f**: 0.51 using CH_2Cl_2 as eluent.

7T-PBI

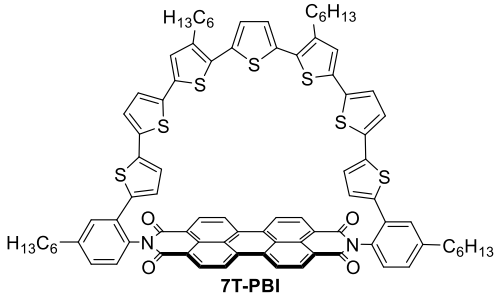

Yield: 1.49 mg, 1.03 µmol, 3%, orange solid. **^{1}H NMR** (600 MHz, CD_2Cl_2): δ/ppm = 8.75 (d, ^3J = 8.4 Hz, 4H), 8.71 (d, ^3J = 7.9 Hz, 4H), 7.54 (d, ^4J = 1.8 Hz, 2H), 7.39 (dd, ^3J = 8.0 Hz, ^4J = 1.9 Hz, 2H), 7.29 (d, ^3J = 8.0 Hz, 1H), 7.10 (d, ^3J = 3.7 Hz, 2H), 7.07 (s, 2H),), 7.06 (d, ^3J = 3.7 Hz, 2H), 7.05 (s, 2H), 6.85 (d, ^3J = 3.8 Hz, 2H), 6.82 (d, ^3J = 3.8 Hz, 2H), 2.80 (t, ^3J = 7.9 Hz, 4H), 2.79 (t, ^3J = 7.9 Hz, 4H), 1.79 (quin, ^3J = 7.6 Hz, 4H), 1.69 (quin, ^3J = 7.6 Hz, 4H), 1.45-1.35 (m, 24H), 0.95 (t, ^3J = 7.4 Hz, 6H), 0.87 (t, ^3J = 7.4 Hz, 6H). **^{13}C NMR** (150 MHz, CD_2Cl_2): δ/ppm = 164.1, 145.2, 140.9, 139.9, 137.4, 136.7, 136.1, 136.0, 135.6, 135.0, 133.1, 132.3, 131.1, 131.0, 130.4, 130.3, 129.9, 129.4, 127.3, 126.2, 126.1, 125.7, 125.2, 125.1, 123.9, 123.7, 123.6, 36.1, 32.2, 32.1, 31.7, 30.5, 30.1, 29.8, 29.6, 23.1, 23.0, 14.3, 14.2. **HRMS** (MALDI-TOF, positive mode, DCTB in $CHCl_3$): *m/z* calculated for $C_{88}H_{78}N_2O_4S_7$ $[M]^+$: 1450.4007, found: 1450.4001. **UV/Vis** λ_{max} (ε_{max}): CH_2Cl_2: 529 nm (69.2×10^3 L mol^{-1} cm^{-1}). **Fluorescence** λ_{max} (λ_{ex}): Cyclohexane: 527 nm (480 nm), 527 nm (400 nm). **PLQY**: Φ_{fl} = <1%. **R_f**: 0.30 using CH_2Cl_2 as eluent.

Possible Reaction Mechanism for the Macrocyclization

A possible reaction mechanism starting with Pt-complex **74** for the final macrocyclization reaction is proposed exemplarily for **4T-PBI** below (Figure 100). All reaction intermediates (**IN1**-**IN4**) were not isolated.

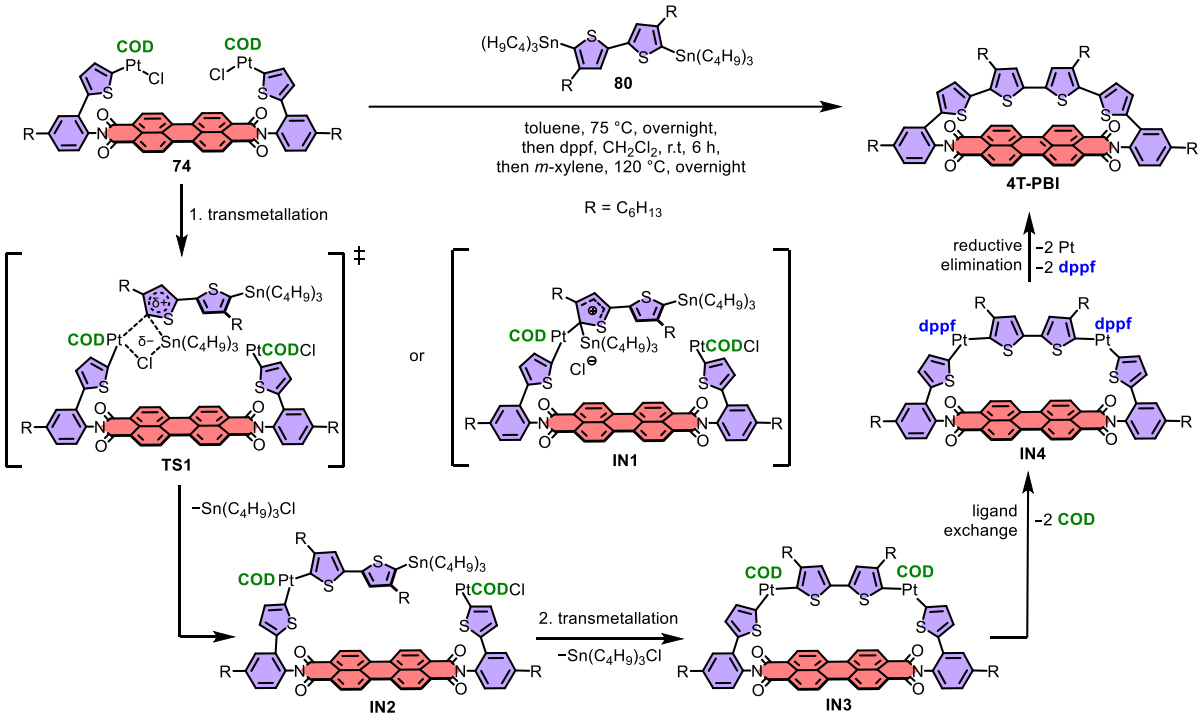

Figure 100. Proposed reaction mechanism for the formation of **4T-PBI** starting from Pt-complex **74**.

The addition of stannylated bithiophene **80** to Pt-precursor **74** leads to one *inter*- (**IN2**) and one *intra*molecular (**IN3**) transmetallation. As proposed by Eaborn *et al.*[176] for similar complex formations of $PtCODCl_2$ with aryl stannanes, this is presumably either achieved *via* a four-centre transition state **TS1** or a Wheland like intermediate **IN1**. This reaction step is conducted under *pseudo* high dilution conditions to favor the desired *intra*molecular Pt-complex formation after the first transmetallation. It is unknown whether both transmetallation steps proceed in a concerted way or stepwise. Concerning the confirmation of the oligothiophene chain, most likely a *cis*-orientation is already present at the Pt-complex step (**IN3**) in order to accommodate for the square-planar Pt-complex geometry and sterical demand of the attached hexyl chains R.

Next, a ligand COD-dppf exchange reaction yields **IN4**. The dppf ligand is utilized to facilitate the subsequent reductive elimination which was demonstrated for *cis*-Pt-(ArAr')

complexes.[178] This last step is conducted at elevated temperatures of 120 °C to initiate the thermally induced reductive elimination.[316]

Table 10. Crystal data and structure refinement for **4T-PBI**.

CCDC number	2143611	
Empirical formula	$C_{77}H_{74}Br_2N_2O_4S_4$	
Formula weight	1379.44 g/mol	
Temperature	100(2) K	
Wavelength	1.54178 Å	
Crystal system	Triclinic	
Space group	$P\bar{1}$	
Unit cell dimensions	a = 8.0721(3) Å	α = 91.307(2)°
	b = 19.3157(6) Å	β = 97.059(2)°
	c = 21.4211(7) Å	γ = 101.619(2)°
Volume	3242.81(19) Å^3	
Z	2	
Density (calculated)	1.413 g/cm^3	
Absorption coefficient	3.208 mm^{-1}	
F(000)	1432	
Crystal size	0.158 × 0.064 × 0.020 mm	
Theta range for data collection	2.338 to 72.465 °	
Index ranges	$-9 \le h \le 9$, $-23 \le k \le 23$, $-26 \le l \le 26$	
Reflections collected	87488	
Independent reflections	12757 [R_{int} = 0.0531]	
Completeness to theta = 67.679 °	99.9%	
Absorption correction	Semi-empirical from equivalents	
Refinement method	Full-matrix least-squares on F^2	
Data / restraints / parameters	12757 / 296 / 914	
Goodness-of-fit on F^2	1.031	
Final R indices [I > 2sigma(I)]	R_1 = 0.0840, wR_2 = 0.2460	
R indices (all data)	R_1 = 0.0947, wR_2 = 0.2585	
Extinction coefficient	n/a	
Largest diff. peak and hole	1.373 and –1.420 e·Å^{-3}	

Table 11. Crystal data and structure refinement for **7T-PBI**.

CCDC number	2143364
Empirical formula	$C_{400.63}\ H_{312}\ Cl_{3.40}\ N_8\ O_{44.25}\ S_{28}$
Formula weight	6964.24 g/mol
Temperature	100(2) K
Wavelength	0.61992 Å
Crystal system	Monoclinic
Space group	$P2_1/n$
Unit cell dimensions	a = 16.717(19) Å α = 90°
	b = 57.42(5) Å β = 90.59(4)°
	c = 37.86(4) Å γ = 90°
Volume	36340(65) $Å^3$
Z	4
Density (calculated)	1.273 g/cm^3
Absorption coefficient	0.179 mm^{-1}
F(000)	14526.1
Crystal size	0.100 × 0.100 × 0.050 mm^3
Theta range for data collection	0.562 to 16.367°.
Index ranges	−15≤h≤15, −52≤k≤52, −34≤l≤34
Reflections collected	200878
Independent reflections	28320 [R_{int} = 0.1509]
Completeness to theta = 16.367°	99.0 %
Absorption correction	None
Refinement method	Full-matrix least-squares on F^2
Data / restraints / parameters	28320 / 10992 / 5088
Goodness-of-fit on F^2	1.327
Final R indices [I>2sigma(I)]	R_1 = 0.1568, wR_2 = 0.3885
R indices (all data)	R_1 = 0.2946, wR_2 = 0.4729
Extinction coefficient	n/a
Largest diff. peak and hole	0.563 and −0.271 $e·Å^{-3}$

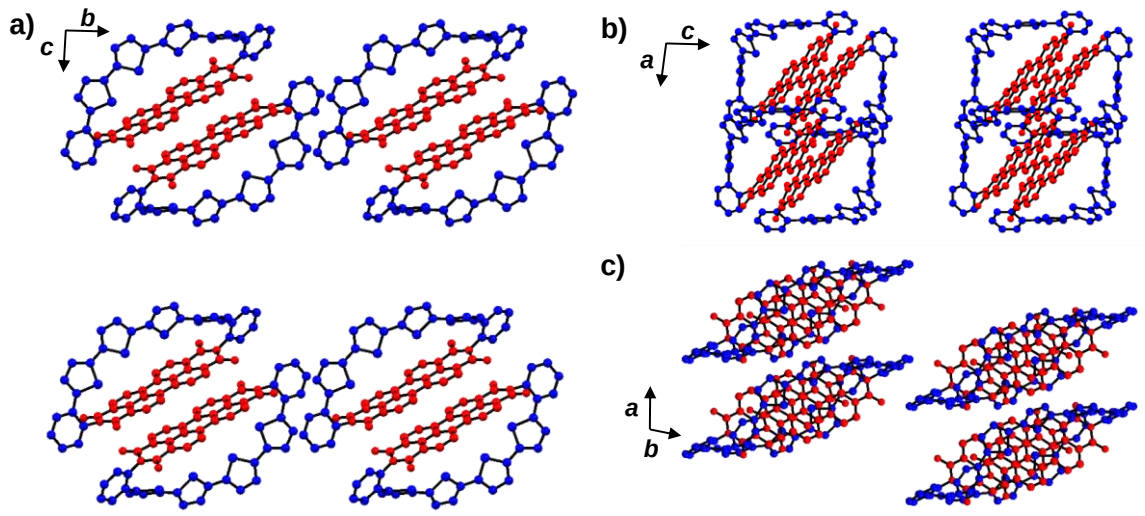

Figure 101. Crystal packing of **4T-PBI** seen along the a) *a*-, b) *b*-, and c) *c*-axes, respectively. PBI chromophores are coloured in red and the oligothiophene bridge in blue. Disordered aliphatic chains as well as solvent molecules were omitted for clarity.

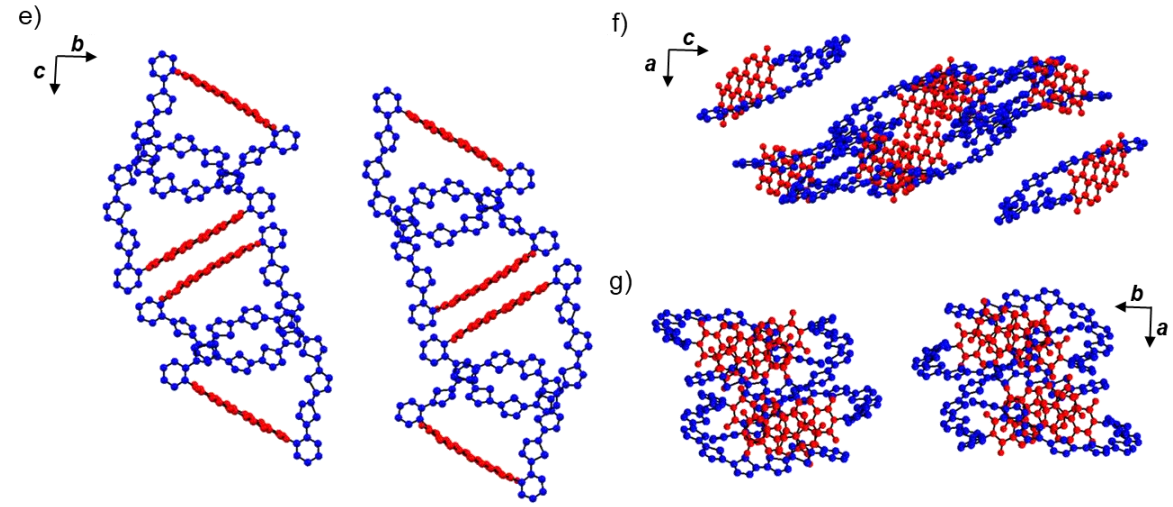

Figure 102. Crystal packing of **7T-PBI** seen along the a) *a*-, b) *b*-, and c) *c*-axes, respectively. PBI chromophores are coloured in red, the oligothiophene bridge in blue. Disordered aliphatic chains as well as solvent molecules were omitted for clarity.

^{1}H NMR Spectra Comparison

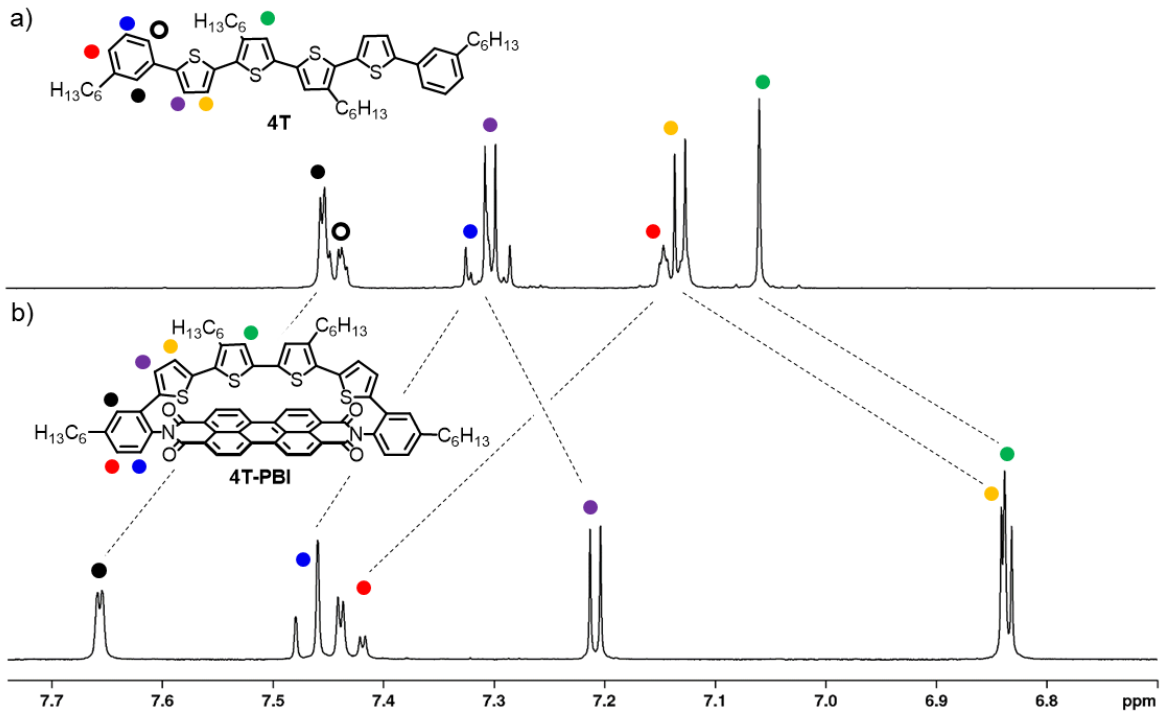

Figure 103. Excerpt of the ^{1}H NMR spectra of a) oligothiophene moiety **4T**[235] and b) **4T-PBI** in CD_2Cl_2 at room temperature.

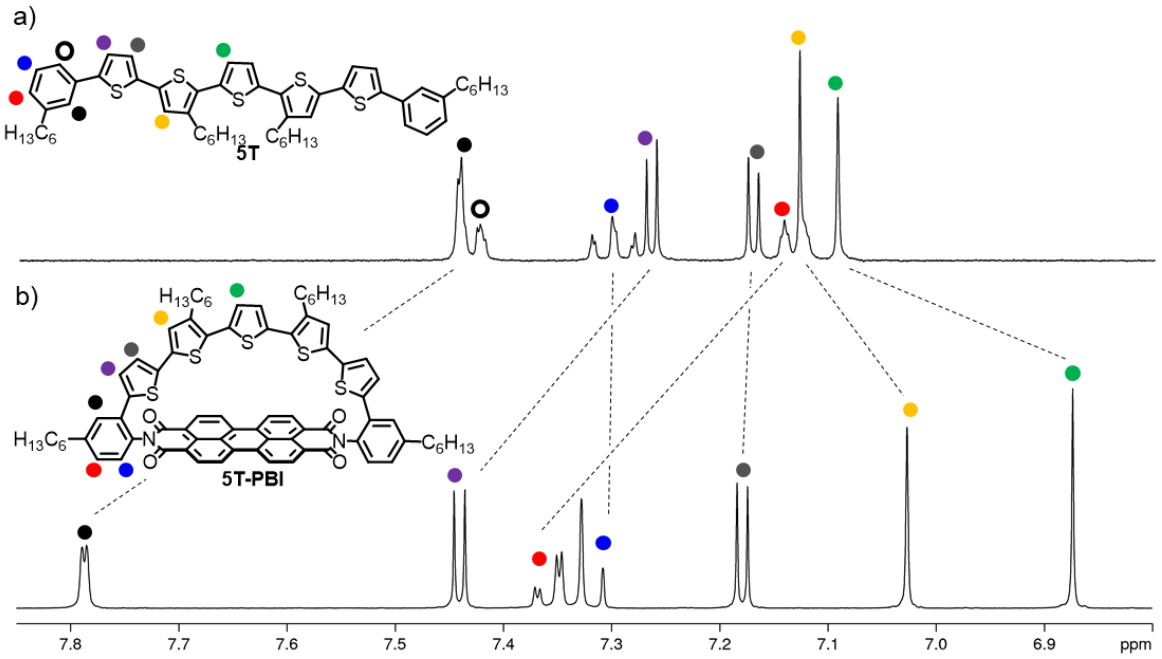

Figure 104. Excerpt of the ^{1}H NMR spectra of a) oligothiophene moiety **5T**[235] and b) **5T-PBI**[262] in CD_2Cl_2 at room temperature.

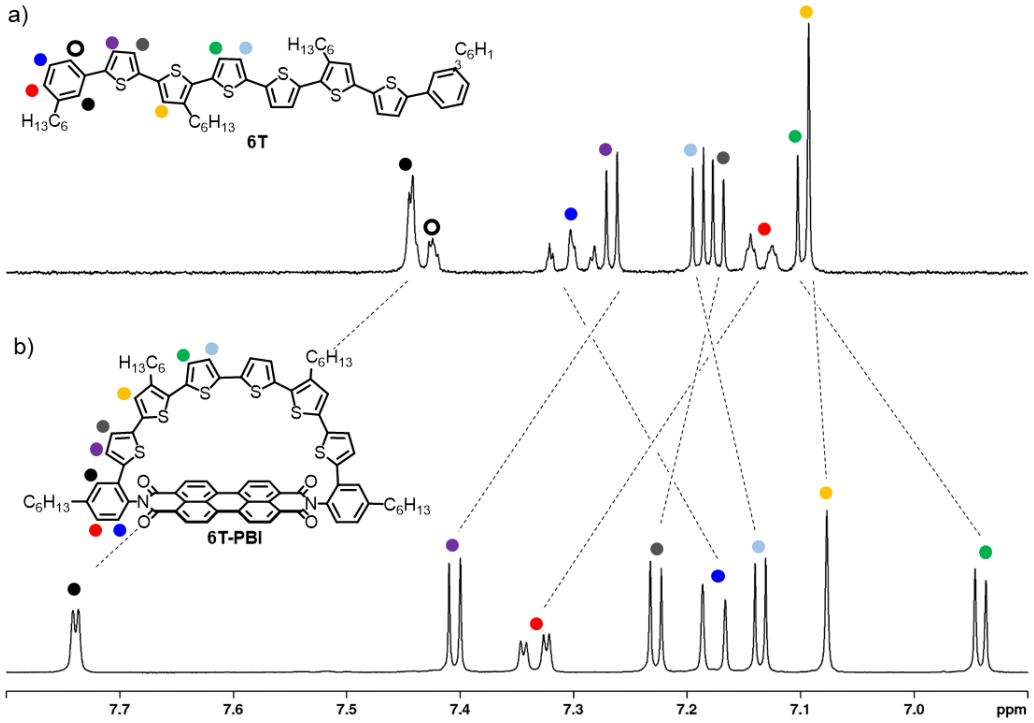

Figure 105. Excerpt of the ^{1}H NMR spectra of a) oligothiophene moiety **6T**[235] and b) **6T-PBI** in CD_2Cl_2 at room temperature.

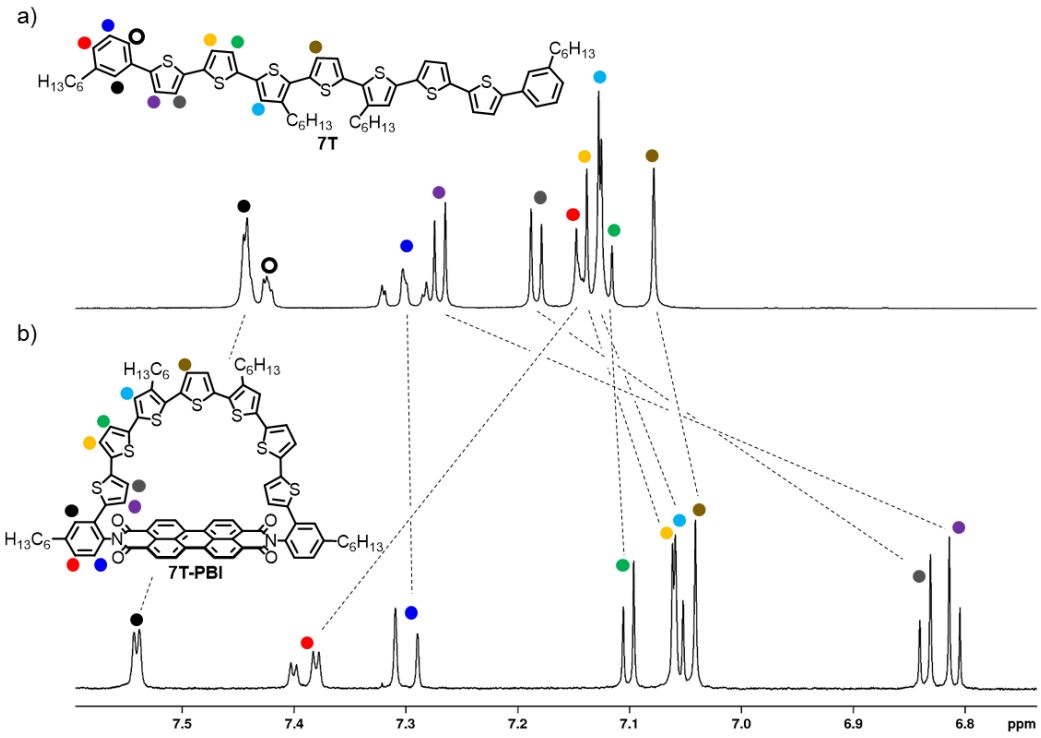

Figure 106. Excerpt of the ^{1}H NMR spectra of a) oligothiophene moiety **7T**[235] and b) **7T-PBI** in CD_2Cl_2 at room temperature.

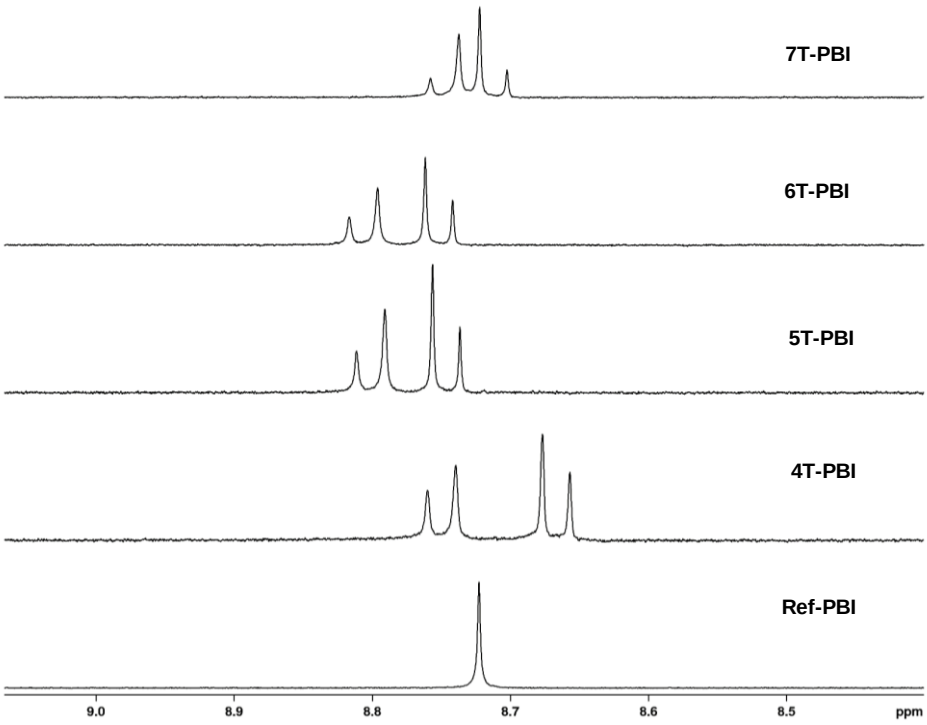

Figure 107. PBI proton signals of **Ref-PBI** in comparison to those of the macrocycles **4T-PBI**, **5T-PBI**[262], **6T-PBI** and **7T-PBI** (from bottom to top). ^{1}H NMR spectra were recorded in CD_2Cl_2 at room temperature at equal concentrations of $c_0 = 10^{-4}$ M.

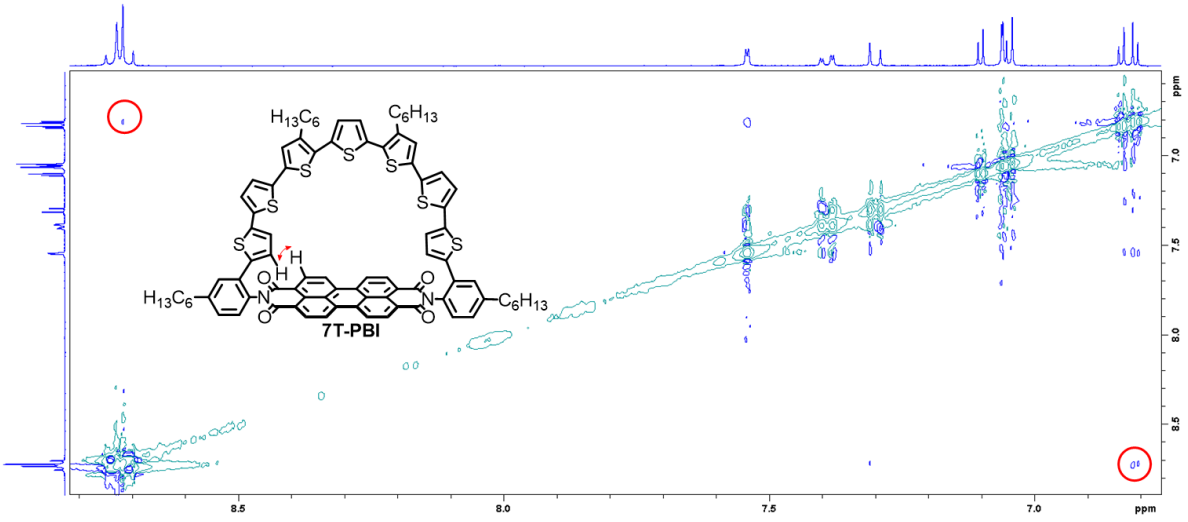

Figure 108. Excerpt of the ROESY spectrum of **7T-PBI** in CD_2Cl_2 at room temperature. The thiophene and PBI proton cross signals are highlighted by red circles.

Spectroelectrochemistry

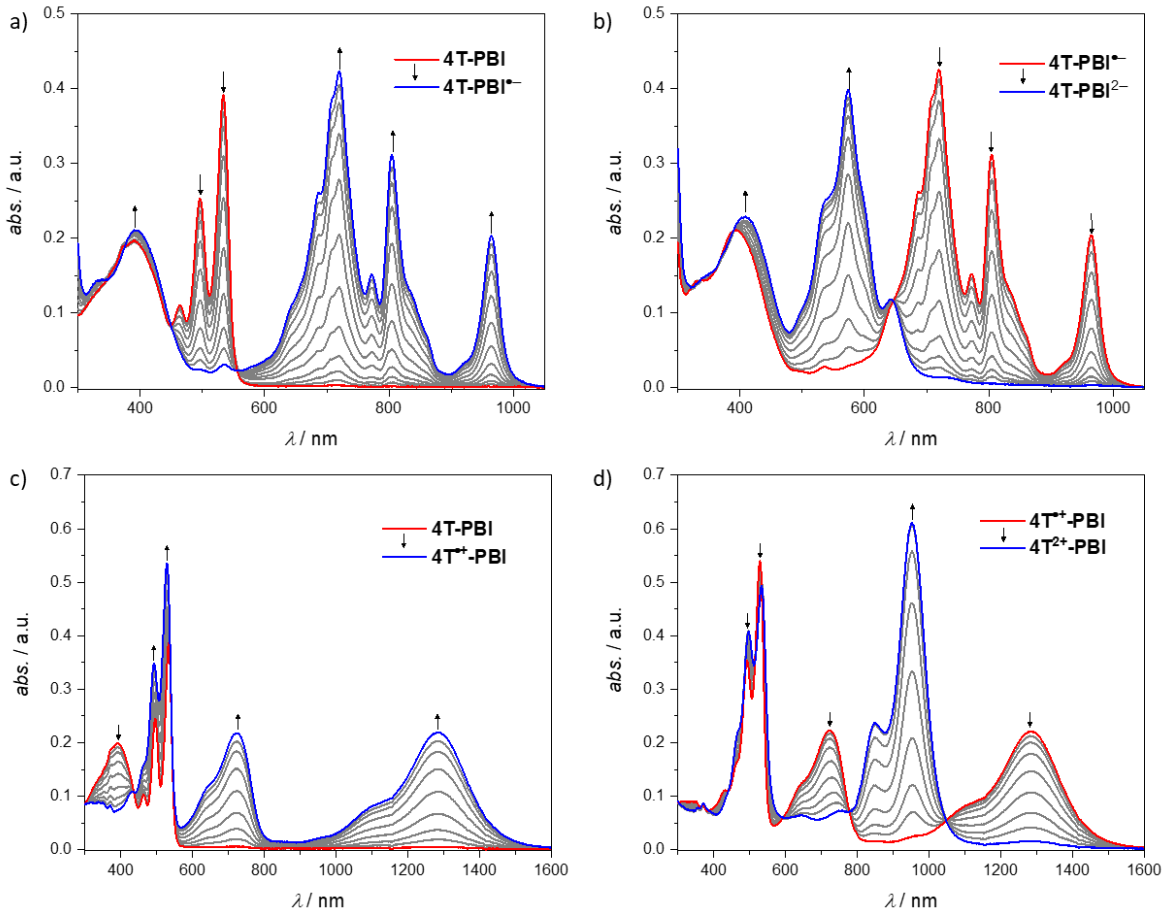

Figure 109. UV/Vis/NIR absorption changes of **4T-PBI** upon electrochemical reduction to a) **4T-PBI**$^{\bullet-}$ and b) **4T-PBI**$^{2-}$ and electrochemical oxidation to c) **4T**$^{\bullet+}$**-PBI** and d) **4T**$^{2+}$**-PBI** in CH_2Cl_2 solutions of Bu_4NPF_6 at r.t. The arrows in the graphs indicate the spectral changes upon decreasing (a,b) and increasing (c,d) electric potential. Spectra at initial (red) and final (blue) potential are always highlighted in a)-d).

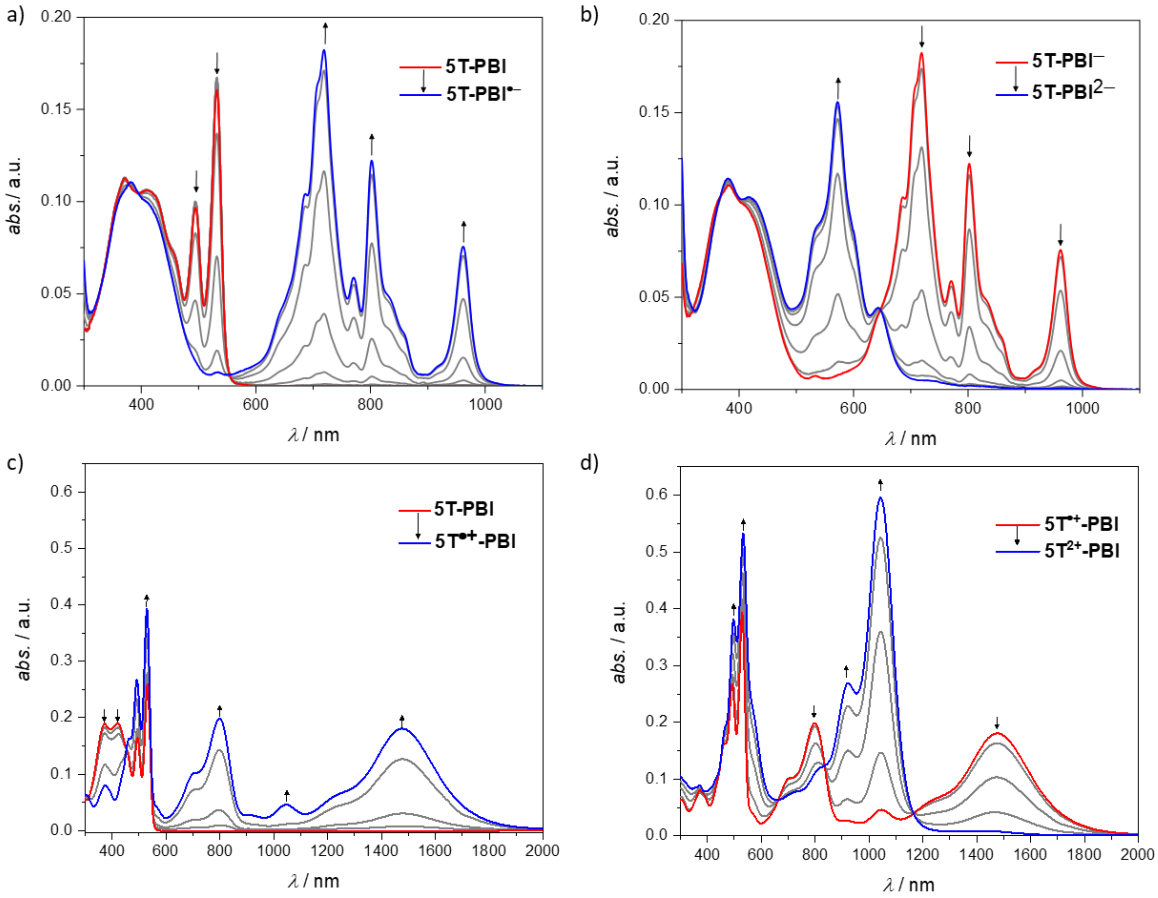

Figure 110. UV/Vis/NIR absorption changes of **5T-PBI**[262] upon electrochemical reduction to a) **5T-PBI**$^{\bullet-}$ and b) **5T-PBI**$^{2-}$ and electrochemical oxidation to c) **5T**$^{\bullet+}$**-PBI** and d) **5T**$^{2+}$**-PBI** in CH_2Cl_2 solutions of Bu_4NPF_6 at r.t. The arrows in the graphs indicate the spectral changes upon decreasing (a,b) and increasing (c,d) electric potential. Spectra at initial (red) and final (blue) potential are always highlighted in a)-d).

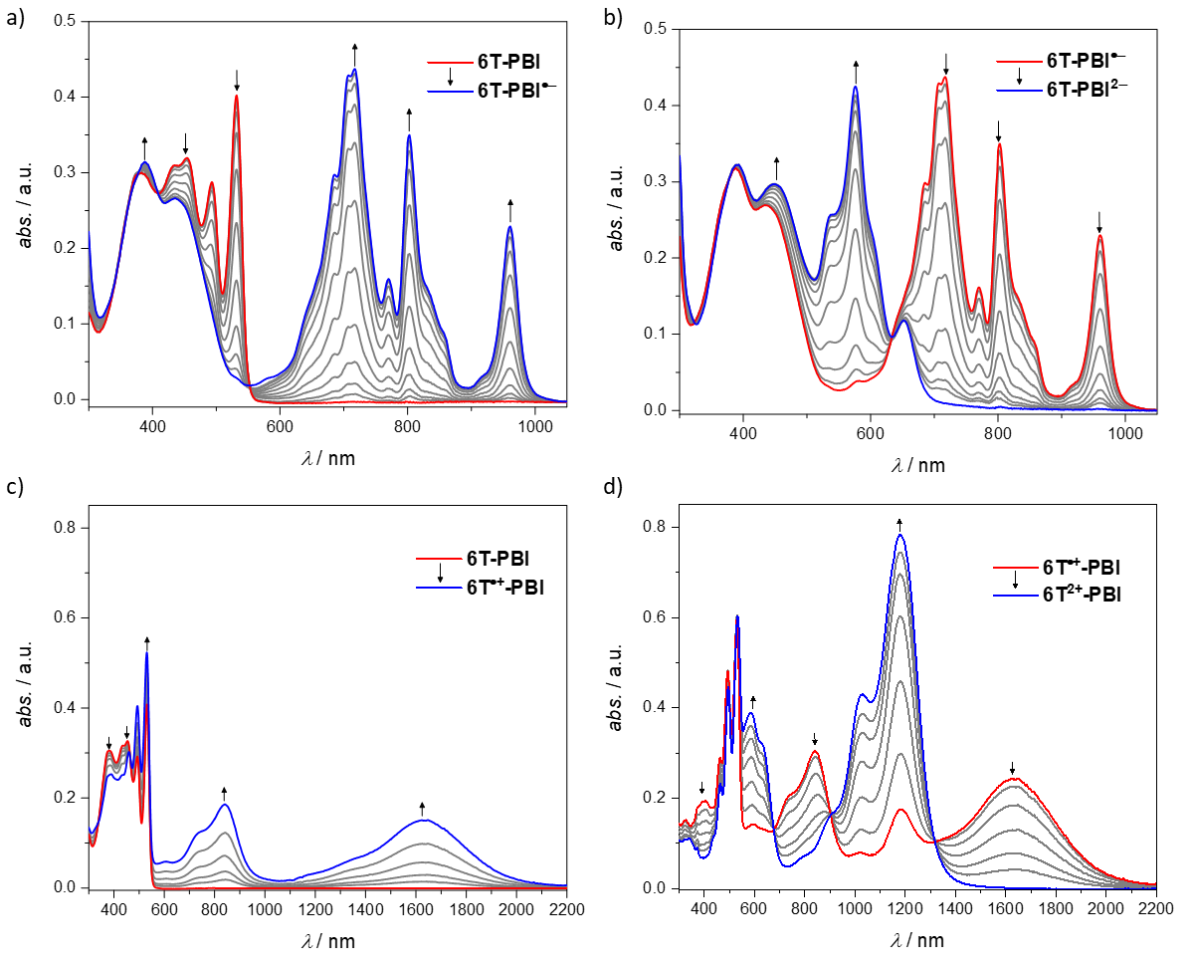

Figure 111. UV/Vis/NIR absorption changes of **6T-PBI** upon electrochemical reduction to a) **6T-PBI**$^{\bullet-}$ and b) **6T-PBI**$^{2-}$ and electrochemical oxidation to c) **6T**$^{\bullet+}$**-PBI** and d) **6T**$^{2+}$**-PBI** in CH_2Cl_2 solutions of Bu_4NPF_6 at r.t. The arrows in the graphs indicate the spectral changes upon decreasing (a,b) and increasing (c,d) electric potential. Spectra at initial (red) and final (blue) potential are always highlighted in a)-d).

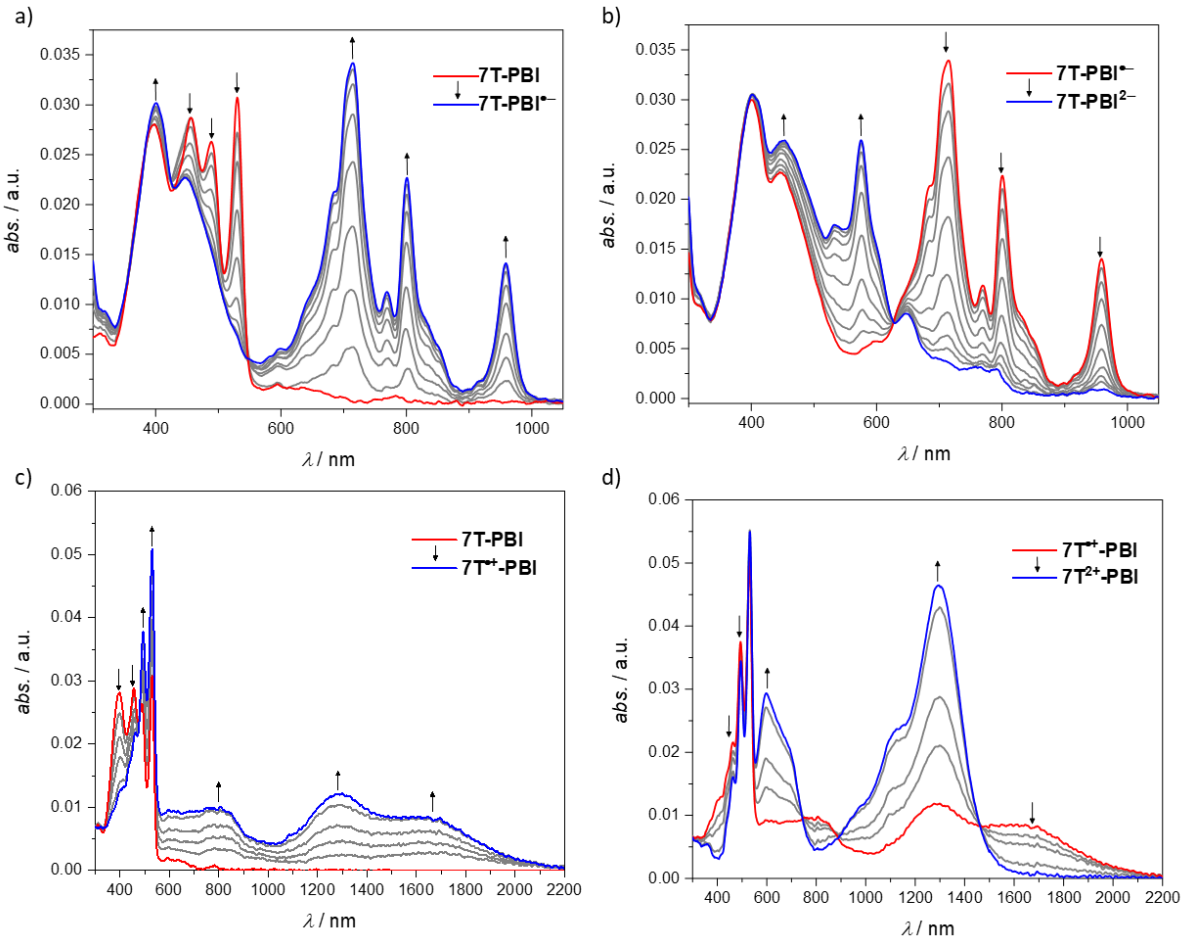

Figure 112. UV/Vis/NIR absorption changes of **7T-PBI** upon electrochemical reduction to a) **7T-PBI**$^{\bullet-}$ and b) **7T-PBI**$^{2-}$ and electrochemical oxidation to c) **7T**$^{\bullet+}$**-PBI** and d) **7T**$^{2+}$**-PBI** in CH_2Cl_2 solutions of Bu_4NPF_6 at r.t. The arrows in the graphs indicate the spectral changes upon decreasing (a,b) and increasing (c,d) electric potential. Spectra at initial (red) and final (blue) potential are always highlighted in a)-d).

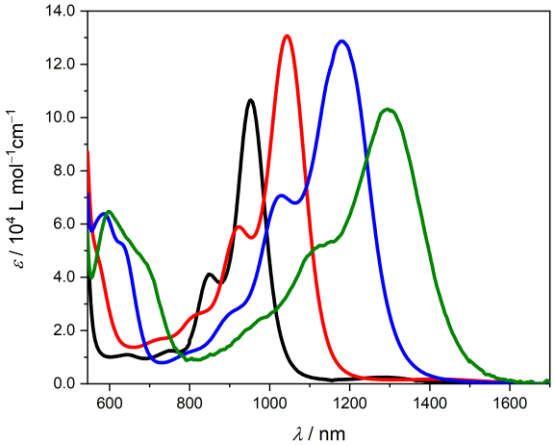

Figure 113. UV/Vis/NIR absorption spectra of the dications of **4T-PBI** (black), **5T-PBI**[262] (red), **6T-PBI** (blue) and **7T-PBI** (green), respectively. All measurements were carried out in CH_2Cl_2 solutions with Bu_4NPF_6 at room temperature ($c_0 = 10^{-4}$ M).

Optical Properties in Cyclohexane

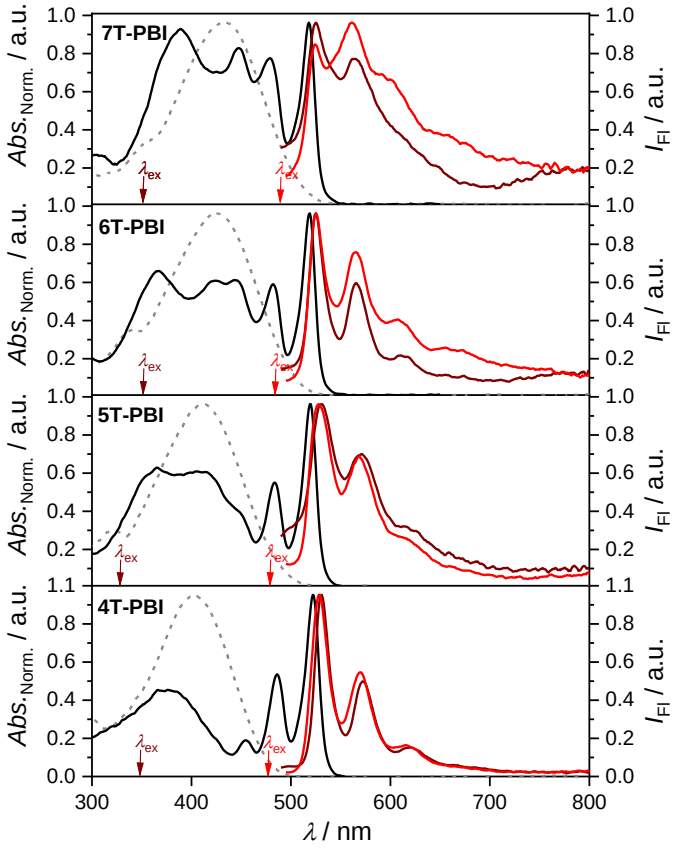

Figure 114. Normalized UV/Vis absorption (black solid, grey dashed) and emission (red, maroon) spectra of **4T-PBI**, **5T-PBI**[262], **6T-PBI** and **7T-PBI** (black, red, maroon) as well as of the corresponding reference donor structures **4T**-**7T**[235] (grey) in cyclohexane at room temperature (c_0 = 10^{-7} M). The wavelengths for excitation (λ_{ex}) at 400 nm (maroon) and 480 nm (red) to obtain the fluorescence spectra are highlighted by arrows.

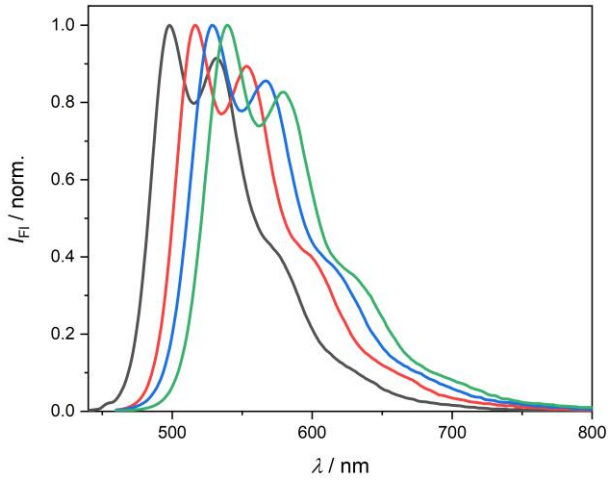

Figure 115. Normalized emission spectra of **4T** (black line), **5T** (red line), **6T** (blue line), and **7T** (green line) in cyclohexane (c_0=10^{-7} M) at room temperature.[235]

DFT and TDDFT calculations

The calculations of the macrocyclic strain energies (ΔE_{strain}) have been performed as described in ref. [262].

Table 12. Macrocyclic strain energies of all macrocycles.

	4T-PBI	**5T-PBI**	**6T-PBI**	**7T-PBI**	**7T-PBI-T**
ΔE_{strain} / kJ·mol^{-1}	19.6	13.9	17.2	22.5	30.6

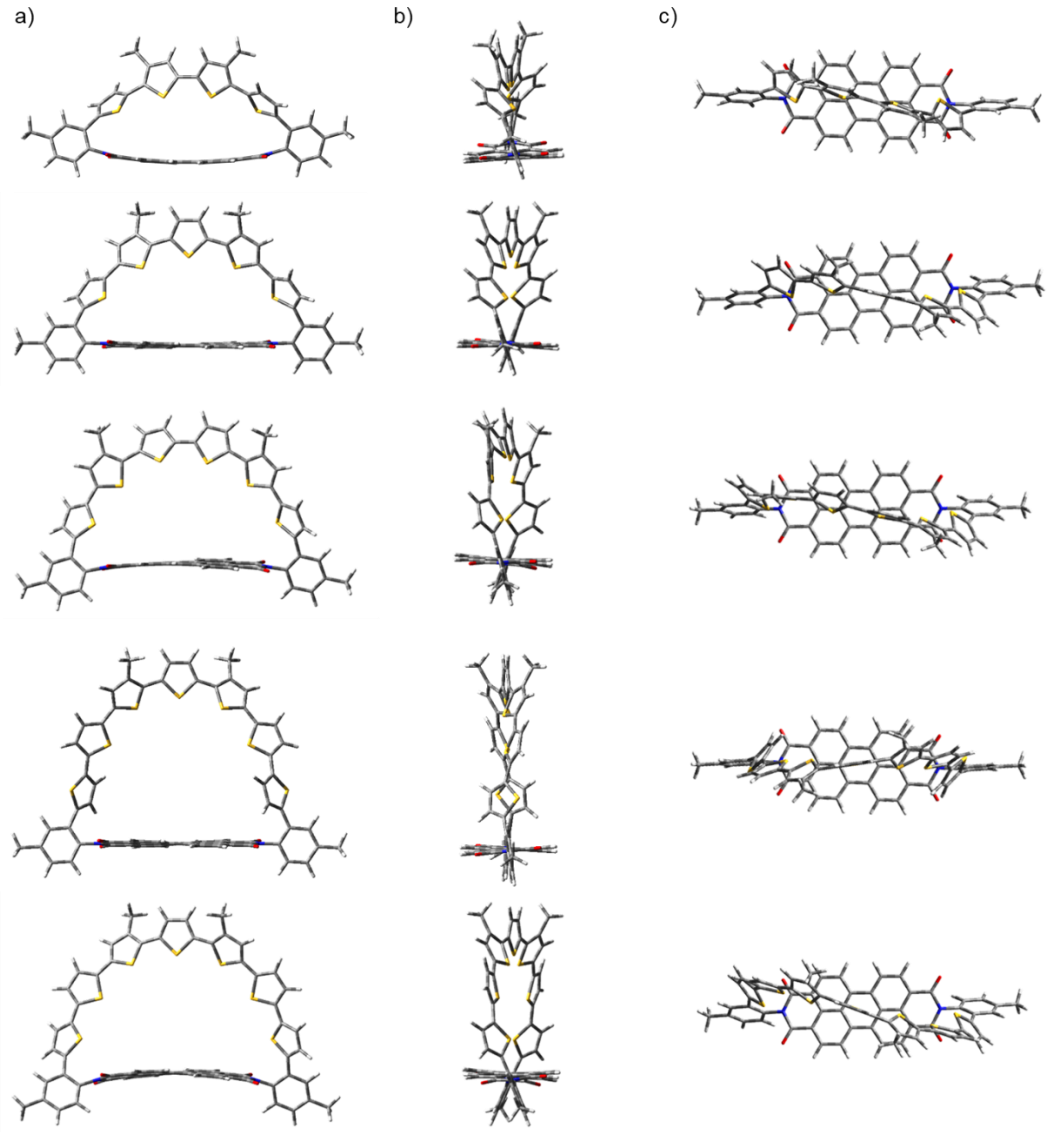

Figure 116. Side view (a), view along the *N*,*N*´-axis (b) and top (c) view onto the π-surface of **4T-PBI**, **5T-PBI**[262], **6T-PBI**, **7T-PBI** and **7T-PBI-T** (from top to bottom). The quantum mechanics calculations were carried out on the level of B3LYP density functional with the 6-31G(d) basis set as implemented in with Gaussian 16. Aliphatic chains were replaced by methyl groups. Color code: carbon = light grey, hydrogen = white, nitrogen = blue, oxygen = red, sulfur = yellow.

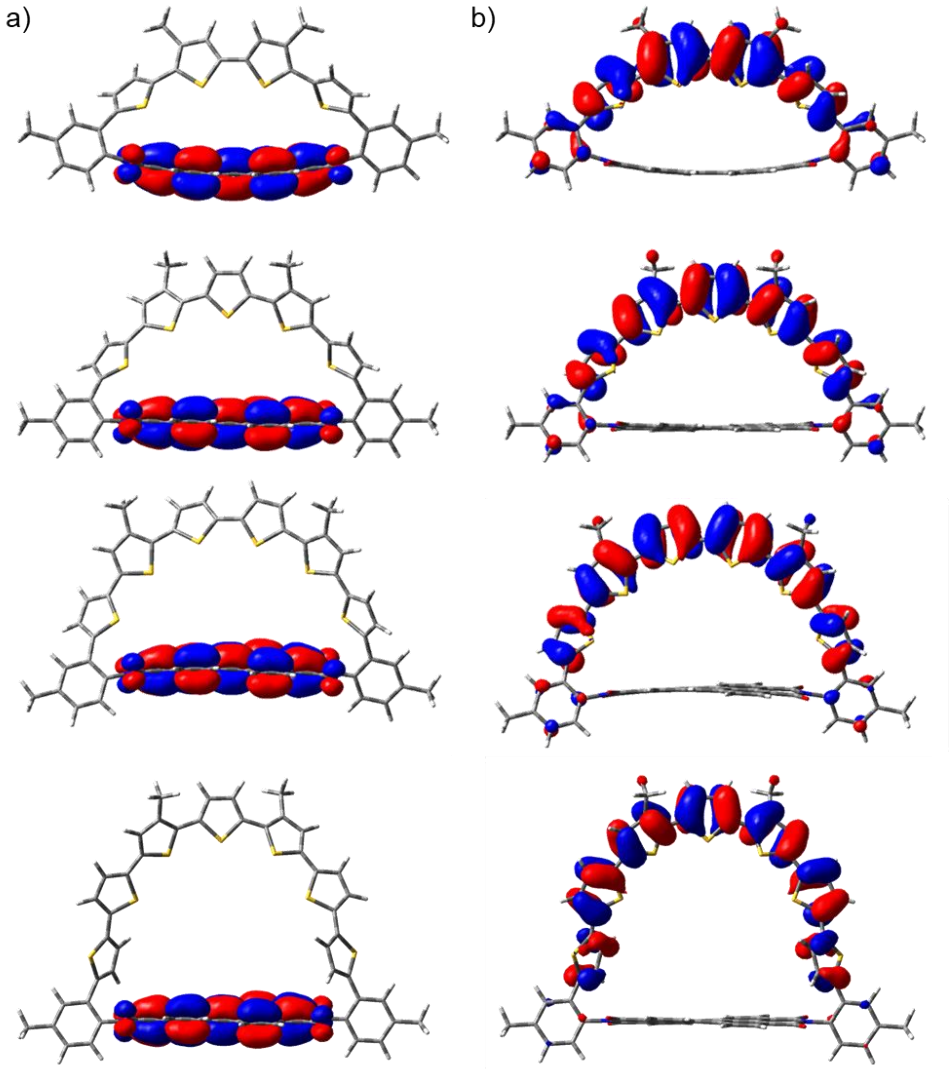

Figure 117. LUMO (a) and HOMO (b) of **4T-PBI**, **5T-PBI**[262], **6T-PB** and **7T-PBI** (from top to bottom) based on geometry optimized structures from DFT calculations. The quantum mechanics calculations were carried out on the level of B3LYP density functional with the 6-31G(d) basis set as implemented in with Gaussian 16. Aliphatic chains were replaced by methyl groups.

Table 13. First excited state (S_1) energy predictions of **4T-PBI**, **5T-PBI**[262], **6T-PB** and **7T-PBI** with TDDFT at the B3LYP/6-31G(d) level of theory (H = HOMO, L = LUMO).

Compound	Excitation Energy / eV	Wavelength / nm	Osc. Strength	Contribution
4T-PBI	1.36	911	0.0000	H → L (100%)
5T-PBI	1.18	1051	0.0000	H → L (100%)
6T-PBI	1.17	1064	0.0000	H → L (100%)
7T-PBI	1.14	1090	0.0002	H → L (100%)

Transient Absorption Spectra

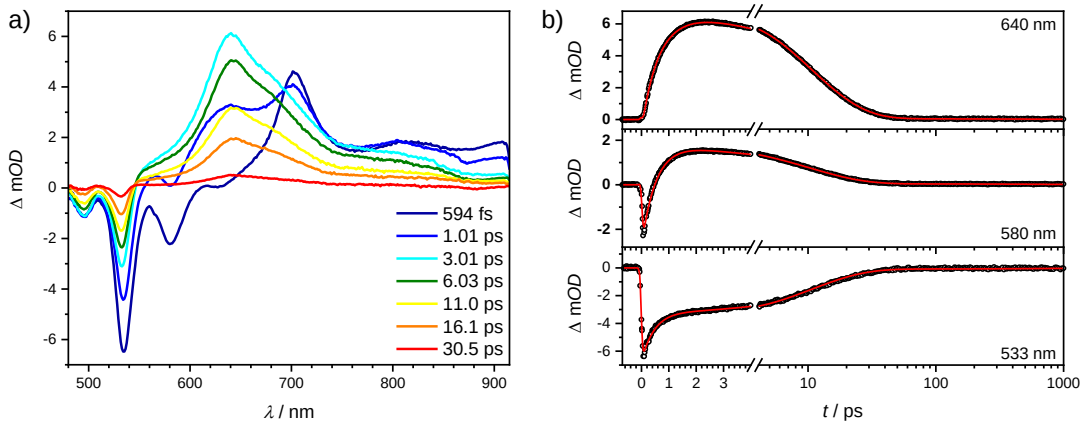

Figure 118. a) Transient absorption spectra of **4T-PBI** in CH_2Cl_2 after excitation at 530 nm and b) time scans and fit (red line) at selected wavelengths.

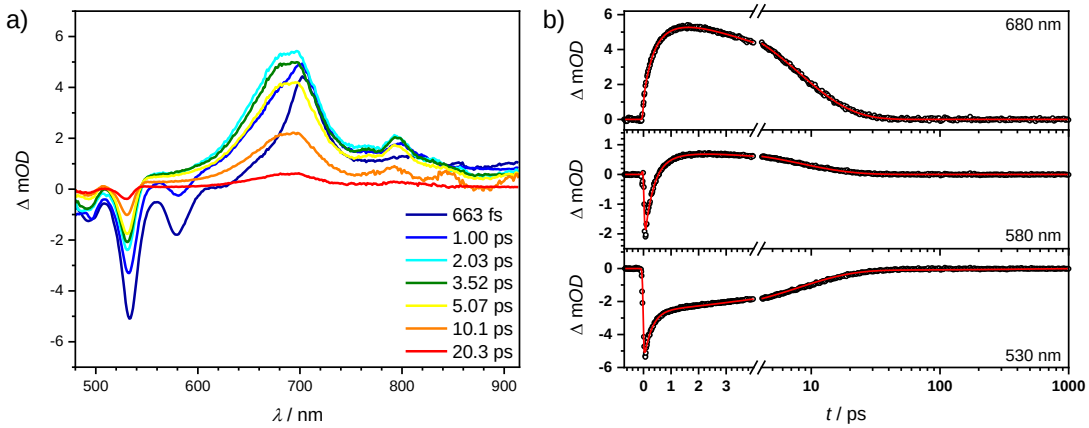

Figure 119. a) Transient absorption spectra of **6T-PBI** in CH_2Cl_2 after excitation at 530 nm and b) time scans and fit (red line) at selected wavelengths.

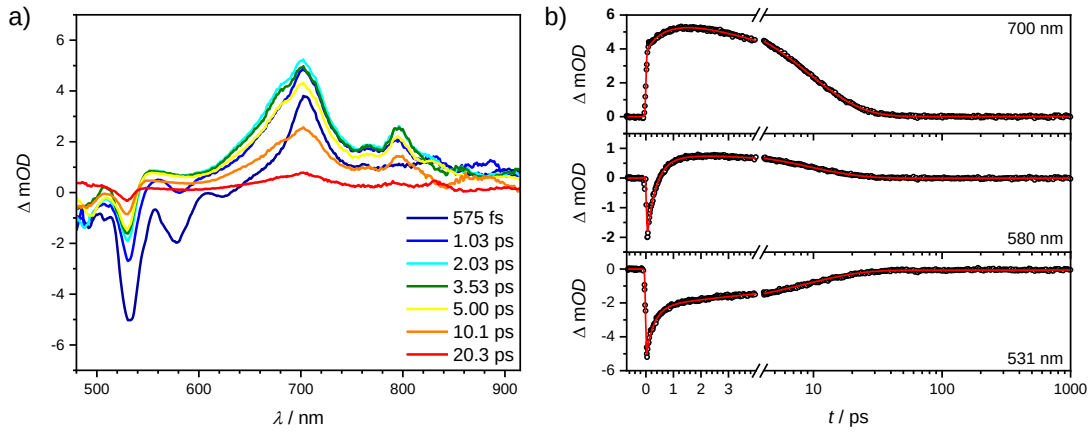

Figure 120. a) Transient absorption spectra of **7T-PBI** in CH_2Cl_2 after excitation at 530 nm and b) time scans and fit (red line) at selected wavelengths.

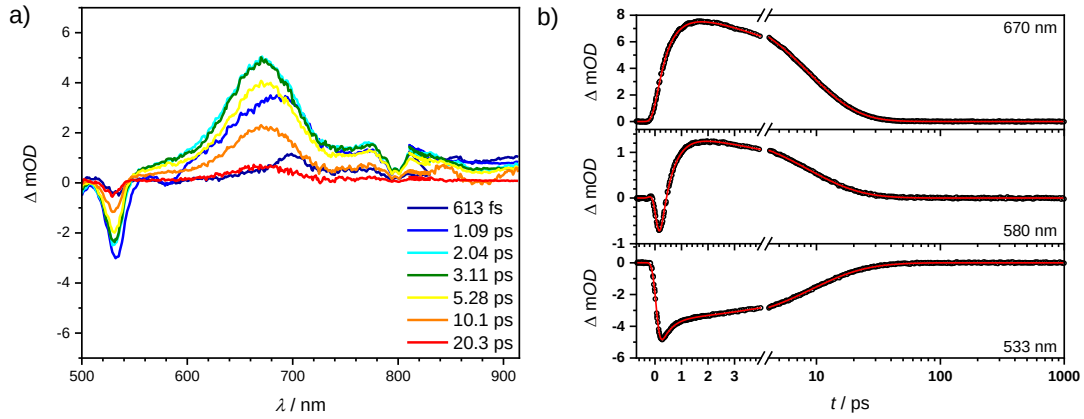

Figure 121. a) UV/Vis region of the transient absorption spectra of **5T-PBI** in CH_2Cl_2 after excitation at 400 nm and b) time scans and fit (red line) at selected wavelengths.

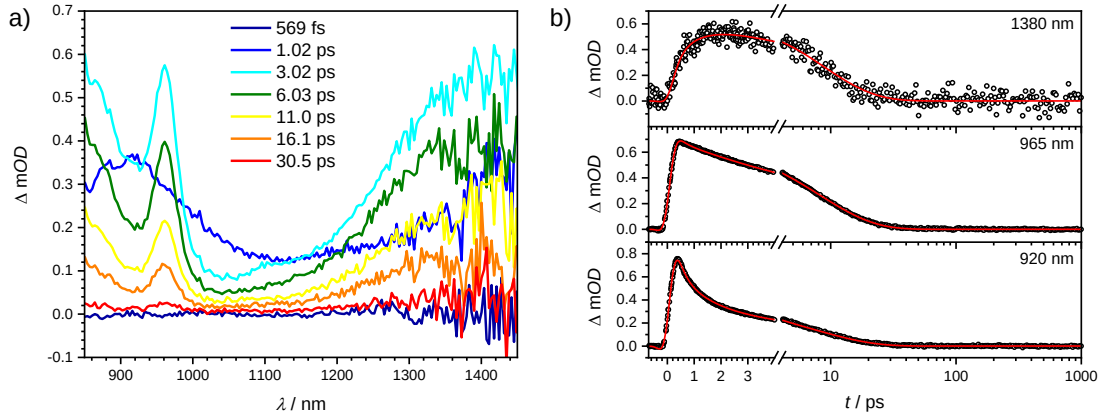

Figure 122. a) NIR region of the transient absorption spectra of **5T-PBI** in CH_2Cl_2 after excitation at 400 nm and b) time scans and fit (red line) at selected wavelengths.

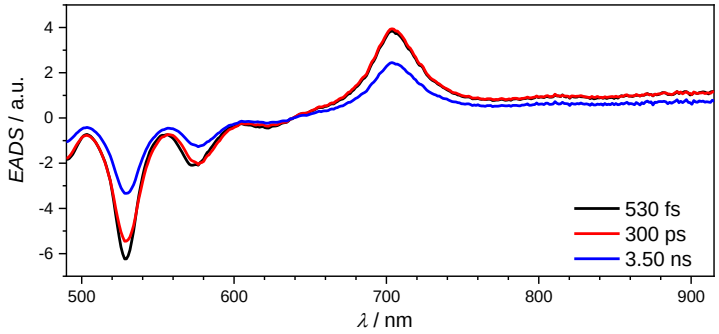

Figure 123. Evolution associated difference spectra (EADS) and lifetimes from a global fit analysis of the transient spectra of a 1:1 mixture comprising **4T** and **Ref-PBI** obtained by excitation at 530 nm in CH_2Cl_2 ($c_0 = 10^{-4}$ M) at room temperature.

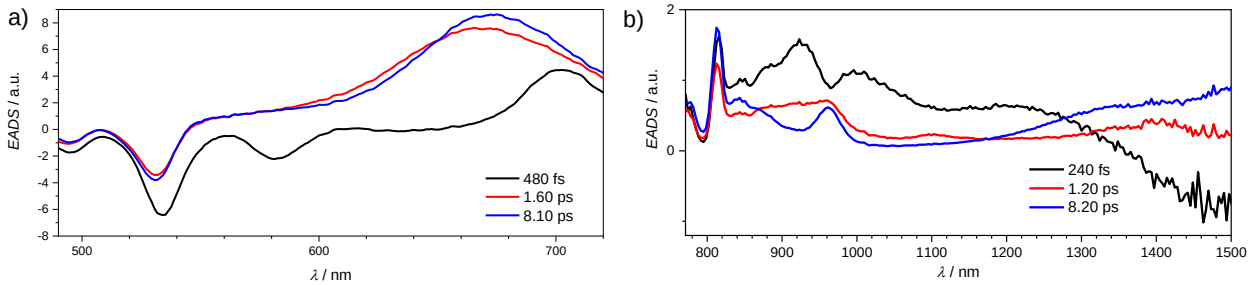

Figure 124. Evolution associated difference spectra (EADS) and lifetimes in the a) UV/Vis and b) NIR region from a global fit analysis of the transient spectra of **5T-PBI** obtained by excitation at 400 nm in CH_2Cl_2 ($c_0 = 10^{-4}$ M) at room temperature.

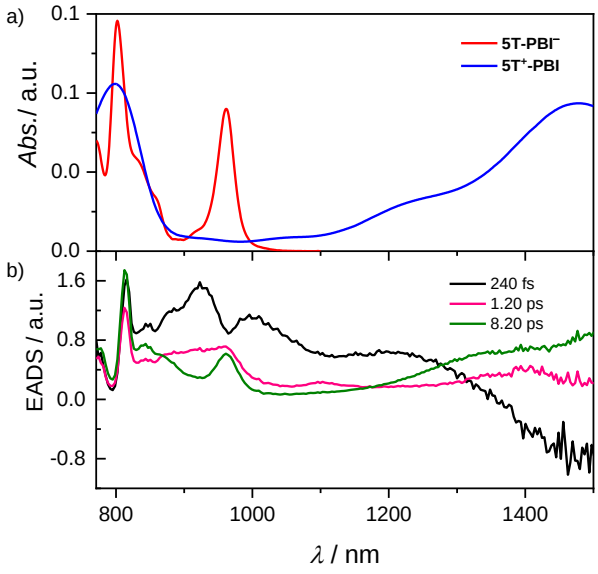

Figure 125. a) Normalized NIR absorption spectra of **5T-PBI** upon electrochemical reduction to **5T-PBI**$^-$ (red line) and electrochemical oxidation to **5T**$^+$**-PBI** (blue line) in CH_2Cl_2 solutions with Bu_4NPF_6 at room temperature ($c_0 = 10^{-4}$ M).[262] b) Evolution associated difference spectra (EADS) and lifetimes from a global fit analysis of the transient spectra of **5T-PBI** obtained by excitation at 400 nm in CH_2Cl_2 ($c_0 = 10^{-4}$ M) at room temperature.

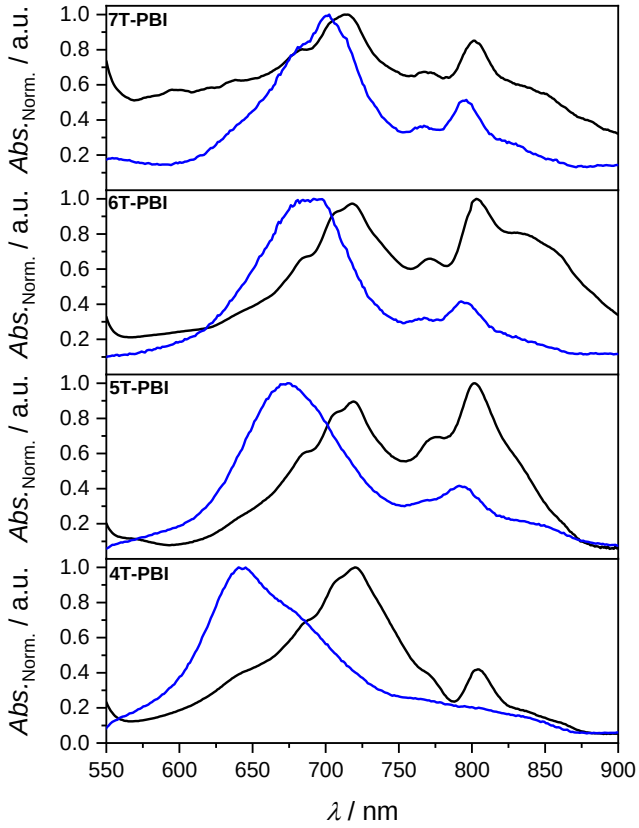

Figure 126. Sum of the normalized anion and cation spectra (black lines) obtained from SEC and the EADS of the normalized "cold" CT/CS state (blue lines) of **4T-PBI**, **5T-PBI**[262], **6T-PB** and **7T-PBI** in CH_2Cl_2 at room temperature.

NMR Spectra

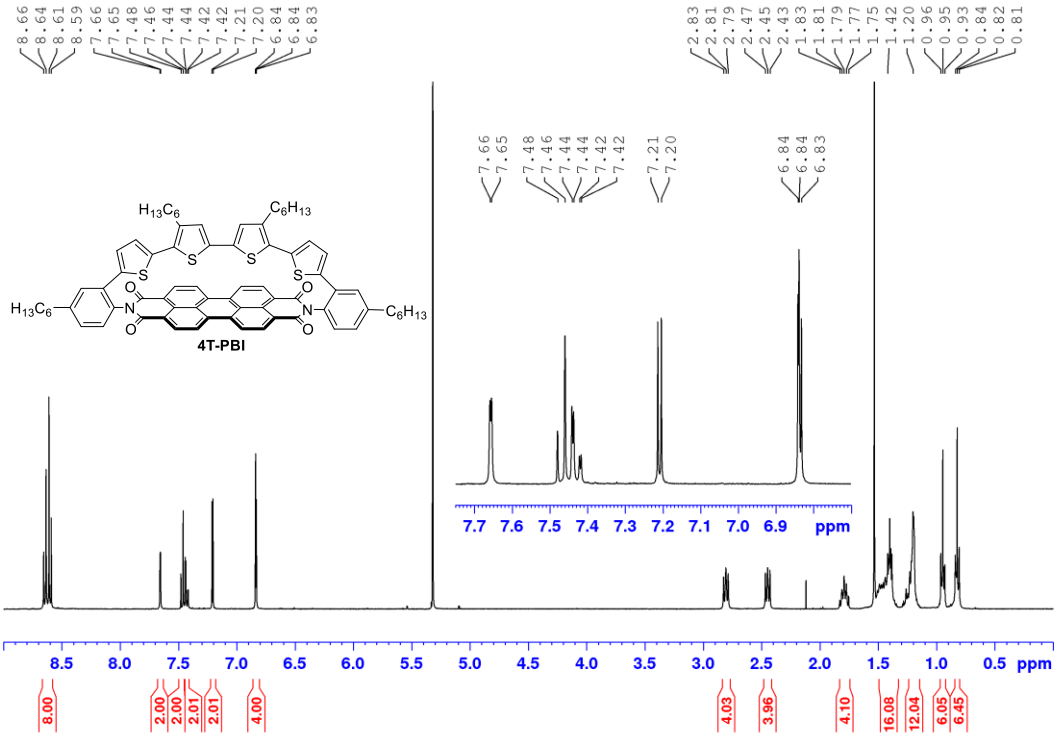

Figure 127. ^{1}H NMR spectrum (400 MHz) of **4T-PBI** in CD_2Cl_2 at 298 K.

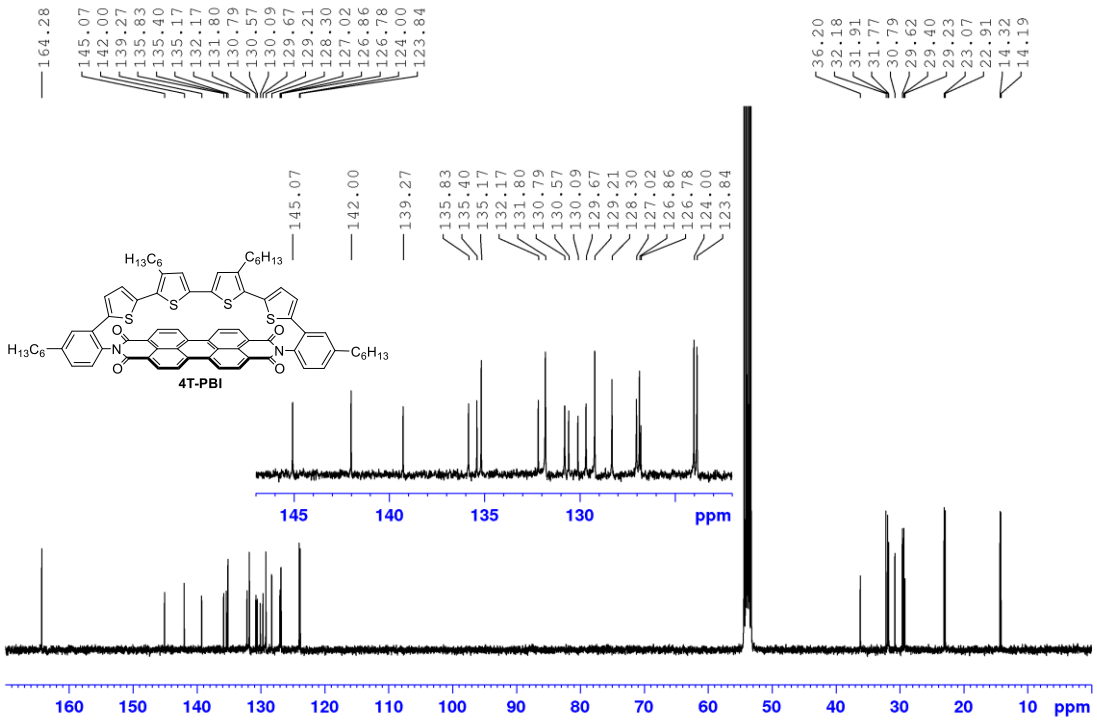

Figure 128. ^{13}C NMR spectrum (101 MHz) of **4T-PBI** in CD_2Cl_2 at 298 K.

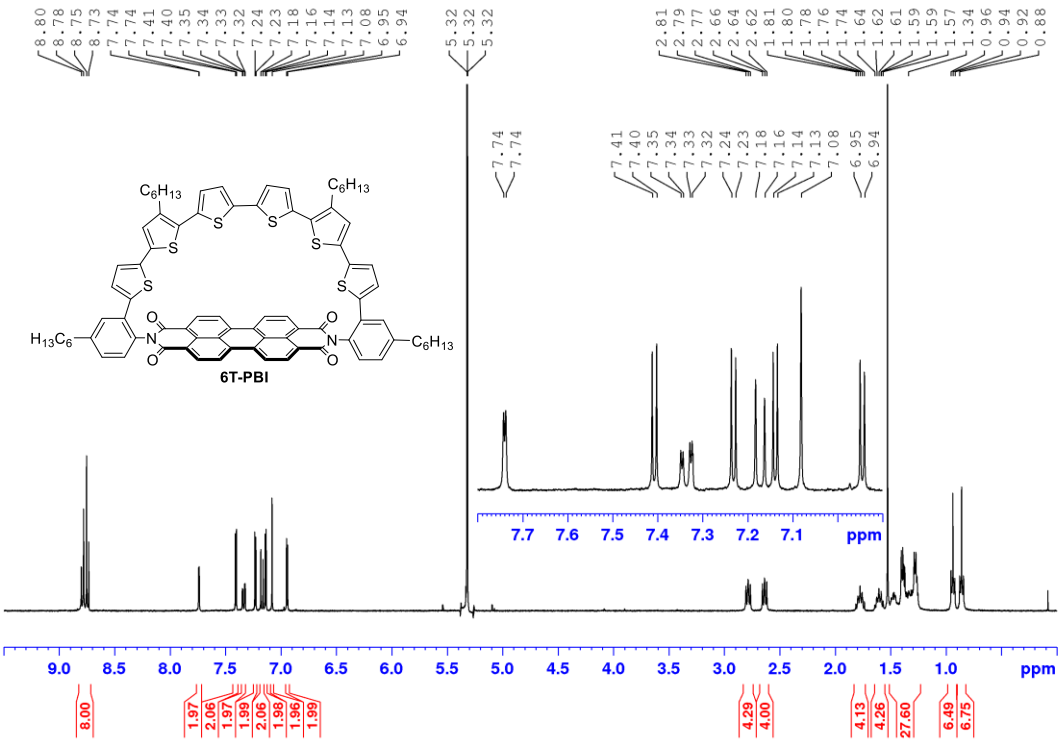

Figure 129. ^{1}H NMR spectrum (400 MHz) of **6T-PBI** in CD_2Cl_2 at 298 K.

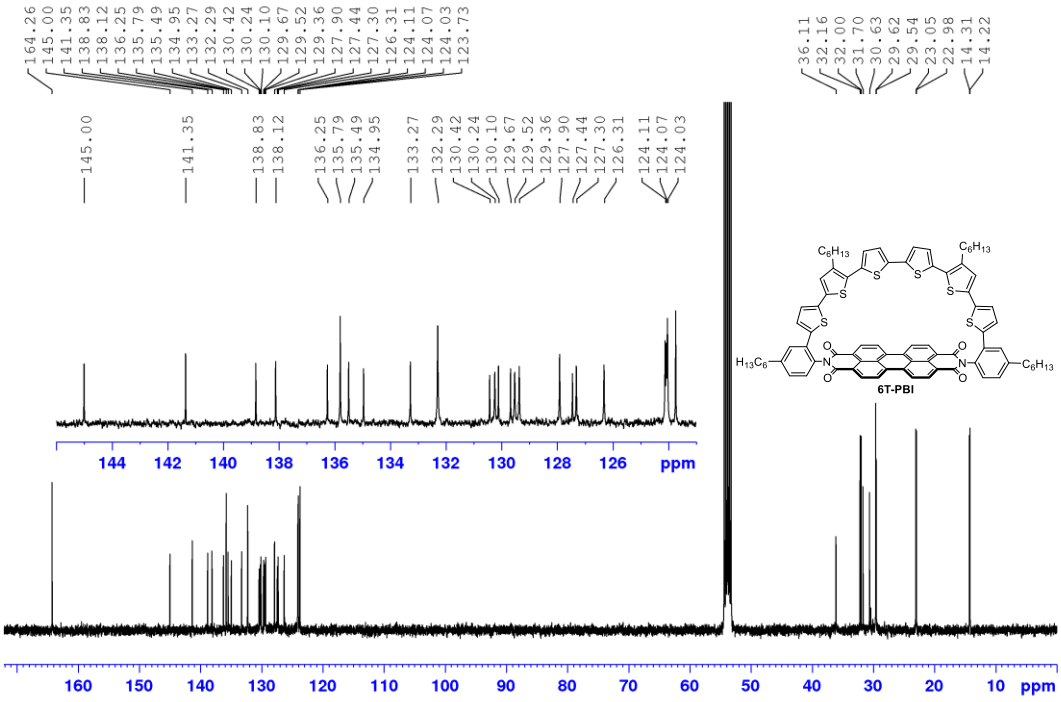

Figure 130. ^{13}C NMR spectrum (101 MHz) of **6T-PBI** in CD_2Cl_2 at 298 K.

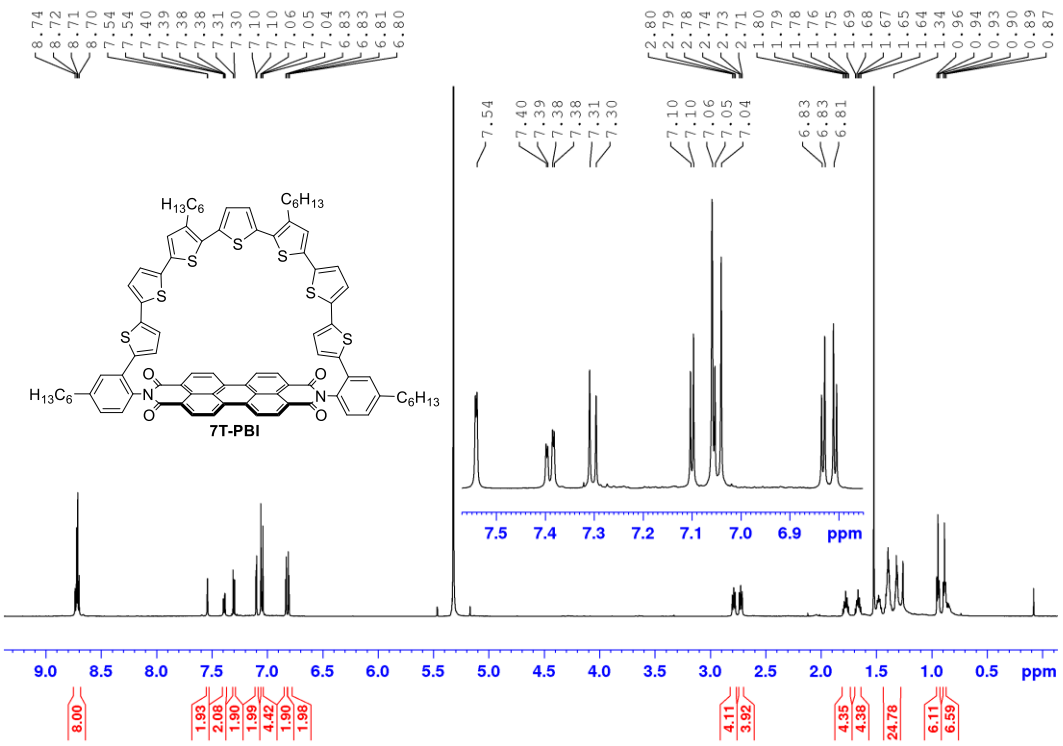

Figure 131. ^{1}H NMR spectrum (600 MHz) of **7T-PBI** in CD_2Cl_2 at 298 K.

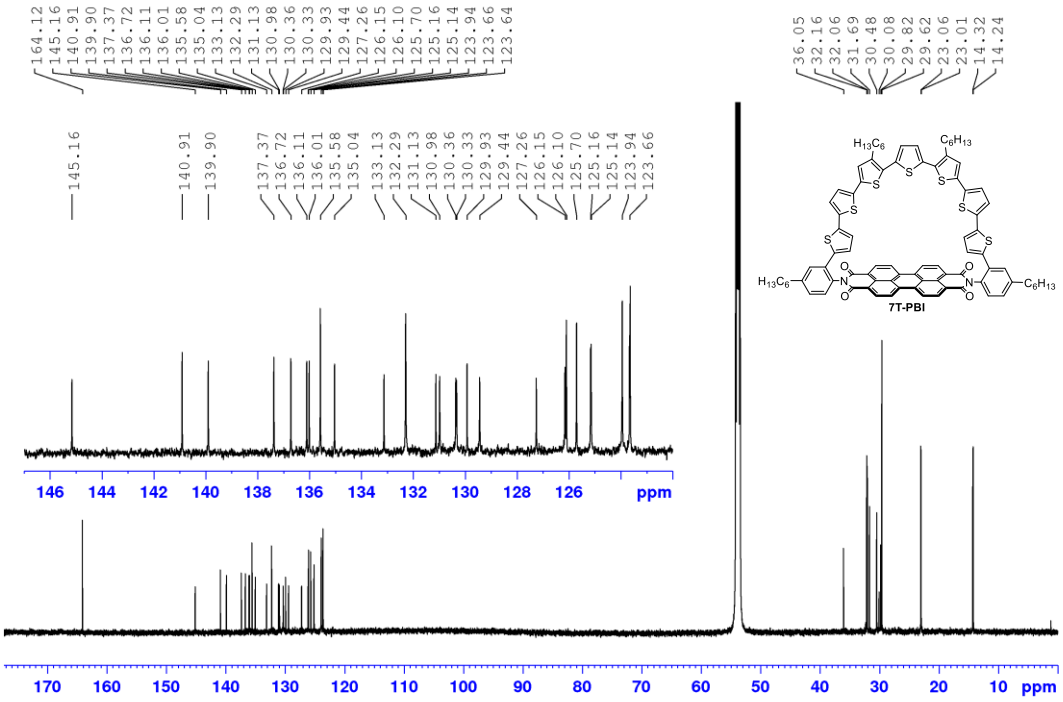

Figure 132. ^{13}C NMR spectrum (150 MHz) of **7T-PBI** in CD_2Cl_2 at 298 K.

Mass Spectra

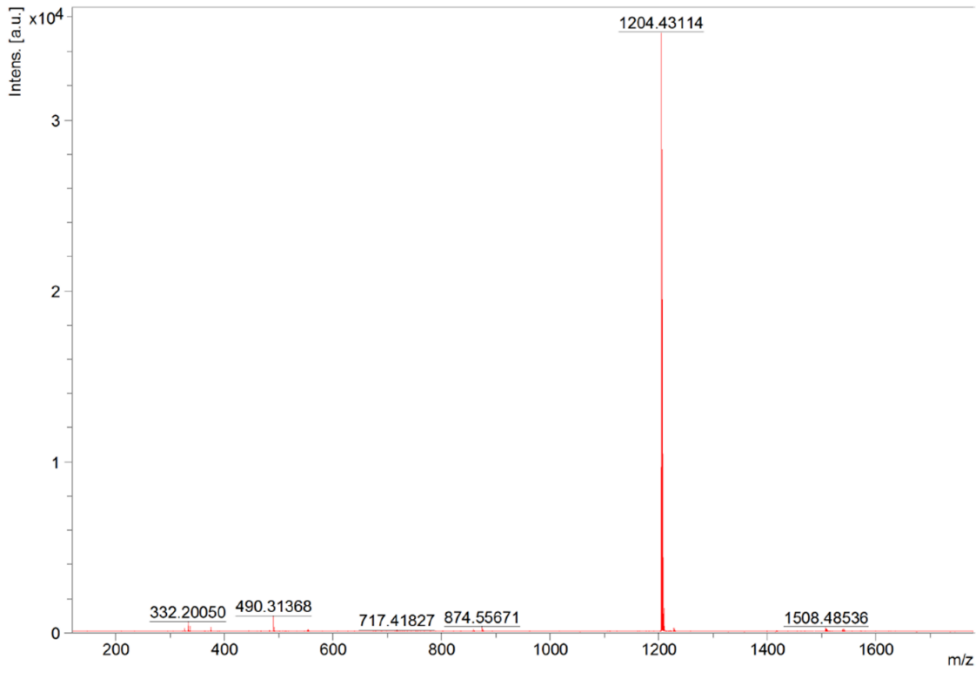

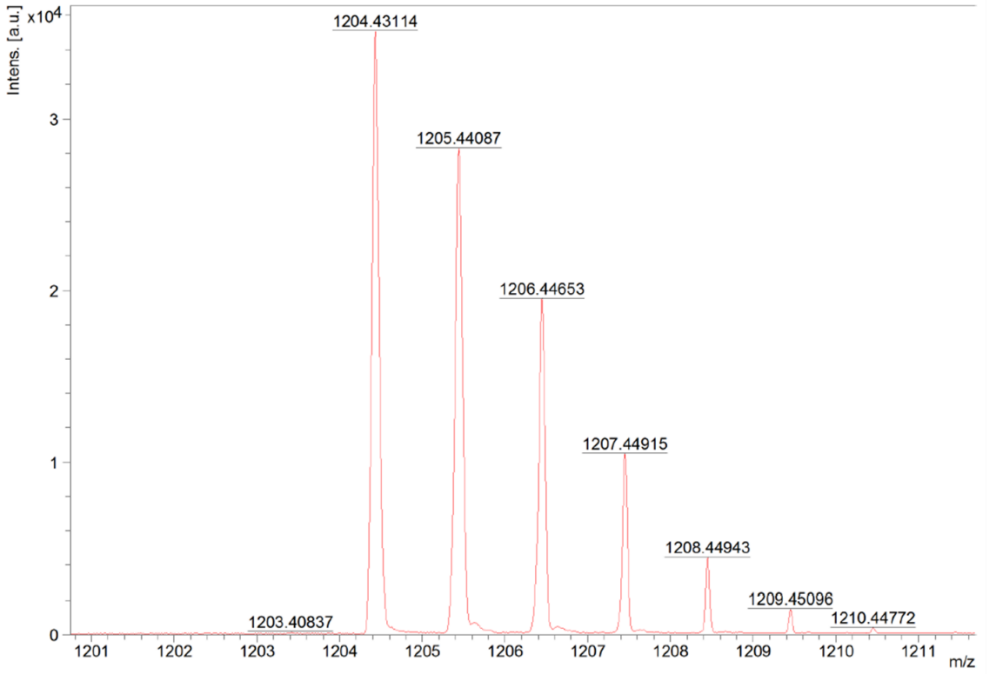

Formula	Mass	Error	mSigma	DblEq	N rule	Electron Configuration
C 76 H 72 N 2 O 4 S 4	1,204.4369	4.8169	28.4696	42.00	ok	odd

Figure 133. HRMS (MALDI-TOF, pos. mode, DCTB in $CHCl_3$) spectra of **4T-PBI**.

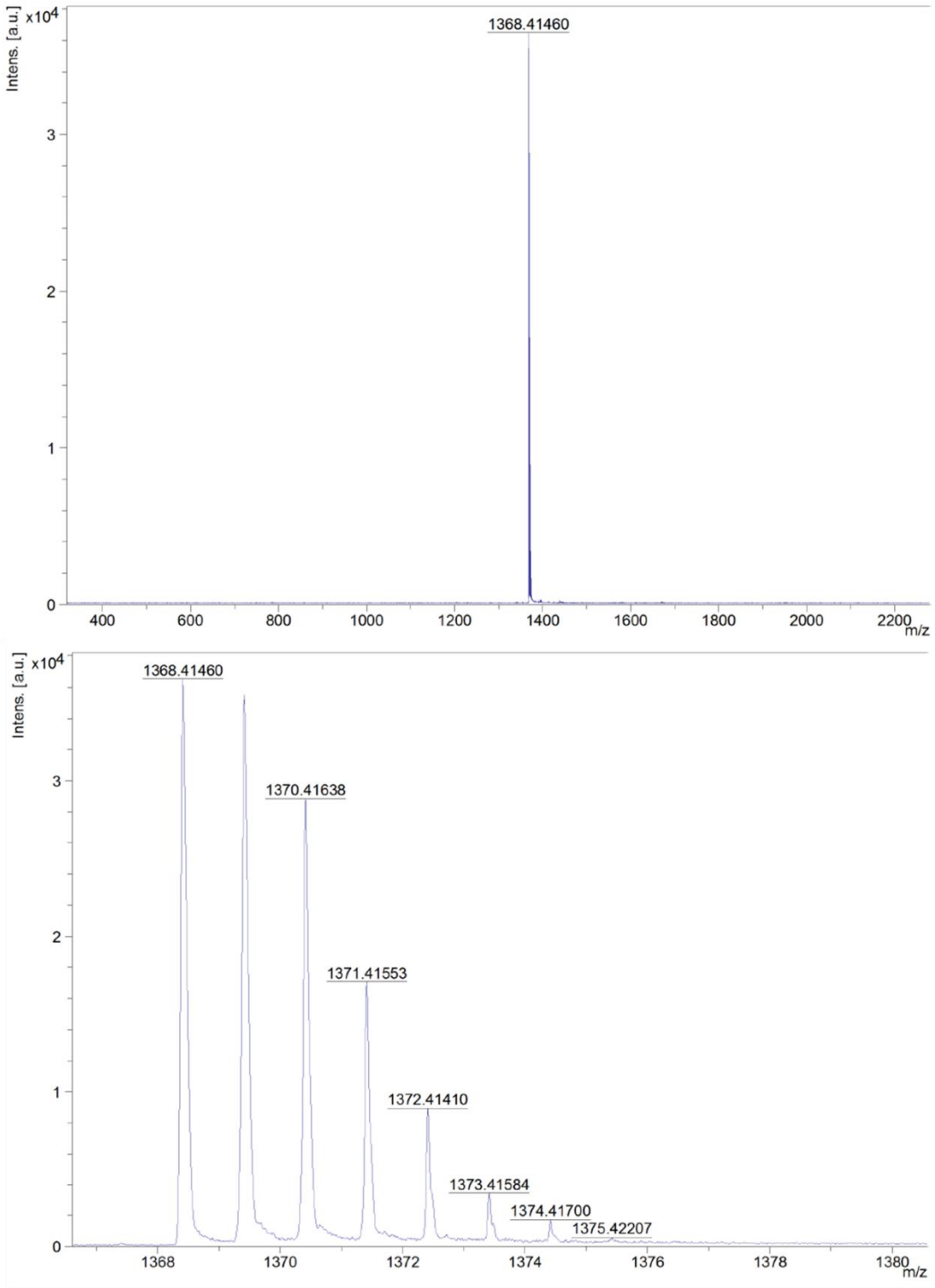

Formula	Mass	Error	mSigma	DblEq	N rule	Electron Configuration
C 84 H 76 N 2 O 4 S 6	1,368.4124	1.6181	30.5827	48.00	ok	odd

Figure 134. HRMS (MALDI-TOF, pos. mode, DCTB in $CHCl_3$) spectra of **6T-PBI**.

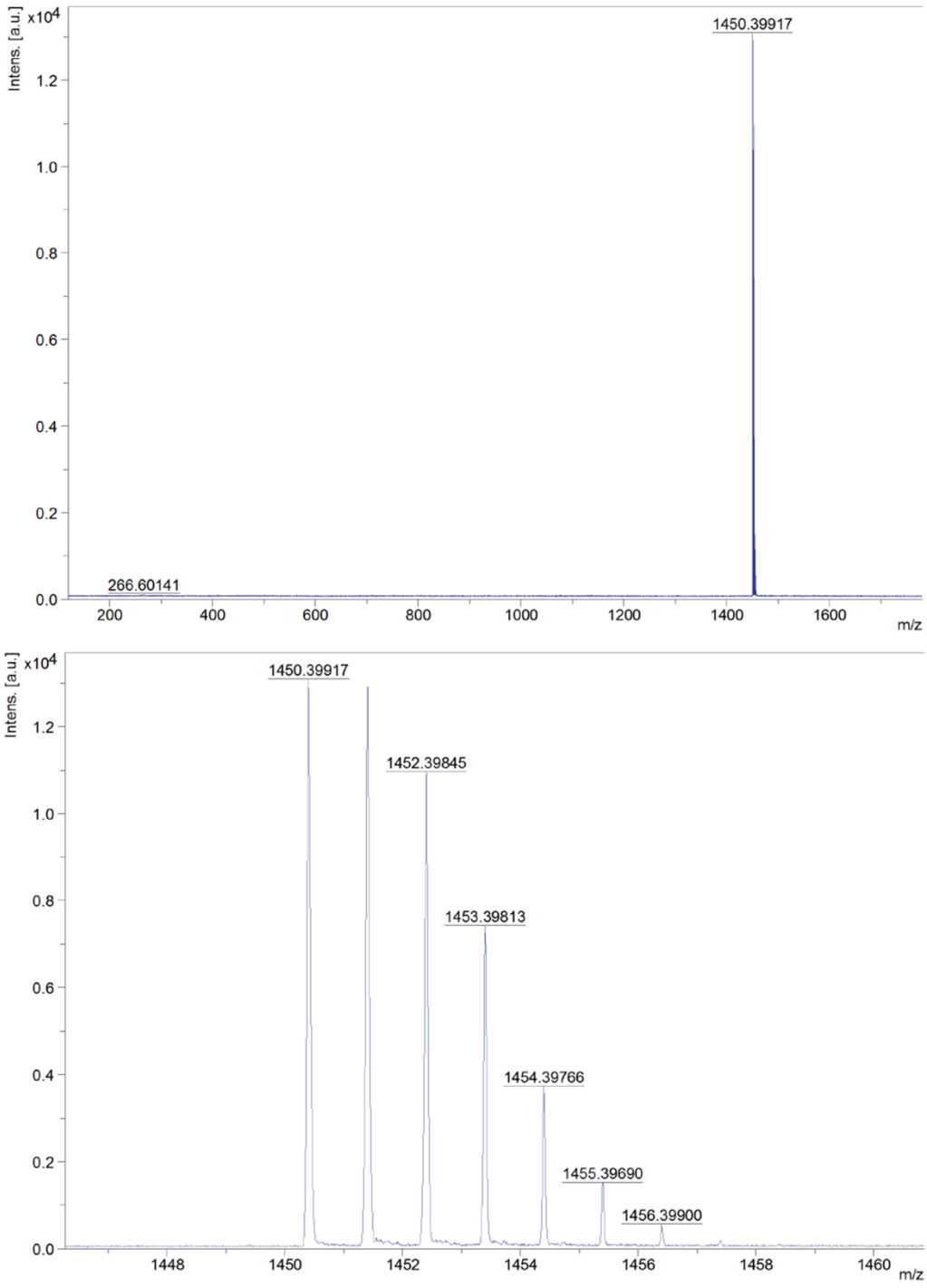

Formula	Mass	Error	mSigma	DblEq	N rule	Electron Configuration
C 88 H 78 N 2 O 4 S 7	1,450.4001	0.6455	30.9377	51.00	ok	odd

Figure 135. HRMS (MALDI-TOF, pos. mode, DCTB in $CHCl_3$) spectra of **7T-PBI**.

Cartesian Coordinates Received from DFT Calculations

Final Geometry:

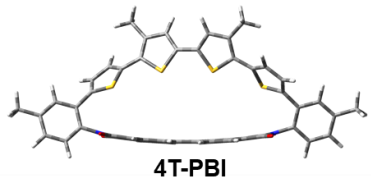

Total energy: −4156.52965648 Hartrees

C1	−1.38008	−2.4548	2.49154	N23	5.64274	−1.86188	−0.23876	H45	−0.84145	−2.49328	3.43073
C2	−2.77272	−2.33778	2.54206	O24	5.75967	−2.02287	2.04354	H46	−3.2923	−2.28207	3.49268
C3	−3.51181	−2.25279	1.37498	O25	5.55296	−1.93331	−2.52719	H47	−3.58146	−2.33876	−3.19967
C4	−2.85715	−2.32836	0.12148	C26	−4.9705	−2.00822	1.46299	H48	−1.13233	−2.53379	−3.34605
C5	−1.43412	−2.44224	0.06109	C27	−5.08095	−2.04637	−1.03646	H49	3.57179	−2.353	3.19976
C6	−0.68586	−2.48016	1.2804	O28	−5.56092	−1.91046	2.52724	H50	1.12188	−2.53802	3.34617
C7	−3.61717	−2.2719	−1.07194	N29	−5.65038	−1.83875	0.2388	H51	0.83116	−2.49697	−3.43061
C8	−2.98112	−2.37415	−2.29686	O30	−5.76797	−1.99949	−2.04348	H52	3.28285	−2.29576	−3.49258
C9	−1.58853	−2.48259	−2.36472	C31	−7.02679	−1.40547	0.28671	H53	−8.99081	1.31137	−0.19926
C10	−0.79281	−2.48742	−1.21744	C32	7.02092	−1.43428	−0.28672	H54	−10.11352	−2.67671	0.91918
C11	0.78255	−2.4905	1.21756	C33	−7.36183	−0.07259	−0.02105	H55	−7.72708	−3.34485	0.85597
C12	0.67563	−2.48305	−1.28028	C34	−8.72323	0.28037	0.0146	H56	7.71317	−3.37657	−0.85592
C13	1.42404	−2.44807	−0.06098	C35	−9.7282	−0.63263	0.3384	H57	10.10235	−2.71832	−0.91918
C14	2.84752	−2.34	−0.12138	C36	−9.35428	−1.94651	0.65018	H58	8.99619	1.27442	0.19914
C15	3.60777	−2.28652	1.07203	C37	−8.01666	−2.32577	0.62098	H59	−11.2878	0.86963	0.28823
C16	2.9713	−2.38604	2.29696	C38	8.00697	−2.35869	−0.62097	H60	−11.68304	−0.5525	1.26766
C17	1.57828	−2.48878	2.36483	C39	9.34616	−1.98497	−0.6502	H61	−11.72627	−0.65524	−0.49339
C18	1.36994	−2.46061	−2.49142	C40	9.72552	−0.67264	−0.33846	H62	11.29133	0.82316	−0.28883
C19	2.76304	−2.34927	−2.54196	C41	8.72435	0.24453	−0.01469	H63	11.72333	−0.70309	0.49369
C20	3.50248	−2.2672	−1.37489	C42	7.36149	−0.10279	0.02098	H64	11.68084	−0.60113	−1.26743
C21	5.07246	−2.06701	1.03653	C43	−11.18084	−0.21759	0.35272	C65	6.38627	0.92981	0.41481
C22	4.96216	−2.02862	−1.46293	C44	11.17987	−0.26363	−0.35276	C66	6.52603	1.83978	1.43897

S67	4.87301	1.20986	−0.42572	H78	−5.33524	3.47958	−2.37712	H89	−1.05587	5.84574	−0.6773
C68	5.4269	2.72593	1.58158	C79	3.15484	3.21169	0.52027	C90	−3.14157	3.22456	−0.52036
C69	7.38044	1.83372	2.10705	C80	2.86866	4.55126	0.73651	C91	−3.85198	5.61612	−1.1299
C70	4.42397	2.51903	0.65607	S81	1.70537	2.33146	0.04957	H92	−3.91439	5.73209	−2.22031
H71	5.34936	3.45746	2.37726	C82	1.49208	4.84779	0.53316	H93	−4.85476	5.36876	−0.76907
C72	−6.38235	0.95595	−0.41491	C83	0.71616	3.77324	0.15343	H94	−3.56926	6.59077	−0.71783
H73	−6.51845	1.86663	−1.43894	H84	1.07982	5.84132	0.67746	C95	3.87498	5.60026	1.13008
S74	−4.8678	1.22957	0.42543	C85	−0.70062	3.77614	−0.1535	H96	3.9378	5.71589	2.2205
C75	−5.41569	2.74825	−1.58155	C86	−1.47216	4.85388	−0.5331	H97	4.87675	5.34883	0.76928
H76	−7.37296	1.86421	−2.10691	S87	−1.69569	2.33839	−0.04978	H98	3.59627	6.57609	0.71807
C77	−4.41352	2.5371	−0.65618	C88	−2.84994	4.56298	−0.73646				

Final Geometry:

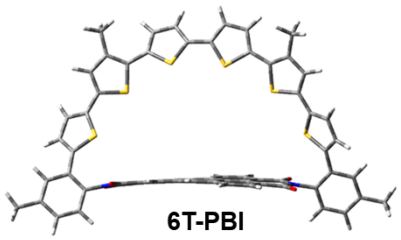

Total energy: −5260.15960267 Hartrees

C1	−1.24767	−2.70419	2.49259	C13	1.47298	−2.69604	−0.14993	O25	5.55371	−2.57148	−2.74899
C2	−2.64295	−2.72593	2.58879	C14	2.89791	−2.73542	−0.25987	C26	−4.89796	−2.85391	1.58617
C3	−3.42467	−2.77079	1.44706	C15	3.69759	−2.8873	0.8991	C27	−5.08416	−2.93797	−0.90959
C4	−2.80824	−2.75576	0.17238	C16	3.09408	−2.96752	2.14229	O28	−5.45736	−2.8565	2.67104
C5	−1.38337	−2.70511	0.06552	C17	1.70182	−2.89925	2.26121	N29	−5.64041	−2.95487	0.38872
C6	−0.59373	−2.71697	1.25909	C18	1.33911	−2.47185	−2.56621	O30	−5.79482	−3.04867	−1.89457
C7	−3.60933	−2.80042	−0.99503	C19	2.73492	−2.48189	−2.66266	C31	−7.05554	−3.23179	0.51191
C8	−3.00619	−2.762	−2.2405	C20	3.51629	−2.62991	−1.5294	C32	7.15671	−3.10566	−0.61931
C9	−1.61373	−2.68169	−2.35352	C21	5.1729	−3.00661	0.80411	C33	−8.04248	−2.2589	0.27002
C10	−0.78218	−2.65515	−1.2321	C22	4.99122	−2.68506	−1.67131	C34	−9.38733	−2.65373	0.42891
C11	0.87157	−2.7666	1.14645	N23	5.73142	−2.89539	−0.48827	C35	−9.7628	−3.94661	0.78795
C12	0.68366	−2.59721	−1.33978	O24	5.88172	−3.20421	1.777	C36	−8.75109	−4.88993	1.01324

C37	−7.41719	−4.52907	0.87657	C63	−0.73274	5.85273	−0.37461	H89	−11.86988	−3.44822	0.84456
C38	7.58513	−4.33556	−1.11811	S64	−1.75575	4.52657	0.14515	H90	−11.41275	−4.78505	1.91242
C39	8.93911	−4.62523	−1.23494	C65	0.68568	5.86826	−0.09712	H91	−11.52147	−5.04695	0.17096
C40	9.90158	−3.68376	−0.84609	C66	1.54949	6.9462	−0.09308	H92	11.98756	−3.11058	−0.74359
C41	9.45862	−2.4554	−0.3564	C67	2.89756	6.59775	0.16587	H93	11.67143	−4.7826	−0.2588
C42	8.09365	−2.13285	−0.22813	C68	3.09521	5.24578	0.38177	H94	11.63405	−4.34158	−1.96682
C43	−11.21832	−4.32245	0.93751	S69	1.56368	4.39141	0.25359	H95	−8.62856	1.91701	−1.83916
C44	11.37611	−3.99184	−0.9602	C70	4.31483	4.52211	0.66941	H96	−9.49441	−0.51731	−1.43723
C45	−7.78397	−0.87794	−0.16061	S71	4.46354	2.83805	0.18598	H97	9.15707	−0.66046	1.96102
S46	−6.41231	0.07897	0.36485	C72	6.07184	2.71661	0.86243	H98	8.19154	1.71232	2.50283
C47	−6.95266	1.48057	−0.53915	C73	6.44531	3.92607	1.40989	H99	−7.78017	4.21004	−0.65249
C48	−8.13687	1.20241	−1.18842	C74	5.46504	4.95208	1.31789	H100	−3.55712	7.03551	−1.7573
C49	−8.60112	−0.117	−0.97128	H75	−0.67618	−2.68002	3.41285	H101	−1.04785	7.68352	−1.49322
C50	7.74613	−0.81842	0.33132	H76	−3.13419	−2.7226	3.55594	H102	1.21813	7.96381	−0.26919
C51	8.37096	−0.18595	1.38402	H77	−3.63414	−2.80213	−3.12416	H103	3.70718	7.31719	0.16329
C52	7.85117	1.09909	1.67575	H78	−1.18717	−2.65843	−3.34932	H104	7.41575	4.08276	1.86976
C53	6.82347	1.47976	0.83708	H79	3.72185	−3.08946	3.01851	C105	5.67523	6.32986	1.88741
S54	6.50604	0.22021	−0.34114	H80	1.27427	−2.9706	3.25425	H106	6.04445	7.03405	1.1296
C55	−6.21177	2.72497	−0.55765	H81	0.76853	−2.36421	−3.48108	H107	4.74481	6.7427	2.29087
S56	−4.46353	2.76697	−0.52876	H82	3.22648	−2.38664	−3.62498	H108	6.41549	6.30504	2.69365
C57	−4.44038	4.52348	−0.60969	H83	−10.16034	−1.90479	0.28645	C109	−6.08616	6.49423	−0.72968
C58	−5.73095	5.0321	−0.67717	H84	−9.00754	−5.90569	1.30358	H110	−5.38134	7.09974	−0.15062
C59	−6.71444	4.00489	−0.6481	H85	−6.63227	−5.25793	1.05354	H111	−6.08158	6.87991	−1.75825
C60	−3.1756	5.22602	−0.61999	H86	6.8406	−5.06924	−1.41115	H112	−7.09054	6.66098	−0.32694
C61	−2.8473	6.44031	−1.19624	H87	9.25022	−5.58858	−1.63139				
C62	−1.48241	6.79011	−1.05815	H88	10.18907	−1.70036	−0.0803				

Final Geometry:

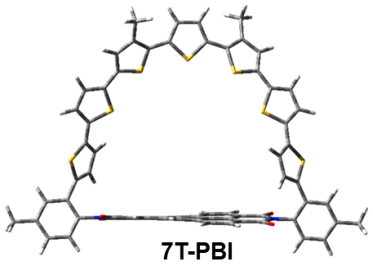

Total energy: −5811.97392424 Hartrees

C1	1.18375	−2.92766	−2.58157	N23	−5.64139	−3.5225	0.69818	C45	8.03833	−1.82903	0.09666
C2	2.57409	−2.96034	−2.73763	O24	−5.8768	−3.81577	−1.56253	S46	6.91261	−0.56943	−0.37017
C3	3.40055	−3.11638	−1.63753	O25	−5.38053	−3.15916	2.94681	C47	7.58992	0.55912	0.79086
C4	2.83737	−3.18241	−0.34025	C26	4.86274	−3.24593	−1.84504	C48	8.63050	−0.03026	1.47814
C5	1.42091	−3.10117	−0.16897	C27	5.13993	−3.57124	0.62182	C49	8.88351	−1.36508	1.08153
C6	0.58187	−3.03069	−1.32613	O28	5.38051	−3.15864	−2.94688	C50	−8.0385	−1.82887	−0.09645
C7	3.68254	−3.34419	0.78483	N29	5.64135	−3.52257	−0.69834	C51	−8.8839	−1.3647	−1.08103
C8	3.13327	−3.36602	2.05556	O30	5.87676	−3.81632	1.5623	C52	−8.6309	−0.02984	−1.4775
C9	1.75112	−3.2371	2.23472	C31	7.01119	−3.93662	−0.91549	C53	−7.5901	0.55936	−0.79039
C10	0.87607	−3.11318	1.15373	C32	−7.01122	−3.93662	0.91524	S54	−6.91258	−0.56941	0.37029
C11	−0.87609	−3.11289	−1.1538	C33	8.11481	−3.14768	−0.54766	C55	7.10725	1.91541	0.94315
C12	−0.58189	−3.03096	1.32608	C34	9.39904	−3.67737	−0.78995	S56	5.42877	2.35281	0.68748
C13	−1.42094	−3.10115	0.16891	C35	9.60804	−4.93225	−1.35881	C57	5.7377	4.03465	1.08622
C14	−2.8374	−3.18237	0.34016	C36	8.48387	−5.69046	−1.71295	C58	7.06822	4.20908	1.41504
C15	−3.68257	−3.34386	−0.78495	C37	7.20644	−5.19397	−1.49018	C59	7.83421	3.02257	1.33515
C16	−3.1333	−3.36544	−2.05569	C38	−7.20641	−5.1941	1.48967	C60	4.68731	5.02723	1.07967
C17	−1.75114	−3.23654	−2.23482	C39	−8.4838	−5.69069	1.7124	S61	4.65689	6.23582	1.74525
C18	−1.18377	−2.92819	2.58154	C40	−9.60801	−4.93243	1.35849	C62	3.46538	6.98871	1.56169
C19	−2.57411	−2.96085	2.73759	C41	−9.39908	−3.67742	0.7899	C63	2.55673	6.33931	0.73605
C20	−3.40058	−3.11661	1.63746	C42	−8.11488	−3.14764	0.54763	S64	3.21259	4.81198	0.16457
C21	−5.13997	−3.57091	−0.622	C43	11.00375	−5.45961	−1.59495	C65	−2.55656	6.3393	−0.73617
C22	−4.86277	−3.24617	1.84495	C44	−11.00369	−5.45989	1.59457	C66	−3.46521	6.98862	−1.56188

C67	−4.65676	6.23577	−1.74527	H85	1.36507	−3.26807	3.24688	H103	9.64238	−1.99162	1.53671
C68	−4.68723	5.02729	−1.07951	H86	−3.79392	−3.49743	−2.90595	H104	−9.64291	−1.99112	−1.53615
S69	−3.21248	4.81209	−0.16443	H87	−1.3651	−3.2673	−3.24698	H105	−9.16872	0.47711	−2.27096
C70	−5.73768	4.03478	−1.08586	H88	−0.57361	−2.82772	3.47162	H106	7.48542	5.17684	1.67086
S71	−5.42878	2.35288	−0.68738	H89	−3.02513	−2.89044	3.72166	H107	8.90175	2.9814	1.52109
C72	−7.10736	1.91563	−0.94264	H90	10.25846	−3.06268	−0.53945	H108	5.45984	6.56199	2.39843
C73	−7.83434	3.02289	−1.33433	H91	8.60846	−6.67048	−2.16681	H109	−5.45972	6.56187	−2.39848
C74	−7.06828	4.20934	−1.41431	H92	6.33681	−5.78471	−1.76084	H110	−8.90193	2.98182	−1.51999
C75	1.22076	6.73541	0.34665	H93	−6.33674	−5.78487	1.76016	H111	−7.48548	5.17717	−1.6699
S76	0.00006	5.51943	0.00042	H94	−8.60834	−6.6708	2.16606	H112	−1.26176	8.90549	−0.32003
C77	−1.22055	6.7354	−0.34689	H95	−10.25854	−3.06271	0.53959	H113	1.26213	8.90548	0.31922
C78	−0.68275	7.99928	−0.18981	H96	11.76202	−4.70733	−1.35728	H114	3.83973	8.39421	3.14636
C79	0.68304	7.99928	0.18924	H97	11.1448	−5.76097	−2.6398	H115	3.47871	9.15712	1.59602
C80	3.22423	8.30831	2.24499	H98	11.20431	−6.34276	−0.97518	H116	2.17473	8.42286	2.53539
C81	−3.22402	8.3081	−2.2454	H99	−11.76199	−4.70745	1.3575	H117	−3.83961	8.39392	−3.14672
H82	0.57359	−2.82697	−3.47163	H100	−11.2044	−6.34266	0.97429	H118	−2.17454	8.42252	−2.53594
H83	3.02512	−2.88972	−3.72168	H101	−11.14456	−5.76191	2.63926	H119	−3.47835	9.15703	−1.5965
H84	3.79389	−3.49823	2.90579	H102	9.16816	0.47653	2.27181				

Final Geometry:

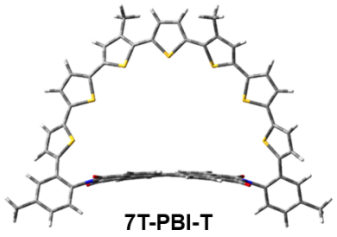

Total energy: −5811.97082142 Hartrees

C1	1.56489	−4.02077	−2.372	C5	1.43074	−4.14808	0.05136	C9	1.39046	−4.27549	2.47817
C2	2.96246	−3.98392	−2.31094	C6	0.77868	−4.11437	−1.22197	C10	0.68882	−4.18222	1.27456
C3	3.6142	−4.0559	−1.09167	C7	3.52693	−4.23603	1.34855	C11	−0.6895	−4.18215	−1.27474
C4	2.8593	−4.14714	0.10265	C8	2.78883	−4.31048	2.5176	C12	−0.77935	−4.11429	1.2218

C13	−1.43141	−4.14793	−0.05153	C49	6.40235	−1.26194	1.48042	H85	0.85475	−4.33103	3.41848
C14	−2.85997	−4.14683	−0.10282	C50	−7.30965	−1.66641	−0.52866	H86	−3.317	−4.38922	−3.46245
C15	−3.52761	−4.23565	−1.34872	C51	−6.40281	−1.26118	−1.48043	H87	−0.85544	−4.33098	−3.41865
C16	−2.78953	−4.31019	−2.51778	C52	−6.06444	0.1125	−1.39555	H88	−1.09879	−3.96367	3.34813
C17	−1.39114	−4.27536	−2.47834	C53	−6.71161	0.78288	−0.37772	H89	−3.55748	−3.90252	3.21461
C18	−1.56554	−4.0206	2.37182	S54	−7.75322	−0.31792	0.50404	H90	9.91607	−2.21487	0.34514
C19	−2.96311	−3.9836	2.31077	C55	6.54547	2.16647	−0.01299	H91	9.63099	−6.47522	−0.08191
C20	−3.61486	−4.05551	1.09149	S56	4.99351	2.93474	0.2495	H92	7.16262	−6.30013	0.01438
C21	−5.00885	−4.25792	−1.4249	C57	5.55602	4.4624	−0.40576	H93	−7.16355	−6.2994	−0.01477
C22	−5.09783	−4.03075	1.06114	C58	6.86914	4.34232	−0.82139	H94	−9.63194	−6.47417	0.08167
N23	−5.70481	−4.13525	−0.21084	C59	7.42093	3.05362	−0.60644	H95	−9.91649	−2.21373	−0.34482
O24	−5.61022	−4.35913	−2.4854	C60	4.65704	5.59219	−0.49134	H96	11.92622	−3.4503	0.05903
O25	−5.77534	−3.9348	2.0706	S61	4.7988	6.78798	−1.16799	H97	11.78776	−4.94528	−0.87969
C26	5.09718	−4.03129	−1.06131	C62	3.66063	7.64255	−1.11519	H98	11.86462	−5.01609	0.88167
C27	5.00816	−4.25851	1.42473	C63	2.62101	7.08859	−0.38064	H99	−11.92676	−3.44892	−0.05828
O28	5.7747	−3.93548	−2.07077	S64	3.09192	5.53394	0.28581	H100	−11.86547	−5.01421	−0.88187
N29	5.70414	−4.13581	0.21068	C65	−2.61985	7.08875	0.38063	H101	−11.78846	−4.94449	0.87952
O30	5.60952	−4.35984	2.48523	C66	−3.6599	7.64348	1.11401	H102	5.38574	0.60736	2.08204
C31	7.15164	−4.17106	0.24036	C67	−4.79815	6.78903	1.16691	H103	6.03241	−1.92865	2.24987
C32	−7.15231	−4.17031	−0.2405	C68	−4.65605	5.59256	0.49153	H104	−6.03314	−1.92785	−2.25003
C33	7.91782	−2.9951	0.34173	S69	−3.09039	5.53342	−0.28446	H105	−5.38585	0.60777	−2.08211
C34	9.31657	−3.11739	0.26115	C70	−5.55508	4.46277	0.40639	H106	7.4267	5.16497	−1.25596
C35	9.95616	−4.34818	0.1074	S71	−4.99354	2.93566	−0.25095	H107	8.4439	2.79052	−0.85433
C36	9.16261	−5.50077	0.03288	C72	−6.54499	2.167	0.01365	H108	5.68728	7.03682	−1.73971
C37	7.77685	−5.40832	0.09442	C73	−7.41956	3.0537	0.60905	H109	−5.68707	7.03862	1.73763
C38	−7.77767	−5.4075	−0.09466	C74	−6.86753	4.34229	0.82403	H110	−8.44207	2.79033	0.85857
C39	−9.16344	−5.49977	−0.03304	C75	1.2583	7.53524	−0.17647	H111	−7.42441	5.1645	1.26029
C40	−9.95684	−4.34706	−0.10735	S76	6.19E−4	6.32299	3.87E−4	H112	−1.29485	9.70662	0.14837
C41	−9.3171	−3.11634	−0.261	C77	−1.25711	7.53528	0.17651	H113	1.29597	9.70657	−0.14957
C42	−7.91835	−2.99423	−0.34168	C78	−0.70355	8.79981	0.09539	H114	4.28434	8.983	−2.68093
C43	11.46242	−4.44105	0.03829	C79	0.70469	8.79978	−0.09604	H115	2.58238	9.15738	−2.21278
C44	−11.46311	−4.43975	−0.03817	C80	3.59133	8.96346	−1.83353	H116	3.85935	9.79977	−1.174
C45	7.30929	−1.66721	0.52877	C81	−3.59103	8.96515	1.83098	H117	−4.28506	8.98585	2.67751
S46	7.75334	−0.31866	−0.50367	H82	1.09814	−3.96379	−3.3483	H118	−3.85794	9.80084	1.17022
C47	6.71177	0.7822	0.37806	H83	3.55684	−3.9029	−3.21478	H119	−2.58247	9.15914	2.21126
C48	6.06425	0.11181	1.39563	H84	3.3163	−4.38958	3.46228				

Final Geometry:

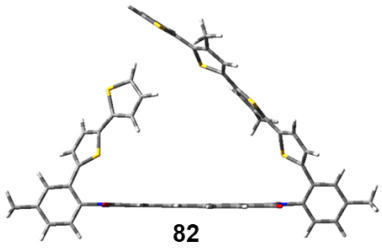

Total energy: −5261.35380099

C1	1.77779	−3.56593	−2.29303	O28	5.97526	−3.14502	−2.27244	H55	7.80792	−4.83561	−0.23091
C2	3.1715	−3.45118	−2.32148	O29	6.02724	−2.9132	0.00416	H56	−6.69862	−5.86012	0.96096
C3	3.88461	−3.26425	−1.15002	O30	6.0657	−2.74727	2.28862	H57	−9.1558	−6.17582	0.98582
C4	3.1975	−3.19398	0.08637	C31	7.4612	−2.73258	−0.03268	H58	−9.65213	−2.10063	−0.26478
C5	1.7723	−3.30329	0.12359	C32	−6.79659	−3.81695	0.33089	H59	12.07405	−1.29626	−0.09143
C6	1.05502	−3.49252	−1.10052	C33	8.02992	−1.45133	0.08263	H60	12.23936	−2.9294	−0.75785
C7	3.92904	−3.01117	1.28504	C34	9.43262	−1.35739	0.09741	H61	12.17239	−2.69239	0.98958
C8	3.25904	−2.94571	2.49427	C35	10.26069	−2.47725	−0.0017	H62	−11.6061	−3.38997	0.20464
C9	1.86471	−3.04605	2.53894	C36	9.6585	−3.73553	−0.1325	H63	−11.39856	−4.99804	−0.50246
C10	1.0992	−3.21615	1.38369	C37	8.2732	−3.8588	−0.14296	H64	−11.43897	−4.80909	1.25154
C11	−0.41153	−3.5965	−1.06285	C38	−7.35766	−5.04073	0.69086	C65	−7.11586	−1.41118	−0.43865
C12	−0.36849	−3.30143	1.4192	C39	−8.7368	−5.215	0.69718	C66	−7.5668	−0.65981	−1.50014
C13	−1.08573	−3.48996	0.19508	C40	−9.58655	−4.16142	0.33481	S67	−5.89946	−0.51645	0.45465
C14	−2.51287	−3.5711	0.22938	C41	−9.00948	−2.93939	−0.01276	C68	−6.93198	0.60285	−1.62472
C15	−3.24448	−3.76291	−0.96786	C42	−7.61728	−2.7324	−0.02599	H69	−8.31143	−1.02925	−2.19685
C16	−2.57167	−3.87324	−2.17214	C43	11.76465	−2.33846	0.03378	H70	−7.13939	1.30295	−2.42712
C17	−1.17597	−3.78917	−2.21525	C44	−11.08604	−4.34549	0.323	C71	7.23705	−0.21706	0.22203
C18	−1.09298	−3.19829	2.60836	H45	1.26294	−3.70826	−3.23562	C72	7.42479	0.78835	1.14307
C19	−2.48953	−3.27366	2.63268	H46	3.71483	−3.50046	−3.25915	S73	5.93509	0.2049	−0.87076
C20	−3.20262	−3.45837	1.46105	H47	3.83652	−2.80867	3.40227	C74	6.531	1.87869	0.99456
C21	−4.72498	−3.85691	−0.95741	H48	1.38441	−2.98366	3.50804	H75	8.17651	0.72816	1.92255
C22	−4.68276	−3.52529	1.52106	H49	−3.14865	−4.02241	−3.07854	C76	5.64329	1.73272	−0.05386
C23	−5.35448	−3.71313	0.29719	H50	−0.69428	−3.87689	−3.18176	H77	6.53805	2.75193	1.63823
C24	−5.37926	−4.0502	−1.96855	H51	−0.57846	−3.05012	3.55022	C78	0.59996	6.96125	1.37036
N25	−5.30443	−3.41862	2.56672	H52	−3.03566	−3.18602	3.56588	S79	0.27428	5.60046	−0.81987
N26	5.35792	−3.11487	−1.21883	H53	9.87838	−0.36917	0.16951	C80	1.72088	6.09309	1.2473
O27	5.40592	−2.88193	1.27144	H54	10.27689	−4.62497	−0.22488	C81	1.72066	5.29982	0.12044

H82	2.53109	6.08073	1.96986	C93	0.44834	7.91518	2.5273	H104	−4.64087	9.20447	0.42594
C83	2.68977	4.31783	−0.30751	H94	0.06453	8.8891	2.20685	C105	−5.14412	2.00745	−0.46278
C84	2.88265	3.78004	−1.56167	H95	−0.24158	7.52824	3.28843	C106	−3.94237	2.11369	0.20389
S85	3.81483	3.6021	0.82769	H96	1.41415	8.0772	3.0163	S107	−5.60674	3.56857	−1.12343
C86	3.92594	2.81705	−1.64812	C97	−1.52564	7.51832	0.00979	C108	−3.38942	3.42587	0.17738
H87	2.30274	4.0906	−2.42543	C98	−2.10684	7.71151	−1.22939	H109	−3.45978	1.26638	0.67963
C88	4.55217	2.6122	−0.42702	S99	−2.57528	8.16871	1.26389	C110	−4.16767	4.31852	−0.50705
C89	4.28919	2.14208	−2.94587	C100	−3.36555	8.37298	−1.17692	H111	−2.44451	3.69301	0.6376
H90	5.3713	2.01872	−3.05429	H101	−1.62814	7.40312	−2.15258	H112	−3.98393	5.36942	−0.68798
H91	3.83952	1.14406	−3.02739	C102	−3.74964	8.68577	0.09918	C113	−0.28306	6.83091	0.30834
H92	3.92911	2.73147	−3.79525	H103	−3.9521	8.62013	−2.0552	C114	−5.98759	0.84304	−0.64995

Final Geometry:

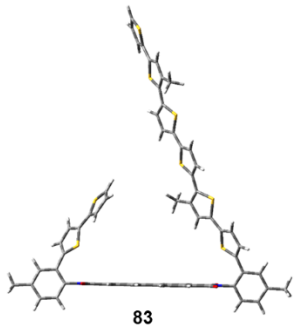

Total energy: −6364.98284625

C1	−5.64751	1.28653	2.56757	C14	−5.87876	−2.97995	0.01477	C27	−5.79203	4.97295	−1.00024
C2	−5.61086	2.68441	2.59947	C15	−5.82852	−3.72875	1.21565	O28	−5.51676	5.50305	2.54838
C3	−5.66643	3.41488	1.42516	C16	−5.75619	−3.07139	2.4313	N29	−5.67542	5.58393	0.26669
C4	−5.76078	2.74125	0.18295	C17	−5.72784	−1.6738	2.48127	O30	−5.8661	5.64536	−2.01534
C5	−5.79479	1.31234	0.14123	C18	−5.98413	−1.52556	−2.37019	C31	−5.65367	7.02927	0.30391
C6	−5.73749	0.57728	1.36807	C19	−6.00445	−2.9238	−2.40298	C32	−5.95315	−7.26875	−0.10711
C7	−5.81988	3.49032	−1.01744	C20	−5.95298	−3.65402	−1.2285	C33	−4.47936	7.74771	0.01882
C8	−5.91171	2.8331	−2.23194	C21	−5.85929	−5.21152	1.19861	C34	−4.55746	9.15234	0.01658
C9	−5.94178	1.43557	−2.28184	C22	−5.96691	−5.13497	−1.29893	C35	−5.74193	9.83952	0.28685
C10	−5.88395	0.65377	−1.12642	N23	−5.91324	−5.82365	−0.07176	C36	−6.88839	9.0901	0.58254
C11	−5.77276	−0.89235	1.32505	O24	−5.8423	−5.88245	2.21721	C37	−6.84164	7.70044	0.58592
C12	−5.90932	−0.81604	−1.16995	O25	−6.01446	−5.74414	−2.35656	C38	−7.19269	−7.89233	−0.23334
C13	−5.85373	−1.55094	0.05697	C26	−5.615	4.89497	1.49365	C39	−7.2924	−9.27921	−0.21886

C40	−6.14772	−10.073	−0.06837	S70	11.69506	−0.77667	1.04906	H100	6.53099	0.19773	1.70929
C41	−4.91247	−9.43266	0.04606	C71	12.96615	−0.16126	−1.09695	H101	8.9296	−0.80186	1.7357
C42	−4.78102	−8.0325	0.02856	C72	11.65931	0.3647	−1.28658	H102	13.74856	−0.0514	−1.84156
C43	−5.78913	11.34932	0.26247	H73	−5.60076	0.75808	3.51222	C103	11.2721	1.09985	−2.54357
C44	−6.24983	−11.57983	−0.03035	H74	−5.53639	3.21795	3.5411	H104	10.34637	0.70785	−2.97982
C45	−3.18762	7.11927	−0.30479	H75	−5.95762	3.42357	−3.14078	H105	11.11715	2.17103	−2.36221
S46	−2.44948	5.88031	0.6934	H76	−6.01147	0.96625	−3.25583	H106	12.06138	1.00642	−3.29575
C47	−1.03684	5.79033	−0.34431	H77	−5.72027	−3.66178	3.34064	C107	1.44305	1.84539	1.71622
C48	−1.1481	6.69759	−1.3784	H78	−5.66868	−1.20431	3.4559	H108	1.88244	1.00518	1.16748
C49	−2.35266	7.44483	−1.34952	H79	−6.02537	−0.99731	−3.3152	H109	2.09542	2.04951	2.57492
C50	−3.43485	−7.45319	0.18175	H80	−6.05826	−3.45769	−3.34578	H110	0.47649	1.51821	2.11154
C51	−2.49223	−7.79921	1.1218	H81	−3.64958	9.71405	−0.18461	C111	−0.15439	−5.38433	−0.54212
C52	−1.25549	−7.11827	0.97529	H82	−7.82336	9.59628	0.80977	C112	0.01018	−4.76888	−1.76448
S53	−2.77552	−6.25854	−0.92088	H83	−7.73368	7.12046	0.80153	S113	1.19051	−4.98965	0.51773
C54	0.03344	4.86244	−0.0592	H84	−8.08177	−7.27776	−0.33581	C114	1.20284	−3.99645	−1.85799
S55	1.59242	5.0134	−0.84299	H85	−8.26761	−9.74837	−0.32339	H115	−0.69595	−4.88539	−2.57992
C56	2.22104	3.58798	−0.01909	H86	−4.00872	−10.02931	0.13279	C116	1.9465	−4.02419	−0.71072
C57	1.26612	3.06014	0.8423	H87	−4.78532	11.78072	0.20199	H117	1.4977	−3.45026	−2.74743
C58	0.04588	3.78737	0.80324	H88	−6.27441	11.74829	1.16076	H118	2.89175	−3.53832	−0.50962
C59	3.56769	3.16193	−0.32401	H89	−6.35978	11.71375	−0.60144	C119	14.36182	−1.45312	0.60287
C60	4.34068	3.51736	−1.41625	H90	−5.26564	−12.0504	−0.11652	C120	14.63237	−1.91303	1.87514
C61	5.63865	2.96152	−1.41232	H91	−6.7001	−11.92259	0.91024	S121	15.73607	−1.75432	−0.45127
C62	5.90137	2.16087	−0.31674	H92	−6.87776	−11.95848	−0.84509	C122	15.92466	−2.49361	2.00882
S63	4.50068	2.11357	0.74153	H93	−0.39601	6.8031	−2.15325	H123	13.9275	−1.82327	2.69503
C64	7.09677	1.4223	0.00778	H94	−2.6228	8.18039	−2.09929	C124	16.63935	−2.47621	0.84273
C65	7.30623	0.4947	1.01077	H95	−2.69624	−8.51419	1.91143	H125	16.30735	−2.90183	2.93789
C66	8.60916	−0.04842	1.02419	H96	−0.40323	−7.27604	1.62798	H126	17.64055	−2.84296	0.66109
C67	9.44139	0.44578	0.03391	H97	−0.82049	3.49965	1.39073	C127	−1.23177	−6.24206	−0.08831
S68	8.56534	1.63208	−0.93151	H98	3.96768	4.15025	−2.21426	C128	13.16733	−0.80996	0.10134
C69	10.82754	0.11311	−0.20144	H99	6.35832	3.12564	−2.20746				

Final Geometry:

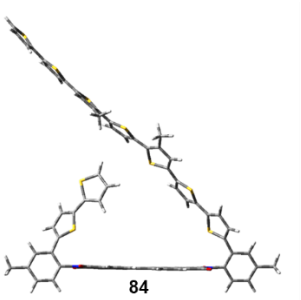

Total energy: −6916.79919220

C1	−4.76574	−3.33627	−2.54625	C27	−2.73108	−6.48876	0.9554	S53	−6.72693	4.1609	0.8939
C2	−3.893	−4.42814	−2.59844	O28	−2.12305	−6.62247	−2.58872	S54	12.65529	1.81769	−0.7929
C3	−3.51969	−5.08392	−1.43828	N29	−2.24091	−6.85952	−0.31483	C55	11.2952	1.82429	0.32048
C4	−4.0242	−4.64502	−0.18996	O30	−2.41131	−7.10862	1.95604	C56	11.73209	1.56278	1.60414
C5	−4.91071	−3.52497	−0.12705	C31	−1.35809	−8.00332	−0.37683	C57	13.12616	1.33753	1.6985
C6	−5.28714	−2.86475	−1.33983	C32	−9.98826	3.38333	0.26725	C58	9.95625	2.08509	−0.14971
C7	−3.6442	−5.32026	0.99541	C33	0.00582	−7.89373	−0.05293	C59	9.47264	2.08916	−1.44118
C8	−4.13606	−4.89196	2.21598	C34	0.77944	−9.06903	−0.09331	C60	8.08595	2.37361	−1.56352
C9	−4.99736	−3.79193	2.2872	C35	0.24522	−10.31171	−0.43592	C61	7.48337	2.59282	−0.33063
C10	−5.39606	−3.09089	1.14743	C36	−1.11526	−10.37901	−0.7647	S62	8.66648	2.47517	0.96942
C11	−6.19936	−1.71313	−1.2751	C37	−1.90465	−9.23529	−0.73123	C63	2.35483	4.1273	−0.20716
C12	−6.28637	−1.92223	1.21453	C38	−11.36233	3.25306	0.4546	C64	1.88428	4.98335	−1.1953
C13	−6.6646	−1.26328	0.00148	C39	−12.18297	4.37559	0.47613	C65	0.48088	5.19058	−1.10429
C14	−7.52516	−0.12329	0.06681	C40	−11.64264	5.65651	0.30111	C66	−0.14241	4.51718	−0.07508
C15	−7.91904	0.54031	−1.12058	C41	−10.2626	5.77092	0.12396	S67	1.03037	3.56038	0.80684
C16	−7.47333	0.07616	−2.34591	C42	−9.40811	4.65433	0.10452	C68	−1.53634	4.50344	0.29794
C17	−6.62511	−1.03356	−2.41812	C43	1.10822	−11.55161	−0.45466	S69	−2.77789	5.02881	−0.82971
C18	−6.77405	−1.42437	2.42454	C44	−12.53119	6.87834	0.30426	C70	−4.05772	4.71028	0.33132
C19	−7.60835	−0.30314	2.48044	C45	0.66633	−6.64203	0.35224	C71	−3.52422	4.20677	1.50086
C20	−7.98491	0.3503	1.31982	S46	0.49415	−5.13034	−0.52146	C72	−2.11423	4.09057	1.48235
C21	−8.79859	1.73294	−1.07832	C47	2.07725	−5.17189	1.51193	C73	6.10929	2.8766	0.01879
C2	−8.84289	1.55519	1.4169	C48	1.55732	−6.48616	1.38983	S74	4.97023	3.59848	−1.11083
N23	−9.18098	2.18593	0.20297	C49	−7.96856	4.87273	−0.11906	C75	3.69135	3.66432	0.09491
O24	−9.17477	2.31131	−2.0844	C50	−7.3932	5.67171	−1.08086	C76	4.1567	3.14918	1.29333
O25	−9.23192	2.00358	2.48434	C51	−5.9762	5.70998	−1.02609	C77	5.49812	2.71052	1.25057
C26	−2.58529	−6.23186	−1.52807	C52	−5.44309	4.9425	−0.01099	C78	7.38814	2.39292	−2.8989

C79	2.72746	5.6618	−2.2439	H98	−13.15127	6.91941	−0.60051	H117	3.6567	6.06276	−1.82535
H80	−5.02687	−2.85295	−3.48007	H99	−13.21319	6.87403	1.16241	C118	15.19453	1.24272	0.20424
H81	−3.49296	−4.77643	−3.54472	H100	2.76048	−4.86682	2.2975	C119	15.8129	1.01167	−1.00704
H82	−3.83672	−5.42356	3.11294	H101	1.79956	−7.29376	2.07205	S120	16.39139	1.31193	1.48929
H83	−5.35232	−3.4908	3.26555	H102	−7.98092	6.19519	−1.82698	C121	17.22677	0.88205	−0.90892
H84	−7.78912	0.59468	−3.24488	H103	−5.36495	6.28767	−1.71157	H122	15.26407	0.91711	−1.93809
H85	−6.29767	−1.3564	−3.39909	H104	11.05948	1.50723	2.45354	C123	17.68572	1.01245	0.37303
H86	−6.50359	−1.90032	3.35947	H105	13.62978	1.09158	2.62738	H124	17.8736	0.69108	−1.75828
H87	−7.96782	0.07601	3.43115	H106	10.09666	1.86074	−2.29966	H125	18.70402	0.95242	0.73273
H88	1.83901	−8.99017	0.13274	H107	−0.05386	5.85551	−1.77554	C126	1.89746	−2.89222	0.37679
H89	−1.5589	−11.33014	−1.0485	H108	−4.13407	3.94925	2.36034	C127	1.15737	−1.9195	−0.26054
H90	−2.96111	−9.28903	−0.97552	H109	−1.53236	3.73597	2.32655	S128	3.38753	−2.20296	1.00262
H91	−11.78386	2.26035	0.57761	H110	3.54177	3.09843	2.18549	C129	1.76772	−0.6329	−0.23871
H92	−13.25267	4.25512	0.62871	H111	6.01153	2.28171	2.10455	H130	0.19134	−2.12014	−0.71183
H93	−9.81885	6.75674	0.01605	H112	8.01667	1.92524	−3.66303	C131	2.97044	−0.6247	0.41293
H94	2.16898	−11.30306	−0.35237	H113	6.43556	1.85302	−2.87105	H132	1.32415	0.2538	−0.67834
H95	0.98154	−12.11241	−1.38804	H114	7.17298	3.41577	−3.23401	H133	3.63673	0.2107	0.58367
H96	0.84521	−12.22981	0.36734	H115	2.17659	6.49224	−2.69634	C134	13.7877	1.42269	0.4904
H97	−11.94398	7.80082	0.34518	H116	3.00543	4.9748	−3.05364	C135	1.59761	−4.2991	0.55912

Final geometry:

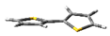

79

Total energy: −1104.81669881 Hartrees

C1	0.00000	3.21057	−0.05036	H7	−2.27318	0.80799	0.4783	C13	0.00000	−3.21057	−0.05036
C2	−1.26892	2.7657	0.19851	C8	0.14867	−0.71017	0.06763	H14	2.11707	−3.42706	0.33872
C3	−1.35485	1.34567	0.26702	C9	1.35485	−1.34567	0.26702	H15	−0.3497	−4.22987	−0.14378
S4	1.11645	1.89317	−0.22313	S10	−1.11645	−1.89317	−0.22313	C16	−0.14867	0.71017	0.06763
H5	0.3497	4.22987	−0.14378	C11	1.26892	−2.7657	0.19851				
H6	−2.11707	3.42706	0.33872	H12	2.27318	−0.80799	0.4783				

Chapter 6

Summary and Conclusion

The aim of this work was the synthesis as well as subsequent optical and redox investigations of unprecedented macrocyclic perylene bis(dicarboximides) (PBI)-oligothiophene dyads.
Besides serving as model compounds for their polymeric analogues, the versatile applicable and easy to synthesize linear oligothiophenes reveal chain size-dependent properties not only in the neutral but also in the charged state (*Chapter 2.1*). By bending these linear strands into cyclo[*n*]thiophenes (C[*n*]Ts, *n* = amount of thiophene subunits) interesting new optical and redox features can be observed also in comparison to [*n*]cycloparaphenylenes ([*n*]CPPs, *n* = amount of phenyl subunits) as a closely related compound class (*Chapter 2.2*). The combination of electron-rich oligothiophenes with electron-deficient PBIs leads to donor-acceptor (D-A) dyads with highly interesting processes in the excited state such as Förster resonance energy transfer (FRET) or photoinduced electron transfer (PET) which can be monitored by transient absorption (TA) spectroscopy (*Chapter 2.3*).

Within the above described contentual framework this thesis describes the synthesis and opto-electronical characterization of linear phenyl end-capped oligothiophenes **4T**-**7T** and D-A dyads composed of semi- (**4T-PBI** to **7T-PBI**) or full (**(5T)$_2$-PBI**) oligothiophene donor circles which all embed an accepting PBI moiety. Initially meant to serve as reference compounds for the bent oligothiophene bridges in the macrocycles the oligothiophene chains **4T-7T** (Figure 136a) themselvs revealed interesting properties (*Chapter 3*).
While in the neutral state the also commonly observed structureless absorption and fine structured emission spectra displayed nothing unusual (Figure 136b), in the oligothiophene series **4T**-**7T** a very remarkable “zig-zag” trend in the first oxidation potential was detected (Figure 136c). As described in *Chapter 2.1.3*, normally a gradual decrease of the first oxidation potential with increasing chain length is observed. However, **5T** and **7T** show radical cation formation at much higher energy values than expected. This phenomenon could be explained with the different aliphatic decoration pattern in the focal part of the chains (Figure 136a).

Upon oxidation a quinoid structure is adopted which leads to a planarization of the strand and a shrinkage of the thiophene-thiophene interring distances. On the one hand, for **5T** and **7T** this causes steric encumbrance of the hexyl chains due to the close spatial proximity, which involves a destabilization of the cationic state (Figure 136c). On the other hand, in the case of **4T** and **6T** the aliphatic chains point away from each leading to no noticeable destabilization of the charged species and therefore also to no impact on the oxidation potential.

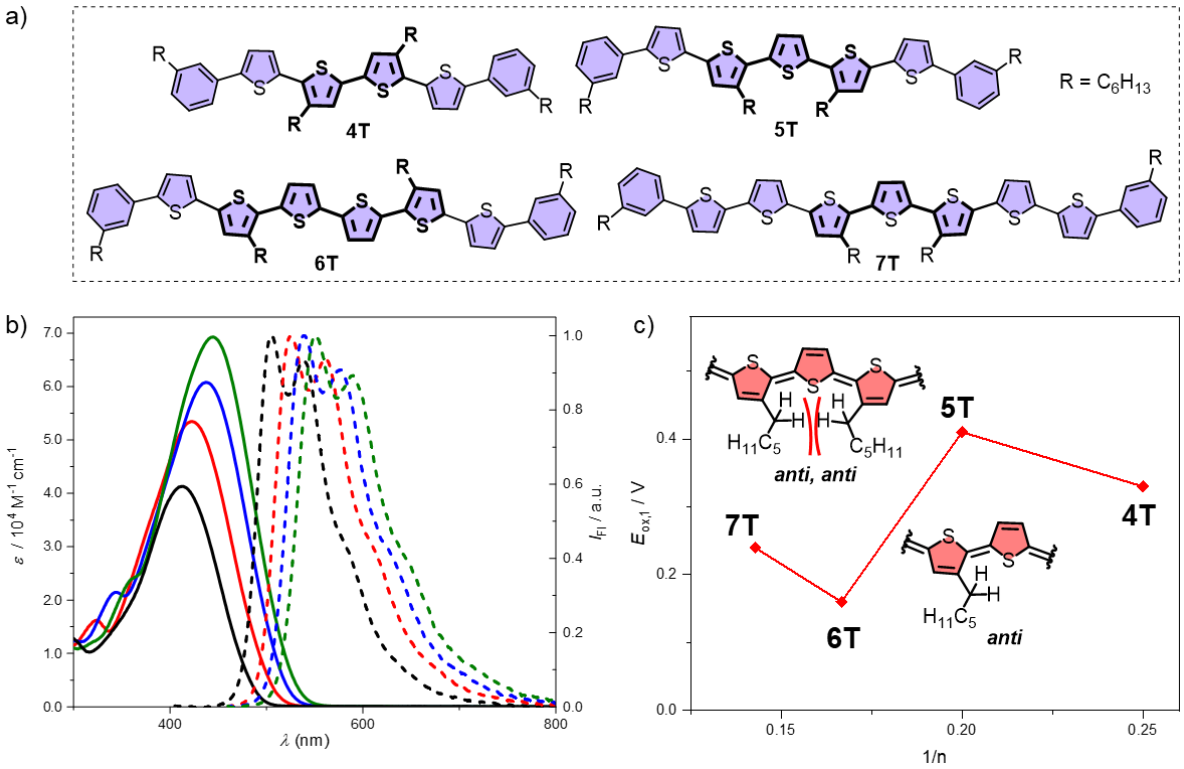

Figure 136. a) Chemical structures of neutral **4T**-**7T** (*Chapter 3*) with the aliphatic decoration pattern highlighted in bold print. b) UV/Vis absorption (solid lines, c_0 = 10^{-5} M) and normalized emission spectra (dashed lines, λ_{ex} = 400 nm, c_0 = 10^{-7} M) of **4T** (black), **5T** (red), **6T** (blue) and **7T** (green) in CH_2Cl_2 at room temperature.[235] c) Graphic illustration of the first oxidation potential $E_{ox,1}$ vs. the inverse total number of thiophene units n for **4T**-**7T** in CH_2Cl_2 solutions at room temperature (c_0 = 10^{-4} M). The lines serve as guide to the eye. The insets show the focal part of **5T** and **7T** (top) as well as **4T** and **6T** (bottom) in the quinoid onefold oxidized state.

With all linear reference oligothiophenes **4T**-**7T** optically and electronically investigated *Chapter 4* and *Chapter 5* introduce entirely novel macrocyclic D-A architectures composed of (semi-) cyclic oligothiophenes with an embedded core PBI moiety (Figure 137a). Here, the large dimension between the two imide units of a PBI dye has been tethered covalently by an oligothiophene chain for the first time. In total, the synthesis of all five macrocycles involved four steps with a final macrocyclization reaction itself consisting of a “one pot” three step Pt-

mediated reaction cascade. In a combination of intra- and intermolecular reactions, two and four C-C bonds were formed for **4T-PBI** to **7T-PBI** and **(5T)$_2$-PBI**, respectively.

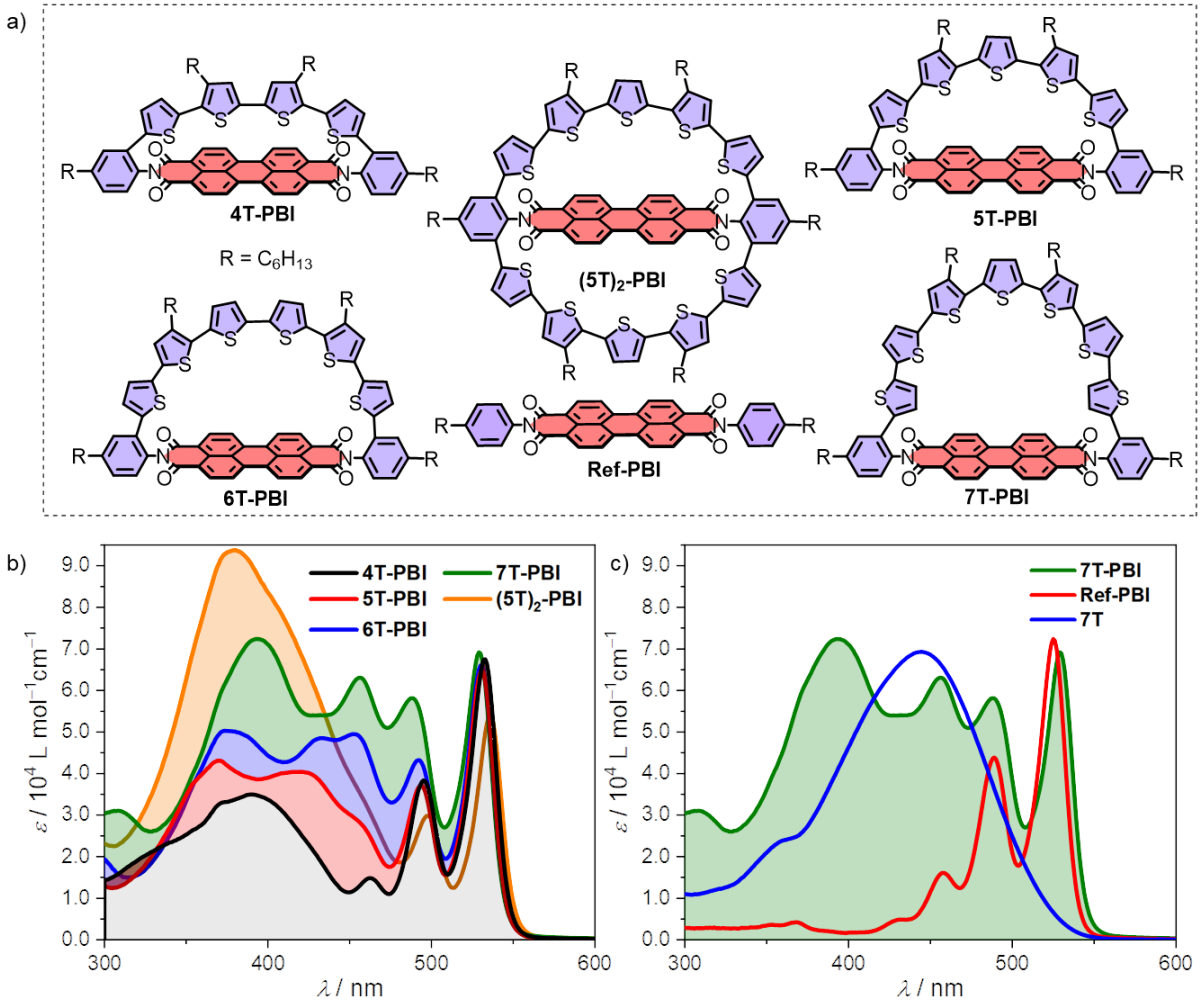

Figure 137. a) Chemical structures of **4T-PBI** to **7T-PBI**, **(5T)$_2$-PBI** and **Ref-PBI** described in *Chapter 4* and *5*. b) UV/Vis spectra of **4T-PBI** (black line), **5T-PBI** (red line)[262], **6T-PBI** (blue line), **7T-PBI** (green line) and **(5T)$_2$-PBI** (orange line) as well as c) **7T-PBI** (green line), **7T**(blue line)[235] and **Ref-PBI(**red line)[262] in CH_2Cl_2 at room temperature ($c_0 = 10^{-5}$ M).

Installation of oligothiophene bridges to span the PBI's imide positions leads to mostly photophysically independent chromophores. Due to a complete spatial separation of their HOMOs and LUMOs at the oligothiophene and PBI segment, the absorption spectra of **4T-PBI** to **7T-PBI** and **(5T)$_2$-PBI** show no charge transfer bands, which is in stark contrast to PBI dyads with conjugated donor units attached in *e.g.* bay-position.

Despite this lack of electronic communication between the D and A, all UV/Vis spectra of the macrocycles (Figure 137b) do not simply consist of a sum of their respective reference structures **4T-7T** and **Ref-PBI** (Figure 137c). Here, in the thiophene region (below 450 nm)

bridge size-dependent vibronic fine structures can be observed. This is mainly due to the rigid bridge geometry in which different dihedral angles between the thiophene units lead to distinct conjugation lengths and therefore may cause band splittings in the absorption.
This effect is most pronounced for both larger macrocycles **6T-PBI** and **7T-PBI**. In contrast, the almost strainless dyads **5T-PBI** and **(5T)$_2$-PBI** shown an absorption maximum for the bridge moiety, which is in accordance with the expectations for a cisoid oligothiophene chain.

This *cis*-arrangement of the thiophenes in the bent macrocyclic chains was also confirmed by X-ray analysis of **(5T)$_2$-PBI** and **4T-PBI** (Figure 138a, b). In case of the largest single-bridged system **7T-PBI** (Figure 138c), also strain releasing *trans*-configurations can be found in the bridge. According to NMR spectroscopy this also seems to be present in solution.

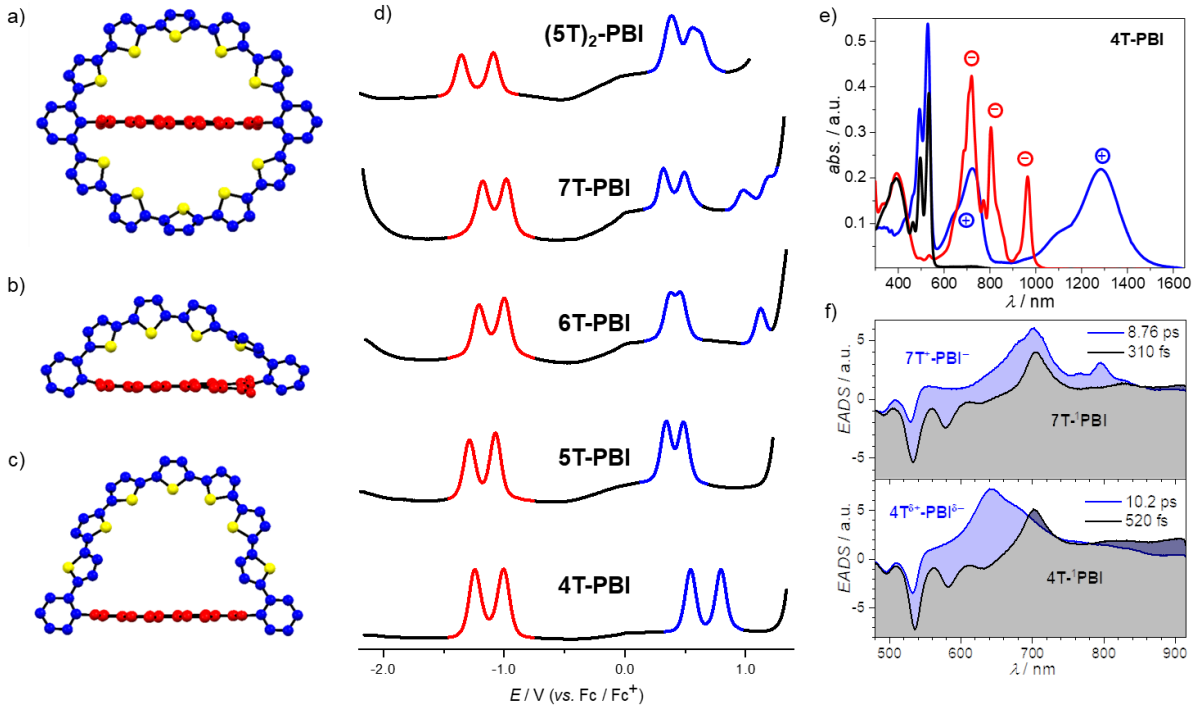

Figure 138. Front view of the molecular structure of a) **(5T)$_2$-PBI**[262], b) **4T-PBI** and c) **7T-PBI** obtained from single crystal structure analysis with the PBI segment coloured in red, the oligothiophene in blue and Sulphur atoms highlighted in yellow. The aliphatic chains as well as solvent molecules were omitted for clarity. d) DPV spectra of **4T-PBI**, **5T-PBI**[262], **6T-PBI**, **7T-PBI** and **(5T)$_2$-PBI**[262] (from bottom to top). e) UV/Vis/NIR absorption spectra of **4T-PBI** (black line) upon electrochemical reduction to **4T-PBI$^{\bullet-}$** (red line) and electrochemical oxidation to **4T$^{\bullet+}$-PBI** (blue line). All measurements were carried out in CH_2Cl_2 solutions with Bu_4NPF_6 at room temperature ($c_0 = 10^{-4}$ M). f). Evolution associated difference spectra and lifetimes from a global fit analysis of the transient spectra of macrocycles **4T-PBI** and **7T-PBI** obtained by excitation at 530 nm in CH_2Cl_2 ($c_0 = 10^{-4}$ M).

Due to a highly efficient PET especially in polar solvents such as CH_2Cl_2 all macrocycles are non-emissive, which is entirely different compared to their reference structures **4T**-**7T** (40%-

54%) and **Ref-PBI** (98%), which exhibit high quantum yields in chlorinated solvents. Therefore, the fluorescence spectra of **4T-PBI** to **7T-PBI** and **(5T)$_2$-PBI** were recorded in a low polar cyclohexane solvent. Still, the quantum yields of all macrocycles remained below 1%.

One advantage of two distinguishable spectral regions for D and A of the macrocyclic dyads **4T-PBI** to **7T-PBI** and **(5T)$_2$-PBI** is the possibility to photoexcite both chromophores selectively. Upon excitation of the PBI segment at 480 nm the typical fine structured emission of the PBI's S_0-S_1 transition could be observed. Exclusive excitation of the oligothiophene moiety at 400 nm also revealed PBI emission which is a strong indication for a FRET from the donating chain to the accepting PBI. Nevertheless, due to the extremely low quantum yields this is an almost neglectable process.

As oxidation of the donor (blue) and reduction of the acceptor (red) can be controlled independently from each other (Figure 138d), the mentioned spectral discriminability is accompanied by electronic decoupling of the macrocyclic segments. Overall, the macrocyclic reduction potentials do not differ more than 0.1 V from the values of **Ref-PBI**. On the other hand, due to the special aliphatic decoration of reference strands **5T** and **7T** these oxidation potentials can not directly be compared to those of the respective macrocyclic bridge in **5T-PBI** and **7T-PBI**. However, all oxidation potentials of the macrocycles are in about the same range as those of **4T-7T**. Most interestingly, the potential difference of the first and second oxidation ($E_{ox,2} - E_{ox,1}$) decreases from **4T-PBI** (0.26 V) to **6T-PBI** (0.08 V), indicating a gradual stabilization of the dicationic state within this series. In contrast a *trans* arrangement of the thiophenes closest to the phenyl rings in the **7T-PBI** donor bridge lead again to an increase of the potential difference of 0.18 V, which can be compared to the free **7T** chain (0.19 V). Opposite to the single bridged PBIs (**4T-PBI** to **7T-PBI**), in every oxidation event of **(5T)$_2$-PBI** two electrons, presumably one from each bridge, are transferred. Although being independent from each other in the neutral state (see discussion above) in the doubly charged state an intramolecular bridge cation-cation communication leads to a subsequent stepwise oxidation to the tri- and tetracationic state, which was concluded from the top DPV spectrum (blue, right wave) in Figure 138d.

Spectroelectrochemistry (SEC) was utilized to unravel the electronic nature of the charged macrocyclic species by identifying the respective spectral signatures (Figure 138e). Subsequently, the SEC spectra were compared to the TA data, which simplified the interpretation thereof. The TA spectra delivered valuable insights into the excited state dynamics of **4T-PBI** to **7T-PBI** (Figure 138f) and **(5T)$_2$-PBI** in CH_2Cl_2 upon excitation of the respective PBI segment at 530 nm. After the relaxation of the PBI S_1 state (black line) into the "cold" charge transfer/charge separated state (CT/CSS, blue line) the (partial) charges recombine within a few picoseconds. The entire process is one of the fastest for PBI-oligothiophene dyads known in literature, which is presumably due to the extremely close proximity of donor and acceptor within the rigid macrocyclic scaffold. Based on the EADS, a bridge size-dependent phenomenon upon photoexcitation within the series of **4T-PBI** to **7T-PBI** was observed (Figure 138f). While a CT state with partial charges residing at donor and acceptor segment could be identified for the small macrocycle **4T-PBI** a CSS was detected for the larger analogues. The fastest (partial) charge separation process is found for the double bridged **(5T)$_2$-PBI** due to a higher probability for this process to occur.

In summary, five novel oligothiophene-PBI donor-acceptor macrocycles as well as the respective non-cyclic reference compounds were successfully synthesized in this thesis. All compounds were intensively investigated regarding their optical properties and redox behavior. Single crystal X-ray analysis provided valuable insights in the structural arrangements of the macrocycles and here reveals highly strained bridge segments in accordance to NMR spectra analysis of the compounds in solution. Additionally, TA spectroscopy in combination with SEC of the dyads confirmed the formation of a bridge size-dependent transition of full to partial charge separation (CSS and CT), which almost completely quenches the fluorescence. Finally, this entirely new macrocyclic D-A dyad class allows for excited state fine tuning and very fast electron transfer processes, which could also inspire researchers in the field of material sciences for new molecular ingredients of the active layers or interfaces in tailored organic photovoltaic devices.

Chapter 7
Zusammenfassung und Fazit

Ziel dieser Arbeit war die Synthese und optisch-spektroskopische Untersuchung von neuartigen makrozyklischen Perylenbis(dicarboximid)- Oligothiophen Dyaden.
Neben der Verwendung als Modell-Verbindungen für Polmeranaloga, offenbaren die vielseitig einsetzbaren und leicht zu synthetisierenden linearen Oligothiophene kettenlängenabhängige Eigenschaften nicht nur im neutralen, sondern auch im geladenen Zustand (*Kapitel 2.1*). Durch Verbiegen dieser linearen Stränge in zyklische [*n*]Oligothiophene (C[*n*]Ts, *n* = Anzahl der Thiophen-Untereinheiten) können neue und interessante optische und elektronische Merkmale gerade auch im Vergleich zu [*n*]Cycloparaphenylenen ([*n*]CPPs, *n* = Anzahl der Phenyl-Untereinheiten) als nah verwandte Verbindungsklasse beobachtet werden (*Kapitel 2.2*). Die Kombination dieser elektronenreichen C[*n*]Ts mit elektronendefizitären PBIs führt zu Donor-Akzeptor (D-A) Dyaden mit hoch interessanten Prozessen im angeregten Zustand, wie z.B. Förster-Resonanzenergietransfer (FRET) oder photoinduziertem Elektronentransfer (PET), welche durch Transiente Absorptions-(TA) Spektroskopie spektral erfasst werden können (*Kapitel 2.3*).

Eingliedernd in den oben genannten inhaltlichen Rahmen beschreibt diese Doktorarbeit die Synthese und optisch-spektroskopische Charakterisierung von linearen phenylsubstituierten Oligothiophenen **4T-7T** und D-A Dyaden mit halben (**4T-PBI** bis **7T-PBI**) oder ganzen (**(5T)$_2$-PBI**) Donor Oligthiophenringen, welche alle eine elektronenarme PBI Einheit einbetten. Die Oligothiophenketten **4T-7T** (Abbildung 1a), welche ursprünglich für die gebogenen Oligothiophenbrücken der Makrozyklen als Referenzverbindungen dienen sollten, zeigten selber interessante Eigenschaften (*Kapitel 3*).
Während im neutralen Zustand die auch üblicherweise strukturlosen Absorptions-und fein strukturierten Emissionsspektren innerhalb der Oligothiophenserie **4T-7T** nichts Ungewöhnliches darstellten (Abbildung 1b), konnte ein bemerkenswerter „Zick-Zack“-Trend im ersten Oxidationspotential entdeckt werden. Wie in *Kapitel 2.1.3* beschrieben,

wird hier normalerweise eine graduelle Abnahme des ersten Oxidationspotentials mit zunehmender Kettenlänge beobachtet. **5T** und **7T** zeigen jedoch eine Radikalkationbildung bei sehr viel höheren Energiewerten, als erwartet. Dieses Phänomen konnte mit dem unterschiedlichen aliphatischen Substitutionsmuster im zentralen Abschnitt der Ketten erklärt werden (Abbildung 1c). Nach Oxidation wird eine quinoide Struktur gebildet, was zu einer Planarisierung und einer Minderung des Thiophen-Thiophen Zwischenringabstands führt. Dies bewirkt auf der einen Seite eine sterische Hinderung der Hexylketten durch räumliche Nähe für **5T** und **7T**, was eine Destabilisierung des kationisches Zustandes nach sich zieht (Abbildung 1c). Auf der anderen Seite, im Fall von **4T** und **6T**, zeigen die aliphatischen Ketten voneinander weg, was zu keiner erkennbaren Destabilisierung des geladenen Zustandes und damit auch zu keiner Beeinflussung des Oxidationspotentials führt.

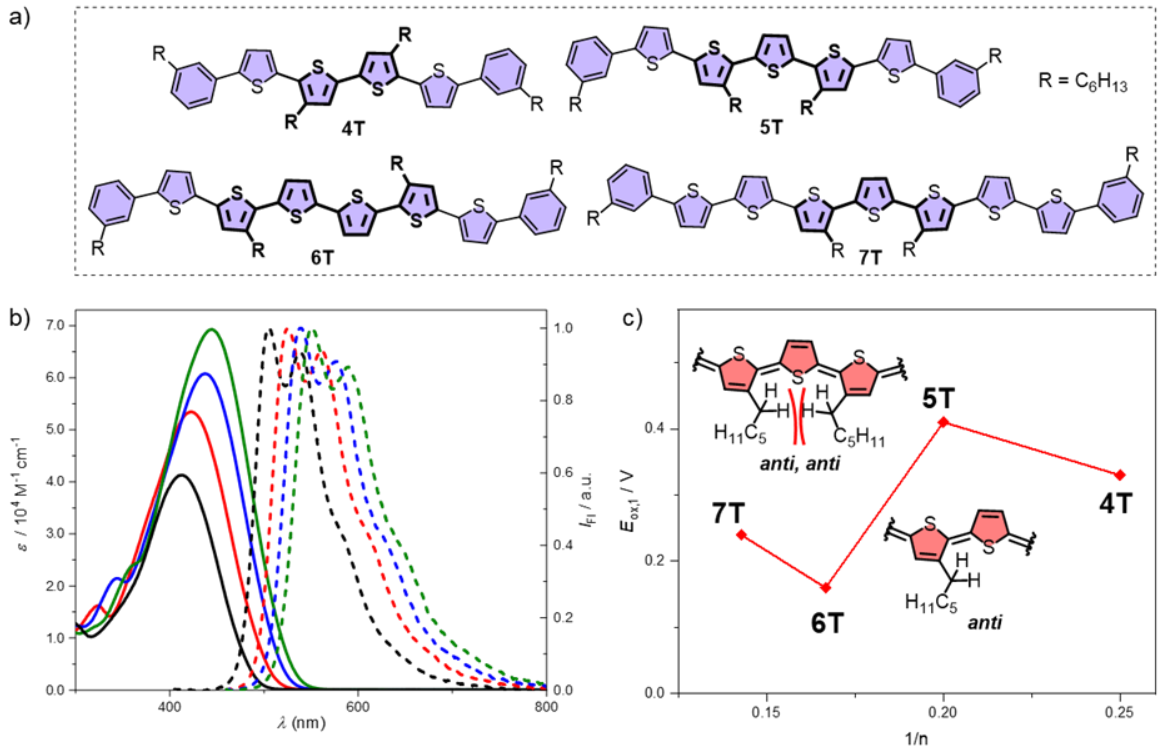

Abbildung 1. a) Chemische Strukturen von neutralen **4T**-**7T** (*Kapitel 3*) mit hervorgehobenen aliphatischen Substitutionsmustern in fetter Schrift. b) UV/Vis-Absorptions- (durchgezogene Linien $c_0 = 10^{-5}$ M) und normierte Emissionsspektren (gestrichelte Linien, $\lambda_{ex} = 400$ nm, $c_0 = 10^{-7}$ M) von **4T** (schwarz), **5T** (rot), **6T** (blau) and **7T** (grün) in CH_2Cl_2 bei Raumtemperatur.[235] c) Graphische Darstellung des ersten Oxidationspotentials $E_{ox,1}$ gegenüber der inversen Anzahl Thiopheneinheiten n von **4T**-**7T** in Lösungen bei Raumtemperatur ($c_0 = 10^{-4}$ M). Die Linien fungieren als visuelle Orientierungshilfe. Der Einsatz zeigt den zentralen Teil von **5T** und **7T** (oben) ebenso, wie **4T** und **6T** (unten) im quinoiden, einfach oxidierten Zustand.

Nach den komplettierten optischen und elektronischen Untersuchungen der linearen Referenzoligothiophene **4T**-**7T** leiten *Kapitel 4* und *Kapitel 5* gänzlich neue makrozyklische D-A Strukturen bestehend aus (halb-) zyklischen Oligothiophenen mit

eingebetteten PBI-Einheiten ein (Abbildung 2a). Hier wird der große Abstand zwischen den zwei Imideinheiten eines PBI Farbstoffmoleküls zum ersten Mal mittels einer Oligothiophen Kette kovalent überbrückt. Insgesamt sind bei der Synthese aller fünf Makrozyklen vier Schritte mit einer finalen Makrozyklisierungsreaktion bestehend aus einer „Eintopf"-Platin vermittelten Dreitschritt-Reaktionskaskade involviert. In einer Kombination aus intra-und intermolekularen Reaktionen werden für **4T-PBI** bis **7T-PBI** bzw. **(5T)$_2$-PBI** jeweils zwei und vier C-C-Bindungen geknüpft.

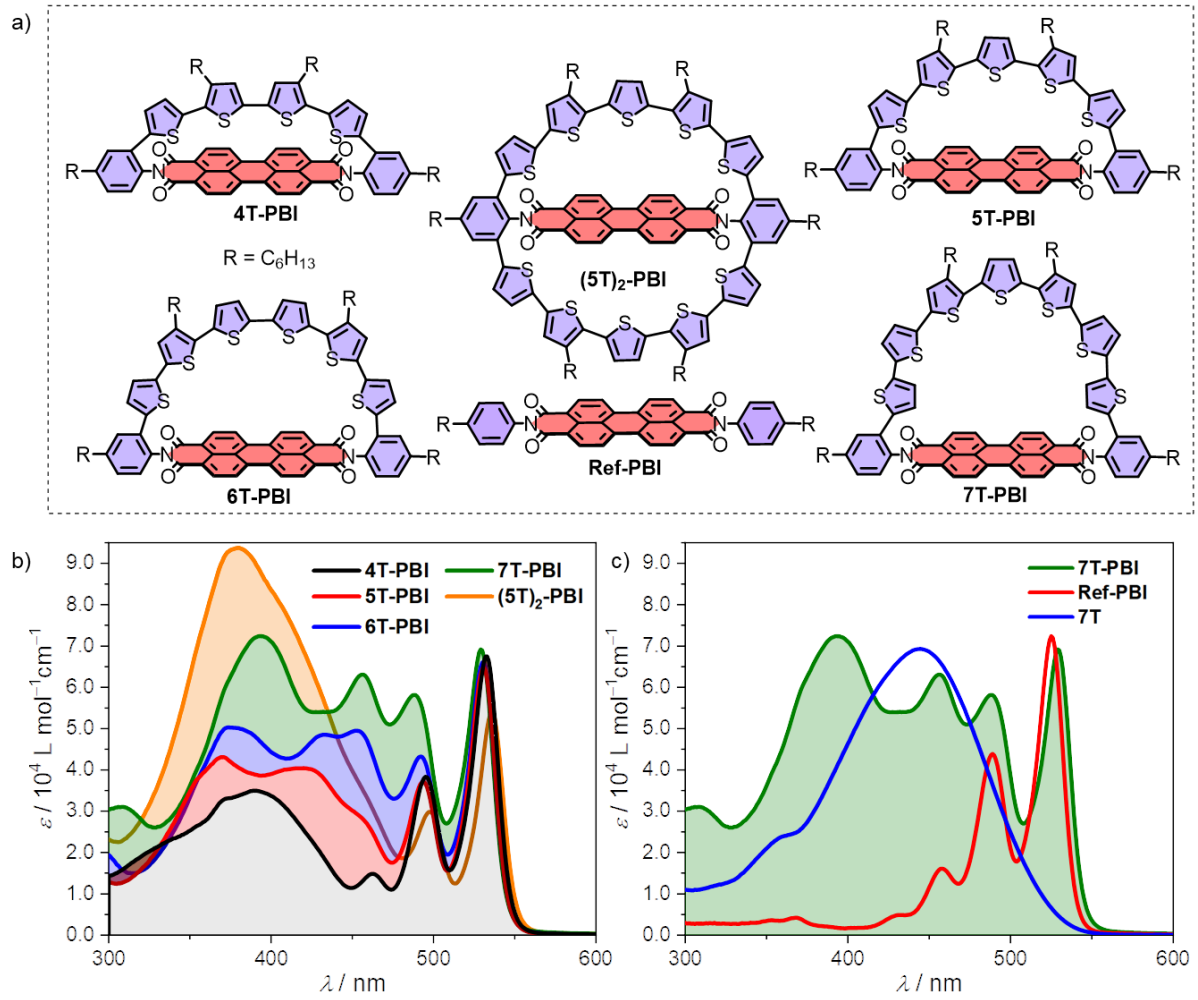

Abbildung 2. a) Chemische Strukturen von **4T-PBI** bis **7T-PBI**, **(5T)$_2$-PBI** und **Ref-PBI**, welche in *Kapitel 4* und *Kapitel 5* beschrieben wurden. b) UV/Vis Spektren von **4T-PBI** (schwarze Line), **5T-PBI** (rote Linie)[262], **6T-PBI** (blaue Linie), **7T-PBI** (grüne Linie) and **(5T)$_2$-PBI** (orange Linie), ebenso wie c) **7T-PBI** (grüne Linie), **7T**(blaue Linie)[235] and **Ref-PBI** (rote Linie)[262] in CH_2Cl_2 bei Raumtemperatur ($c_0 = 10^{-5}$ M).

Die Installation von Oligothiophenen-Brücken zur Überspannung der PBI-Imidpositionen führt insgesamt zu photophysikalisch weitgehend unabhängigen Chromophoren. Aufgrund der vollkommenen räumlichen Separierung der HOMOs bzw. LUMOs am Oligothiophen und PBI Segment, zeigen die Absorptionsspektren von **4T-PBI** bis **7T-PBI** und **(5T)$_2$-PBI** keine Ladungstransferbanden, was einen großen Kontrast zu PBI Dyaden mit verknüpften

Donoreinheiten in Konjugation z.B. in Bucht-Position darstellt. Trotz diesem Fehlen der elektronischen Kommunikation zwischen Donor und Akzeptor, bestehen alle UV/Vis Spektren der Makrozyklen (Abbildung 2b) nicht nur aus der Summe der jeweiligen Referenzabsorptionen von **4T**-**7T** und **Ref-PBI** (Abbildung 2c): In der Thiophenregion (unter 450 nm) können hier von der Brückenlänge abhängige vibronische Feinstrukturen beobachtet werden. Das liegt hauptsächlich in der rigiden Brückengeometrie begründet, in welcher unterschiedliche dihedrale Winkel zwischen den Thiopheneinheiten zu individuellen Konjugationslängen führen und dadurch Bandenaufspaltungen in den Absorptionsspektren bewirken. Dies zeigt sich insbesondere für die beiden mit längeren Oligothiophenen überspannte Derivate **6T-PBI** und **7T-PBI**. Hingegen weisen die nahezu spannungsfreien Dyaden **5T-PBI** und **(5T)$_2$-PBI** ein Absorptionsmaximum für die Brückeneinheit auf, welches im Einklang mit den Erwartungen für die cisoide Oligothiophenkette steht.

Diese *cis*-Anordnung der Thiophene in den gebogenen makrozyklischen Brücken konnte mittels Röngenstrukturanalyse von **4T-PBI** und **(5T)$_2$-PBI** bestätigt werden (Abbildung 3a, b). Im Falle des größten einfach überbrückten Systems **7T-PBI** (Abbildung 3c) konnten auch spannungsreduzierende *trans*-Konfigurationen in der Brücke gefunden werden. Gemäß NMR-Spektroskopie ist diese Anordnung auch in Lösung präsent.

Aufgrund eines hoch effektiven Elektronentransfer besonders in polaren Lösungsmitteln wie Dichlormethan (CH_2Cl_2), sind alle Makrozyklen nichtemittierend, was sie deutlich von den Referenzstrukturen **4T**-**7T** (40%-54%) und **Ref-PBI** (98%), welche hohe Quantenausbeuten in chlorierten Lösungsmitteln aufzeigen, unterscheidet. Daher wurden die Fluoreszenzspektren von **4T-PBI** bis **7T-PBI** und **(5T)$_2$-PBI** in unpolarem Cyclohexan aufgenommen. Dennoch blieben die Quantenausbeuten aller Makrozyklen unter 1%.

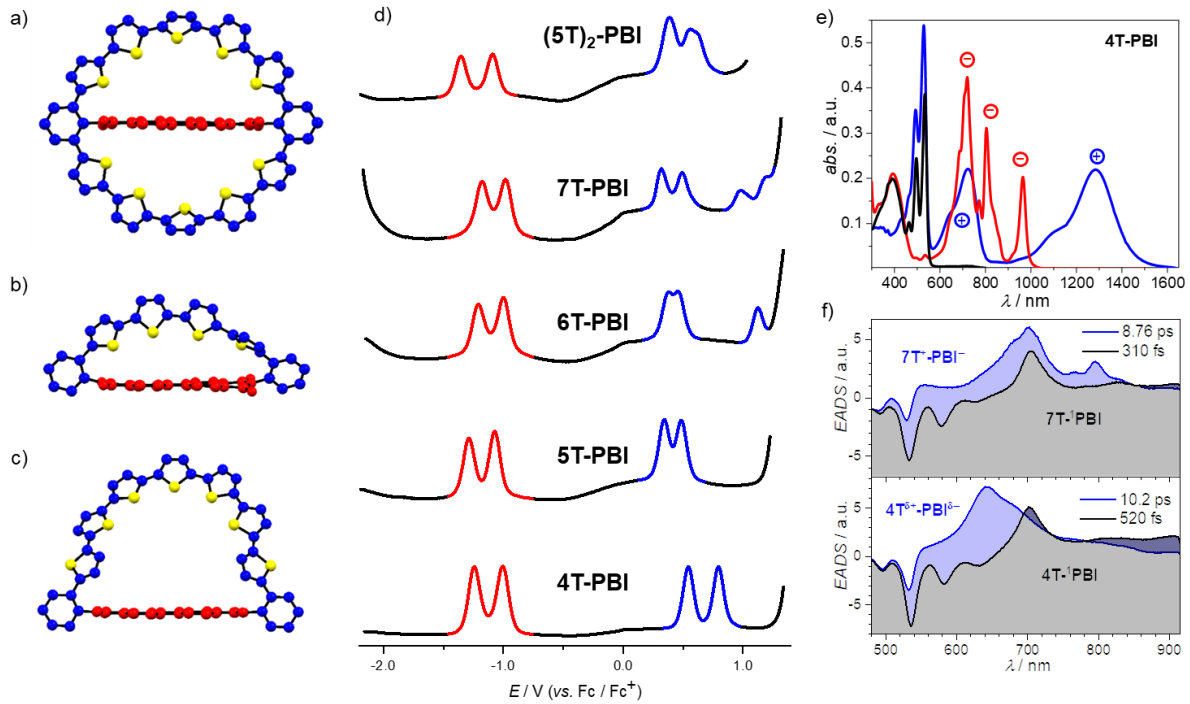

Abbildung 3. Frontanlansicht auf die im Einkristall gefundene molekulare Struktur von a) **(5T)$_2$-PBI**[262], b) **4T-PBI** und c) **7T-PBI** mit den PBI Segmenten in rot und den Oligothiophenen in blau koloriert. Die Schwefelatome sind in gelb hervorgehoben. Die aliphatischen Ketten, sowie Lösungsmittelmoleküle sind aufgrund der Übersichtlichkeit nicht dargestellt. d) DPV Spektren von **4T-PBI**, **5T-PBI**[262], **6T-PBI**, **7T-PBI** und **(5T)$_2$-PBI**[262] (von unten nach oben). e) UV/Vis/NIR (nahinfrarot) Absorptionsspektren von **4T-PBI** (schwarze Linie) nach elektrochemischer Reduktion zu **4T-PBI$^{\bullet-}$** (rote Linie) and elektrochmischer Oxidation zu **4T$^{\bullet+}$-PBI** (blaue Linie). Alle Messungen wurden in CH_2Cl_2 mit Bu_4NPF_6 bei Raumtemperatur durchgeführt ($c_0 = 10^{-4}$ M). f) Evolutionsassoziierte Differenzspektren (EADS) und Lebenszeiten von einer globalen Fit-Analyse der transienten Absorptionsspektren von Makrozyklen **4T-PBI** und **7T-PBI**, welche durch Anregung bei 530 nm in CH_2Cl_2 erhalten wurden ($c_0 = 10^{-4}$ M).

Ein Vorteil von zwei spektral unterscheidbaren Regionen der makrozyklischen Dyaden **4T-PBI** bis **7T-PBI** und **(5T)$_2$-PBI** für Donor und Akzeptor ist die Möglichkeit zur selektiven Lichtanregung beider Chromophore. Nach Anregung des PBI-Segments bei 480 nm konnte die typische, fein strukturierte Emission des PBI S_0-S_1-Übergangs beobachtet werden. Alleinige Anregung des Oligothiophenteils bei 400 nm offenbarte auch PBI-Emission, was ein starker Hinweis für einen FRET von der elektronendonierenden Kette zum elektronenakzeptierenden PBI ist.

Dadurch, dass die Oxidation des Donors (blau) und die Reduktion des Akzeptors (rot) getrennt voneinander gesteuert werden kann (Abbildung 3d), ist die angesprochene spektrale Unterscheidbarkeit begleitet von elektronischer Entkopplung der makrozyklischen Segmente. Insgesamt unterscheiden sich die Reduktionspotentiale der Makrozyklen nicht mehr als 0.1 V von den Werten des **Ref-PBI**'s. Auf der anderen Seite können die Oxidationspotentiale der Referenzstränge **5T** und **7T** durch die besondere aliphatische Substitution nicht direkt mit den jeweligen makrozylischen Brücken in **5T-**

PBI und **7T-PBI** verglichen werden. Dennoch liegen alle Oxidationspotentiale der Makrozyklen im ungefähr gleichen Bereich, wie die von **4T-7T**. Am interessantesten ist hier, dass die Potentialdifferenz der ersten und zweiten Oxidation ($E_{ox,2} - E_{ox,1}$) von **4T-PBI** (0.26 V) zu **6T-PBI** (0.08 V) abnimmt, was auf eine graduelle Stabilisierung des dikationischen Zustandes innerhalb dieser Serie hinweist. Im Gegensatz dazu führt eine *trans*-Anordnung der am nähesten zu den Phenylringen gelegenen Thiophene bei **7T-PBI** wiederum zu einem Anstieg der Potentialdifferenz von 0.18 V, was mit jener der freien **7T** Kette (0.19 V) vergleichbar ist. Gegenteilig zu den einfach überbrückten PBIs (**4T-PBI** bis **7T-PBI**), werden in jedem Oxidationsvorgang von **(5T)$_2$-PBI** zwei Elektronen, wahrscheinlich eines von jeder Brücke, übertragen. Wenngleich unabhängig voneinander im neutralen Zustand (siehe obige Diskussion), führt im doppelt-geladenen Zustand eine intramolekulare Kation-Kation Brückenkommunikation zu einer anschließenden schrittweisen Oxidation in den dreifach-und vierfach kationischem Zustand, was aus dem oberen DPV Spektrum (blau, rechte Welle) in Abbildung 3d gefolgert werden konnte.

Spektroelektrochemie (SEC) wurde zur Identifizierung der jeweiligen spektralen Signaturen und der elektronischen Natur der geladenen makrozyklischen Spezies durchgeführt (Abbildung 3e). Anschließend wurden die SEC Spektren mit den TA Daten verglichen, was die Interpretation dieser vereinfachte. Die TA Spektren lieferten wertvolle Einblicke in die Dynamiken im angeregten Zustand von **4T-PBI** bis **7T-PBI** (Abbildung 3f) und **(5T)$_2$-PBI** in CH_2Cl_2 nach Lichtanregung des jeweiligen PBI Segments bei 530 nm. Nach der Relaxation des PBI S_1 Zustands (schwarze Linie) in den „kalten“ Ladungstransfer- (**4T-PBI**) /ladungsgetrennten (CT/CSS, **7T-PBI**) Zustand (blaue Linie), rekombinieren die (Partial-) Ladungen innerhalb weniger Pikosekunden. Der gesamte Prozess ist einer der schnellsten für PBI-Oligothiophendyaden in der Literatur, was vermutlich mit der unmittelbaren Nähe von Donor und Akzeptor innerhalb der rigiden Makrozyklen zu begründen ist. Basierend auf den EADS Spektren konnte in der Serie von **4T-PBI** bis **7T-PBI** ein Brückenlänge-abhängiges Phänomen nach Anregung beobachtet (Abbildung 3f) werden. Während ein CT-Zustand mit Teilladungen angesiedelt auf Donor- und Akzeptorsegment für den kleinsten Makrozyklus **4T-PBI** identifiziert wurde, ist ein CSS für die größeren Analoga vorhanden. Durch die höhere Wahrscheinlichkeit des Stattfindes dieses Prozesses, wurde der schnellste (Teil-) Ladungstrennungsprozess für das doppelt überbrückte **(5T)$_2$-PBI** gefunden.

Zusammenfassend lässt sich sagen, dass innerhalb dieser Doktorarbeit fünf neue Oligothiophen-PBI D-A-Makrozyklen, ebenso wie die jeweiligen linearen Referenzstrukturen erfolgreich synthetisiert werden konnten. Alle Verbindungen wurden bezüglich ihrer optischen Eigenschaften und ihres Redoxverhaltens intensiv untersucht. Die Röntgenstrukturanalyse stellte wertvolle Erkenntnisse hinsichtlich der strukturellen Anordnung der Makrozyklen bereit und zeigte hier in Einklang mit der NMR-Analyse der Proben in Lösung hochgradig gespannte Brückensegmente. Zusätzlich bestätigte die TA-Spektroskopie in Kombination mit der SEC der Dyaden die Bildung eines von der Brückenlänge abhängigen Übergangs von vollständiger zu partieller Ladungstrennung (CSS, CT), welcher in allen Fällen fast gänzlich die Fluoreszenz löscht. Schlussendlich erlaubt diese neue makrozyklische D-A Strukturgattung eine Feinabstimmung des angeregten Zustands und sehr schnelle Elektronentransfer-Prozesse, die auch Forscher im Bereich von Materialwissenschaften für neue molekulare Bestandteile der aktiven Schichten oder Grenzflächen in maßgeschneiderten organischen photovoltaischen Bauelemente inspirieren könnte.

Bibliography

[1] M. R. Wasielewski, *Chem. Rev.* **1992**, *92*, 435-461.

[2] D. Gust, T. A. Moore, A. L. Moore, *Acc. Chem. Res.* **1993**, *26*, 198-205.

[3] J. Barber, *Chem. Soc. Rev.* **2009**, *38*, 185-196.

[4] D. Gust, T. A. Moore, A. L. Moore, *Acc. Chem. Res.* **2001**, *34*, 40-48.

[5] J. R. Durrant, S. A. Haque, E. Palomares, *Chem. Commun.* **2006**, 3279-3289.

[6] V. L. Gunderson, A. L. Smeigh, C. H. Kim, D. T. Co, M. R. Wasielewski, *J. Am. Chem. Soc.* **2012**, *134*, 4363-4372.

[7] Y. Hou, X. Zhang, K. Chen, D. Liu, Z. Wang, Q. Liu, J. Zhao, A. Barbon, *J. Mater. Chem. C* **2019**, *7*, 12048-12074.

[8] J. W. Verhoeven, H. J. van Ramesdonk, M. M. Groeneveld, A. C. Benniston, A. Harriman, *ChemPhysChem* **2005**, *6*, 2251-2260.

[9] F. M. Jradi, D. O'Neil, X. Kang, J. Wong, P. Szymanski, T. C. Parker, H. L. Anderson, M. A. El-Sayed, S. R. Marder, *Chem. Mater.* **2015**, *27*, 6305-6313.

[10] N. B. Siplivy, S. V. Feskov, A. I. Ivanov, *J. Chem. Phys.* **2020**, *153*, 044301.

[11] A. Dhanabalan, J. Knol, J. C. Hummelen, R. A. J. Janssen, *Synth. Met.* **2001**, *119*, 519-522.

[12] D. Veldman, S. C. J. Meskers, R. A. J. Janssen, *Adv. Funct. Mater.* **2009**, *19*, 1939-1948.

[13] C. Yan, S. Barlow, Z. Wang, H. Yan, A. K. Y. Jen, S. R. Marder, X. Zhan, *Nat. Rev. Mater.* **2018**, *3*, 18003.

[14] B. K. Kaletaş, R. Dobrawa, A. Sautter, F. Würthner, M. Zimine, L. De Cola, R. M. Williams, *J. Phys. Chem. A* **2004**, *108*, 1900-1909.

[15] A. Aubele, Y. He, T. Kraus, N. Li, E. Mena-Osteritz, P. Weitz, T. Heumüller, K. Zhang, C. J. Brabec, P. Bäuerle, *Adv. Mater.* **2021**, doi.org/10.1002/adma.20210357.

[16] Y. Rio, W. Seitz, A. Gouloumis, P. Vázquez, J. L. Sessler, D. M. Guldi, T. Torres, *Chem. Eur. J.* **2010**, *16*, 1929-1940.

[17] A. S. Konev, A. F. Khlebnikov, P. I. Prolubnikov, A. S. Mereshchenko, A. V. Povolotskiy, O. V. Levin, A. Hirsch, *Chem. Eur. J.* **2015**, *21*, 1237-1250.

[18] D. González-Rodríguez, T. Torres, M. M. Olmstead, J. Rivera, M. Á. Herranz, L. Echegoyen, C. A. Castellanos, D. M. Guldi, *J. Am. Chem. Soc.* **2006**, *128*, 10680-10681.

[19] Y. Wu, Y. Zhen, Z. Wang, H. Fu, *J. Phys. Chem. A* **2013**, *117*, 1712-1720.

[20] S. Lucas, T. Leydecker, P. Samorì, E. Mena-Osteritz, P. Bäuerle, *Chem. Commun.* **2019**, *55*, 14202-14205.

[21] M. Ahn, M.-J. Kim, D. W. Cho, K.-R. Wee, *J. Org. Chem.* **2021**, *86*, 403-413.

[22] V. Garg, G. Kodis, M. Chachisvilis, M. Hambourger, A. L. Moore, T. A. Moore, D. Gust, *J. Am. Chem. Soc.* **2011**, *133*, 2944-2954.

[23] Y. Sakata, H. Imahori, H. Tsue, S. Higashida, T. Akiyama, E. Yoshizawa, M. Aoki, K. Yamada, K. Hagiwara, S. Taniguchi, T. Okada, *Pure Appl. Chem.* **1997**, *69*, 1951-1956.

[24] M. R. Wasielewski, *Acc. Chem. Res.* **2009**, *42*, 1910-1921.

[25] A. K. Yudin, *Chem. Sci.* **2015**, *6*, 30-49.

[26] M. Iyoda, J. Yamakawa, M. J. Rahman, *Angew. Chem. Int. Ed.* **2011**, *50*, 10522-10553.

[27] M. Hermann, D. Wassy, B. Esser, *Angew. Chem. Int. Ed.* **2021**, *60*, 15743-15766.

[28] M. Iyoda, *J. Synth. Org. Chem., Jpn.* **2012**, *70*, 1157-1163.

[29] D. Myśliwiec, M. Kondratowicz, T. Lis, P. J. Chmielewski, M. Stępień, *J. Am. Chem. Soc.* **2015**, *137*, 1643-1649.

[30] Y. Segawa, A. Yagi, K. Matsui, K. Itami, *Angew. Chem. Int. Ed.* **2016**, *55*, 5136-5158.

[31] Y. Segawa, A. Yagi, K. Itami, *Phys. Sci. Rev.* **2017**, *2*, 1-24.

[32] M. A. Majewski, M. Stępień, *Angew. Chem. Int. Ed.* **2019**, *58*, 86-116.

[33] K. Xu, Z.-Y. Zhang, C. Yu, B. Wang, M. Dong, X. Zeng, R. Gou, L. Cui, C. Li, *Angew. Chem. Int. Ed.* **2020**, *59*, 7214-7218.

[34] E. R. Darzi, R. Jasti, *Chem. Soc. Rev.* **2015**, *44*, 6401-6410.

[35] K. H. Park, W. Kim, J. Yang, D. Kim, *Chem. Soc. Rev.* **2018**, *47*, 4279-4294.

[36] F. Mariano, M. Mazzeo, Y. Duan, G. Barbarella, L. Favaretto, S. Carallo, R. Cingolani, G. Gigli, *Appl. Phys. Lett.* **2009**, *94*, 063510.

[37] R. Fitzner, E. Reinold, A. Mishra, E. Mena-Osteritz, H. Ziehlke, C. Körner, K. Leo, M. Riede, M. Weil, O. Tsaryova, A. Weiß, C. Uhrich, M. Pfeiffer and P. Bäuerle, *Adv. Funct. Mater.* **2011**, *21*, 897-910.

[38] M. Rittner, P. Bäuerle, G. Götz, H. Schweizer, F. J. B. Calleja, M. H. Pilkuhn, *Synth. Met.* **2006**, *156*, 21-26.

[39] H. Yan, Z. Chen, Y. Zheng, C. Newman, J. R. Quinn, F. Dötz, M. Kastler and A. Facchetti, *Nature* **2009**, *457*, 679-686.

[40] F. Zhang, G. Götz, H. D. F. Winkler, C. A. Schalley, P. Bäuerle, *Angew. Chem. Int. Ed.* **2009**, *48*, 6632-6635.

[41] M. Ball, C. Nuckolls, *ACS Cent. Sci.* **2015**, *1*, 416-417.

[42] P. Spenst, F. Würthner, *J. Photochem. Photobiol. C* **2017**, *31*, 114-138.

[43] S. Nishigaki, M. Fukui, H. Sugiyama, H. Uekusa, S. Kawauchi, Y. Shibata, K. Tanaka, *Chem. Eur. J.* **2017**, *23*, 7227-7231.

[44] T. C. Lovell, K. G. Fosnacht, C. E. Colwell, R. Jasti, *Chem. Sci.* **2020**, *11*, 12029-12035.

[45] T. Kuwabara, J. Orii, Y. Segawa, K. Itami, *Angew. Chem. Int. Ed.* **2015**, *54*, 9646-9649.

[46] E. R. Darzi, E. S. Hirst, C. D. Weber, L. N. Zakharov, M. C. Lonergan, R. Jasti, *ACS Cent. Sci.* **2015**, *1*, 335-342.

[47] C. Li, C. Wang, Y. Guo,Y. Jin, N. Yao, Y. Wu, F. Zhang, W. Li, *J. Mater.Chem. C* **2019**, *7*, 3802-3810.

[48] J. M. dos Santos, L. K. Jagadamma, J. Cameron, A. A. Wiles, C. Wilson, P. J. Skabara, I. D. W. Samuel, G. Cooke, *J. Mater. Chem. C* **2021**, *9*, 16257-16271.

[49] F. Würthner, C. R. Saha-Möller, B. Fimmel, S. Ogi, P. Leowanawat, D. Schmidt, *Chem. Rev.* **2016**, *116*, 962-1052.

[50] F. Würthner, *Chem. Commun.* **2004**, 1564-1579.

[51] S. Kumar, J. Shukla, Y. Kumar, P. Mukhopadhyay, *Org. Chem. Front.* **2018**, *5*, 2254-2276.

[52] L. X. Chen, S. Xiao, L. Yu, *J. Phys. Chem. B* **2006**, *110*, 11730-11738.

[53] M. Fujitsuka, K. Harada, A. Sugimoto, T. Majima, *J. Phys. Chem. A* **2008**, *112*, 10193-10199.

[54] W.-S. Li, A. Saeki, Y. Yamamoto, T. Fukushima, S. Seki, N. Ishii, K. Kato, M. Takata, T. Aida, *Chem. Asian. J.* **2010**, *5*, 1566-1572.

[55] J. Guo, Y. Liang, S. Xiao, J. M. Szarko, M. Sprung, M. K. Mukhopadhyay, J. Wang, L. Yu, L. X. Chen, *New J. Chem.* **2009**, *33*, 1497-1507.

[56] S. Chen, Y. Liu, W. Qiu, X. Sun, Y. Ma, D. Zhu, *Chem. Mater.* **2005**, *17*, 2208-2215.

[57] J. Zhang, M. K. R. Fischer, P. Bäuerle, T. Goodson, *J. Phys. Chem. B* **2013**, *117*, 4204-4215.

[58] H. Krüger, S. Janietz, D. Sainova, D. Dobreva, N. Koch, A. Vollmer, *Adv. Funct. Mater.* **2007**, *17*, 3715-3723.

[59] J. L. Segura, H. Herrera, P. Bäuerle, *J. Mater. Chem.* **2012**, *22*, 8717-8733.

[60] A. M. Philip, C. C. Hsu, Z. Wei, M. B. Fridriksson, F. C. Grozema, W. F. Jager, *J. Chem. Phys.* **2020**, *153*, 144302.

[61] M. Ball, B. Fowler, P. Li, L. A. Joyce, F. Li, T. Liu, D. Paley, Y. Zhong, H. Li, S. Xiao, F. Ng, M. L. Steigerwald, C. Nuckolls, *J. Am. Chem. Soc.* **2015**, *137*, 9982-9987.

[62] M. L. Ball, B. Zhang, Q. Xu, D. W. Paley, V. C. Ritter, F. Ng, M. L. Steigerwald, C. Nuckolls, *J. Am. Chem. Soc.* **2018**, *140*, 10135-10139.

[63] M. Ball, B. Zhang, Y. Zhong, B. Fowler, S. Xiao, F. Ng, M. Steigerwald, C. Nuckolls, *Acc. Chem. Res.* **2019**, *52*, 1068-1078.

[64] M. L. Ball, B. Zhang, T. Fu, A. M. Schattman, D. W. Paley, F. Ng, L. Venkataraman, C. Nuckolls, M. L. Steigerwald, *Chem. Sci.* **2019**, *10*, 9339-9344.

[65] A. Mishra, C.-Q. Ma, P. Bäuerle, *Chem. Rev.* **2009**, *109*, 1141-1276.

[66] J. Roncali, *Chem. Rev.* **1997**, *97*, 173-206.

[67] D. Fichou, Handbook of Oligo-and Polythiophenes, Wiley-VCH, Weinheim, **1999**.

[68] T. Otsubo, Y. Aso, K. Takimiya, *Bull. Chem. Soc. Jpn.* **2001**, *74*, 1789-1801.

[69] T. Izumi, S. Kobashi, K. Takimiya, Y. Aso, T. Otsubo, *J. Am. Chem. Soc.* **2003**, *125*, 5286-5287.

[70] K. Müllen, G Wegner, *Elecronic Materials: The Oligomer Approach*, Wiley-VCH, Weinheim, **1998**.

[71] S. S. Zade, N. Zamoshchik, M. Bendikov, *Acc. Chem. Res.* **2011**, *44*, 14-24.

[72] M. Barth, S. Guilerez, G. Bidan, G. Bras, M. Łapkowski, *Electrochim. Acta* **2000**, *45*, 4409-4417.

[73] S. A. Ponomarenko, S. Kirchmeyer, A. Elschner, N. M. Alpatova, M. Halik, H. Klauk, U. Zschieschang, G. Schmid, *Chem. Mater.* **2006**, *18*, 579-586.

[74] G. Horowitz, D. Fichou, X. Peng, Z. Xu, F. Garnier, *Solid State Commun.* **1989**, *72*, 381-384.

[75] F. Garnier, G. Horowitz, X. Peng, D. Fichou, *Adv. Mater.* **1990**, *2*, 592-594.

[76] F. Geiger; M. Stoldt, H. Schweizer,P. Bäuerle, E. Umbach, *Adv. Mater.* **1993**, *5*, 922-925.

[77] N. Noma, T. Tsuzuki, Y. Shirota, *Adv. Mater.* **1995**, *7*, 647-648.

[78] T. Otsubo, Y. Aso, K. Takimiya, *J. Mater. Chem.* **2002**, *12*, 2565-2575.

[79] W. Steinkopf, W. Köhler, *Justus Liebigs Ann. Chem.* **1936**, *522*, 17-27.

[80] W. Steinkopf, R. Leitsmann, K. H. Hofmann, *Justus Liebigs Ann. Chem.* **1941**, *546*, 180-199.

[81] S. Gronowitz, H.-O. Karlsson, *Arkiv Kemi* **1960**, *17*, 89-92.

[82] G. Tourillon, F. Garnier, *J. Electroanal. Chem.* **1982**, *135*, 173-178.

[83] I. Osaka, R. D. McCullough, *Acc. Chem. Res.* **2008**, *41*, 1202-1214.

[84] J. Hassan, M. Sévignon, C. Gozzi, E. Schulz, M. Lemaire, *Chem. Rev.* **2002**, *102*, 1359-1470.

[85] P. E. Fanta, *Synthesis* **1974**, *1974*, 9-21.

[86] K. Tamao, S. Kodama, I. Nakajima, M. Kumada, A. Minato, K. Suzuki, *Tetrahedron* **1982**, *38*, 3347-3354.

[87] C. L. Jones, S. J. Higgins, *J. Mater. Chem.* **1999**, *9*, 865-874.

[88] U. Mitschke, P. Bäuerle, *J. Chem. Soc., Perkin Trans. 1* **2001**, 740-753.

[89] M. Pagels, G. Götz, T. Fischer, P. Bäuerle, J. Heinze, *Electrochim. Acta* **2011**, *56*, 3419-3428.

[90] N. Miyaura, A. Suzuki, *Chem. Rev.* **1995**, *95*, 2457-2483.

[91] G. Bidan, A. De Nicola, V. Enée, S. Guillerez, *Chem. Mater.* **1998**, *10*, 1052-1058.

[92] J. K. Stille, *Angew. Chem. Int. Ed. Engl.* **1986**, *25*, 508-524.

[93] B. Carsten, F. He, H. J. Son, T. Xu, L. Yu, *Chem. Rev.* **2011**, *111*, 1493-1528.

[94] G. Götz, S. Scheib, R. Klose, J. Heinze, P. Bäuerle, *Adv. Funct. Mater.* **2002**, *12*, 723-728.

[95] D. Demeter, J. Roncali, S. Jungsuttiwong, F. Melchiorre, P. Biagini, R. Po, *J. Mater. Chem. C* **2015**, *3*, 7756-7761.

[96] R. Fitzner, E. Mena-Osteritz, K. Walzer, M. Pfeiffer, P. Bäuerle, *Adv. Funct. Mater.* **2015**, *25*, 1845-1856.

[97] P. Espinet, A. M. Echavarren, *Angew. Chem. Int. Ed.* **2004**, *43*, 4704-4734

[98] S. Gronowitz, *Thiophene and its Derivatives*, Wiley, New York, **1991**.

[99] S. Gronowitz; A.-B. Hörnfeldt, *Thiophenes*, Elsevier, Oxford, **2004**.

[100] J. Tsuji, *Palladium Reagents and Catalysts*, Wiley, Chichester, **1995**.

[101] S. S. Zalesskiy, V. P. Ananikov, *Organometallics* **2012**, *31*, 2302-2309.

[102] L. Zhang, N. S. Colella, B. P. Cherniawski, S. C. B. Mannsfeld, A. L. Briseno, *ACS Appl. Mater. Interfaces* **2014**, *6*, 5327-5343.

[103] F. P. V. Koch, P. Smith, M. Heeney, *J. Am. Chem. Soc.* **2013**, *135*, 13695-13698.

[104] Z. Xu, D. Fichou, G. Horowitz, F. Garnier, *J. Electroanal. Chem.* **1989**, *267*, 339-342.

[105] D. Fichou, G. Horowitz, B. Xu, F. Garnier, *Synth. Met.* **1990**, *39*, 243-259.

[106] P. Bäuerle, *Adv. Mater.* **1992**, *4*, 102-107.

[107] A. Facchetti, M.-H. Yoon, C. L. Stern, G. R. Hutchison, M. A. Ratner, T. J. Marks, *J. Am. Chem. Soc.* **2004**, *126*, 13480-13501.

[108] L. Guyard, C. Dumas, F. Miomandre, R. Pansu, R. Renault-Méallet, P. Audebert, *New J. Chem.* **2003**, *27*, 1000-1006.

[109] Y. Zheng, T. Ohto, D. Liu, H.-J. Butt, T. Ikeda, *Synth. Met.* **2013**, *181*, 1-9.

[110] D. Rohde, L. Dunsch, A. Tabet, H. Hartmann, J. Fabian, *J. Phys. Chem. B* **2006**, *110*, 8223-8231.

[111] P. Bäuerle, U. Segelbacher, A. Maier, M. Mehring, *J. Am. Chem. Soc.* **1993**, *115*, 10217-10223.

[112] J. A. E. H. van Haare, E. E. Havinga, J. L. J. van Dongen, R. A. J. Janssen, J. Cornil, J.-L. Brédas, *Chem. Eur. J.* **1998**, *4*, 1509-1522.

[113] F. Zhang, G. Götz, E. Mena-Osteritz, M. Weil, B. Sarkar, W. Kaim, P. Bäuerle, *Chem. Sci.* **2011**, *2*, 781-784.

[114] M. B. Camarada, P. Jaque, F. R. Díaz, M. A. del Valle, *J. Polym. Sci. B Polym. Phys.* **2011**, *49*, 1723-1733.

[115] J. Casado, R. Ponce Ortiz, J. T. López Navarrete, *Chem. Soc. Rev.* **2012**, *41*, 5672-5686.

[116] K. Meerholz, J. Heinze, *Electrochim. Acta* **1996**, *41*, 1839-1854.

[117] J.-L. Brédas, G. B. Street, *Acc. Chem. Res.* **1985**, *18*, 309-315.

[118] J. Cornil, D. Beljonne, J.-L. Brédas, *J. Chem. Phys.* **1995**, *103*, 842-849.

[119] Y. Gao, C.-G. Liu, Y.-S. Jiang, *J. Phys. Chem. A* **2002**, *106*, 5380-5384.

[120] V. M. Geskin, J.-L. Brédas, *ChemPhysChem* **2003**, *4*, 498-505.

[121] M. Bednarz, P. Reineker, E. Mena-Osteritz, P. Bäuerle, *J. Lumin.* **2004**, *110*, 225-231.

[122] M. G. Hill, K. R. Mann, L. L. Miller, J. F. Penneau, *J. Am. Chem. Soc.* **1992**, *114*, 2728-2730.

[123] G. Brocks, *J. Chem. Phys.* **2000**, *112*, 5353-5363.

[124] G. A. Diaz-Quijada, N. Weinberg, S. Holdcroft, B. M. Pinto, *J. Phys. Chem. A* **2002**, *106*, 1266-1276.

[125] H. J. Egelhaaf, D. Oelkrug, W. Gebauer, M. Sokolowski, E. Umbach, T. Fischer, P. Bäuerle, *Opt. Mater.* **1998**, *9*, 59-64.

[126] F. Effenberger, F. Würthner, F. Steybe, *J. Org. Chem.* **1995**, *60*, 2082-2091.

[127] F. D'Anna, F. Pandolfi, D. Rocco, S. Marullo, M. Feroci, L. Mattiello, *New J. Chem.* **2021**, *45*, 11636-11643.

[128] R. Colditz, D. Grebner, M. Helbig, S. Rentsch, *Chem. Phys.* **1995**, *201*, 309-320.

[129] R. S. Becker, J. Seixas de Melo, A. L. Macanita, F. Elisei, *Pure Appl. Chem.* **1995**, *67*, 9-16.

[130] R. S. Becker, J. Seixas de Melo, A. L. Maçanita, F. Elisei, *J. Phys. Chem.* **1996**, *100*, 18683-18695.

[131] E. Kayahara, V. K. Patel, S. Yamago, *J. Am. Chem. Soc.* **2014**, 136, 2284-2287.

[132] M. Iyoda, H. Shimizu, *Chem. Soc. Rev.* **2015**, *44*, 6411-6424.

[133] H. Ito, Y. Mitamura, Y. Segawa, K. Itami, *Angew. Chem. Int. Ed.* **2015**, *54*, 159-163.

[134] L. Wang, S.-H. Chen, D. He, Q.-J. Li, Y.-L. Liu, M.-S. Wang, *J. Phys. Chem. C* **2020**, *124*, 11081-11091.

[135] S. Yasutomo, Š. Petr, M. Sanae, O. Haruka, I. Kenichiro, *Chem. Lett.* **2011**, *40*, 423-425.

[136] J. Krömer, I. Rios-Carreras, G. Fuhrmann, C. Musch, M. Wunderlin, T. Debaerdemaeker, E. Mena-Osteritz, P. Bäuerle, *Angew. Chem. Int. Ed.* **2000**, *39*, 3481-3486.

[137] R. Jasti, J. Bhattacharjee, J. B. Neaton, C. R. Bertozzi, *J. Am. Chem. Soc.* **2008**, *130*, 17646-17647.

[138] T. Iwamoto, Y. Watanabe, Y. Sakamoto, T. Suzuki, S. Yamago, *J. Am. Chem. Soc.* **2011**, *133*, 8354-8361.

[139] S. M. Bachrach, *J. Chem Educ.* **1990**, *67*, 907-908.

[140] C. E. Colwell, T. W. Price, T. Stauch, R. Jasti, *Chem. Sci.* **2020**, *11*, 3923-3930.

[141] E. M. Kosower, *Acc. Chem. Res.* **1982**, *15*, 259-266.

[142] K. Li, Z. Xu, H. Deng, Z. Zhou, Y. Dang, Z. Sun, *Angew. Chem. Int. Ed.* **2021**, *60*, 7649-7653.

[143] E. Mena-Osteritz, P. Bäuerle, *Adv. Mater.* **2006**, *18*, 447-451.

[144] E. Mena-Osteritz, *Adv. Mater.* **2002**, *14*, 609-616.

[145] T. Iwamoto, Y. Watanabe, T. Sadahiro, T. Haino, S. Yamago, *Angew. Chem. Int. Ed.* **2011**, *50*, 8342-8344.

[146] J. Xia, J. W. Bacon, R. Jasti, *Chem. Sci.* **2012**, *3*, 3018-3021.

[147] H. Shimizu, J. D. Cojal González, M. Hasegawa, T. Nishinaga, T. Haque, M. Takase, H. Otani, J. P. Rabe, M. Iyoda, *J. Am. Chem. Soc.* **2015**, *137*, 3877-3885.

[148] S. K. Maier, S.-S. Jester, U. Müller, W. M. Müller, S. Höger, *Chem. Commun.* **2011**, *47*, 11023-11025.

[149] S. K. Maier, G. Poluektov, S.-S. Jester, H. M. Möller, S. Höger, *Chem. Eur. J.* **2016**, *22*, 1379-1384.

[150] M. Iyoda, *Pure Appl. Chem.* **2010**, *82*, 831-841.

[151] K. Nakao, M. Nishimura, T. Tamachi, Y. Kuwatani, H. Miyasaka, T. Nishinaga, M. Iyoda, *J. Am. Chem. Soc.* **2006**, *128*, 16740-16747.

[152] M. Williams-Harry, A. Bhaskar, G. Ramakrishna, T. Goodson, M. Imamura, A. Mawatari, K. Nakao, H. Enozawa, T. Nishinaga, M. Iyoda, *J. Am. Chem. Soc.* **2008**, *130*, 3252-3253.

[153] M. Iyoda, K. Tanaka, H. Shimizu, M. Hasegawa, T. Nishinaga, T. Nishiuchi, Y. Kunugi, T. Ishida, H. Otani, H. Sato, K. Inukai, K. Tahara, Y. Tobe, *J. Am. Chem. Soc.* **2014**, *136*, 2389-2396.

[154] H. Shimizu, J. D. Cojal González, M. Hasegawa, T. Nishinaga, T. Haque, M. Takase, H. Otani, J. P. Rabe, M. Iyoda, *J. Am. Chem. Soc.* **2015**, *137*, 3877-3885.

[155] K. Asai, A. Fukazawa, S. Yamaguchi, *Chem. Commun.* **2015**, *51*, 6096-6099.

[156] R. Azumi, E. Mena-Osteritz, R. Boese, J. Benet-Buchholz, P. Bäuerle, *J. Mater. Chem.* **2006**, *16*, 728-735.

[157] P. J. Evans, E. R. Darzi, R. Jasti, *Nat. Chem.* **2014**, *6*, 404-408.

[158] J. Xia, R. Jasti, *Angew. Chem. Int. Ed.* **2012**, *51*, 2474-2476.

[159] F. Sibbel, K. Matsui, Y. Segawa, A. Studer, K. Itami, *Chem. Commun.* **2014**, *50*, 954-956.

[160] Y. Segawa, P. Šenel, S. Matsuura, H. Omachi, K. Itami, *Chem. Lett.* **2011**, *40*, 423-425.

[161] Y. Segawa, S. Miyamoto, H. Omachi, S. Matsuura, P. Šenel, T. Sasamori, N. Tokitoh, K. Itami, *Angew. Chem. Int. Ed.* **2011**, *50*, 3244-3248.

[162] E. S. Hirst, R. Jasti, *J. Org. Chem.* **2012**, *77*, 10473-10478.

[163] S. E. Lewis, *Chem. Soc. Rev.* **2015**, *44*, 2221-2304.

[164] M. R. Golder, R. Jasti, *Acc. Chem. Res.* **2015**, *48*, 557-566.

[165] V. C. Parekh and P. C. Guha, *J. Indian Chem. Soc*. **1934**, 11, 95-100.

[166] J. Franke, F. Vögtle, *Tetrahedron Lett.* **1984**, *25*, 3445-3448.

[167] R. Friederich, M. Nieger, F. Vögtle, *Chem. Ber.* **1993**, *126*, 1723-1732.

[168] H. Takaba, H. Omachi, Y. Yamamoto, J. Bouffard, K. Itami, *Angew. Chem. Int. Ed.* **2009**, *48*, 6112-6116.

[169] S. Yamago, Y. Watanabe, T. Iwamoto, *Angew. Chem. Int. Ed.* **2010**, *49*, 757-759.

[170] C. Huang, Y. Huang, N. G. Akhmedov, B. V. Popp, J. L. Petersen, K. K. Wang, *Org. Lett.* **2014**, *16*, 2672-2675.

[171] Z. Sun, N. Miyamoto, S. Sato, H. Tokuyama, H. Isobe, *Chem. Asian. J.* **2017**, *12*, 271-275.

[172] M. Hermann, D. Wassy, J. Kohn, P. Seitz, M. U. Betschart, S. Grimme, B. Esser, *Angew. Chem. Int. Ed.* **2021**, *60*, 10680-10689.

[173] G. Fuhrmann, J. Krömer, P. Bäurele, *Synth. Met.* **2001**, *119*, 125-126.

[174] G. Fuhrmann, T. Debaerdemaeker, P. Bäuerle, *Chem. Commun.* **2003**, 948-949.

[175] F. Zhang, P. Bäuerle, *J. Am. Chem. Soc.* **2007**, *129*, 3090-3091.

[176] C. Eaborn, K. J. Odell, A. Pidcock, *J. Chem. Soc., Dalton Trans.* **1978**, 357-368.

[177] M. Sato, E. Mogi, S. Kumakura, *Organometallics* **1995**, *14*, 3157-3159.

[178] S. Shekhar, J. F. Hartwig, *J. Am. Chem. Soc.* **2004**, *126*, 13016-13027.

[179] P. L. Holland, R. A. Andersen, R. G. Bergman, J. Huang, S. P. Nolan, *J. Am. Chem. Soc.* **1997**, *119*, 12800-12814.

[180] N. I. Nijegorodov, W. S. Downey, M. B. Danailov, *Spectrochim. Acta A* **2000**, *56*, 783-795.

[181] Y. Segawa, A. Fukazawa, S. Matsuura, H. Omachi, S. Yamaguchi, S. Irle, K. Itami, *Org. Biomol. Chem.* **2012**, *10*, 5979-5984.

[182] L. Adamska, I. Nayyar, H. Chen, A. K. Swan, N. Oldani, S. Fernandez-Alberti, M. R. Golder, R. Jasti, S. K. Doorn, S. Tretiak, *Nano Lett.* **2014**, *14*, 6539-6546.

[183] M. Kasha, *Discuss. Faraday Soc.* **1950**, *9*, 14-19.

[184] J. Krömer, P. Bäuerle, *Tetrahedron* **2001**, *57*, 3785-3794.

[185] E. Mena-Osteritz, F. Zhang, G. Götz, P. Reineker, P. Bäuerle, *Beilstein J. Nanotechnol.* **2011**, *2*, 720-726.

[186] P. J. Evans, E. R. Darzi and R. Jasti, *Nat. Chem.* **2014**, *6*, 404-408.

[187] J. Xia, R. Jasti, *Angew. Chem. Int. Ed*. **2012**, *51*, 2474-2476.

[188] T. J. Sisto, M. R. Golder, E. S. Hirst and R. Jasti, *J. Am. Chem. Soc.* **2011**, *133*, 15800-15802.

[189] R. Jasti and C. R. Bertozzi, *Chem. Phys. Lett.* **2010**, *494*, 1-7.

[190] E. Kayahara, L. Sun, H. Onishi, K. Suzuki, T. Fukushima, A. Sawada, H. Kaji, S. Yamago, *J. Am. Chem. Soc.* **2017**, *139*, 18480-18483.

[191] M. Kardos, D. R.P. 276357, June 14, **1913**.

[192] H. Langhals, *Color Chemistry. Synthesis, Properties and Applications of Organic Dyes and Pigments*, Wiley-VCH, Weinheim, **2004**.

[193] X. Zhan, A. Facchetti, S. Barlow, T. J. Marks, M. A. Ratner, M. R. Wasielewski, S. R. Marder, *Adv. Mater.* **2011**, *23*, 268-284.

[194] R. Blanco, R. Gómez, C. Seoane, J. L. Segura, E. Mena-Osteritz, P. Bäuerle, *Org. Lett.* **2007**, *9*, 2171-2174.

[195] F. S. Kim, X. Guo, M. D. Watson, S. A. Jenekhe, *Adv. Mater.* **2010**, *22*, 478-482.

[196] A. Pron, R. R. Reghu, R. Rybakiewicz, H. Cybulski, D. Djurado, J. V. Grazulevicius, M. Zagorska, I. Kulszewicz-Bajer, J.-M. Verilhac, *J. Phys. Chem. C* **2011**, *115*, 15008-15017.

[197] R. Rybakiewicz, J. Zapala, D. Djurado, R. Nowakowski, P. Toman, J. Pfleger, J.-M. Verilhac, M. Zagorska, A. Pron, *Phys. Chem. Chem. Phys.* **2013**, *15*, 1578-1587.

[198] S. K. Lee, Y. Zu, A. Herrmann, Y. Geerts, K. Müllen, A. J. Bard, *J. Am. Chem. Soc.* **1999**, *121*, 3513-3520.

[199] Z. Chen, B. Fimmel, F. Würthner, *Org. Biomol. Chem.* **2012**, *10*, 5845-5855.

[200] J. Deckers, T. Cardeynaels, L. Lutsen, B. Champagne, W. Maes, *ChemPhysChem* **2021**, *22*, 1488-1496.

[201] P. Gawrys, D. Boudinet, M. Zagorska, D. Djurado, J.-M. Verilhac, G. Horowitz, J. Pécaud, S. Pouget, A. Pron, *Synth. Met.* **2009**, *159*, 1478-1485.

[202] J.-L. Brédas, D. Beljonne, V. Coropceanu, J. Cornil, *Chem. Rev.* **2004**, *104*, 4971-5004.

[203] T. Förster. *Naturwissenschaften* **1946**, *33*, 166-175.

[204] T. Förster, *Ann. Phys.* **1948**, *437*, 55-75.

[205] G. D. Scholes, *Annu. Rev. Phys. Chem.* **2003**, *54*, 57-87.

[206] J. R. Lakowicz, *Principles of Fluorescence Spectroscopy*, Springer, New York, **2006**.

[207] H. Langhals, A. J. Esterbauer, A. Walter, E. Riedle, I. Pugliesi, *J. Am. Chem. Soc.* **2010**, *132*, 16777-16782.

[208] C. Menelaou, J. t. Schiphorst, A. M. Kendhale, P. Parkinson, M. G. Debije, A. P. H. J. Schenning, L. M. Herz, *J. Phys. Chem. Lett.* **2015**, *6*, 1170-1176.

[209] A. Muñoz-Losa, C. Curutchet, B. P. Krueger, L. R. Hartsell, B. Mennucci, *Biophys. J.* **2009**, *96*, 4779-4788.

[210] B. P. Krueger, G. D. Scholes, G. R. Fleming, *J. Phys. Chem. B* **1998**, *102*, 5378-5386.

[211] R. Roy, S. Hohng, T. Ha, *Nat. Methods* **2008**, *5*, 507-516.

[212] E. Ploetz, E. Lerner, F. Husada, M. Roelfs, S. Chung, J. Hohlbein, S. Weiss, T. Cordes, *Sci. Rep.* **2016**, *6*, 33257.

[213] P. Moroz, Z. Jin, Y. Sugiyama, D. A. Lara, N. Razgoniaeva, M. Yang, N. Kholmicheva, D. Khon, H. Mattoussi, M. Zamkov, *ACS Nano* **2018**, *12*, 5657-5665.

[214] R. Paul, S. Suklabaidya, S. A. Hussain, *Mater. Today: Proc.* **2020**, *46*, 6301-6303.

[215] D. L. Dexter, *J. Chem. Phys.* **1953**, *21*, 836-850.

[216] F. Strieth-Kalthoff, M. J. James, M. Teders, L. Pitzer, F. Glorius, *Chem. Soc. Rev.* **2018**, *47*, 7190-7202.

[217] E. Vauthey, *ChemPhysChem* **2012**, *13*, 2001-2011.

[218] R. A. Marcus, *J. Chem. Phys.* **1956**, *24*, 966-978.

[219] A. Heckmann, C. Lambert, *Angew. Chem. Int. Ed.* **2012**, *51*, 326-392.

[220] N. S. Hush, *Electrochim. Acta* **1968**, *13*, 1005-1023

[221] N. S. Hush, *Coord. Chem. Rev.* **1985**, *64*, 135-157.

[222] J. Schäfer, M. Holzapfel, B. Mladenova, D. Kattnig, I. Krummenacher, H. Braunschweig, G. Grampp, C. Lambert, *J. Am. Chem. Soc.* **2017**, *139*, 6200-6209.

[223] G. J. Kavarnos, *Top. Curr. Chem*. **1990**, *156*, 21-58.

[224] G. J. Kavarnos, *Fundamentals of Photoinduced Electron Transfer*, Wiley-VCH, Weinheim, **1993**.

[225] A. Weller, *Z. Phys. Chem.* **1982**, *133*, 93-98.

[226] A. Nowak-Król, B. Fimmel, M. Son, D. Kim, F. Würthner, *Faraday Discuss.* **2015**, *185*, 507-527.

[227] R. Berera, R. van Grondelle, J. T. M. Kennis, *Photosynth. Res.* **2009**, *101*, 105-118.

[228] E. P. Farr, J. C. Quintana, V. Reynoso, J. D. Ruberry, W. R. Shin, K. R. Swartz, *J. Chem. Educ.* **2018**, *95*, 864-871.

[229] M. Koch, M. Myahkostupov, D. G. Oblinsky, S. Wang, S. Garakyaraghi, F. N. Castellano, G. D. Scholes, *J. Am. Chem. Soc.* **2017**, *139*, 5530-5537.

[230] M. E. El-Khouly, D. H. Choi, S. Fukuzumi, *J. Photochem. Photobiol. A* **2011**, *218*, 17-25.

[231] Y. Ie, T. Uto, N. Yamamoto, Y. Aso, *Chem. Commun.* **2009**, 1213-1215.

[232] R. Ponnapati, M. J. Felipe, R. Advincula, *Macromolecules* **2011**, *44*, 7530-7537.

[233] A. L. Jones, M. K. Gish, C. J. Zeman, J. M. Papanikolas, K. S. Schanze, *J. Phys. Chem. A* **2017**, *121*, 9579-9588.

[234] M. K. Gish, A. L. Jones, J. M. Papanikolas, K. S. Schanze, *J. Phys. Chem. C* **2018**, *122*, 18802-18808.

[235] K. Bold, M. Stolte, F. Würthner, *Org. Mater.* **2021**, *3*, 119-127.

[236] J. E. Anthony, **2008**, *47*, 452-483.

[237] J. Roncali, P. Blanchard, P. Frère, *J. Mater. Chem.* **2005**, *15*, 1589-1610.

[238] H. Shi, C. Liu, Q. Jiang, J. Xu, *Adv. Electron. Mater.* **2015**, *1*, 1500017.

[239] B. S. Ong, Y. Wu, Y. Li, P. Liu, H. Pan, **2008**, *14*, 4766-4778.

[240] A. Mishra, P. Bäuerle, *Angew. Chem. Int. Ed.* **2012**, *51*, 2020-2067.

[241] P. Bäuerle, K.-U. Gaudl, F. Würthner, N. S. Sariciftci, M. Mehring, H. Neugebauer, C. Zhong, K. Doblhofer, *Adv. Mater.* **1990**, *2*, 490-494.

[242] P. Bäuerle, F. Würthner, G. Götz, F. Effenberger, *Synthesis* **1993**, *1993*, 1099-1103.

[243] G. Barbarella, M. Zambianchi, A. Bongini, L. Antolini, *Adv. Mater.* **1993**, *5*, 834-838.

[244] J. Heinze, R. Bilger, K. Meerholz, *Ber. Bunsen-Ges. Phys. Chem.* **1988**, *92*, 1266-1271.

[245] P. Bäuerle, F. Pfau, H. Schlupp, F. Würthner, K.-U. Gaudl, M. B. Caro, P. Fischer, *J. Chem. Soc., Perkin Trans. 2* **1993**, 489-494.

[246] F. Würthner, R. Schmidt, *ChemPhysChem* **2006**, *7*, 793-797.

[247] H. Nikoofard, M. Gholami, *C. R. Chim.* **2014**, *17*, 1034-1040.

[248] A. M. Brouwer, *Pure Appl. Chem.* **2011**, 83, 2213-2228.

[249] P. Bäuerle, T. Fischer, B. Bidlingmeier, J. P. Rabe, A. Stabel, *Angew. Chem. Int. Ed. Engl.* **1995**, *34*, 303-307.

[250] R. Englman, J. Jortner, *Mol. Phys.* **1970**, *18*, 145-164.

[251] P. Bäuerle, U. Segelbacher, K.-U. Gaudl, D. Huttenlocher, M. Mehring, *Angew. Chem. Int. Ed. Engl.* **1993**, *32*, 76-78.

[252] K. Deuchert, S. Hünig, *Angew. Chem. Int. Ed. Engl.* **1978**, *17*, 875-886.

[253] S. Hünig, *Pure Appl. Chem.* **1990**, *62*, 395-406.

[254] S. Hünig, W. Schenk, *Liebigs Ann. Chem.* **1979**, 1523-1533.

[255] K. Hesse, S. Hünig, *Liebigs Ann. Chem.* **1985**, *1985*, 708-714.

[256] R. Rausch, M. I. S. Röhr, D. Schmidt, I. Krummenacher, H. Braunschweig, F. Würthner, *Chem. Sci.* **2021**, *12*, 793-802.

[257] A. B. Pun, A. Asadpoordarvish, E. Kumarasamy, M. J. Y. Tayebjee, D. Niesner, D. R. McCamey, S. N. Sanders, L. M. Campos, M. Y. Sfeir, *Nat. Chem.* **2019**, *11*, 821-828.

[258] D. Bialas, E. Kirchner, M. I. S. Röhr, F. Würthner, *J. Am. Chem. Soc.* **2021**, *143*, 4500-4518.

[259] M. Takahashi, K. Masui, H. Sekiguchi, N. Kobayashi, A. Mori, M. Funahashi, N. Tamaoki, *J. Am. Chem. Soc.* **2006**, *128*, 10930-10933.

[260] N. Kiriy, A. Kiriy, V. Bocharova, M. Stamm, S. Richter, M. Plötner, W.-J. Fischer, F. C. Krebs, I. Senkovska, H.-J. Adler, *Chem. Mater.* **2004**, *16*, 4757-4764.

[261] M.-A. Sato, K. Fukui, Synth. Met. 2007, 157, 619-626.

[262] K. Bold, M. Stolte, K. Shoyama, M. Holzapfel, A. Schmiedel, C. Lambert, F. Würthner, Angew. Chem. Int. Ed. **2022**, *61*, e202113598.

[263] F. Vögtle, *Reizvolle Moleküle der Organischen Chemie*, Teubner Studienbücher, Leipzig, **1989**.

[264] F. Diederich, *Angew. Chem. Int. Ed.* **1988**, *27*, 362-386; *Angew. Chem.* **1988**, *100*, 372-396.

[265] Z. Liu, S. K. M. Nalluri, J. F. Stoddart, *Chem. Soc. Rev.* **2017**, *46*, 2459-2650.

[266] D. Canevet, E. M. Pérez, N. Martín, *Angew. Chem. Int. Ed.* **2011**, *50*, 9248-9259; *Angew. Chem.* **2011**, *123*, 9416-9427.

[267] Y. Xu, M. von Delius, *Angew. Chem. Int. Ed.* **2020**, *59*, 559-573; *Angew. Chem.* **2020**, *132*, 567-582.

[268] E. L. Spitler, C. A. Johnson II, M. M. Haley, *Chem. Rev.* **2006**, *106*, 5344-5386.

[269] F. Diederich, H. A. Staab, *Angew. Chem. Int. Ed.* **1978**, *17*, 372-374; *Angew. Chem.* **1978**, *90*, 383-385.

[270] D. Ajami, O. Oeckler, A. Simon, R. Herges, *Nature* **2003**, *426*, 819-821.

[271] Z. S. Yoon, A. Osuka, D. Kim, *Nat. Chem.* **2009**, *1*, 113-122.

[272] M. Rickhaus, M. Jirasek, L. Tejerina, H. Gotfredsen, M. D. Peeks, R. Haver, H.-W. Jiang, T. D. W. Claridge, H. L. Anderson, *Nat. Chem.* **2020**, *12*, 236-241.

[273] Y. Nakamura, I.-W. Hwang, N. Aratani, T. K. Ahn, D. M. Ko, A. Takagi, T. Kawai, T. Matsumoto, D. Kim, A. Osuka, *J. Am. Chem. Soc.* **2005**, *127*, 236-246.

[274] F. Schlosser, J. Sung, P. Kim, D. Kim, F. Würthner, *Chem. Sci.* **2012**, *3*, 2778-2785.

[275] Y. S. Sung, M.-C. Yoon, J. M. Lim, H. Rath, K. Naoda, A. Osuka, D. Kim, *Nat. Chem.* **2015**, *7*, 418-422.

[276] K. Kaiser, L. M. Scriven, F. Schulz, P. Gawel, L. Gross, H. L. Anderson, *Science* **2019**, *365*, 1299-1301.

[277] J. Pruchyathamkorn, W. J. Kendrick, A. T. Frawley, A. Mattioni, F. Caycedo-Soler, S. F. Huelga, M. B. Plenio, H. L. Anderson, *Angew. Chem. Int. Ed.* **2020**, *59*, 16455-16458.

[278] K. J. Weiland, T. Brandl, K. Atz, A. Prescimone, D. Häussinger, T. Šolomek, M. Mayor, *J. Am. Chem. Soc.* **2019**, *141*, 2104-2110.

[279] G. Povie, Y. Segawa, T. Nishihara, Y. Miyauchi, K. Itami, *Science* **2017**, *356*, 172-175.

[280] S. H. Pun, Q. Miao, *Acc. Chem. Res.* **2018**, *51*, 1630-1642.

[281] N. Aratani, D. Kim, A. Osuka, *Acc. Chem. Res.* **2009**, *42*, 1922-1934.

[282] P. S. Bols, H. L. Anderson, *Acc. Chem. Res.* **2018**, *51*, 2083-2092.

[283] P. Qian, C. A. Siebert, P. Wang, D. P. Canniffe, N. Hunter, *Nature* **2018**, *556*, 203-208.

[284] L.-J. Yu, M. Suga, Z.-Y. Otomo, J.-R. Shen, *Nature* **2018**, *556*, 209-213.

[285] R.J. Cogdell, A. Gall, J. Köhler, *Q. Rev. Biophys.* **2006**, *39*, 227-324.

[286] A. Nowak-Król, F. Würthner, *Org. Chem. Front.* **2019**, *6*, 1272-1318.

[287] M. Mahl, K. Shoyama, A.-M. Krause, D. Schmidt, F. Würthner, *Angew. Chem. Int. Ed.* **2020**, *59*, 13401-13405.

[288] B. Zhang, H. Soleimaninejad, D. J. Jones, J. M. White, K. P. Ghiggino, T. A. Smith, W. W. H. Wong, *Chem. Mater.* **2017**, *29*, 8395-8403.

[289] Y. S. Chong, M. D. Smith, K. D. Shimizu, *J. Am. Chem. Soc.* **2001**, *123*, 7463-7464.

[290] F. Yang, C. Liu, D. Yin, Y. Xu, M. Wu, W. Wei, *Chem. Commun.* **2019**, *55*, 14335-14338.

[291] M. A. Majewski, M. Stępień, *Angew. Chem. Int. Ed.* **2019**, *58*, 86-116.

[292] A. Reiko, G. Midori, H. Kazumasa, M. Mutsuyoshi, *Bull. Chem. Soc. Jpn.* **2003**, *76*, 1561-1567.

[293] R. Renner, M. Stolte, J. Heitmüller, T. Brixner, C. Lambert, F. Würthner, *Mater. Horiz.* **2022**, *9*, 350-359.

[294] H. Thakellapalli, B. Farajidizaji, T. W. Butcher, N. G. Akhmedov, B. V. Popp, J. L. Petersen, K. K. Wang, *Org. Lett.* **2015**, *17*, 3470-3473.

[295] K. Adachi, Y. Hirao, K. Matsumoto, T. Kubo, H. Kurata, *Org. Lett.* **2014**, *16*, 5870-5873.

[296] T. Sakai, T. Satou, T. Kaikawa, K. Takimiya, T. Otsubo, Y. Aso, *J. Am. Chem. Soc.* **2005**, *127*, 8082-8089.

[297] T. Liu, J. Yang, F. Geyer, F. S. Conrad-Burton, R. Hernández Sánchez, H. Li, X. Zhu, C. P. Nuckolls, M. L. Steigerwald, S. Xiao, *Angew. Chem. Int. Ed.* **2020**, *59*, 14303-14307.

[298] W. E. Benjamin, D. R. Veit, M. J. Perkins, E. Bain, K. Scharnhorst, S. McDowall, D. L. Patrick, J. D. Gilbertson, *Chem. Mater.* **2014**, *26*, 1291-1293.

[299] W. Kabsch, *Acta Crystallogr. D* **2010**, *66*, 125-132.

[300] Bruker, **2014**, XPREP Version 2014/2, Bruker AXS Inc., Madison.

[301] G. M. Sheldrick, *Acta Crystallogr. A* **2008**, *64*, 112-122.

[302] N. Auerhammer, A. Schulz, A. Schmiedel, M. Holzapfel, J. Hoche, M. I. S. Röhr, R. Mitric, C. Lambert, *Phys. Chem. Chem. Phys.* **2019**, *21*, 9013-9025.

[303] Gaussian 16, Revision B.01, M. J. Frisch, G. W. Trucks, H. B. Schlegel, G. E. Scuseria, M. A. Robb, J. R. Cheeseman, G. Scalmani, V. Barone, G. A. Petersson, H. Nakatsuji, X. Li, M. Caricato, A. V. Marenich, J. Bloino, B. G. Janesko, R. Gomperts, B. Mennucci, H. P. Hratchian, J. V. Ortiz, A. F. Izmaylov, J. L. Sonnenberg, D. Williams-Young, F. Ding, F. Lipparini, F. Egidi, J. Goings, B. Peng, A. Petrone, T. Henderson, D. Ranasinghe, V. G. Zakrzewski, J. Gao, N. Rega, G. Zheng, W. Liang, M. Hada, M. Ehara, K. Toyota, R. Fukuda, J. Hasegawa, M. Ishida, T. Nakajima, Y. Honda, O. Kitao, H. Nakai, T. Vreven, K. Throssell, J. A. Montgomery, Jr., J. E. Peralta, F. Ogliaro, M. J. Bearpark, J. J. Heyd, E. N. Brothers, K. N. Kudin, V. N. Staroverov, T. A. Keith, R. Kobayashi, J. Normand, K. Raghavachari, A. P. Rendell, J. C. Burant, S. S. Iyengar, J. Tomasi, M. Cossi, J. M. Millam, M. Klene, C. Adamo, R. Cammi, J. W. Ochterski, R. L. Martin, K. Morokuma, O. Farkas, J. B. Foresman, and D. J. Fox, Gaussian, Inc., Wallingford CT, **2016**.

[304] For a similar half-life time determination of two rotamers, see ref. [290].

[305] For a similar determination of strain energies, see ref. [61].

[306] K. Bold, M. Stolte, K. Shoyama, A.-M. Krause, A. Schmiedel, M. Holzapfel, C. Lambert, F. Würthner, *Chem. Eur. J.* **2022**, e202200355.

[307] H. Thakellapalli, S. Li, B. Farajidizaji, N. N. Baughman, N. G. Akhmedov, B. V. Popp, K. K. Wang, *Org. Lett.* **2017**, *19*, 2674-2677.

[308] C. Li, C. Wang, Y.Guo, Y. Jin, N. Yao, Y. Wu, F. Zhang, W. Li, *J. Mater.Chem. C* **2019**, *7*, 3802-3810.

[309] T. C. Lovell, Z. R. Garrison, R. Jasti, *Angew. Chem. Int. Ed.* **2020**, *59*, 14363-14367.

[310] Z.-L. Qiu, C. Tang, X.-R. Wang, Y.-Y. Ju, K.-S. Chu, Z.-Y. Deng, H. Hou, Y.-M. Liu, Y.-Z. Tan, *Angew. Chem. Int. Ed.* **2020**, *59*, 20868-20872.

[311] J. Huang, H. Fu, Y. Wu, S. Chen, F. Shen, X. Zhao, Y. Liu, J. Yao, *J. Phys. Chem. C* **2008**, *112*, 2689-2696.

[312] P. Spenst, F. Würthner, *Angew. Chem. Int. Ed.* **2015**, *54*, 10165-10168.

[313] M. Zhang, H. Fan, X. Guo, Y. Yang, S. Wang, Z.-G. Zhang, J. Zhang, X. Zhan, Y. Li, *Polym. Chem.* **2011**, *49*, 2746-2754.

[314] G. M. Sheldrick, *Acta Crystallogr. A* **2015**, *71*, 3-8.

[315] G. M. Sheldrick, *Acta Crystallogr. C* **2015**, *71*, 3-8.

[316] J. M. Brown, N. A. Cooley, *Chem. Rev.* **1988**, *88*, 1031-1046.

Individual Contribution

The coauthors of the manuscripts included in this cumulative thesis are informed and agree with the reprint and the respective individual contributions as stated below.

Unusual Zig-Zag Effect in the Electrochemical Oxidation of Phenyl End-Capped α-Oligothiophenes

K. Bold, M. Stolte, F. Würthner, *Org. Mater.* **2021**, *3*, 119-127.

Author	**K. B.**	**M. S.**	**F. W.**
Design of research	45%	10%	45%
Synthesis	100%	–	–
Compound Characterization	100%	–	–
Optical investigations	100%	–	–
Electronic investigations	100%	–	–
Publication writing	50%	10%	40%
Publication correction	10%	30%	60%
Publication coordination	10%	30%	60%

Macrocyclic Donor–Acceptor Dyads Composed of a Perylene Bisimide Surrounded by Oligothiophene Bridges

K. Bold, M. Stolte, K. Shoyama, M. Holzapfel, A. Schmiedel, C. Lambert, F. Würthner, *Angew. Chem. Int. Ed.* **2022**, *61*, e202113598; *Angew. Chem.* **2022**, *134*, e202113598.

Author	**K. B.**	**M. S.**	**K. S.**	**M. H.**	**A. S.**	**C. L.**	**F. W.**
Design of research	35%	10%	–	–	–	–	55%
Synthesis	100%	–	–	–	–	–	–
Compound Characterization	100%	–	–	–	–	–	–
Optical investigations	100%	–	–	–	–	–	–
Electronic investigations	100%	–	–	–	–	–	–
(TD)DFT calculations	100%	–	–	–	–	–	–
Crystallographic analysis	–	–	100%	–	–	–	–
TA measurements	–	–	–	–	100%	–	–
TA spectra analysis	–	–	–	80%	–	20%	–
Publication writing	60%	20%	–	–	–	–	20%
Publication correction	15%	40%	5%	–	–	10%	30%
Publication coordination	20%	30%	–	–	–	–	50%

Macrocyclic Donor−Acceptor Dyads Composed of Oligothiophene Half-Cycles and Perylene Bisimides

K. Bold, M. Stolte, K. Shoyama, A.-M. Krause, A. Schmiedel, M. Holzapfel, C. Lambert, F. Würthner, *Chem. Eur. J.* **2022**, e202200355.

Author	**K. B.**	**M. S.**	**K. S.**	**A. K.**	**A. S.**	**M. H.**	**C. L.**	**F. W.**
Design of research	55%	10%	–	–	–	–	–	35%
Synthesis	100%	–	–	–	–	–	–	–
Compound Characterization	100%	–	–	–	–	–	–	–
Optical investigations	100%	–	–	–	–	–	–	–
Electronic investigations	100%	–	–	–	–	–	–	–
(TD)DFT calculations	100%	–	–	–	–	–	–	–
Crystallographic analysis	–	–	50%	50%	–	–	–	–
TA measurements	–	–	–	–	100%	–	–	–
TA spectra analysis	–	–	–	–	–	80	20%	–
Publication writing	60%	20%	–	–	–	–	–	20%
Publication correction	15%	40%	–	–	–	–	15%	30%
Publication coordination	20%	50%	–	–	–	–	–	30%

Danksagung

Mein besonderer Dank gilt meinem Doktorvater Prof. Dr. Frank Würthner für die Bereitstellung dieses außerordentlich interessanten Forschungsprojektes, die stetige Unterstützung und die zahlreichen Ratschläge zur Weiterentwicklung des Themas. Desweiteren möchte ich mich bei ihm für die Bereitstellung der exzellenten Arbeitsbedingungen und den äußerst schnellen und effizienten fachlichen Austausch bedanken.

Als nächstes danke ich Dr. Matthias Stolte für sehr hilfreiche Diskussionen, die wirklich herausragende Betreuung und die Hilfe beim Verfassen und Überarbeiten von Manuskripten. In diesem Zuge möchte ich auch Dr. Chantu R. Saha-Möller, sowie Dr. Kazutaka Shoyama insbesondere für zahlreiche synthetische Tipps und Dr. David Bialas für die Hilfestellung bei Fragestellungen zu theoretischer Chemie danken. Zusätzlich bedanke ich mich bei allen vier Personen für die Betreuung im Rahmen der Subgroups.

Zu weiterem großen Dank bin ich Dr. Kazutaka Shoyama und Ana-Maria Krause für die Durchführung von Kristallstrukturanalysen mit jedem noch so winzigen Kristall und die damit verdundene, sehr zeitaufwendige Datenauswertung verpflichtet.

Ebenfalls bedanke ich mich bei Dr. Kazutaka Shoyama für die große Hilfe bei der Durchführung von theoretischen Rechnungen. Bei Michael Moos möchte ich mich für die Einführung in die manchmal sehr „spannenden“ spektroelektrochemischen Messungen bedanken. Dr. Matthias Güne, Patrizia Altenberger und Stefanie Schmitt danke ich für die Aufnahme zahlreicher NMR-Spektren. Desweiteren bedanke ich mich bei Dr. Michael Büchner und Juliane Adelmann für alle massenspektrometrischen Untersuchungen.

Für die Messung von transienter Absorption und die damit zusammenhängende Auswertung möchte ich mich bei Alexander Schmiedel und Dr. Marco Holzapfel bedanken. Prof. Dr. Christoph Lambert danke ich für die sehr angenehme Kooperation, die tollen fachlichen Hilfestellungen und die stets sehr unterhaltsamen E-Mails.

Für das Korrekturlesen dieser Arbeit bedanke ich mich bei Dr. Rebecca Renner und Dr. Matthias Stolte.

Petra Seufert-Baumbach, Anja Rausch, Julius Albert und Maximilian Roth möchte ich für die Organisation eines stets reibungslosen Laboralltags und die Bestellung von Chemikalien und Materialien danken. Bei Christiana Toussaint, Eleonore Klaus, Sarah Bullnheimer und Lisa Weidner danke ich für die große Hilfe bei administratorischen und organisatorischen Fragestellungen.

Für die synthetische Unterstützung bin ich Anja Rausch und Julius Albert zum Dank verpflichtet. In diesem Zusammenhang gilt auch ein großes Dankeschön die Praktikanten Nils Schopper, Maximilian Dietz, Tilman Schneider und Yvonnen Vonhausen, sowie die Bachelor-Studierenden Jonas Bachmann und Franziska Schneider. Desweiteren möchte ich dem Auszubildenden Lukas Schmidt für die Synthese zahlreicher Verbindungen danken.

Ein großer Dank gilt dem gesamten Arbeitskreis Würthner, sowie bei den Arbeitskreisen Beuerle und Nowak-Król für die enorme Hilfsbereitschaft untereinander, die überragende Laboratmosphäre, den tollen fachlichen Austausch, die interessanten Pausengespräche und die schöne Zeit auch außerhalb des Labors.

Zuletzt möchte ich meinen Eltern und Julia für die unerbittliche Unterstützung und immerwährende Rückendeckung während des gesamten Studiums und der Doktorarbeit danken.

List of Publications

Isomerisation, reactivity and coordination chemistry of a new hybrid, multi-functional phosphazane

A. J. Plajer, K. Bold, F. J. Rizzuto, R. García-Rodríguez, T. K. Ronson, D. S. Wright, *Dalton Trans.* **2017**, *46*, 12775-12779.

Unusual Zig-Zag Effect in the Electrochemical Oxidation of Phenyl End-Capped α-Oligothiophenes

K. Bold, M. Stolte, F. Würthner, *Org. Mater.* **2021**, *3*, 119-127.

Macrocyclic Donor−Acceptor Dyads Composed of a Perylene Bisimide Surrounded by Oligothiophene Bridges

K. Bold, M. Stolte, K. Shoyama, M. Holzapfel, A. Schmiedel, C. Lambert, F. Würthner, *Angew. Chem. Int. Ed.* **2022**, *61*, e202113598; *Angew. Chem.* **2022**, *134*, e202113598.

Macrocyclic Donor−Acceptor Dyads Composed of Oligothiophene Half-Cycles and Perylene Bisimides

K. Bold, M. Stolte, K. Shoyama, A.-M. Krause, A. Schmiedel, M. Holzapfel, C. Lambert, F. Würthner, *Chem. Eur. J.* **2022**, e202200355.